

**CORRELATING MICROSTRUCTURE TO LOCALIZED
CORROSION AND HYDROGEN EMBRITTLEMENT OF
13 Wt.% Cr MARTENSITIC STAINLESS STEEL**

By

SUNIL KUMAR BONAGANI

CHEM01201204004

Bhabha Atomic Research Centre, Mumbai, India

A thesis submitted to the

Board of Studies in Chemical Sciences

In partial fulfillment of requirements

For the Degree of

DOCTOR OF PHILOSOPHY

of

HOMI BHABHA NATIONAL INSTITUTE



March, 2018

Certificate

will be

Uploaded

Soon

STATEMENT BY AUTHOR

This dissertation has been submitted in partial fulfillment of requirements for an advanced degree at Homi Bhabha National Institute (HBNI) and is deposited in the Library to be made available to borrowers under rules of the HBNI.

Brief quotations from this dissertation are allowable without special permission, provided that accurate acknowledgement of source is made. Requests for permission for extended quotation from or reproduction of this manuscript in whole or in part may be granted by the Competent Authority of HBNI when in his or her judgment the proposed use of the material is in the interests of scholarship. In all other instances, however, permission must be obtained from the author.

Sunil Kumar Bonagani

DECLARATION

I, hereby declare that the investigation presented in the thesis has been carried out by me. The work is original and has not been submitted earlier as a whole or in part for a degree / diploma at this or any other Institution / University.

Sunil Kumar Bonagani

LIST OF PUBLICATIONS ARISING FROM THE THESIS

Journal:

1. “Effect of tempering treatments on microstructure and intergranular corrosion of 13wt% Cr martensitic stainless steel”, Sunil Kumar, V. Kain, Vishwanadh B, *Corrosion*, **2017**, 73 (4)., 362-378.
2. “Influence of hydrogen on mechanical properties and fracture of tempered 13 wt.% Cr martensitic stainless steel”, Sunil Kumar Bonagani, Vivekanand Kain, Manpreet Singh, B. Vishwanadh, *Materials Science Engineering A*, **2017**, 700., 140-151.
3. “Influence of tempering treatment on microstructure and pitting Corrosion of 13 wt.% Cr martensitic stainless steel”, Sunil Kumar Bonagani, B. Vishwanadh, Vivekanand Kain, *Corrosion Science*, **2018**, 131., 340-354.
4. “Influence of tempering treatments on mechanical properties and hydrogen embrittlement of 13wt.% Cr martensitic stainless steel”, Sunil Kumar Bonagani, Vivekanand Kain, B. Vishwanadh, N. Naveen, *manuscript under review in International Journal of Pressure Vessels & Piping*, **2018**.
5. “An XPS and electrochemical study of surface films formed on 13wt.% Cr martensitic stainless steel: Effect of tempering”, Sunil Kumar Bonagani, Vivekanand Kain, Rumu Halder, *manuscript under preparation*.

Conference/Symposium & Presentations:

1. “Effect of austenitizing and tempering on microstructure & intergranular corrosion behaviour of Type 420 martensitic stainless steel”, Sunil Kumar & Vivekanand Kain; *NMD-ATM 2013, IIT (BHU), Varanasi*.
2. “Susceptibility to hydrogen embrittlement of tempered martensitic stainless steel 420B”, Sunil Kumar, Manpreet Singh & Vivekanand Kain; *NMD-ATM 2014, Pune*.
3. “Effect of austenitization temperature and time on microstructural and corrosion behaviour of Type 420 martensitic stainless steel”, Sunil Kumar & Vivekanand Kain; *CORSYM 2014, IIT Bombay*.
4. “Hydrogen embrittlement of UNS 42000 martensitic stainless steel: Effect of tempering treatments”, Sunil Kumar, Vivekanand Kain, Manpreet Singh & Vishwanadh B; *Proceedings of International Corrosion Conference and Expo (CORCON)-2015*.
5. “Effect of tempering treatments on microstructure and intergranular corrosion of 13wt.% Cr martensitic stainless steel”, Sunil Kumar, Vivekanand Kain & Vishwanadh B; *Proceedings of International Corrosion Conference and Expo (CORCON)-2016*.
6. “Influence of tempering treatments on microstructure & localized corrosion of 13wt.% Cr martensitic stainless steel”, Sunil Kumar, Vivekanand Kain & Vishwanadh B; *Microstructure 2016, IIT Bombay*.

Sunil Kumar Bonagani

DEDICATED

To

My parents (Venkatalaxmi - Ramulu)

&

My wife (Swathi) and loving Son (Arjun)

&

all my teachers

ACKNOWLEDGEMENTS

I would take this opportunity to thank all who supported me throughout this thesis work.

At the outset, I would like to express my deep sense of gratitude to my guide **Prof. Vivekanand Kain** for initiating me into the research field of materials and corrosion. His suggestions and guidance at every stage of this work has been very crucial and I am grateful to him for helping me at every stage for completing this work.

I am also thankful to **Prof. Gautam Kumar Dey, Chairman and Prof. P. K. Pujari and Prof. A.K. Tyagi, member of doctoral committee** for their valuable suggestions and discussions.

Special thanks to Dr B. Viswanath, MSD, BARC for his tremendous help in electron microscopy studies. His enthusiastic and scientific approach towards research is a source of inspiration to me.

My special thanks to my lab mate Cdr Tenneti Sharma and Materials Group, BARC colleagues, D. Harish, Dr. N. Naveen Kumar and Sai Ram for their help and sharing scientific knowledge.

Thanks are also due to Dr. Amit Verma, Miss. Malvika, Mrs. Rumu Haldar for their timely help in XRD and XPS characterization. I would take this opportunity to thank Ravi Hankare, Mahindra Patil and Vivek Choudhari for their assistance in sample preparation.

I would take this opportunity to thank my colleagues from corrosion engineering section for their technical suggestions, encouragement and cooperative attitude which have greatly helped in my research work. Special thanks to my colleague Shri Vivekanand Dubey for his technical suggestions in electrochemical experiments. I am very grateful to Dr. M. Kiran Kumar, for his diversified help at several stages.

I greatly acknowledge the support provided by Smt Smita and Dr. Bhupesh from ACD, BARC in hydrogen analysis. I thank Mrs. Riya Modal and Prof. Samjdar for their help in EBSD studies. I

am very thankful to Mr. Manpreet Singh from PEC, Chandigarh, who worked as project student and helped me in carrying out SSRT experiments.

I take this opportunity to express my heartfelt gratitude to my parents for their blessings and support for what I am today. I thank the support and guidance received from my school teacher Shri Praveen Kumar for grooming my carrier.

Finally, most importantly, I would like to express tons of thanks to my wife **Swathi Priya** for her support, patience and encouragement and my little son **Arjun Bonagani**.

Sunil Kumar Bonagani

CONTENTS

	Page No.
ABSTRACT	xii
LIST OF ABBREVIATIONS	xiv
LIST OF FIGURES	xv
LIST OF TABLES	xxii
Chapter 1	1
Introduction	1
1.1 Background	1
1.2 Objectives of the study.....	4
1.3 Structure of the thesis.....	5
Chapter 2	7
Literature review	7
2.1 Martensitic Stainless Steels: Overview	7
2.1.1. Role of alloying elements	9
2.2. Heat treatment of martensitic stainless steels.....	11
2.2.1. Annealing and Austenitization	11
2.2.2. Tempering.....	16
2.2.2.1. Microstructural changes with tempering treatments.....	17
2.2.2.2. Cr depletion associated with carbide precipitation in MSSs	19
2.3. Degradation modes in martensitic stainless steels	21
2.3.1. Intergranular corrosion	22
2.3.1.1. Evaluating the susceptibility to IGC of stainless steels	23
2.3.1.2. Effect of tempering treatments on IGC of MSSs.....	24
2.3.2. Pitting corrosion	27
2.3.2.1. Effect of tempering treatments on pitting corrosion	27
2.3.3. Changes in mechanical properties with tempering treatments	29
2.4. HE in martensitic steels.....	33
2.4.1. Cooperative relation between temper embrittlement and HE	37

Chapter 3	39
Microstructural changes in austenitized & tempered conditions.....	39
3.1. Background	39
3.2. Experimental	39
3.2.1. Materials and heat treatments	39
3.2.2. Microstructural Characterization.....	41
3.3. Results and Discussion.....	43
3.3.1. Transformation temperatures and Austenitization	43
3.3.2. Microstructural changes with tempering temperature	46
3.3.2.1. XRD analysis	46
3.3.2.2. Characterization by SEM.....	47
3.3.2.3. Characterization by TEM.....	50
3.3.2.4. XRD analysis of the precipitates extracted from tempered specimens.....	57
3.3.2.5. TEM analysis of the extracted precipitates	59
3.3.2.6. TEM-EDS analysis	60
3.3.2.7. EBSD studies on austenitized and tempered specimens.....	63
3.4. Highlights.....	67
Chapter 4	69
Effect of tempering treatments on intergranular corrosion	69
4.1. Background	69
4.2. Experimental	70
4.2.1. Susceptibility to IGC by immersion tests in 5% HNO ₃ solution.....	70
4.2.2. Susceptibility to IGC by electrochemical measurements	70
4.2.2.1. Potentiodynamic polarization in H ₂ SO ₄ solutions	71
4.2.2.2. Potentiostatic polarization.....	71
4.2.2.3. DL-EPR test for DOS determination	71
4.2.2.4. Potentiodynamic polarization in 5% HNO ₃ solution.....	73
4.2.3. GI-XRD analysis of surface films after electrochemical tests	73
4.2.4. X-ray photoelectron spectroscopy (XPS) analysis	73
4.3. Results and Discussion.....	74

4.3.1. 5% Nitric acid immersion test - Susceptibility to IGC	74
4.3.2. Potentiodynamic polarization tests	78
4.3.3. DL-EPR test for determination of DOS with tempering temperature	85
4.3.4. Potentiodynamic polarization studies in 5% HNO ₃ solution.....	95
4.3.5. Electrochemical impedance spectroscopy studies in 5% HNO ₃ solution	100
4.3.6. Surface film formed in 5% HNO ₃ solution at passive potential: XPS study.....	103
4.4 Highlights	111
Chapter 5	113
Influence of tempering treatments on pitting corrosion.....	113
5.1. Background	113
5.2. Experimental	114
5.2.1. Electrochemical measurements	114
5.2.2. Surface film characterization by XPS	115
5.3. Results and Discussion.....	116
5.3.1. Electrochemical results in chloride solution.....	116
5.3.1.1. Potentiodynamic polarization	116
5.3.1.2 Potentiostatic polarization.....	121
5.3.1.3 Electrochemical impedance spectroscopy	123
5.3.2 Surface film characterization by XPS	125
5.4. Highlights.....	129
Chapter 6	130
Temper and hydrogen embrittlement: Effect of tempering	130
6.1. Background	130
6.2. Experimental	131
6.2.1. Hardness measurements	131
6.2.2. Charpy V-notch Impact testing.....	131
6.2.3. Slow strain rate tensile tests.....	132
6.2.4. Electrochemical Hydrogen charging and quantification of hydrogen.....	133
6.2.5. Hydrogen pre-charging and hydrogen charging during staining.....	133
6.3. Results and Discussion.....	135
6.3.1. Variation of hardness with tempering temperature	135

6.3.2. Changes in mechanical properties with tempering	136
6.3.3. Changes in impact toughness and fracture behaviour with tempering temperature..	138
6.3.4. Susceptibility to HE with tempering temperature	140
6.3.5. Mechanism of internal (pre-charged) HE with tempering temperature	151
6.3.5.1. Tempered at 300 and 550 °C	151
6.3.5.1.1. Confirming the role of phosphorous segregation on HE	154
6.3.5.2. Tempered at 700 °C	156
6.3.6. Effect of hydrogen charging during straining on MSS tempered at 700 °C.....	159
6.4. Highlights.....	164
Chapter 7	166
Conclusions.....	166
SCOPE FOR FUTURE WORK	169
REFERENCES.....	170

ABSTRACT

The present study is aimed to develop an in-depth understanding of the influence of different tempering treatments on microstructural changes, electrochemical behavior, localized corrosion, mechanical properties and hydrogen embrittlement (HE) of 13wt.% Cr martensitic stainless steels (MSS). The 13wt.% Cr MSSs showed quench cracks after austenitization at & above 1040 °C followed by oil/air cooling. Austenitization at 1020 °C for 30 min followed by oil quenching did not produce δ -ferrite stringers and quench cracks and was used in the present study. The austenitized specimens were tempered at temperatures in the range 300 - 700 °C for 2.5 h. Microstructural examination of the specimens by transmission electron microscopy (TEM) & X-ray diffraction (XRD) revealed formation of nano-sized M_3C type carbides at lower tempering temperature of 300 °C, whereas formation of nano-sized Cr-rich $M_{23}C_6$ carbides at 550 °C and sub-micron sized Cr-rich $M_{23}C_6$ type carbides at higher tempering temperature of 700 °C. Formation of Cr-rich carbide precipitates led to Cr-depletion zone of 7 - 9 nm at carbide-matrix interfaces in tempered condition at 550 °C and Cr concentration fell to 76% of matrix concentration in Cr depleted regions. XRD & TEM studies also showed that the nano-sized retained austenite film present at lath interfaces decreased with increased tempering temperature and no retained austenite was detected after tempering at 550 & 700 °C. Nitric acid immersion test results and SEM examination showed that the specimens tempered above 450°C (corrosion rate of more than 2.5 mm/y) were susceptible to interlath corrosion and the preferential attack was along the martensitic lath interfaces. The second anodic current density peak in anodic polarization of tempered MSSs in H_2SO_4 solution is shown to be due to the presence of Cr depletion associated with carbide precipitation. The 0.03 M H_2SO_4 solution is shown to be suitable for double loop electrochemical potentiokinetic reactivation (DL-EPR) test for measuring the degree of sensitization (DOS). The DL-EPR values in 0.03 M sulfuric acid solution correlated well with immersion test corrosion rates in 5% HNO_3 . Potentiodynamic polarization studies in 5% HNO_3 solution also showed the occurrence of sensitization after tempering. The Fe/Cr ratio of the surface film is shown to be higher for the specimen tempered at 550 °C compared to that for the austenitized condition. Tempering decreased the pitting potential and increased the metastable pitting frequency in 0.1 M NaCl solution. Especially tempering at 550 °C makes it highly prone to pitting corrosion. The pits initiated at the carbide-matrix interface region. The passive film formed at corrosion potential in 0.1M NaCl solution is enriched with Fe species in 550 °C tempered condition whereas Cr enriched passive film is formed in austenitized

condition. The decreased localized corrosion resistance for the specimen tempered at 550 °C is attributed to the presence of narrow Cr depletion regions and less protective, Fe-rich surface film formation. The strain to failure increased with increasing tempering temperature whereas yield strength and ultimate tensile strength decreased in tensile tests. The MSS tempered at 550 °C showed brittle intergranular fracture after Charpy impact tests indicating its susceptibility to temper embrittlement. The austenitized condition is highly susceptible to HE and showed cracking during hydrogen pre-charging. The susceptibility to HE depends not only on the strength but also on microstructure. Drastic reduction in strength and strain to failure is observed for specimen tempered at 550 °C after hydrogen pre-charging as compared to specimens tempered at 300 and 700 °C. This is due to synergistic interaction of hydrogen with impurity segregation at 550 °C. The critical hydrogen required for brittle fracture of MSS specimen decreased in presence of impurity segregation. There was no change in the yield strength but the strain to failure was significantly reduced from 14.4% to 3.7% with 9 wppm of bulk hydrogen for 700 °C tempered condition after hydrogen pre-charging. Compared to hydrogen pre-charging, effect of hydrogen charging during straining was more pronounced on the mechanical properties as both ductility and yield strength decreased for specimen tempered at 700 °C. A change in the fracture mode from ductile dimples to mixed and IG fracture was observed with the increase of cathodic current density. Hydrogen enhanced decohesion embrittlement (HEDE) is the dominant mechanism for hydrogen pre-charged and with hydrogen charging during straining conditions. The results obtained in the present study suggest that 13wt.% Cr MSS when tempered at 700 °C, provides optimum mechanical properties, moderate resistance to localized corrosion and hydrogen embrittlement.

LIST OF ABBREVIATIONS

DL-EPR	Double Loop-Electrochemical Potentiokinetic Reactivation
DOS	Degree of Sensitization
EBS	Electron Back Scattered Diffraction
EDS	Energy Dispersive Spectroscopy
EIS	Electrochemical Impedance Spectroscopy
EPR	Electrochemical Potentiokinetic Reactivation
HE	Hydrogen Embrittlement
HEDE	Hydrogen Enhanced De-Cohesion
HELP	Hydrogen Enhanced Localized Plasticity
IGC	Intergranular Corrosion
LWRs	Light Water Reactors
MSSs	Martensitic Stainless Steels
OCP	Open Circuit Potential
PAG	Prior Austenite Grain
PWRs	Pressurized Water Reactors
SAD	Selected Area Diffraction
SCC	Stress Corrosion Cracking
SCE	Saturated Calomel Electrode
SEM	Scanning Electron Microscopy
SSRT	Slow Strain Rate Tensile Tests
TEM	Transmission Electron Microscopy
XPS	X-Ray Photo Electron Spectroscopy
XRD	X-Ray Diffraction

LIST OF FIGURES

No.	Figure caption	Page No.
Fig. 2.1	Ternary phase diagram of Fe-Cr-C with Cr = 13wt.%. C1 and C2 are carbides of Type $M_{23}C_6$ and M_7C_3 (M = Fe, Cr) respectively.	9
Fig. 2.2	Influence of austenitization temperature on the carbide dissolution and carbide density.	13
Fig. 2.3	Amount of retained austenite with austenitizing temperature.	13
Fig. 2.4	Effect of austenitizing temperature and duration on hardness of Type 420 stainless steel.	14
Fig. 2.5	Impact energy versus austenitizing time and temperature for Type 420 MSS.	15
Fig. 2.6	(a) Scanning transmission electron microscopy image of low C MSS showing PAG boundary and carbides and (b) Cr distribution across PAG boundary and carbide. Line A and C shows Cr depletion zones.	20
Fig. 2.7	(a) DL-EPR curve in 0.5M H_2SO_4 solution for 550 °C tempered specimen of Type 410 showing reactivation current density is higher than activation current density and (b) variation in different electrochemical properties with tempering temperature.	25
Fig. 2.8	(a) DL-EPR curves in 0.1 M H_2SO_4 solution and (b) DL-EPR curves in 0.01 M H_2SO_4 solution for Type 403 MSS in as-quenched and tempered at 550 °C.	26
Fig. 2.9	SEM fractographs of the Type 420 martensitic stainless steel components showing intergranular fracture: (a) valve seat and stem rod.	32
Fig. 2.10	Optical images of the valve seat showing the (a) crack propagation along the PAGDs and (b) region at the crack face showing IG cracking/corrosion.	33
Fig. 3.1	Dilatometry of the as-received 13wt.% Cr MSS showing the transformation temperatures (A_{c1} , A_{c3} and M_s) during heating and cooling. Arrow indicates heating and cooling stages	43
Fig. 3.2	(a) Optical and (b) SEM images of 13wt.% Cr MSS in austenitized condition showing PAG boundaries and lath martensitic structure.	44
Fig. 3.3	Optical images of 13wt.% Cr MSS after austenitization at 1040 °C followed by oil quenching showing (a) ferrite striger in martensitic matrix and (b) quench cracks along PAG boundaries. FE-SEM images after austenitization at (a) 1100 °C and (b) 1200 °C for 1 h followed by air colling showing quench cracks along PAG.	45

Fig. 3.4	(a) X-ray Diffraction patterns for 13 wt.% Cr MSS in austenitized and different tempered conditions and (b) expanded view of the XRD peaks showing the retained austenite peak with tempering temperature.	47
Fig. 3.5	Microstructures of the 13wt.% Cr martensitic stainless steel after etching in Villela's reagent: (a) austenitized at 1020 °C for 30 min, (b) tempered at 300 °C, (c) tempered at 550 °C and (d) tempered at 700 °C. All the tempering treatments are for 2.5 h.	48
Fig. 3.6	TEM micrographs of the austenitized specimen, (a) bright filed image showing lath martensitic structure with retained austenite at lath interfaces, (b) dark field image showing the retained austenite, (c) SAD pattern of the retained austenite-lath interface region (d) bright filed image showing undissolved carbides and (e) SAD pattern of the undissolved carbide (inset showing the TEM-EDS of carbide).	51
Fig. 3.7	TEM micrographs of 13 wt.% Cr MSS tempered at 300 °C, (a) bright filed image showing lath martensite with retained austenite and M ₃ C type carbides, (b) magnified image of (a) showing retained austenite at lath interfaces, (c) dark filed image showing carbides and (d) SAD pattern of the carbide showing as M ₃ C type carbide.	53
Fig. 3.8	TEM micrographs of the specimen tempered at 550 °C (a) showing lath martensitic structure with in PAG and undissolved carbides (b) showing the lath interface covered by precipitation of fine nano-sized carbides and also presence of nano-sized carbides in laths and carbides at PAG boundary (c) SAD pattern of the carbide present at PAG boundary.	54
Fig. 3.9	TEM micrographs of the specimen tempered at 700 °C (a) showing carbides at lath interfaces, (b) magnified image of (a) showing sub-micron sized carbides at lath interfaces, (c) SAD pattern of the matrix and (d) SAD pattern of the lath interface round shaped carbide.	55
Fig. 3.10	TEM images showing dislocations as indicated by arrow marks within the martensitic laths in (a) austenitized condition, tempered at (b) 300 °C, (c) 550 °C and (d) 700 °C. All tempering treatments are done for 2.5 h.	57
Fig. 3.11	XRD patterns of the precipitates extracted from specimens tempered at 550 and 700 °C along with the standard XRD pattern of M ₂₃ C ₆ carbide, showing extracted precipitates are M ₂₃ C ₆ type carbides.	58
Fig. 3.12	TEM images of the extracted carbide precipitates: (a) tempered at 550 °C showing nano-sized precipitates and (b) tempered at 700 °C showing sub-microscon sized carbides.	59
Fig. 3.13	TEM-EDS analysis across the carbide-matrix interface region of specimen tempered at 550 °C (a) showing the region used for TEM-EDS analysis and (b) showing the Cr concentration profiles of carbide-matrix interface regions.	61

Fig. 3.14	(a) TEM image of the specimen tempered at 550 °C showing the undissolved carbide and (b) schematic of TEM- EDS analysis location and Cr concentrations.	63
Fig. 3.15	(a) FE-SEM image, (b) orientation map, (c) low and high angle grain boundaries distribution in austenitized condition obtained by EBSD technique.	64
Fig. 3.16	(a) Orientation map and (b) low and high angle grain boundaries distribution in 13wt.% Cr MSS tempered at 700 °C condition obtained by EBSD technique.	65
Fig. 3.17	(a) FE-SEM image, (b) orientation map, (c) phase distribution and (d)-(f) shows the low and high angle grain boundaries distribution in the 13wt.% Cr MSS tempered at 700 °C obtained by EBSD technique (dotted lines in image (a) and (b) indicate the PAG boundaries).	66
Fig. 4.1	Corrosion rates in 5 % HNO ₃ immersion test with tempering temperatures showing regimes of uniform and intergranular corrosion. All the tempering treatments are for 2.5 h.	74
Fig. 4.2	Cross-sectional optical microscopy images of 13wt.% Cr martensitic stainless steel showing absence of intergranular attack in (a) austenitized and (b) tempered at 400 °C for 2.5 h specimens and severe attack in (c) 550 °C for 2.5 h and (d) 650 °C for 2.5 h tempered specimen after IGC test in 5% HNO ₃ solution.	75
Fig. 4.3	SEM images of IGC tested (a) 550 °C for 2.5 h, (b) 700 °C for 2.5 h tempered specimens and (c) and (d) are magnified images of (a) and (b) showing corrosion attack preferentially along the lath boundaries. (arrow indicating the corrosion attack at martensitic laths).	76
Fig. 4.4	Potentiodynamic polarization curves in (a) 0.25 M and (b) 0.03 M H ₂ SO ₄ solutions and (c) variation of second anodic peak current density with tempering temperature for austenitized and tempered specimens in 0.03 M H ₂ SO ₄ solution. All the tempering treatments are for 2.5 h.	79
Fig. 4.5	XRD patterns of specimen tempered at 550 °C for 2.5 h before and after potentiodynamic polarization in 0.25 M H ₂ SO ₄ showing presence of carbides in black layer formed after polarization.	81
Fig. 4.6	(a) Potentiodynamic polarization curves in 0.03 M H ₂ SO ₄ solution for 550 °C tempered specimens for different durations (b) Variation of second anodic peak current density with tempering duration at 550°C.	82
Fig. 4.7	Variation of second anodic peak charge density in 0.25 M H ₂ SO ₄ solution (a) with tempering temperature and (b) with tempering at 550 °C up to 500 h.	83
Fig. 4.8	Potentiostatic tests held at 0 mV _{SCE} in 0.03 M H ₂ SO ₄ solution.	84

Fig. 4.9	DL-EPR curves of 550 °C for 100 h tempered specimen in different concentrations of H ₂ SO ₄ solution.	86
Fig. 4.10	DL-EPR values and corrosion rates in 5 % HNO ₃ immersion test with tempering temperatures. All the specimens are tempered for 2.5 h.	88
Fig. 4.11	FE-SEM images of the DL-EPR tested surface (a) austenitized, (b) tempered at 550 °C for 2.5 h and (c) magnified image of (b).	89
Fig. 4.12	DL-EPR tests stopped at (a) 1 st anodic peak potential in the forward scan (P ₁), (b) start of the reactivation scan (P ₂), (c) start of the 2 nd anodic peak in the reactivation scan (P ₃) and (d) after complete EPR test (P ₄).	92
Fig. 4.13	Cross-sectional images of the 550 °C for 2.5 h tempered specimen tested at different potentials, (a) 1 st anodic peak potential in the forward scan (P ₁), (b) start of the reactivation scan (P ₂), (c) start of the 2 nd anodic peak in the reactivation scan (P ₃) and (d) after complete EPR test (P ₄), (e) opposite side of the EPR tested cross-sectional image. Arrow indicate EPR test attacked regions and (f) magnified view of the depth of attacked regions in the cross-sectional surface (shown in Fig. 4.13(c)) after DL-EPR test stopped at potential P ₃ .	94
Fig. 4.14	Potentiodynamic polarization curves of austenitized and different tempered specimens in 5% HNO ₃ solution.	96
Fig. 4.15	SEM images of (a) austenitized, (b) tempered at 300 °C, (c) magnified view of (b) and (d) tempered at 550 °C for 2.5 h after potentiodynamic polarization in 5% HNO ₃ solution.	99
Fig. 4.16	EIS spectra of the 13wt.% Cr martensitic stainless steel in different tempered conditions in 5% HNO ₃ solution at 25 °C, (a) Nyquist plot, inset of (a) shows the expanded view of specimen tempered at 550 °C, (b) bode plot and (c) Equivalent circuit used for fitting the experimental EIS data.	100
Fig. 4.17	XPS survey scan of the surface film formed on austenitized condition at 0.5V _{SCE} in 5% HNO ₃ solution.	103
Fig. 4.18	High resolution XPS spectra of (a) Fe 2p _{3/2} , (b) Cr 2p _{3/2} and (c) O 1s element present in the surface film formed on austenitized condition in 5% HNO ₃ solution without sputtering.	106
Fig. 4.19	High resolution XPS spectra of (a) Fe 2p _{3/2} , (b) Cr 2p _{3/2} and (c) O 1s element present in the surface film formed on austenitized condition in 5% HNO ₃ solution after sputtering for 30 s	107
Fig. 4.20	High resolution XPS spectra of (a) Fe 2p _{3/2} , (b) Cr 2p _{3/2} and (c) O 1s element present in the surface film formed on specimen tempered at 550 °C condition in 5% HNO ₃ solution without and after sputtering for 30 s.	108
Fig. 4.21	Variation in atomic concentrations of Cr ³⁺ , Fe ³⁺ and Fe ²⁺ chemical species in surface film formed in 5% HNO ₃ solution with sputtering time: (a) austenitized and (b) tempered at 550 °C. (c) Cr ³⁺ (Cr ₂ O ₃) atomic	110

	concentration of the surface film formed on austenitized and tempered at 550 °C with sputtering time.	
Fig. 5.1	Potentiodynamic polarization curves of austenitized and different tempered specimens in 0.1 M NaCl solution.	117
Fig. 5.2	Optical images showing the pit morphology of (a) austenitized condition, (b) tempered at 300 °C, (c) tempered at 550 °C and (d) tempered at 700 °C.	119
Fig. 5.3	(a) SEM image of the specimen tempered at 550 °C after polarization test (inset showing attack at PAG boundaries and laths), (b) magnified image of (a) showing pitting at undissolved carbide-matrix interface region and (c) SEM-EDS analysis showing the undissolved Cr- rich carbide.	120
Fig. 5.4	Potentiostatic polarization on austenitized and specimens tempered at 300 and 700 °C in 0.1M NaCl solution (a) showing current transients from meta stable pitting with time, (b) typical current transient showing the pit growth and repassivation, (c) meta stable pitting events with time and (d) potentiostatic polarization of specimen tempered at 550 °C in 0.1M NaCl solution at 20 mV _{SCE} above E _{corr} .	123
Fig. 5.5	(a) Nyquist, (b) Bode plot and (c) polarization resistance plots for austenitized and tempered specimens recorded at OCP.	124
Fig. 5.6	Experimental and fitted narrow XPS spectra of (a) Fe 2p _{3/2} , (b) Cr 2p _{3/2} and (c) O 1s of the surface film formed on austenitized specimen in 0.1 M NaCl solution at OCP.	126
Fig. 5.7	Experimental and fitted narrow XPS spectra of (a) Fe 2p _{3/2} , (b) Cr 2p _{3/2} and (c) O 1s of the surface film formed on specimen tempered at 550 °C in 0.1 M NaCl solution at OCP.	128
Fig. 6.1	(a) Specimen design used for SSRT tests and (b) SSRT unit used to generate stress-strain plots.	132
Fig. 6.2	Variation of hardness with tempering temperature for 13wt.% Cr martensitic stainless steel. All the tempering treatments are for 2.5 h.	135
Fig. 6.3	(a) Engineering stress-strain curves and fracture surface at the central region of the 13wt.% Cr MSS after SSRT in air in different conditions, (b) austenitized, (c) tempered at 300 °C, (d) tempered at 550 °C (e) tempered at 700 °C. Tempering duration is 2.5 h.	137
Fig. 6.4	SEM images of the fracture surface of (a) austenitized and tempered at (b) 300 °C, (c) 550 °C and (d) 700 °C after Charpy V-notch impact tests. Tempering duration is 2.5 h.	139
Fig. 6.5	SEM images of the fracture surface of specimens tempered at (a) 550 °C for 100h and (b) 550 °C for 500h after Charpy V-notch impact tests.	140
Fig. 6.6	Optical images after hydrogen pre-charging: (a) austenitized condition showing cracks along PAG boundaries after hydrogen pre-charging for 3 h and (b) PAG boundaries etched during hydrogen pre-charging, (c)	141

	tempered at 550 °C for 2.5 h and (d) tempered at 700 °C for 2.5 h showing no cracks.	
Fig. 6.7	(a) Engineering stress- strain curves of specimen tempered at 300 °C for 2.5 h with and without hydrogen and (b) fracture surface of hydrogen pre-charged specimen showing IG fracture.	142
Fig. 6.8	(a) Engineering stress- strain curves of specimens tempered at 550 °C for 2.5 h with and without hydrogen and fracture surface of hydrogen charged specimen showing IG fracture (b) 550 °C - 3 h pre-charging and (c) 550 °C - 15 h pre-charging.	143
Fig. 6.9	(a) Engineering stress-strain curves of the uncharged and hydrogen pre-charged specimen tempered at 700 °C for different hydrogen pre-charging durations and (b) showing duration of hydrogen pre-charging vs. strain to failure and concentration of bulk hydrogen in the fracture surface.	144
Fig. 6.10	(a) Fracture surfaces of uncharged tempered 13wt% Cr martensitic stainless steel after SSRT in air and (b) magnified view of the central region (blue box) of (a) showing ductile dimples.	146
Fig. 6.11	Fracture surface of the 1h hydrogen pre-charged tempered specimen showing (a) intergranular and ductile fracture, (b), (c) and (d) are the magnified images corresponding to regions marked A, B and C respectively in image (a). Blue color marked regions are showing the brittle intergranular regions in Fig. 6.11(a).	147
Fig. 6.12	Fracture surface of the 3h hydrogen pre-charged tempered specimen showing (a) intergranular and ductile fracture, (b), (c), (d), and (e) are the magnified images corresponding to regions marked B, C, D and E respectively in image (a). Blue color marked regions are showing the brittle intergranular regions in Fig. 6.12(a).	148
Fig. 6.13	Fracture surface of the 15h hydrogen pre-charged tempered specimen showing (a) more of intergranular and ductile fracture, (b), (c) and (d) are the magnified images corresponding to regions marked as B, C and D respectively in image (a). The inset in Fig. 6.13(b) shows the intergranular cracking along the prior austenite grain boundaries.	149
Fig. 6.14	Fracture surface of the 17h hydrogen pre-charged tempered specimen showing (a) IG fracture along the prior austenitic grain boundaries, (b), (c) and (d) are the magnified images corresponding to regions marked as B, C and D respectively in image (a).	150
Fig. 6.15	(a) Engineering stress- strain curve of 550°C/100 h specimen in uncharged and hydrogen pre-charged for 3h conditions, fracture surface of (b) uncharged and & (c) hydrogen pre-charged 550 °C/100 specimen after SSRT respectively.	155

- Fig. 6.16** SEM images of the fracture surface of the tempered specimen tested at 20 mA/cm² (a) fracture head showing brittle fracture, (b) and (c) are the magnified images corresponding to regions marked as B and C in image (a) showing IG cracking along prior austenite grain boundaries. **160**
- Fig. 6.17** SEM images of the fracture surface of the tempered MSS tested at 5 mA/cm² (a) fracture head showing brittle fracture, (b), (c) and (d) are the magnified images corresponding to regions marked as B, C and D in image (a) showing IG cracking along prior austenite grain boundaries. **161**
- Fig. 6.18** SEM images of the fracture surface of the tempered MSS tested at 0.01mA/cm² (a) fracture head showing mixed fracture, (b), (c) and (d) are the magnified images corresponding to regions marked as B, C and D in image (a) showing IG cracking along prior austenite grain boundaries at edges and ductile fracture in the central region. **162**

LIST OF TABLES

No.	Table Caption	Page no.
2.1	Role alloying elements in a 13wt.% Cr stainless steel.	10
2.2	Typical martensitic stainless steels with their chemical composition [ASTM A276/A276M-16a].	11
2.3	Microstructural changes in as quenched 12wt.% Cr-0.1wt.% C MSS as a function of tempering temperatures.	18
2.4	Evidence of P segregation (a few atomic layers only) at grain boundaries: AES analyses done on IG fracture surface after tempering at 550/650 °C.	31
2.5	Different hydrogen trap sites with their binding energy.	35
3.1	Chemical composition (in wt.%) of the 13 wt.% Cr MSS used in the present study.	40
4.1	DL-EPR electrolyte concentrations (deaerated) used for evaluating the DL-EPR value of the specimen tempered at 550 °C for 100 h.	72
4.2	Comparison of electrochemical parameters obtained from the polarization curves in 0.25 M H ₂ SO ₄ with different tempering treatments.	80
4.3	DL-EPR values of the specimen tempered at 550 °C for 100 h in different concentrations of H ₂ SO ₄ solution.	87
4.4	Potentiodynamic polarization test results for austenitized and specimens tempered at different temperatures in 5% HNO ₃ solution.	98
4.5	Fitted results to the experimental EIS data of tempered specimens in 5% HNO ₃ solution at corrosion potential at room temperature.	101
4.6	Parameters used for the deconvolution of the narrow XPS spectra with the main chemical species present in passive film, atomic percentage (%) and Fe/Cr ratio of passive film without sputtering	105
4.7	Fe/Cr ratio of the surface film formed in 5% HNO ₃ solution with sputtering time.	109
5.1	Potentiodynamic polarization test results for austenitized and specimens tempered at different temperatures in 0.1 M NaCl solution.	118
6.1	Mechanical properties of the 13wt.% Cr MSS tempered at different temperatures with and without hydrogen pre-charging.	145
6.2	Mechanical properties of tempered MSS in air and with different cathodic current densities during straining with a strain rate of 1×10^{-6} /s.	159

Chapter 1

Introduction

1.1 Background

Martensitic stainless steels (MSSs) are important class of structural materials and used as parts of pumps, valve seats, stem rods, nut and bolts in light water reactors (LWRs), pressurized water reactors (PWRs) and also in other industries because of their better mechanical properties and moderate corrosion resistance (Sedriks, 1996, Scott, 2000, Chandra *et al.*, 2013). These are based on the Fe-Cr-C ternary system and contain 11.5 to 18.0% Cr and 0.1–1.2% C to obtain a fully austenitized condition at elevated temperatures (Sedriks, 1996, Kose *et al.*, 2014, Anjos, 2015). These MSS are typically heated to a temperature in the austenite phase region (980 to 1100 °C) in accordance with chemical composition and then cooled at a suitable rate to obtain martensite with body centered tetragonal crystal structure in as-quenched condition (Kose *et al.*, 2014, Barlow *et al.*, 2012). The hardened MSSs are too brittle for processing and tempering is therefore commonly employed to improve ductility and toughness. The tempering treatments decrease the dislocation density induced during quenching from austenitization temperature and induce precipitation of secondary phases such as carbides. The precipitation and coarsening of the carbides during the tempering treatments play a key role in determining the properties of the MSS in service conditions (Tao *et al.*, 2014). Therefore, microstructure of the MSS is one of the important aspects affecting environmental degradation of MSS. The prevailing degradation modes of these steels after

tempering treatments are intergranular corrosion (IGC), pitting corrosion, temper embrittlement, hydrogen embrittlement (HE) and stress corrosion cracking (SCC). Types 410, 420 and 440 are the commonly used grades under the martensitic class of stainless steels. Valve seats and stem rods fabricated using materials equivalent to Type 420 stainless steel have been used in PWRs and significant number of failures were reported due to HE and SCC (Scott, 2000). Recent experiences in Indian PWRs showed failures of valve seat and stem rods components during the start-up of the reactor and reason for failure was identified to be improper heat treatments during manufacturing which led to embrittlement of the MSS components (Chandra *et al.*, 2013). So it is important to understand the conditions that would eliminate the degradation of the MSSs in service.

The characterization of the precipitates formed during the austenitization and tempering heat treatments should be useful for establishing a proper heat treatment scheme of MSSs and also provide a better interpretation on the material performance in a given environment. Different types of carbide precipitates such as $M_2(C, N)$, M_3C , M_7C_3 , $M_{23}C_6$ and M_6C ($M = Fe$ and Cr) were shown to form during tempering treatments (Prabhu Gaunkar *et al.*, 1980, Tao *et al.*, 2014, Lu *et al.*, 2015, Chakraborty *et al.*, 2015, Lu *et al.*, 2015a). The type of the carbides formed during tempering treatment is dependent on chemical composition of the material, tempering temperature and duration (Prabhu Gaunkar *et al.*, 1980, Tao *et al.*, 2014). The Cr-rich carbide precipitation is expected to deplete Cr concentration in carbide-matrix interface regions. There are limited studies directed towards the nature of the precipitates formed and presence of Cr depletion at carbide-matrix interface (sensitization) regions after tempering treatments (Nakamichi *et al.*, 2008). The sensitized regions become susceptible to localized corrosion if the Cr concentration falls to below 11-12wt.% in carbide-matrix interface region. The susceptibility to IGC, correlations between corrosion rates and degree of sensitization are established for austenitic stainless steels (Cihal *et*

al., 2004). No such studies are reported for 13wt.% Cr MSS for choosing an optimized tempering temperature to avoid IGC. The 400 series SS components are not pickled in HNO₃ solutions due to their susceptibility to IGC and HE (Chandra *et al.*, 2013). The surface oxide film formed over Cr depleted (sensitized) regions is known to be weak (and not stable), therefore, leading to preferential corrosion attack.

Pitting corrosion of sensitized stainless steels has been shown to be dependent on the number of carbide interfaces and also the carbide interfaces with Cr depletion regions (Kain *et al.*, 1989, Chandra *et al.*, 2013a, Park *et al.*, 2005). The reported studies on pitting corrosion of MSSs showed decreased corrosion resistance with tempering temperature (Lu *et al.*, 2015, Taji *et al.*, 2015). But still, there are unanswered questions in the domain of microstructure (carbide precipitation and extent of Cr depletion at carbide-matrix interfaces) and nature of the passive film and its properties on pit initiation mechanisms in 13wt.% Cr MSS with different tempering treatments.

As mentioned above, tempering is commonly employed to improve ductility and toughness. The effect of tempering treatments on mechanical properties of MSS has been a topic of interest over the past few decades as the properties are tailored by the heat treatments. But, studies showed that these MSSs are susceptible to temper embrittlement when tempered in the temperature range of 450 to 600 °C. The reason for the embrittlement is impurity elements such as phosphorous (P) segregation at grain boundaries leading to brittle fracture along the grain boundaries (Prabhu Gaunkar *et al.*, 1980, Tsay *et al.*, 2002). The MSS are prone to HE due to their high strength. Most of the MSS components failed due to HE in PWR primary water were tempered at lower tempering temperatures (Scott, 2000). In general, HE susceptibility decreases with increase of tempering temperature for martensitic steels as tempering decreases the strength of the martensite and increases ductility (Liu *et al.*, 2013, Siddiqui *et al.*, 2005, Li *et al.*, 2017). A considerable amount

of research has been carried out on different metallic materials to understand the detrimental effects of hydrogen on steels (Liu *et al.*, 2013, Siddiqui *et al.*, 2005), however there has been little research directed towards cooperative interaction of hydrogen and impurity segregations in alloy steels (Xu *et al.*, 2012, Yoshino *et al.*, 1974, Liu *et al.*, 2008). But systematic studies on HE of 13wt.% Cr MSS in different tempered conditions and the synergistic interaction between temper embrittlement and HE have not been reported in literature to the best of author's knowledge. The influence of hydrogen on the mechanical properties of the MSS in different conditions is an important issue to be considered for integrity of the structural components used in PWRs. Hence this study is an organized attempt to develop an in-depth understanding of different tempering treatments influence on microstructural changes, electrochemical behavior, localized corrosion, mechanical properties and HE of 13wt.% Cr MSS.

1.2 Objectives of the study

The broad objective of the present study is: (a) to investigate the microstructural changes occurring with different tempering treatments of 13wt.% Cr MSS and (b) to establish tempered martensite microstructure's susceptibility to IGC, pitting corrosion and HE and their degradation mechanisms. This study is expected to help in choosing (with a mechanistic basis) an optimum tempering temperature for 13wt.% Cr MSS to avoid the degradation by localized corrosion and HE. The specific objectives set for the present study are as follows:

- (a) Detailed microstructural characterization of 13wt.% Cr MSS with austenitization and tempering treatments using transmission electron microscopy (TEM), scanning electron microscopy (SEM)-electron back scattered diffraction (EBSD) and X-ray diffraction (XRD).

- (b) Effect of different tempering treatments on susceptibility to IGC by immersion and electrochemical tests followed by characterization of exposed surfaces. Characterization of surface films using electrochemical impedance spectroscopy (EIS) and X-ray photo electron spectroscopy (XPS) techniques. Modifying the existing double loop-electrochemical potentiokinetic reactivation (DL-EPR) test solution for determining the degree of sensitization (DOS) with tempering treatments and correlating with immersion test corrosion rates.
- (c) Evaluating the susceptibility to pitting corrosion with tempering treatments and characterizing the surface films by EIS and XPS.
- (d) Evaluating the mechanical properties e.g., Charpy impact, Vickers hardness and tensile tests with different tempering treatments.
- (e) HE susceptibility with tempering treatments using slow strain rate tensile (SSRT) testing after hydrogen pre-charging and hydrogen charging during straining followed by fracture surface examination.

1.3 Structure of the thesis

The thesis is divided into seven chapters. Chapter 1 gives the current state of information and gap areas in knowledge related to MSSs, objectives of the work and the framework of the thesis. A brief literature review of the topics directly relevant to the present investigation is given in Chapter 2. The sub-sections in Chapter 2 presents literature survey on MSSs, heat treatments, effect of tempering treatments on microstructural changes, localized corrosion, mechanical properties and HE. The cooperative interaction between the temper embrittlement and HE is also discussed in this Chapter 2. The results obtained in the present work are provided in Chapter 3, 4, 5 and 6. A brief introduction of the work carried out and the material heat treatments, experimental details of

the techniques used are described in detail in corresponding chapters. The main conclusions drawn from the present work are given in Chapter 7.

Chapter 2

Literature review

This chapter is an overview of the information available on MSSs, heat treatments of MSSs, microstructural changes with the heat treatments and the potential degradation issues of the MSSs such as temper embrittlement and environmentally induced degradation (IGC, pitting corrosion and HE)

2.1 Martensitic Stainless Steels: Overview

MSSs are based on the iron (Fe)-chromium (Cr)- carbon (C) ternary system and contain at least 11.5 to 18.0% Cr and 0.1–1.2% C to obtain a fully austenitized condition at elevated temperatures and provide a wide combination of hardness and strength in addition to moderate corrosion resistance (Sedriks, 1996, Kose *et al.*, 2014, Anjos, 2015). MSSs are widely used in many industries like nuclear power plants, steam generators, mixer blades, pressure vessels, turbine blades, oil and gas valves, naval applications and chlorinated plastic injection molds requiring hardness, strength and wear resistance in addition to corrosion resistance (Kose *et al.*, 2014, Bhambri, 1996, Lippold *et al.*, 2005). Valve seats and stem rods in nuclear reactors have utilized the 13wt.% Cr MSSs (Scott, 2000). MSSs, as the name implies, derive strength (hardened) from the transformation of austenite to martensite (body centered tetragonal (BCT) structure) on quenching or cooling to room temperature or subzero temperature from austenitization temperature (Smith, 1986). MSSs possess good corrosion resistance in hardened condition but the corrosion resistance is lower as compared to austenitic and ferritic stainless steels.

MSSs are hardened by heating above austenitization temperature followed by quenching. The martensite start temperature (M_s) is dependent on the alloying elements, austenitization temperature and also on cooling rate (Barlow *et al.*, 2012, Higgins, 1983). Depending on the carbon content, the quenched martensite can be hard or brittle. Tempering is commonly employed to restore the ductility and toughness. The obtained mechanical properties are strongly dependent on tempering temperature and duration. The tempering treatments decrease the dislocation density induced during quenching from austenitization temperature and cause nucleation of new secondary phases such as carbides. The precipitation and coarsening of the secondary phases (mainly carbides) during the tempering treatments play a key role in determining the properties of the MSS in service conditions (Tao *et al.*, 2013). The 13wt.% Cr steel used in the present study belongs to MSS family.

The martensitic steels (a) contain carbon and strengthened by iron carbide precipitations when tempered at lower temperatures and by alloy carbides on tempering at high temperatures, (b) have a low carbon content but are strengthened by precipitation of particles of copper (Cu) or intermetallics, (c) are strengthened by precipitation of both intermetallics and alloys carbides. The dominant strengthening mechanism in the MSSs is the martensitic transformation and the heat treatments should be designed to prevent δ - ferrite phase formation, with no or minimal retained austenite and the martensite transformation range should be above room temperature (to reduce retained austenite content). This is dependent on the alloying elements present in the steel. The added alloying elements are chosen to achieve: (a) martensite start (M_s) and finish (M_f) temperatures that are not too low, (b) austenitization (c) corrosion resistance and (d) high strength. Table 2.1 shows the role of alloying additions in MSSs.

Fig. 2.1 shows the ternary diagram of 13wt.% Cr MSS with C content. Martensitic transformation is attained in Fe- 13wt.% Cr steels by addition of C or Ni such that the austenite phase field extends to about 17% Cr (Davis, 1994). From Fig. 2.1, MSSs experiences the following sequential solid state phase transformations during heat treatment: $\alpha + C1 \rightarrow \alpha + \gamma + C1 \rightarrow \gamma \rightarrow \gamma + \delta \rightarrow \delta$. The chemical composition of the MSSs and heating rate determine the exact temperatures of the phase transformations. The equilibrium carbides formed are C1 ($M_{23}C_6$) and C2 (M_7C_3) as shown in Fig. 2.1.

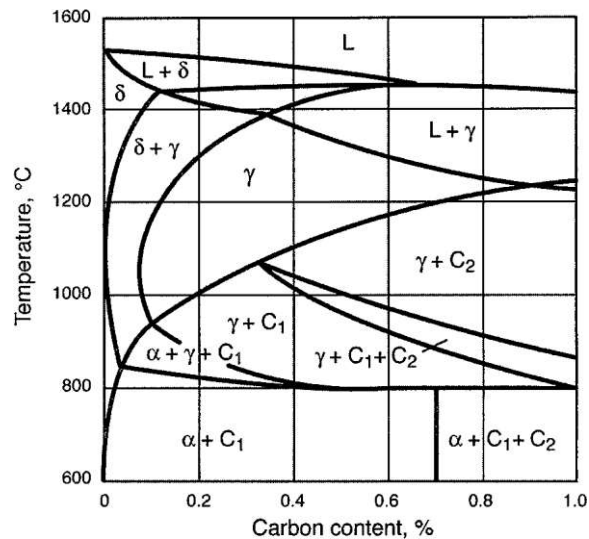


Fig. 2.1 Ternary phase diagram of Fe-Cr-C with Cr = 13wt.%, C1 and C2 are carbides of Type $M_{23}C_6$ and M_7C_3 ($M = Fe, Cr$) respectively (Davis, 1994).

2.1.1. Role of alloying elements

Chromium imparts corrosion resistance and also acts as a strong ferrite stabilizer, favoring the ferrite phase at high temperatures at the expense of austenite. Therefore, the need of austenitic structure at higher temperatures limits the maximum Cr content in MSS. The stainless property is achieved by the formation of chromium oxide (Cr_2O_3) film on the steel surface. It is generally believed that the Cr content for the stainless property is about 11 wt.% for Fe-Cr alloys (Sedriks,

1996). A binary Fe-Cr alloy containing more than 10.5 wt.% Cr cannot be austenitized at elevated temperatures and the austenite stabilizers such as C, N, Ni and Mn are added for allowing addition of Cr contents more than 10.5 wt.% (Barlow *et al.*, 2011, Avner, 1997). Carbon is a strong austenite stabilizer and the addition C, allows addition of higher levels of Cr without forming the ferrite phase at higher temperatures. The addition of C also increases the hardness and wear resistance of MSS. Typical C content of MSS grades are between 0.1 to 1.2 wt.% The C content also influence the corrosion resistance as C has a strong chemical affinity for Cr leading to formation and precipitation of Cr-rich carbides. Depending on the properties required, C and Cr concentration levels are selected. The other alloying elements added to MSS are molybdenum (Mo) and vanadium (V) which increase the hardenability, temper resistance and also these elements are strong carbide formers like Cr (Barlow *et al.*, 2011, Avner, 1997). Nb is also added in small amounts to MSSs for refinement of the austenite grain size.

Table 2.1 Role alloying elements in a 13 wt.% Cr MSS (Barlow *et al.*, 2011, Avner, 1997)

Element	Purpose
C	Improves strength and strong austenite stabilizer
Si	Ferrite stabilizer and solid solution strengthener
Mn	Austenite stabilizer and solid solution strengthener
Cr	Ferrite stabilizer, promotes passivation, strong carbide former and resist tempering by forming secondary carbides like $Cr_{23}C_6$ and Cr_7C_3 .

The standard MSS is Type 410 stainless steel and different sub-grades of MSS are available based on alloying additions to it. Different types of commercial MSSs with their chemical compositions are given in Table 2.2. As shown in Table 2.2, Type 440 MSSs have the higher C contents in order to have greater hardness and primary carbides after austenitization, promoting wear resistance.

The higher Cr contents are required to have corrosion resistance as much as the Cr required for consumption by formation of primary carbides.

Table 2.2 Typical martensitic stainless steels with their chemical composition (all in wt.%) (ASTM A 276/A276M-16a).

UNS No.	AISI Type	C	Mn (max)	P (max)	S (max)	Si (max)	Cr	Ni	Mo	Others
S40300	403	0.15	1.00	0.040	0.030	0.50	11.5- 13.0	---	--	--
S41000	410	0.08- 0.15	1.00	0.040	0.030	0.50	11.5- 13.5	Nb 0.05- 0.30
S41400	0.15	1.00	0.040	0.030	1.00	11.5- 13.5	1.25- 2.50
S42000	420	0.15 min	1.00	0.040	0.030	1.00	12.0- 14.0
S42010	0.15- 0.30	1.00	0.040	0.030	1.00	13.5- 14.0	0.35- 0.85	0.40- 0.85
S43100	431	0.20	1.00	0.040	0.030	1.00	15.0- 17.0	1.25- 2.50
S44002	440A	0.60- 0.75	1.00	0.040	0.030	1.00	16.0- 18.0	0.75
S44003	440B	0.75- 0.95	1.00	0.040	0.030	1.00	16.0- 18.0	0.75
S44004	440C	0.95- 1.2	1.00	0.040	0.030	1.00	16.0- 18.0	0.75

2.2. Heat treatment of martensitic stainless steels

2.2.1. Annealing and Austenitization

The typical heat treatment cycle for MSSs involves annealing, austenitizing and tempering. In industrial practices, annealing is carried out at temperatures from 730 to 830 °C for several hours

followed by air cooling or furnace cooling. Annealing is carried to soften the steel for fabrication purposes (cold working and machining) by producing a fully ferritic matrix with coarse, globular and spheroidized carbides.

Austenitizing involves heating to and hold at suitable austenitization temperature to form austenite and to dissolve the carbides fully or partially followed by cooling in air or oil to transform austenite to martensite. The resultant microstructure consists of either lath or plate martensite which is dependent on the C content in MSS. The phenomenological theory of martensitic transformation in MSSs is beyond the scope of the present discussion and is discussed in-depth in literature (Christian, 1994). The transformation of austenite (γ) to martensite (α') always maintains the crystallographic orientation relationship of $(111)_{\gamma} // (011)_{\alpha'}$, $[101]_{\gamma} // [111]_{\alpha'}$ and leads to lath morphology (Tsai, 2002, Krauss, 1990, Honeycombe, 1995). As rapid cooling imparts a very high degree of hardness, the steel is returned to furnace for another cycle (at a lower temperature) of heat treatment, so called tempering to relieve residual stresses, improve toughness and ductility. These heat treatments cause changes in microstructure of MSS and affect the mechanical and corrosion properties.

The cooling rate employed while quenching from the austenitization temperature is a critical aspect as the rapid cooling induces possibility of quench cracks. The possibility of quench cracking increases with C content and large amounts of Cr because the volume expansion associated with austenite to martensite transformation increases with C and Cr content. Slow cooling from austenitization produces high amounts of retained austenite in quenched structure which is not desirable for mechanical properties. So, cooling rate for C containing MSSs should be chosen carefully to avoid quench cracks and also to avoid retained austenite. Barlow et al. studied in detail the effect of austenitization on microstructure and hardness of Type 420 stainless steel (Barlow *et*

al., 2012). Barlow's results also showed increased retained austenite, hardness and carbide dissolution with increase of austenitization temperature and showed the complete carbide dissolution at temperatures higher than 1170 °C for Type 420 stainless steel with C content of 0.472% (Heat 1) and 0.471% (Heat 2) as shown in Figs. 2.2-2.3 (Barlow *et al.*, 2012).

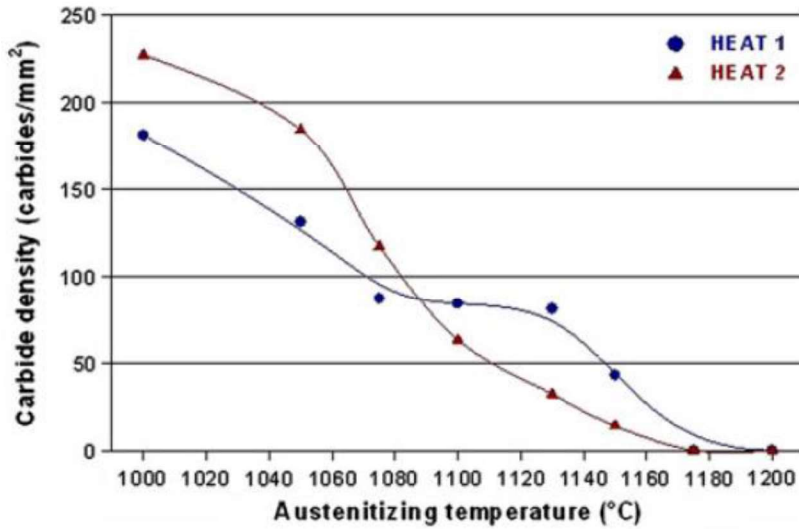


Fig. 2.2 Influence of austenitization temperature on the carbide dissolution and carbide density; Heat 1: 0.472% C, Heat 2: 0.471% C (Barlow *et al.*, 2012).

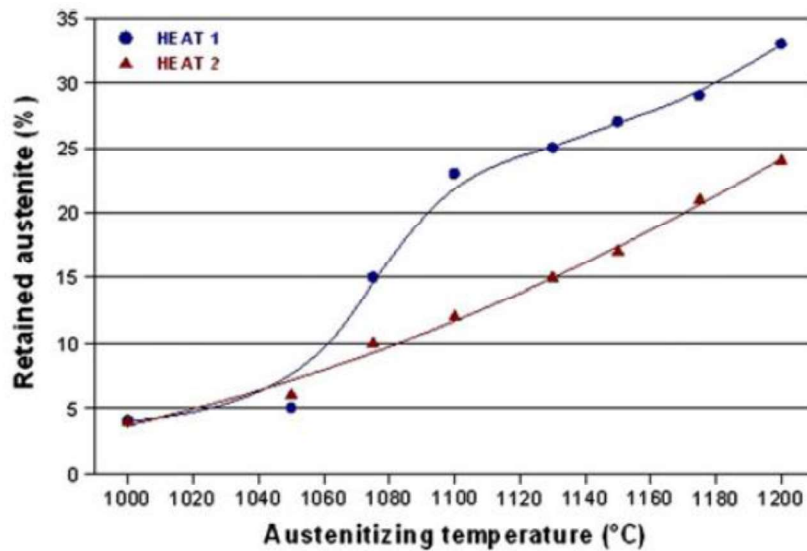


Fig. 2.3 Amount of retained austenite with austenitizing temperature (Barlow *et al.*, 2012).

The effect of austenitization temperature and duration followed by air cooling on Type 420 stainless steel was studied by Isfahany et al. and they showed that the optimum austenitization heat treatment for better mechanical properties such as impact toughness, ductility and hardness is austenitizing at 1050 °C for 60 s as shown in Figs. 2.4-2.5 (Isfahany *et al.*, 2011).

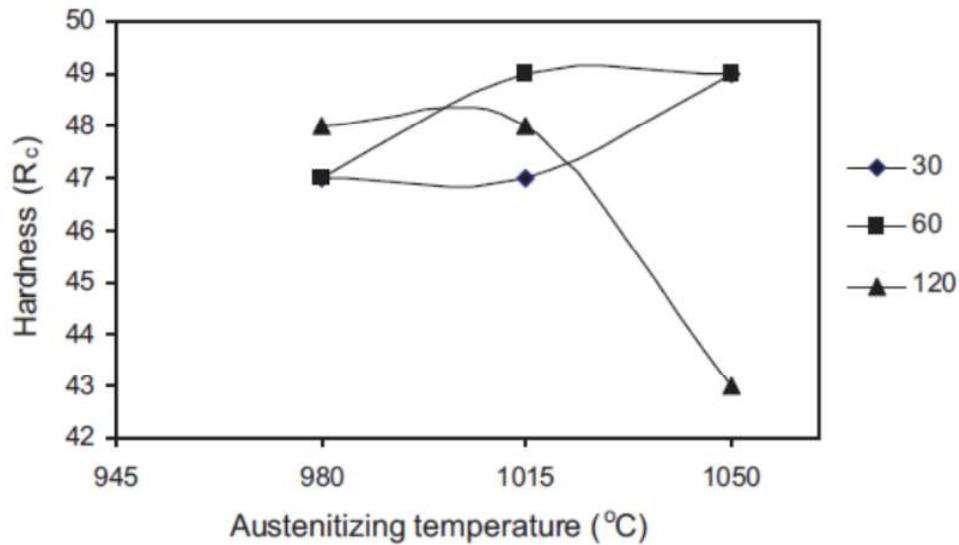


Fig. 2.4 Effect of austenitizing temperature and duration (in minutes) on hardness of Type 420 stainless steel (Isfahany *et al.*, 2011).

The changes in mechanical properties were attributed to the combination of two factors. First, the increase of the alloying elements such as Cr and C in the austenite with the increase of temperature and second, the presence of retained austenite within lath martensite which usually increases with austenitizing temperature and time and has a detrimental effect on hardness. Combination of these factors led to the highest hardness in the specimen austenitized at 1050 °C as compared to austenitization at 980 and 1015 °C.

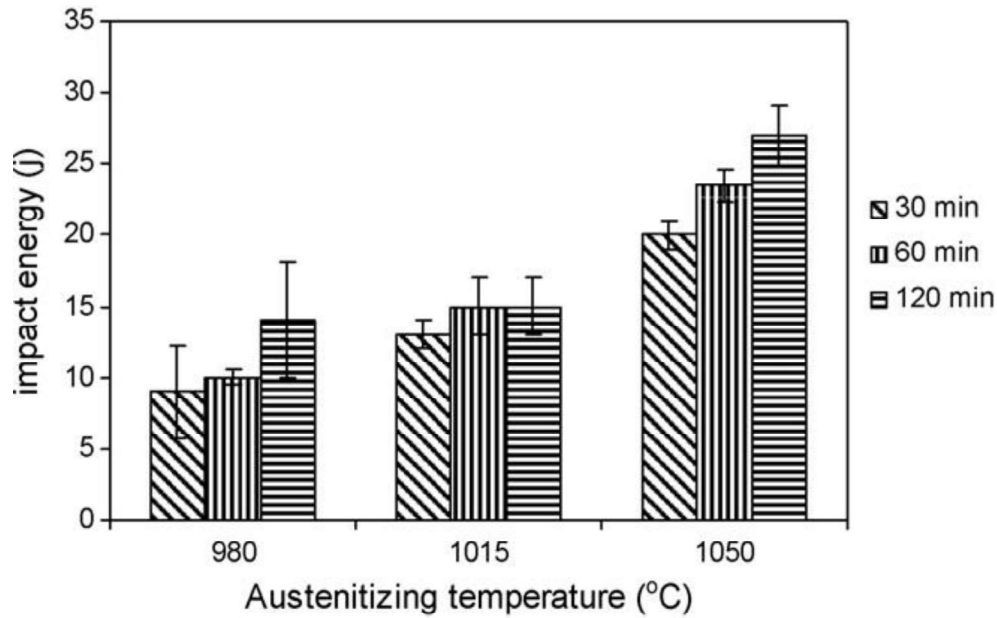


Fig. 2.5 Impact energy versus austenitizing time and temperature for Type 420 MSS (Isfahany *et al.*, 2011).

The MSSs with higher alloying elements can be hardened by air cooling but for thicker sections of MSSs, oil cooling is preferred for complete martensitic transformation (Barlow *et al.*, 2012). Garcia de Andres *et al.* (1998) showed that the increase of austenitizing temperature decreased carbide percentage from 9.9% to 6.6% in MSS with 13wt.% Cr and 0.45wt.%. Garcia de Andres *et al.* also demonstrated that upon austenitizing in the range of 1000–1050 °C, grain growth remains to a limited extent due to the presence of the undissolved carbides in the austenite grain boundaries during heating. In this range of temperature of 1000 to 1050 °C, there was a moderate austenite grain growth and tensile strength was not greatly changed (Garcia de Andres *et al.*, 1998). Previous studies have been showed that M_s temperature decreases with increase of austenitization temperature. It has been shown by Tsai *et al.* that M_s temperature for Type 410 stainless steel with 12.80 wt.% Cr and 0.12 wt.% C after austenitization at 900, 1000, 1100 and 1200 °C with a cooling rate of 100 °C are 320, 285, 280 and 245 °C respectively (Tsai *et al.*, 2002).

M_s temperature is dependent on the chemical composition and the equation given by Higgins shows that M_s temperature decreases with dissolution of alloying elements in steels at high temperatures (all alloy elements are in wt.%) (Higgins, 1983).

$$M_s = 500 - 333C - 34Mn - 35V - 20Cr - 17Ni - 11Mo - 10Cu - 5W - 15Co + 30Al \dots \dots (2.1)$$

Among all the elements shown in equation (2.1), C has strong influence on M_s temperature. The extent of dissolution of carbides increases with austenitization temperature and decreases M_s temperature. The M_s temperature of Type 420 stainless steel is reported to be in the temperature range of 300 °C to 70 °C and M_f temperature is estimated to be approximately 150 -200 °C lower than M_s temperature (Barlow *et al.*, 2012). Therefore, depending upon the composition and processing history, MSSs consist of martensite, retained austenite, undissolved carbides and δ -ferrite. Since the material is metallurgically complex, a meticulous control of heat treatment is necessary for formation of a fully martensitic structure without forming δ -ferrite and retained austenite. Therefore, for the given composition of the steel, strength and corrosion resistance completely depend on the amount of carbon and other alloying elements in the austenite. However, grain coarsening, decarburization and retention of austenite should be avoided by lowering the austenitization duration. The austenitization temperature and duration is very important in austenitization of MSS and is a crucial step for obtaining better mechanical properties after tempering treatment.

2.2.2. Tempering

The as-quenched martensite is highly brittle and the presence of residual stress could obviously deteriorate the mechanical and corrosion properties of MSSs. The as-quenched MSSs are heat treated in the temperature range of 150 to 750 °C (below the austenite start temperature (Ac_1)) to

modify the mechanical properties (Prabhu Gaunkar *et al.*, 1980, Isfahany *et al.*, 2011). This process is termed tempering, in which the as-quenched microstructure approaches the equilibrium under the influence of thermal activation.

Since, the as-quenched martensite is a super saturated solid solution of C in α -Fe, tempering of martensite in general begins with rejection of excess C to precipitate carbides. The nucleation, growth and coarsening of the precipitates occur during the tempering treatment. The precipitation strengthening is one of the strengthening mechanisms for MSSs. Besides the strength, the nano-sized precipitates formed during the tempering treatments also provide microstructural stability, resistance to creep and hydrogen damage (Yokota *et al.*, 2003, Maruyama *et al.*, 2001, Abe, 2004). The precipitate size, volume fraction and distribution are very important for controlling and obtaining better mechanical properties in tempered condition. The retained austenite, which is an untransformed austenite, does not remain stable during tempering. Therefore, tempering treatments decrease the dislocation density induced during quenching from austenitization temperature and cause nucleation of new secondary phases such as carbides and decreases the retained austenite volume fraction. The precipitation and coarsening of the secondary phases (mainly carbides) during the tempering treatments play a key role in determining the properties of the MSS in service conditions (Tao *et al.*, 2014).

2.2.2.1. Microstructural changes with tempering treatments

Lu *et al.* showed the formation of M_3C type of carbides at lower tempering temperature of 300 °C and formation of $M_{23}C_6$ carbides after tempering at 500 and 650 °C in 13wt.% Cr MSS. The precipitation sequence in 13 wt.% Cr MSS is suggested to be Fe-rich M_3C carbide \rightarrow Cr-rich $M_{23}C_6$ (Lu *et al.*, 2015) but no direct evidence of carbide transformation was shown by these authors.

Table 2.3 Microstructural changes in as quenched 12wt.% Cr-0.1wt.% C MSS as a function of tempering temperatures (Prabhu Gaunkar *et al.*, 1980).

Tempering temperature, °C	Type of precipitates	Location	Dislocation density in matrix
Up to 150	no precipitation	--	very high
150-350	M ₃ C	martensitic laths	very high
350-500	M ₃ C to M ₇ C ₃	martensitic laths	
550-650	M ₇ C ₃	martensitic laths	Reduced
	M ₂₃ C ₆	interfaces	
650-750	M ₂₃ C ₆	interfaces	Very low
	M ₂ (C,N)	martensitic laths	

Prabhu Gaunkar *et al.* (1980) also reported the formation of M₃C type carbides in the lower tempering temperature range of 150 to 350°C, M₃C and M₇C₃ type carbides in the tempering temperature range of 350 to 500 °C, formation of M₇C₃ and M₂₃C₆ type carbides in the temperature range of 550 to 650 °C and M₂₃C₆ and M₂(C, N) (M= Fe and Cr) type carbides in higher tempering temperature of 650 to 750 °C in 12wt.% Cr MSS (Prabhu Gaunkar *et al.*, 1980).

Microstructural changes observed in as quenched 12wt.% Cr MSS as a function of tempering temperatures are shown in Table 2.3. Tao *et al.* also characterized the precipitates formed in X12CrMoWVNb10-1-1 steel after different tempering treatments and showed the precipitation sequence of carbide phase with increasing tempering temperature as: Fe-rich M₃C → Cr-rich M₇C₃ → Cr-rich M₂₃C₆ (Tao *et al.*, 2014). Tao *et al.* also showed that the precipitation of carbides occurs in the first tempering treatments and transformations of the carbides from Cr-rich M₇C₃ to Cr-rich

$M_{23}C_6$ occurs in the second stage tempering (double tempering) (Tao *et al.*, 2014). The stable carbide for MSS at a tempering temperature of 700 °C is $M_{23}C_6$ (equilibrium carbide with ferrite phase at 700 °C is $M_{23}C_6$) (Prabhu Gaunkar *et al.*, 1980, Tao *et al.*, 2014, Lu *et al.*, 2015, Chakraborty *et al.*, 2015, Lu *et al.*, 2015a, Thomson *et al.*, 1992). Janovec *et al.* investigated the carbides formed in 12wt.% Cr steel after austenitizing at 1100 °C and 1300 °C followed by tempering at 750 °C (Janovec *et al.*, 1998). Previous studies on modified 12-13wt.% Cr steels also showed formation of M_3C , M_7C_3 and $M_{23}C_6$ type carbides during tempering treatments (Thomson *et al.*, 1992). The carbides or precipitates formed are different after different tempering treatments for MSSs. Thomson *et al.* showed the transformation of carbides from Fe-rich M_3C → Cr-rich M_7C_3 → Cr-rich $M_{23}C_6$ with tempering duration at 700 °C in 12CrMoV power plant steel (Thomson *et al.*, 1992). The formation of $M_{23}C_6$ carbides at lath and other boundaries above tempering temperature of 500 °C was observed by Irvine *et al.* and it grows at the expense of M_7C_3 carbides (Irvine *et al.*, 1960). The size of the carbide precipitates also changed from nano to sub-microscopic size with increase of tempering treatments (Lu *et al.*, 2015a).

Therefore, the type of the carbides formed during tempering treatment is dependent on chemical composition of the material, tempering temperature and duration. The precise control of temperature and time is necessary for obtaining desired mechanical properties by controlling nature of the precipitates, size and distribution.

2.2.2.2. Cr depletion associated with carbide precipitation in MSSs

After carbides nucleation, the growth involves migration of the carbide forming elements to the carbides and significantly modify the interface chemical composition. The carbides formed in stainless steels are generally Cr-rich carbides. The precipitation of the Cr-rich carbides would result in Cr depletion at the interface of carbide and matrix region. The phenomenon of Cr

depletion at carbide-matrix interface in austenitic stainless steels was first proposed by Bain et al. (Bain *et al.*, 1933) and is well studied in austenitic stainless alloys. The Cr depletion widths reported for sensitized austenitic stainless alloys are several tens of nm from the grain boundary/carbide interface (Bruemmer *et al.*, 1994, Chen *et al.*, 1990, Kain *et al.*, 2002). Stawstrom et al. proposed that the austenitic stainless steels are susceptible to corrosion only when the grain boundaries have Cr depletion zone of 20 nm width with a concentration of less than 13 at.% (Stawstrom *et al.*, 1969). Nakamichi et al. showed the width of the Cr depletion region measured across prior austenite grain (PAG) boundary in between Cr-rich carbides is around 10 to 15 nm in low carbon MSS tempered at 650 °C (Nakamichi *et al.*, 2008) and showed no Cr-depletion at carbide-matrix interface, as shown in Fig. 2.6. No detailed studies are available in literature on Cr depletion profiles associated with carbide precipitation in MSSs.

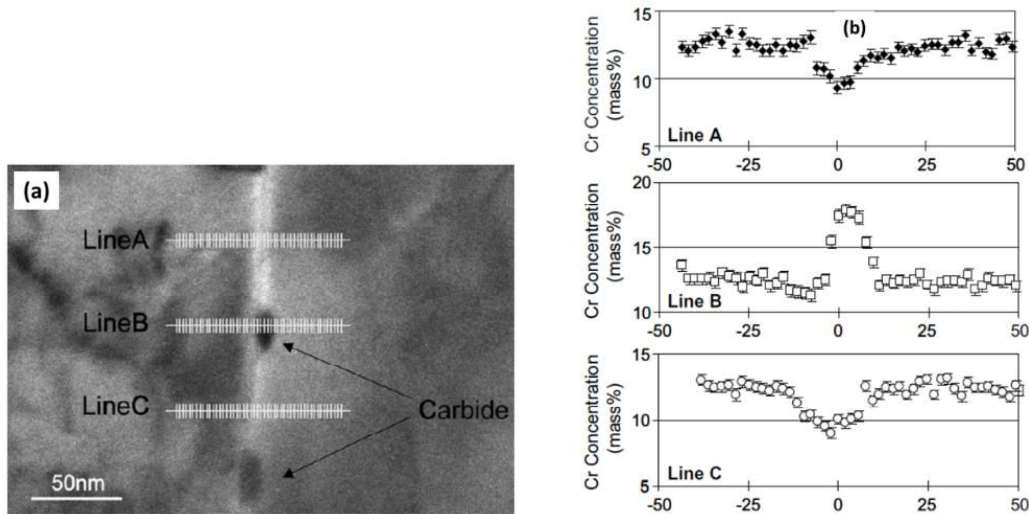


Fig. 2.6 (a) Scanning transmission electron microscope image of low C MSS showing PAG boundary and carbides and (b) Cr distribution across PAG boundary and carbide. Line A and C shows Cr depletion zones (Nakamichi *et al.*, 2008).

So far, to the best of author's knowledge, no technical papers are available on the extent of Cr-depletion region at the carbide-matrix interface regions in tempered 13wt.% Cr MSS used in the present investigation and the size and nature of the precipitates with different tempering treatments. Since, MSSs are always used in a tempered condition, localized corrosion (pitting and intergranular) is a potential degradation issue due to the precipitation of Cr-rich carbides at PAG boundaries and at martensitic lath boundaries.

The corrosion resistance of the stainless steels (SS) is because of the protective passive film formed over the surfaces. This thin, tenacious and self-healing oxide film forms on the surfaces containing more than 11wt.% Cr (Sedriks, 1996). But SSs are prone to localized forms of corrosion viz, pitting, intergranular, crevice and stress corrosion cracking under certain conditions if the Cr concentration falls below 12wt.% at carbide-matrix interface regions. Therefore, final microstructure of the MSS obtained after austenitization and tempering dictates the corrosion and mechanical properties. The characterization of the precipitates formed during the austenitization and tempering heat treatments contributes to a better understanding of the precipitation process and provides a better interpretation on the material performance in a given environment.

2.3. Degradation modes in martensitic stainless steels

The MSSs are sensitive to tempering temperature and susceptible to temper embrittlement and temper martensite embrittlement. The MSSs used in tempered condition may suffer environmentally induced degradation such as localized corrosion (IGC, pitting and crevice corrosion), SCC and HE.

2.3.1. Intergranular corrosion

IGC is a form of localized corrosion that preferentially attacks at and along the grain boundaries with negligible corrosion of the grain matrix (Fontana, 1987). IGC occurs in sensitized regions of stainless steels as a result of inadequate heat treatments during welding or in-service (Kain *et al.*, 1992). IGC attack leads to premature failure of the stainless steel by grain dropping and thinning. The reason for attack at grain boundaries are (1) due to depletion of an alloying element at grain boundaries e.g. depletion of Cr (in stainless steels) leading to less protective passive film at depleted grain boundaries and (2) enrichment of alloying additions e.g. Si and P in stainless steels (Fontana, 1987). Sensitization refers to the chromium carbide precipitation at the grain boundary with concomitant depletion of Cr in the immediately adjacent regions at grain boundaries to a level below 12 wt.%, thereby making the Cr depleted regions prone to localized corrosion attack (Kain *et al.*, 1992, Palit *et al.*, 1993). The Cr will deplete in the surrounding metal matrix and results in inhomogeneous Cr distribution at the interface of the carbide and matrix.

The passive films formed over Cr depleted regions are weak and not stable and leads to preferential corrosion attack (Cihal *et al.*, 2004). It is also to be noted that sensitization results in two aspects in the stainless steels, (a) formation of chromium carbides at grain boundaries and (b) formation of chromium depletion regions adjacent to these carbides at grain boundaries (Kain *et al.*, 2002). Martensite induced sensitization is another type of sensitization where the intragranular attack is reported due to precipitation of Cr-rich carbides at martensite formed in Type 304 austenitic stainless steels (Kain *et al.*, 2005). IGC is a potential degradation problem in MSSs due to the precipitation of Cr-rich carbides at PAG boundaries and in the martensitic lath boundaries if the Cr concentration in the depleted regions falls below 11-12wt.%.

2.3.1.1. Evaluating the susceptibility to IGC of stainless steels

The susceptibility to IGC of austenitic and ferritic stainless steels is assessed by acid immersion tests as per ASTM A 262 and ASTM A763 respectively (ASTM A 262, ASTM A 763). The corrosion behavior of stainless steels is often determined using electrochemical tests. As IGC is primarily under anodic control, it would be expected that the anodic polarization curve of sensitized material would be different from that of non-sensitized material. Hence, polarization curves produced by the potentiodynamic method have been used to indicate occurrence of sensitization and to compare degrees of sensitization. Potentials in anodic-polarization that lead to attack are also used as guides for the potentiostatic etching method (Cihal, 1980). Over the last three decades, electrochemical techniques are used by many researchers to assess the sensitization and associated Cr depletion regions in stainless steels. Electrochemical potentiokinetic reactivation (EPR) is another method that has been used quantitatively and nondestructively to evaluate IGC susceptibility of stainless steels.

EPR (single and double loop) tests which are quick, quantitative and nondestructive were used to evaluate the susceptibility to IGC by establishing degree of sensitization (DOS) (Cihal, 1980, Cihal *et al.*, 2004, Majidi *et al.*, 1984). DOS essentially measures the extent of Cr depletion (including that induced by precipitation of chromium carbides at the grain boundaries or any other phase formations, e.g., σ phase) (Chandra *et al.*, 2013a, Lo *et al.*, 2011). The double loop EPR (DL-EPR) test was initially developed for Type 304 /304L austenitic stainless steels and most of the literature on evaluating the susceptibility to IGC by electrochemical corrosion tests addresses austenitic stainless steels. There are enough literature evidences and theoretical studies indicating that the IGC in austenitic stainless steels is mainly governed by the Cr depleted regions (Sahlaoui *et al.*, 2002, Akashi *et al.*, 1980). A good correlation between the results of EPR test and susceptibility

to IGC or stress corrosion cracking is available for austenitic stainless steels (Cihal, 1980, Cihal *et al.*, 2004, Majidi *et al.*, 1984, Stansbury & Buchanan, 2000).

Other electrochemical methods such as EIS have been used successfully for investigating the IGC behavior of the austenitic stainless steels (Arutunow *et al.*, 2011, Arutunow *et al.*, 2009). The modifications in the test solution, which was originally developed for austenitic stainless steels, were done and successfully used for evaluating IGC resistance of austenitic Type 316(UNS S31600)/316L(UNS S31603), duplex, martensitic and ferritic stainless steels (Cihal *et al.*, 2004). It has been established very clearly that EPR tests result in attack on the Cr depleted regions and not on the chromium carbides (Kain *et al.*, 2002). It has also been shown that although the Cr depletion regions are very narrow, the attacked regions during EPR tests are much wider and that the depth (the minimum level of Cr in the depletion regions) essentially dictates the DOS value (and not the width of Cr depletion regions) (Ahmedabadi *et al.*, 2013, Kain *et al.*, 2002). But good correlations between the EPR test results and susceptibility to IGC are not available for 13wt.% Cr MSS.

2.3.1.2. Effect of tempering treatments on IGC of MSSs

The MSSs have received little attention in literature and only a few technical papers are reported on evaluating IGC behavior of these steels by electrochemical techniques (Muller *et al.*, 2015, Alonso *et al.*, 1999, Taji *et al.*, 2015, Aquino *et al.*, 2009). The solution of 0.5 M sulfuric acid (H_2SO_4) + 0.01 M potassium thiocyanate (KSCN) is conventionally used for evaluating DOS of austenitic stainless steels (Cihal, 1980). Alonso *et al.* studied IGC behavior of Type 410 stainless steel in 0.5 M H_2SO_4 solution using different electrochemical techniques such as potentiodynamic anodic polarization, potentiostatic polarization and DL-EPR technique (Alonso *et al.*, 1999) as shown in Fig. 2.7(a)-(b). The electrochemical results obtained by different electrochemical

techniques were compared as a function of tempering temperatures and showed DL-EPR is the best method to discriminate DOS with tempering temperature (Alonso *et al.*, 1999) as shown in Fig. 2.7(b). However, the DOS value reported for the specimen tempered at 550 °C condition in Alonso *et al.* study is more than 1 as shown in Fig. 2.7(a). The reactivation current density is more than the activation current density in DL-EPR curve and is attributed to the increase in the surface roughness due to excessive dissolution in 0.5 M H₂SO₄ solution. But modifications in the test solution were carried out by researchers to decrease the current density values in activation and reactivation scan during DL-EPR tests of MSSs.

The effect of tempering temperatures on DOS and pitting corrosion of Type 403 stainless steel was studied and a correlation between the pitting tendency and sensitization with the tempering temperatures was shown (Taji *et al.*, 2015).

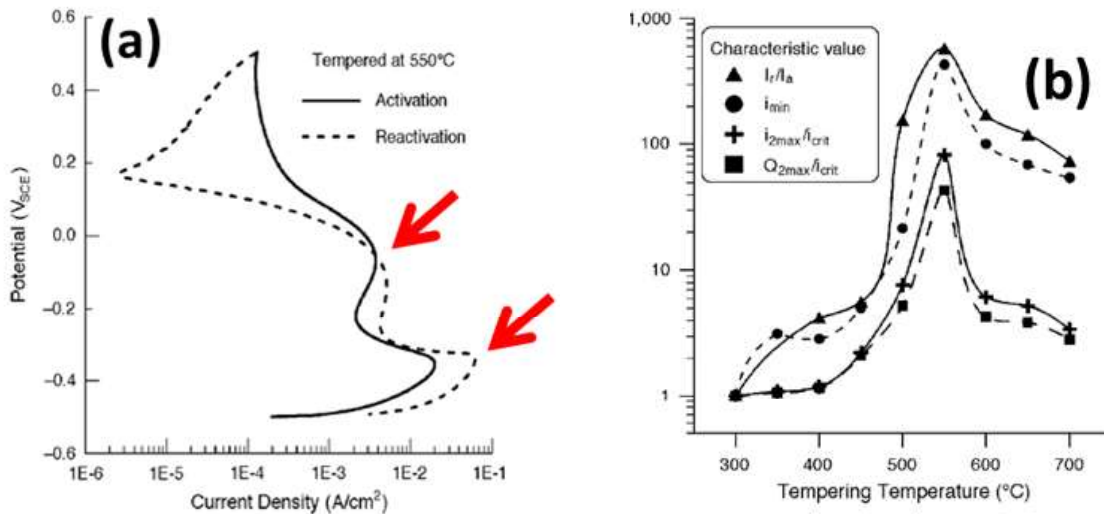


Fig. 2.7 (a) DL-EPR curve in 0.5M H₂SO₄ solution for 550 °C tempered specimen of Type 410 showing reactivation current density is higher than activation current density and (b) variation in different electrochemical properties with tempering temperature (Alonso *et al.*, 1999).

The solution used for evaluating the DOS is 0.01M H₂SO₄. The activation and reactivation scans in DL-EPR of Type 403 and 410 SS (12 wt.% Cr) have two anodic peaks (Fig. 2.7 & 2.8) as reported and the microstructural features which are causing the two anodic peaks in anodic polarization were not established in these studies (Alonso *et al.*, 1999, Taji *et al.*, 2015).

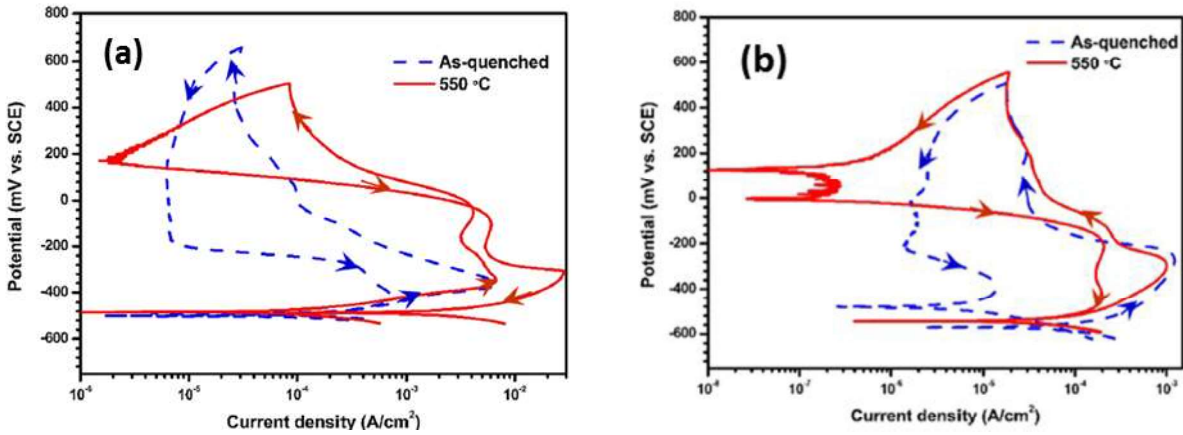


Fig. 2.8 (a) DL-EPR curves in 0.1 M H₂SO₄ solution and (b) DL-EPR curves in 0.01 M H₂SO₄ solution for Type 403 MSS in as-quenched and tempered at 550 °C.

Aquino *et al.* studied the IGC behavior of the super MSS weldments and demonstrated the peak potentials causing the attack at matrix and interfaces with carbide precipitation (Aquino *et al.*, 2009). With the best of author's knowledge, no technical papers are available for 13wt.% Cr MSS showing the Cr depleted regions at the carbide matrix interface and IGC behavior with different tempering treatments. The solutions used in A262, ASTM and A763, ASTM standard tests (the boiling solution of 65% nitric acid and the boiling solution of 50% sulfuric acid - 25g ferric sulfate) for evaluating the susceptibility to IGC are too aggressive for 13wt.% Cr MSSs and these tests do not have the ability to detect low levels of degree of sensitization. The 5% HNO₃ solution at room temperature has been shown in a previous study to establish the susceptibility to IGC of MSSs but post microstructural characterization of the exposed specimens was not done to show and explain nature of attack in MSSs (Sedriks, 1996, Cihal, 1984).

2.3.2. Pitting corrosion

Pitting corrosion is a form of localized corrosion and results in formation of small holes in metal and is dependent on the environment (Fontana, 1987). The materials showing active passive behavior are generally prone to pitting corrosion. The breakage of the passive film in the presence of aggressive ions like chloride, exposes the underlying metal to the environment and accelerated dissolution of the exposed metal occurs due to the presence of the large cathodic area. This process produces small holes or pits on the metal surface. The pits formed on the metal surface act as stress raisers and also decrease the strength of the component. The mechanism of pitting corrosion involves the electrochemical reactions and the local environment should be able to drive the current exchange between the exposed metal area and its surrounding passive region (Stansbury & Buchanan, 2000). The breakage of the passive film can be caused by different factors and mechanisms (Stansbury & Buchanan, 2000). The susceptibility to pitting corrosion of stainless steels and the other alloys in chloride containing solutions can be established using potentiodynamic, potentiostatic polarization and critical pitting temperature measurements (Fontana, 1987, Stansbury & Buchanan, 2000). The determination of the pitting potential in chloride solution using anodic polarization technique gives a rapid screening of the materials susceptibility to pitting corrosion.

2.3.2.1. Effect of tempering treatments on pitting corrosion

In general, pit nucleation occurs at the surface-active sites/heterogeneities such as inclusions, precipitates and the regions with weak passive films (Sedriks, 1996). Pitting corrosion of sensitized stainless steels has been shown to be dependent on the carbide interfaces and also the carbide interfaces having Cr depletion regions (Park *et al.*, 2005, Vignal *et al.*, 2014). The surface oxide film formed over Cr depleted regions (sensitized regions) is weak and not stable therefore leads to

preferential corrosion attack (Stansbury & Buchanan, 2000). Until now, a few studies are available on the pitting corrosion behavior of MSS with different tempering treatments (Lu *et al.*, 2015a, Lu *et al.*, 2016, Taji *et al.*, 2015, Qi *et al.*, 2017).

In a study by Taji *et al.* showed decreased pitting resistance after tempering at 550 °C for Type 403 stainless steel with 11.2 wt.% Cr and this behavior is attributed to sensitization after tempering at 550 °C (Taji *et al.*, 2015). Aquino *et al.* also showed a decrease in pitting corrosion resistance with increase in degree of sensitization in super martensitic weldments (Aquino *et al.*, 2009). The decreased pitting resistance for 13wt.% Cr MSS tempered at 500 °C was reported by Lu *et al.* and the reason for least pitting resistance was established to be due to massive precipitation of nano-sized carbides at this tempering temperature (Lu *et al.*, 2015). But these studies have not included the compositions of the passive films formed at metal-solution interfaces on austenitized and tempered conditions but have a direct influence on the pitting corrosion resistance.

The thin passive film composed of Cr₂O₃ formed on surface of the stainless steel makes it resistant to localized attack. The Cr₂O₃ is one of the constituents of the passive film and the exact composition and thickness of the passive film is a study of interest for several researchers and is dependent on many factors such as microstructure, alloying elements, environment (aerated, deaerated, alkaline, neutral or acidic), temperature and time (Sedriks, 1996). The nature of the passive films formed on the stainless steels has been studied using EIS and surface analytical techniques. By X-ray electron spectroscopy (XPS), chemical states of the elements present in the passive film formed on stainless steels are obtained for better knowledge on chemical composition and structure of the passive film (Asami *et al.*, 1979, Freire *et al.*, 2010, Jung *et al.*, 2012).

It has been showed that the passive films formed in neutral or alkaline environments are duplex in nature with an inner layer is enriched in Cr_2O_3 and outer layer is enriched in oxides/hydroxides of Fe (Lorang *et al.*, 1994, Freire *et al.*, 2010). The surface films formed on Type 420 stainless steel in chloride solution with aerated and deaerated conditions was studied and it was shown that the surface film contained oxides and hydroxides of Fe and Cr (Marcelina *et al.*, 2015). There are no detailed reported studies on the nature of the passive films formed on tempered 13wt.% Cr MSSs in chloride solutions and their influence on pitting corrosion. Therefore, still the question remains on how to relate microstructure (carbide precipitation and extent of Cr depletion at carbide matrix interface) and passive film properties with pit initiation in 13wt.% Cr MSS with different tempering treatments.

2.3.3. Changes in mechanical properties with tempering treatments

MSSs such as Type 403, 410 & 420 are used as parts of pumps, valve seats, stem rods, nut and bolts in LWRs and also in other industries because of their good mechanical properties and moderate corrosion resistance (Scott, 2000). The effect of tempering treatments on mechanical properties of these steels has been a topic of interest over the past few decades as the properties of these steels could be tailored by austenitizing and tempering treatments (Wang *et al.*, 2013, Barbadikar *et al.*, 2015). The final microstructure obtained after heat treatments, plays an important role in controlling the mechanical properties. MSSs, often did not show decrease in hardness with increase of tempering temperature at fixed tempering duration. The phenomenon of secondary hardening associated with fine carbide precipitation was also observed for some of the MSSs with tempering (Isfahany *et al.*, 2011).

Significant reduction in impact toughness value with an intergranular fracture was observed for MSSs after tempering. It has been reported in the previous studies that 12wt.% Cr MSSs are

susceptible to temper embrittlement in the temperature range of 450 to 600 °C (Prabhu Gaunkar *et al.*, 1980, Bhambri, 1986, Tsay *et al.*, 2002). The room temperature impact notch toughness of these steels decreased significantly in the tempering temperature range of 400– 600 °C and MSSs were brittle with intergranular fracture as reported by Prabhu *et al.* and also by other researchers (Prabhu Gaunkar *et al.*, 1980, Bhambri, 1986, Tsay *et al.*, 2002, Chakraborty *et al.*, 2015). The phenomenon of temper embrittlement, (i.e. decrease in notch impact toughness of the material) has been known for a long time in the case of low alloy steels when subjected to tempering in the temperature range of 400-600 °C (Dieter, 1988). The hardness and tensile properties of the materials tempered in these temperature range are not sensitive but the ductile to brittle transition temperature (DBTT) is raised by 100 °C (Dieter, 1988).

In 12 wt.% Cr MSSs, only reversible temper embrittlement was observed as compared to tempered martensite and irreversible temper embrittlement (Prabhu Gaunkar *et al.*, 1980). The susceptibility to embrittlement increases with the tempering time in the temperature range of 350 to 600 °C, reaches maximum and then decreases with the prolonged duration of tempering (over aging). This is called as reversion process. The embrittlement is believed to be segregation of impurity elements e.g. phosphorous, tin, silicon and antimony or the alloying elements (Cr). The role of carbon on the embrittlement is still uncertain (Prabhu Gaunkar *et al.*, 1980). These impurities segregate at microstructural features and the evidence was reported by Prabhu Gaonkar *et al.* by analyzing the fracture surface by auger electron spectroscopy and is shown in Table 2.4. The segregation of Group IVA, VA, and transition elements occurs along high-energy interfaces, e.g. at PAG boundaries. These act as preferential paths for brittle crack propagation. These elements are believed to decrease the cohesive energy of the grain boundaries and are dependent on the material's yield strength, grain size and microstructure.

At a given concentration of these elements segregation to PAGBs can change the brittle fracture path from a cleavage plane to grain boundaries (IG) (Prabhu Gaunkar *et al.*, 1980, Briant *et al.*, 1978). The changes in mechanical properties in Type 410 SS with tempering treatments were also studied by Chakroborty *et al.* who observed brittle IG fracture for Type 410 SS tempered at 550 °C for 1h in Charpy V-notch impact tests done at room temperature (Chakroborty *et al.*, 2015)

Table 2.4 Evidence of P segregation (a few atomic layers only) at grain boundaries: AES analysis done on IG fracture surface after tempering at 550/650 °C (Prabhu Gaunkar *et al.*, 1980).

Condition	Detected element	On the surface	After sputtering of 5 atomic layers
550°C/1h	P	9	0
	Cr	21.5	20.5
	Fe	78.5	77.5
550°C/100h	P	25	0
	Cr	30.7	20.5
	Fe	69.3	77.5
650°C/1h	P	12.4	0
	Cr	27.3	22.2
	Fe	72.6	75.7

The surface analysis carried out on the fracture surface of Type 410 SS tempered at 550 °C for 1h by auger electron spectroscopy did not show the evidence of P or S segregation to PAG boundaries. The phenomenon of temper embrittlement was attributed to presence of Fe₂C type carbides in the matrix and M₂₃C₆ type carbides at the PAGBs (Chakroborty *et al.*, 2015). Other researchers also reported that the temper embrittlement in MSSs such as Type 403, 16Cr-2Ni SS was due to secondary hardening associated with precipitation of M₂C and M₇C₃ (M = Fe & Cr) type carbides (Lim *et al.*, 1993, Balan, 1998). But, many studies have identified the reason for temper embrittlement to be due to P segregation at the grain boundaries and successfully detected the presence of the P along the grain boundaries on temper embrittled samples using in-situ auger

electron spectroscopy analysis (Prabhu Gaunkar *et al.*, 1980, Tsay *et al.*, 2002, Ning, 1991). The presence of impurity segregation (P) is also detected and reported by nondestructive electrochemical methods using picric acid based solutions as the picric acid has higher sensitivity to attack at the P segregated grain boundaries (Viswanathan, 1985, Zhai *et al.*, 2015).

The failures of the Type 420 stainless steel components in the initial stages of the service used in boric acid solution at a temperature 120 °C was reported by Chandra *et al.* and as shown in Fig. 2.9 (Chandra *et al.*, 2013), both valve seat and stem rod fabricated from Type 420 stainless steel showed IG fracture along PAG boundaries and the failures were attributed to temper embrittlement phenomenon. Apart from IG cracking, IGC attack at several locations on the surface of the valve seat and rod were also observed by Chandra *et al.* as shown in Fig. 2.10 and attributed to acid pickling of these materials in nitric acid solution.

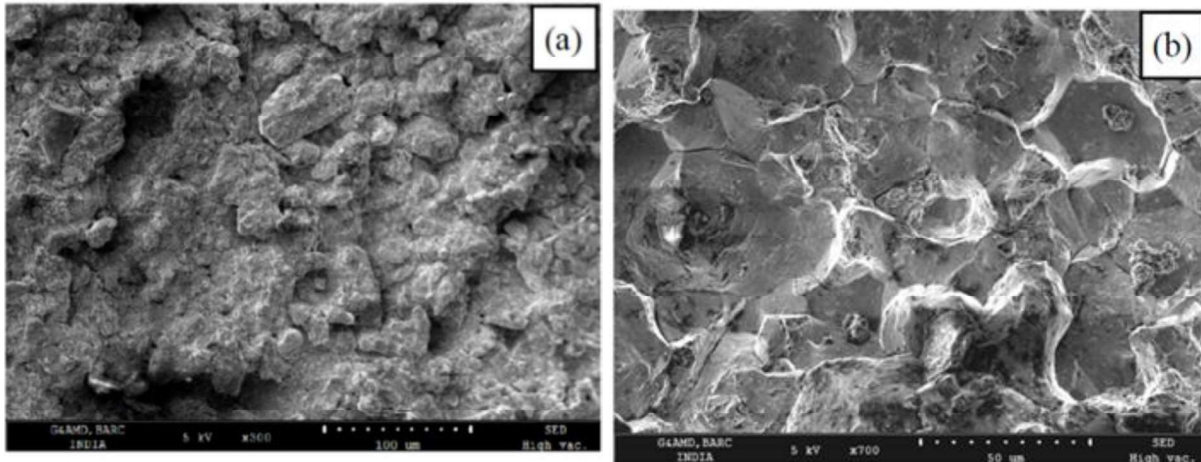


Fig. 2.9 SEM fractographs of the Type 420 martensitic stainless steel components showing intergranular fracture: (a) valve seat and stem rod (Chandra *et al.*, 2013).

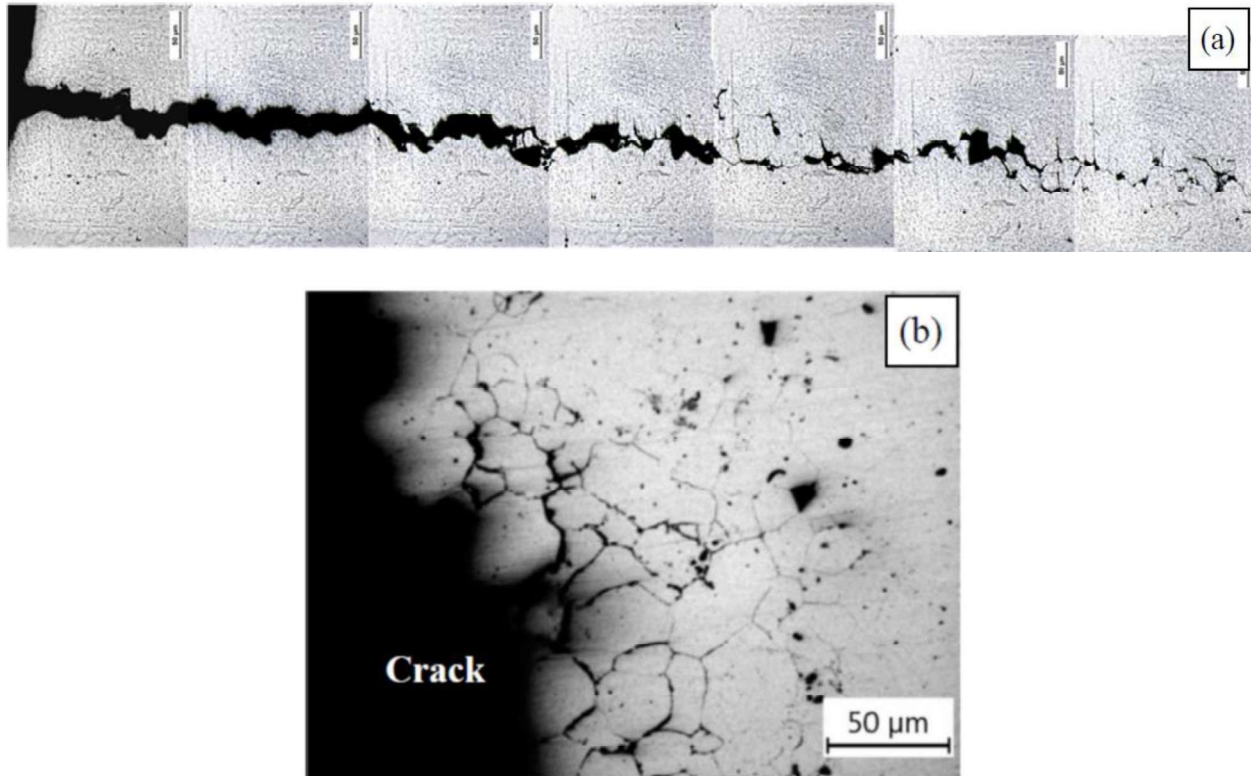


Fig. 2.10 Optical images of the valve seat showing the (a) crack propagation along the PAGBs and (b) region at the crack face showing IG cracking/corrosion (Chandra *et al.*, 2013).

2.4. HE in martensitic steels

The tempered martensitic microstructure obtained after the heat treatments play an important role in controlling mechanical properties. However, HE is a serious degradation issue for MSSs because of their high strength. The phenomenon of HE in steels is due to the presence of dissolved hydrogen that leads to sudden failure or delayed rupture. HE can be either (a) internal hydrogen embrittlement (IHE), which is due to the pre-existing hydrogen in the steel matrix, or (b) hydrogen environment embrittlement (HEE), wherein the hydrogen is picked up from the environment such as aqueous corrosion process, cathodic protection and hydrogen gas (Tiwari *et al.*, 2000, Lu *et al.*, 2013, Lynch, 2011). The MSSs components failed by HE phenomenon in PWR primary water were tempered at lower tempering temperatures (Scott, 2000).

Hydrogen forms as a corrosion reaction by-product and radiolysis of coolant water are the main sources for pick-up by materials, though hydrogen gas is also added in PWRs coolant water (Scott, 1994). The main effects of hydrogen on steels are decrease in ductility, toughness, and true stress at fracture and accelerated crack growth (Tiwari *et al.*, 2000, Lu *et al.*, 2013, Lynch, 2011). As hydrogen enters the steel lattice, it embrittles it over a period of time and is dependent on several factors such as, amount of hydrogen, microstructure, applied/residual stress, whether hydrogen is present internally or entering during the straining and also on temperature (Tiwari *et al.*, 2000, Lai *et al.*, 2013, Nanninga, 2010). The atomic hydrogen will diffuse into the metal and occupy the interstitial sites or trapping sites due its small volume. The diffusion of hydrogen is also dependent on several factors such as temperature, applied stress/ residual stress and also the presence of traps (defects) inside the material and is discussed in several reviews and papers (Olden *et al.*, 2008, Bhadeshia, 2016, Lynch, 2012). The different trap sites available in a material with their binding energy (activation) are given in Table 2.5.

The interaction of hydrogen with these traps decides the residence time of the hydrogen in those particular traps. If the interaction energy (trap-hydrogen binding energy) is higher than the diffusional activation energy in interstitial site, then those trap sites are called as potential hydrogen trap sites/sinks (Pressouyre, 1979, Bhadeshia, 2016). The traps with the binding energies lower than 50 kJ/mol are considered as reversible traps while higher binding energies are considered as irreversible traps. The tempered martensite microstructure consists of retained austenite, precipitates, inclusions, dislocations and grain/lath boundaries. The interaction of hydrogen with these traps is responsible for changes in the mechanical properties of the steels tempered at different temperatures.

Table 2.5 Different hydrogen trap sites with their binding energy (Bhadeshia, 2016, Li et al., 2017).

Trapping sites	Binding energy (kJ/mol)
Reversible trap sites (binding energy < 50kJ/mol)	
Interstitial sites in Fe based alloy	4-8
Grain boundaries	17.8-18.6
Dislocations	26.4-26.8
Austenite/martensite interface	22
Lath boundary	17.8-18.6
Irreversible trap sites (binding energy > 50kJ/mol)	
Ferrite/cementite interfaces	66.3-68.4
Fe ₃ C interface	84
MnS interface	72

In general, HE susceptibility decreases with increase of tempering temperature for martensitic steels as tempering decreases the strength of the martensite and increases its ductility (Siddiqui *et al.*, 2005, Li *et al.*, 2017). The high Cr-martensitic steels are also susceptible to intergranular SCC in environments where hydrogen is produced when H is effectively trapped at PAGB (Hippesley *et al.*, 1988). For high strength steels, such as dual phase, martensitic, complex phase and transformation induced plasticity steels, it has been pointed out that the steels with tensile strength higher than 1000 MPa are susceptible to HE and this limit dictates their use in automotive applications (Depover *et al.*, 2016, Matsuoka *et al.*, 2006, Eliaz *et al.*, 2002). The sensitivity to HE increases with increasing steel strength levels. But there are no such trends observed for steels

with strength values between 400 and 1000 MPa indicating that the microstructure of such steels plays a predominant role despite the fast diffusion rates of hydrogen in the high strength steels with ferritic or martensitic structures (Michler *et al.*, 2010, Sun *et al.*, 2011). Lai *et al.* showed pronounced decrease in strength and ductility of air-hardened Type 410 SS as compared to 410 SS tempered at 700 °C in gaseous hydrogen environment by tensile testing at crosshead speed of 1.2×10^{-4} mm/s (Lai *et al.*, 2013).

A study on the internal HE of maraging and mild steels was conducted by Tiwari *et al.* and showed decrease in total elongation, increase in modulus and work hardening after hydrogen charging (Tiwari *et al.*, 2000). Also observed was a strong ductility loss with intergranular cracking under combined effect of tensile straining and hydrogen in 9Cr-1Mo steel tempered at a higher temperature (760°C, hardness lower than 350 HV) (Maday, 2005). The results obtained showed definite dependence on the strain rate, mode of hydrogen charging, microstructure of the material. HE needs time for hydrogen adsorption and its diffusion into the steel (Louthan Jr, 2008, Venezuela *et al.*, 2015) and diffusivity of hydrogen in martensitic steels is low due to high defect density (Olden *et al.*, 2008, Venezuela *et al.*, 2015). Therefore, slower strain rates are favorable for hydrogen diffusion and its absorption. Several papers are available on strain rate influence on HE of steels and showed increased susceptibility to HE with slower strain rates (Dieter, 1988, Bal *et al.*, 2016). A considerable amount of research has been carried out to understand the detrimental effects of hydrogen on steels (Bhadeshia, 2016, Lynch, 2012, Lu *et al.*, 2013, Djukic *et al.*, 2015). But it is difficult to predict the service life of a chosen metallic material in the hydrogen environment. So, HE is a complex phenomenon and still a fully developed and practically applicable model does not exist to predict the failures due to hydrogen in metallic materials.

In general, two methods of hydrogen charging are used for establishing the effects of hydrogen in steels for steels used in hydrogen bearing environments: (i) electrochemical hydrogen charging and (ii) gaseous hydrogen charging (Liu *et al.*, 2014). The method of hydrogen charging is also shown to influence the mechanical properties of the investigated steels (Escobar *et al.*, 2012, Escobar *et al.*, 2012a, Biggiero *et al.*, 1995). The electrochemical hydrogen charging causes different trap sites for hydrogen becoming more active as compared to gaseous hydrogen charging at elevated temperatures (Wallaert *et al.*, 2014). Tensile testing is commonly used and could be the first in a row of tests to evaluate the susceptibility of metallic materials to HE (Michler *et al.*, 2010). The hydrogen enhanced localized plasticity (HELP), absorption induced de-cohesion (AIDE) and hydrogen enhanced de-cohesion (HEDE) are the recognized mechanisms for the HE of high strength and martensitic steels (Michler *et al.*, 2010, Bhadeshia, 2016, Lynch, 2012, Lu *et al.*, 2013, Djukic *et al.*, 2015, Dadfarnia *et al.*, 2010).

2.4.1. Cooperative relation between temper embrittlement and HE

The quenched and tempered alloy steels have shown cracking along the PAG boundaries under the conditions of HE or SCC (Hippesley *et al.*, 1988). The cracking associated with impurity segregation in these quenched and tempered alloy steels was also characterized by brittle IG cracking along the PAG boundaries (temper embrittlement). So, studies were done to understand the cooperative interaction between these two types of embrittlement in different alloy systems. The synergistic interaction between segregation induced temper embrittlement and HE has been observed in low alloy and other alloy steels (Yoshini *et al.*, 1974, Bandyopadhyay *et al.*, 1983, Xu *et al.*, 2012). Xu *et al.* studied, the effect of hydrogen concentration on strength and plasticity of temper embrittled and de-embrittled 2.25Cr-1Mo steel and observed higher HE susceptibility to temper embrittled steel (Xu *et al.*, 2012). The Ni-Cr, Ni-Cr-Mo and Cr-Mo steels also showed

higher HE susceptibility when heat treated in temper embrittlement temperature range of 370 °C to 565 °C. The susceptibility to HE of 9Cr-1Mo tempered steel, aged for 5000 h with hardness of 270 HV was similar to that of normalized condition with the hardness of 390 HV (Hippesley *et al.*, 1988).

The steels tempered in the temper embrittled temperature range showed ductile fracture in tensile tests carried out in air but the presence of hydrogen in these specimens significantly reduced the ductility (Hippesley *et al.*, 1988). The impurity elements such as P and sulphur are known to play significant role in embrittlement. The increased sensitivity to HE caused by the impurity segregation is attributed to a) inhibiting the hydrogen recombination by segregated impurities or b) both the embrittling elements (i.e. H and P) are segregating at the grain boundaries to decrease the cohesive strength (Hippesley *et al.*, 1988). Therefore, the strength criteria alone cannot be used for assessing material's susceptibility to HE for materials (including MSSs) with strength between 600 to 1000 MPa. The microstructural changes taking place during aging or tempering plays an important role in determining the material susceptibility to HE (Li *et al.*, 2017). So, the influence of tempering temperature on HE of steels depends on the type of steel rather than the strength of the tempered martensite.

Chapter 3

Microstructural changes in austenitized & tempered conditions

3.1. Background

Microstructure is one of the important aspects affecting the mechanical properties and corrosion of MSSs. The characterization of the precipitates formed during the austenitization and tempering heat treatments contributes to a better understanding of the precipitation process and provides a better interpretation on the material performance in a given environment. The microstructural changes in 13 wt.% Cr MSS with tempering temperatures were investigated in the present work using XRD, SEM and TEM coupled with nano-beam sized electron probe-energy dispersive spectroscopy (EDS) analysis and provided in this Chapter. From the XRD and TEM results, changes in retained austenite fraction and the different precipitates formed during tempering were established. The present study brings out the important phenomena in this stainless steel: 1) the formation sequence of carbides after tempering at different temperatures, which should be useful for the proper heat treatment scheme of this steel and 2) the existence of narrow Cr depletion of 7 to 9 nm at the nano-sized carbide-matrix interface regions after tempering at 550 °C.

3.2. Experimental

3.2.1. Materials and heat treatments

The chemical composition of the material used in the present study was analyzed using spark-optical emission spectroscopy and is given in Table 3.1. This composition is close to Type 420B

stainless steel as given in Table 2.2. Specimens of size 60 mm x 12 mm x 12 mm were cut from the 55 mm thick as-received (AR) MSS bar. These specimens were austenitized in a muffle furnace at 1040 °C for 1h as per ASTM F899 and also at 1020 °C for 30 min followed by oil quenching. The AR MSS specimens were also austenitized at 1100, 1200 °C for 1 h followed by air cooling to choose austenitization temperature for this study. Based on austenitization at different temperatures, temperature of 1020 °C for 30 min followed by oil quenching was chosen for austenitization of 13wt.% Cr MSS. Dilatometry was carried out to find the transformation temperatures of the studied MSS. The AR MSS was cut into cylindrical samples (5 mm diameter and 10 mm length) using electric discharge machine (EDM) for dilatometry. The specimen was heated from room temperature (25 °C) to 1020 °C with a heating rate of 20 °C/s and held for 30 min at 1020 °C and then cooling to room temperature at a rate of 50 °C/s. Based on this result, the tempering temperature range was chosen in this study.

Table 3.1 Chemical composition (in wt.%) of the 13 wt.% Cr MSS used in the present study.

C	Cr	Mn	Mo	Ni	V	P	S	Cu	Si	Fe
0.31	13.3	0.81	0.09	0.27	0.04	0.025	0.0047	0.48	0.33	Rest

Subsequently, the specimens austenitized at 1020 °C were tempered at different temperatures, from 300 to 700 °C in steps of 50 °C for 2.5 h followed by air cooling. In general, MSSs are subjected to tempering treatments typically for durations varying from 1 to 4 h for improving ductility and toughness (Isfahany *et al.*, 2011, Cheng *et al.*, 2015, Chakraborty *et al.*, 2015). In the present study, tempering treatment was carried out for duration of 2.5 h (Chandra *et al.*, 2013). Some of the austenitized specimens were tempered at 550 °C for 100 h and 500 h followed by air cooling.

3.2.2. Microstructural Characterization

After the heat treatments, all the specimens were mechanically ground on successively finer silicon carbide papers, from 80 to 1200 grit and were polished using a diamond paste of 1 μ m size. The specimens were then cleaned with soap solution and water and then degreased with acetone and dried. The presence of phases in the austenitized and tempered specimens was analyzed by X-ray XRD technique (Bruker make, D8 discover) with Cu K α radiation with step size of 0.02°. The volume fraction of the retained austenite was estimated from the integrated intensities of austenite and martensite peaks (Rajasekhar *et al.*, 2009).

The heat treated specimens were polished to diamond finish as mentioned above and etching was done by swabbing for 20 times with Vilella's reagent (1g picric acid + 5 ml hydrochloric acid + 95 ml ethanol) and microstructural examination was done using optical microscopy, field emission - scanning electron microscopy (FE-SEM; ZEISS make). Elemental composition of the different microstructural features was established with EDS in FE-SEM.

The microstructural changes occurred with different tempering treatments were characterized using TEM (FEI TECHNAI F 200kV). The TEM samples were prepared in two steps. First, a 0.2 mm thick slice was pre-thinned to 80 μ m by grinding on successively finer emery papers of 240 to 600 grit. From such 80 μ m thin sheet, 3 mm discs were punched out. The pre-thinned 3 mm discs of 80 μ m thick specimens were then twin-jet polished in a mixture of 10% perchloric acid and 90% methanol at -40 °C and 20 V potential to create a small hole approximately in the centre of the disk. Selected area diffraction (SAD) patterns were acquired from the precipitates and matrix to identify the phases and precipitates. The chemical composition of the matrix and precipitates was analyzed using TEM-EDS (Oxford instruments). The uncertainty in the EDS measurements is less than 0.5wt.%. It is difficult to precisely analyze the C content in the precipitate by TEM-

EDS and so C content is not reported in the present study and only the elements of Fe and Cr are considered in EDS analysis. The width of the lath in all the conditions is measured using image-J software by taking a minimum of 20 laths for each condition.

The precipitates formed in tempered specimens (550 and 700 °C) were extracted by dissolving the martensitic matrix electrochemically in 10 vol.% hydrochloric acid-methanol solution to identify the precipitates by XRD technique (Tao *et al.*, 2014, Chakraborty *et al.*, 2015). The tempered specimens were ground up to 400 grit emery paper and ultrasonically cleaned in acetone. The dissolution was done by applying a potential difference of 1.5 V between the specimen (anode) and the platinum foil (cathode) for a period of 48 h at room temperature (26 °C). The precipitates were extracted by centrifuging the solution. The extracted precipitates were transferred on glass slide for XRD analysis. The extracted precipitates were dispersed in methanol solution by ultrasonication process, a small drop of the solution was added on to the amorphous carbon coated Cu grid of 3 mm diameter to investigate under TEM.

The microstructural characterization was also done using electron back scattered diffraction and also by transmission electron microscopy (TEM, TECHNAI F200kV). The grain orientation information was obtained by EBSD measurements on electropolished surface of the 13wt.% Cr MSS specimens using EBSD equipped FE-SEM (FEI Quanta 3D). The electropolishing was done in 10% perchloric acid (HClO₄) + 90% methanol (CH₃OH) solution. EBSD measurements were made at an operating voltage of 20 keV at a step size (distance between the two measurements points) of 0.03 μm. TSL OIM 7.1 software was used for analysis of the scan data. Grain boundaries were determined by the grain tolerance angle and any point pair with misorientation exceeding 2° was considered as a boundary. The fraction of the low (misorientation less than 15°) and high angle grain boundaries (misorientation greater than 15°) were determined in tempered specimen.

3.3. Results and Discussion

3.3.1. Transformation temperatures and Austenitization

Fig. 3.1 shows the change in length of the as-received MSS specimen with temperature in dilatometer experiment. The specimen length increased linearly till the 849 °C, then decrease in length is observed till 877 °C. This start of decrease in length indicates the start of phase austenite transformation. The phase transformation is occurred till the temperature of 877 °C. The transformation temperatures, austenite start (A_{c1}) and austenite finish (A_{c3}) temperatures determined from Fig. 3.1 are 849 and 877 °C respectively.

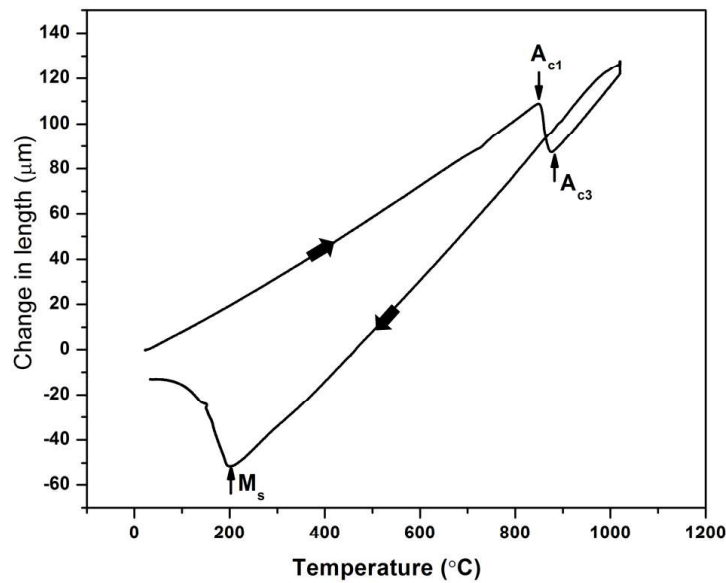


Fig. 3.1 Dilatometry of the as-received 13wt.% Cr MSS showing the transformation temperatures (A_{c1} , A_{c3} and M_s) during heating and cooling. Arrow indicates heating and cooling stages.

Further increase of temperature till 1020 °C and holding at this temperature for 30 min, increased the length due to thermal expansion of austenite phase and dissolution of the precipitates if any. During cooling, rapid expansion of the specimen observed at temperature of 203 °C, which is the martensite start temperature (M_s) from the austenite as shown in Fig. 3.1. The martensite finish

temperature (M_f) is not found from the present experiment as the slope of the curve is still changing when approaching the room temperature as shown in Fig. 3.1.

Fig. 3.2 shows optical and SEM images of the 13wt.% Cr MSS as-quenched condition. The PAG boundaries have been revealed by swab etching using solution of 5g $FeCl_3$ and 1 ml HCl in 100 ml water and measured average PAG size is $17.5 \mu m$ as shown in Fig. 3.2(a). The SEM image of as-quenched condition showed fine lath martensitic structure and round shaped carbides of 0.2 to $0.8 \mu m$ size within the martensitic matrix at discrete locations as shown in Fig. 3.2(b). The austenitization at $1020 \text{ }^\circ C$ for 30 min followed by quenching in oil ensures the transformation of austenite to lath martensite in 13wt.% Cr MSS but is not sufficient to dissolve the carbides completely.

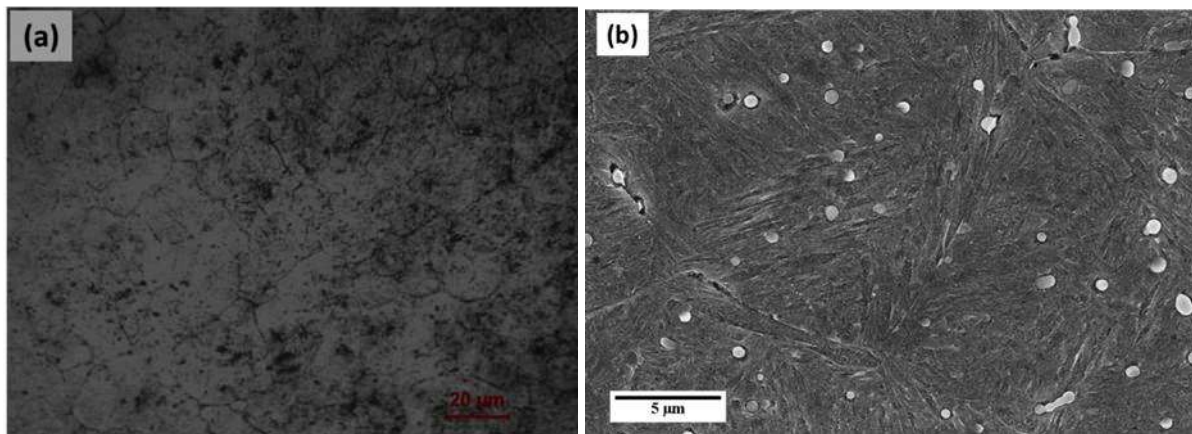


Fig. 3.2 (a) Optical and (b) SEM images of 13wt.% Cr MSS in austenitized condition showing PAG boundaries and lath martensitic structure.

Fig. 3.3 shows the optical images after austenitization at different temperatures followed by oil and air cooling. The formation of δ -ferrite stringers as indicated by arrow marks and also quench cracks were observed after austenitizing at $1040 \text{ }^\circ C$ for 1 h followed by oil quenching as shown in Fig. 3.3(a)-(b). Barlow et al. reported that the complete dissolution of primary carbides ($M_{23}C_6$) occurs at temperature above $1170 \text{ }^\circ C$ (Barlow *et al.*, 2012). However, these 13wt.% Cr MSS are

in general not austenitized above 1100 °C to avoid formation of high temperature δ -ferrite phase which is deleterious to corrosion and mechanical properties.

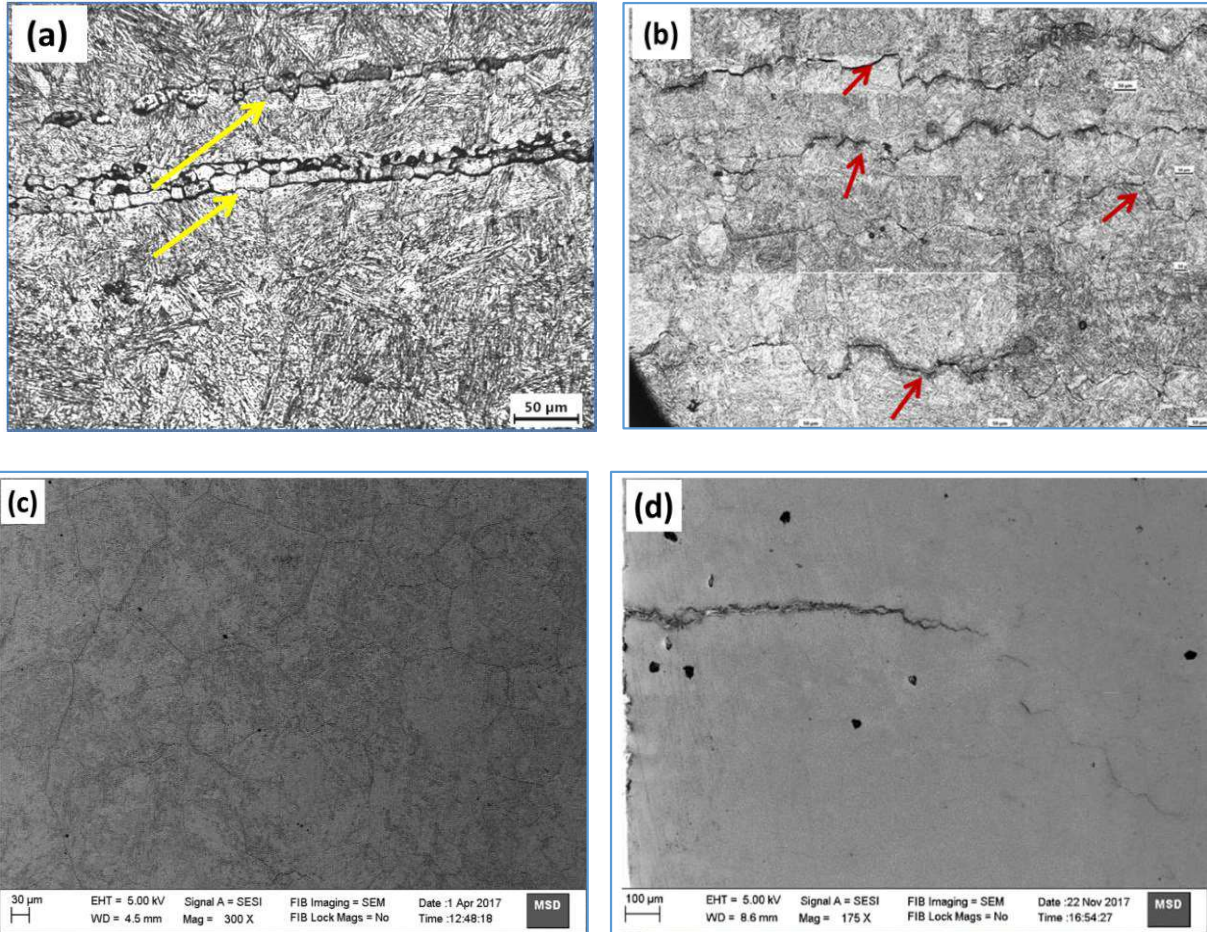


Fig. 3.3 Optical images of 13wt.% Cr MSS after austenitization at 1040 °C followed by oil quenching showing (a) ferrite striger in martensitic matrix and (b) quench cracks along PAG boundaries. FE-SEM images after austenitization at (a) 1100 °C and (b) 1200 °C for 1 h followed by air cooling showing quench cracks along PAG.

The as-received MSS specimens heat treated at 1100 °C and 1200 °C for 1 h followed by air cooling are shown in Figs. 3.3(c) and 3.3(d) respectively. Austenitization at high temperatures increased the PAG size significantly. Austenitization at 1200 °C followed by air cooling also produced quench cracks along PAG boundaries shown in Fig. 3.3(d). With increase of austenitization temperature, the PAG size is increased. The transformation of austenite to martensite increases the

volume and also the elastic strain energy. The quench cracks produced are due to dimensional distortion during cooling from higher austenitizing temperature. Therefore, the austenitization temperature of 1020 °C is chosen in the present investigation to avoid increased PAG size, tendency to form δ – ferrite and also quench cracks. In the subsequent results and discussion, austenitization of 13wt.% Cr MSS refers to heat treatment at 1020 °C for 30 min followed by oil quenching.

3.3.2. Microstructural changes with tempering temperature

3.3.2.1. XRD analysis

The XRD patterns for austenitized and tempered specimens are shown in Fig. 3.4. The significant change in the diffraction patterns is a decrease in austenite peak intensity ($2\theta= 43.53^\circ$) with increase of tempering temperature, as shown in Fig. 3.4. The volume fractions of retained austenite in the austenitized specimen and in specimen tempered at 300 °C are 4.7 and 3.2 % respectively and no retained austenite was found in the specimen tempered at 550 °C or above temperatures. The formation of reverted austenite in 13 wt.% Cr MSS was reported after tempering at 300 °C (Lu *et al.*, 2015), but our studies demonstrated that the retained austenite volume fraction decreased with tempering treatments and no reverted austenite was found after tempering at 300 to 700 °C. The reverted austenite transformation requires presence of Ni in the matrix as Ni stabilizes the austenite phase and promotes reverse austenite transformation (Song *et al.*, 2010). As the Ni concentration in 13 wt.% Cr MSS is low (0.27 wt.%, Table. 3.1), reverted austenite is not expected. It has been reported that the volume fraction of retained austenite decreased in 16% and 26% Cr-Fe alloys and AISI 431 MSS with tempering and retained austenite transformed to carbides and ferrite (Rajasekhar *et al.*, 2009, Inthidech *et al.*, 2006). In the present study also, it is believed that the retained austenite should have transformed to carbides and ferrite in 550 °C and above

tempering conditions. The axial ratio of the martensitic and ferritic phase is too close (10^{-4} to 10^{-5} nm) and separating the two phases by XRD peak 2θ positions is not possible (Lu *et al.*, 2015). So the diffraction peaks are indexed as martensite (M) for all the conditions.

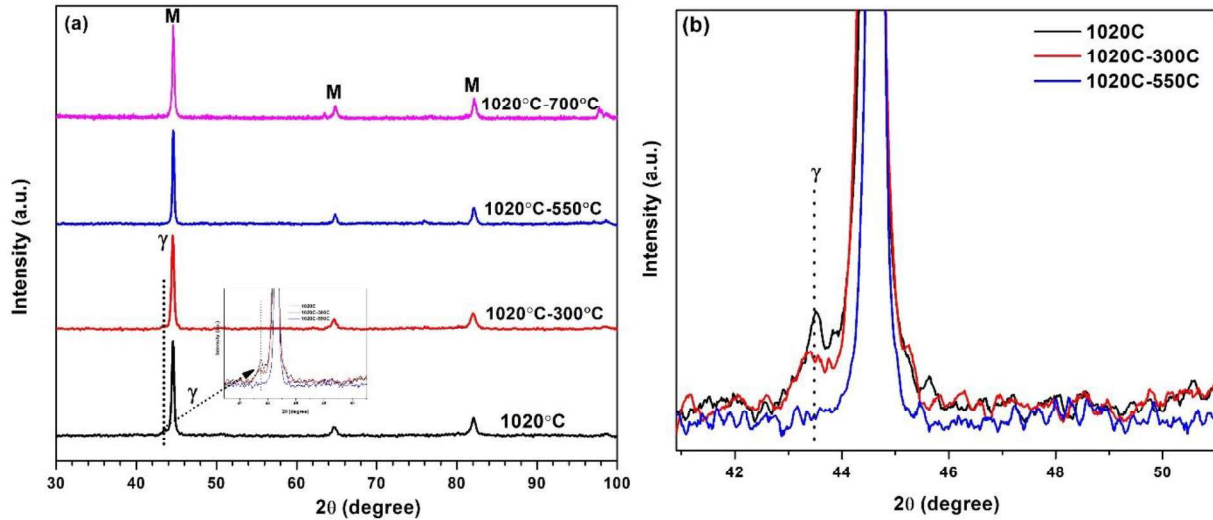


Fig. 3.4 (a) X-ray Diffraction patterns for 13 wt.% Cr MSS in austenitized and different tempered conditions and (b) expanded view of the XRD peaks showing the retained austenite peak with tempering temperature.

3.3.2.2. Characterization by SEM

The SEM images of 13wt.% Cr MSS after austenitization and tempering at different temperatures are shown in Fig. 3.5(a)-(d). As shown in Fig. 3.5(a), the austenitization at 1020 °C for 30 minutes followed by oil quenching produced lath martensitic structure with round shaped carbides of 0.2 to 0.8 μm size within the martensitic matrix. The absence of the ferrite stringers in the austenitized condition was confirmed after etching in Villela's reagent based on its morphology (stringers) and the occurrence of whitish color regions by optical microscopic examination. The δ -ferrite in martensitic stainless steels is known to deteriorate the mechanical properties and corrosion resistance.

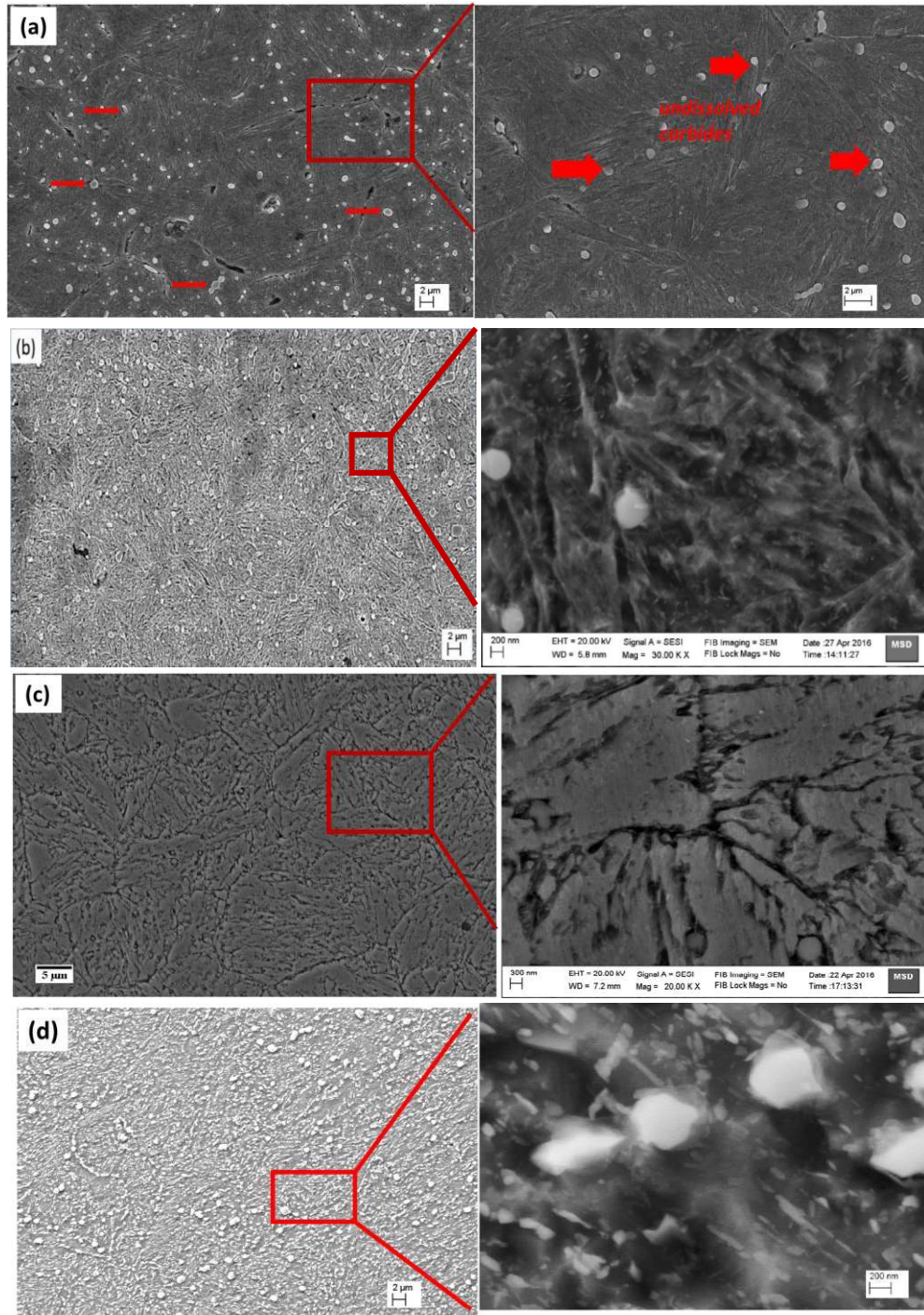


Fig. 3.5 Microstructures of the 13wt.% Cr martensitic stainless steel after etching in Villela's reagent: (a) austenitized at 1020 °C for 30 min, (b) tempered at 300 °C, (c) tempered at 550 °C and (d) tempered at 700 °C. All the tempering treatments are for 2.5 h.

The martensite start (M_s) temperature for 13wt.% Cr MSS used in this study is 203 °C (determined experimentally by dilatometer, Fig. 3.1) and this grade of material is expected to undergo complete

martensitic transformation on quenching in oil from austenitizing temperature. The presence of retained austenite is confirmed by XRD analysis as shown in Fig. 3.4. It is reported that for Type 420 stainless steel, the material after hot forging between 900 and 1000°C and annealed at 700 °C showed a microstructure consisting of ferrite and $M_{23}C_6$ carbides (M is Cr and Fe) (Isfahay *et al.*, 2011). In the same study, it was shown that the carbides present in the austenitized condition were undissolved chromium carbides ($M_{23}C_6$ type) from the austenitization process (Isfahay *et al.*, 2011, Barlow *et al.*, 2012). Therefore, precipitates visible in austenitized condition (Fig. 3.5(a)) are expected to be the undissolved carbides from austenitization treatment and fine carbides might form during quenching. Depending upon the austenitizing temperature, the amount of the dissolved carbides was reported to vary in the microstructure (Barlow *et al.*, 2012).

In the austenitized condition, the martensite formed is super saturated with C and had a high amount of dislocations (Tasi *et al.*, 2002). With increase of tempering temperature, there is a continuous rejection of C from the supersaturated martensitic matrix which leads to a reduction of tetragonality of the matrix and formation of carbides (Prabhu Gaunkar *et al.*, 1980). With the increase of tempering temperature from 300 to 700 °C in the present study, qualitative comparison clearly shows increase of carbide volume fraction and size with tempering temperature, as shown in Fig. 3.5(b)-(d). The carbides formed in 300 and 550 °C are visible in the FE-SEM examination, at higher magnifications, due to their fine size (nano-size). The specimen tempered at 550 °C for 2.5 h after etching in Villela's reagent showed etching of PAG boundaries and also etching along the martensite lath interfaces as shown in Fig. 3.5(c). The carbides precipitated during tempering are seen to be at martensitic lath interfaces as shown in Fig. 3.5(d). It is reported that in the temperature range of 300 – 400 °C, M_7C_3 type carbides precipitate and with further increase of tempering temperatures, these carbides coarsen and partially transform to $M_{23}C_6$ in low C MSS

(Prabhu Gaunkar *et al.*, 1980, Isfahay *et al.*, 2011). The formation of nano-sized and sub-micron sized carbides during tempering treatments are studied by TEM-EDS.

3.3.2.3. Characterization by TEM

The morphology and precipitates formed in austenitized and tempered specimens are further studied in detail.

Austenitized condition: Fig. 3.6 shows the TEM images of the austenitized specimen. As shown in Fig. 3.6(a), austenitization at 1020 °C for 30 min followed by oil quenching produced a fine lath martensite structure with lath width of 70 to 185 nm. The presence of fine retained austenite with a needle shaped morphology, with a width of around 20 nm at some of the lath interfaces, was also observed in the austenitized condition as shown in Fig. 3.6(b). The existence of the retained austenite at the lath interfaces is confirmed by SAD pattern analysis as shown in Fig. 3.6(c). The presence of retained austenite with similar morphology was also reported to be observed in AISI 410 stainless steel (Tasi *et al.*, 2002). Apart from the retained austenite, high amount of dislocations within the laths and round shaped precipitates were observed in the austenitized condition as shown in Fig. 3.6(d). The size of round shaped precipitates are in the range of 0.35 to 0.8 μm and were present heterogeneously at discrete locations in the martensitic matrix. A high amount of dislocations are always formed during the martensite phase transformation and these dislocations are responsible for the strength of martensite (Shi *et al.*, 2015). The SAD pattern acquired from the round shaped precipitate together with TEM-EDS analysis (Fig. 3.6(e)) confirmed that these are Cr-rich M_{23}C_6 type carbides (M = Fe, Cr).

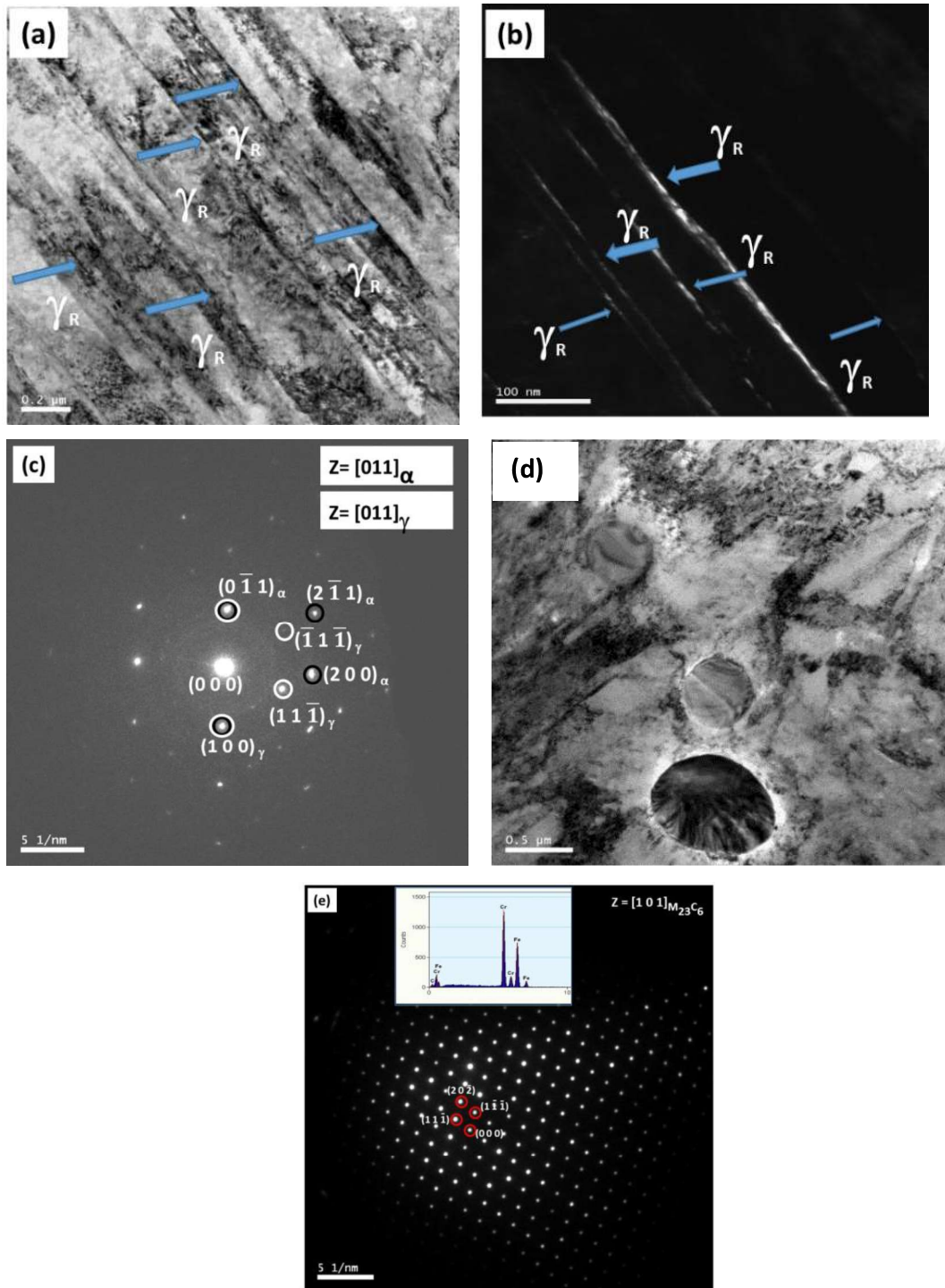


Fig. 3.6 TEM micrographs of the austenitized specimen, (a) bright filed image showing lath martensitic structure with retained austenite at lath interfaces, (b) dark field image showing the retained austenite, (c) SAD pattern of the retained austenite-lath interface region (d) bright filed image showing undissolved carbides and (e) SAD pattern of the undissolved carbide (inset showing the TEM-EDS of carbide).

The calculated lattice parameter of the undissolved Cr-rich $M_{23}C_6$ carbide (FCC structure) from SAD analysis is 10.68 \AA . The reported lattice parameter for $Cr_{23}C_6$ is 10.66 \AA (JCPDF No. 00-035-0783). The average chemical composition (wt.%) of carbide is $58.87 \pm 0.47 \text{ Cr}$, $40.14 \pm 0.42 \text{ Fe}$ and $0.98 \pm 0.13 \text{ Si}$. The size and morphology of the carbides in Fig. 3.6(d) suggest that these are undissolved carbides during the austenitization process and remained in the martensitic matrix after quenching. The chemical composition analysis using TEM-EDS also showed that the average Cr content in lath martensite is 13.4 wt.%.

Tempering at 300 °C: TEM micrographs of the specimen austenitized at 1020 °C and tempered at 300 °C is shown in Fig. 3.7. The microstructure of the specimen tempered at 300 °C is similar to that of austenitized condition with a lath martensitic microstructure of 100 to 200 nm lath width and dislocations within the laths as shown in Fig. 3.7(a). The presence of the retained austenite at the lath interfaces is shown in Fig. 3.7(b)-(c) but is not continuous as observed for austenitized condition. The retained austenite fraction decreased after tempering at 300 °C and re-confirms the XRD observations as shown in Fig. 3.1. The formation of needle shaped precipitates with ~ 150 to 250 nm in length and ~ 20 nm in width at lath interfaces and also within the laths perpendicular to the lath direction is observed after tempering at 300 °C as shown in Fig. 3.7(a). The SADP acquired from the lath interface precipitate is indexed as M_3C type carbide with an orthorhombic structure as shown in Fig. 3.7(d). The faint diffraction spots in the SAD pattern are corresponding to the precipitate and bright spots are from the matrix as shown in Fig. 3.7(d). The presence of the undissolved round shaped $M_{23}C_6$ carbides is also observed and it remained unchanged during tempering. The TEM-EDS analysis showed that these precipitates are Fe-rich carbides with an average Cr of 13.42 wt.% in the carbide. Therefore, there is not much of difference in the Cr content of the M_3C type carbide and that in lath martensite matrix.

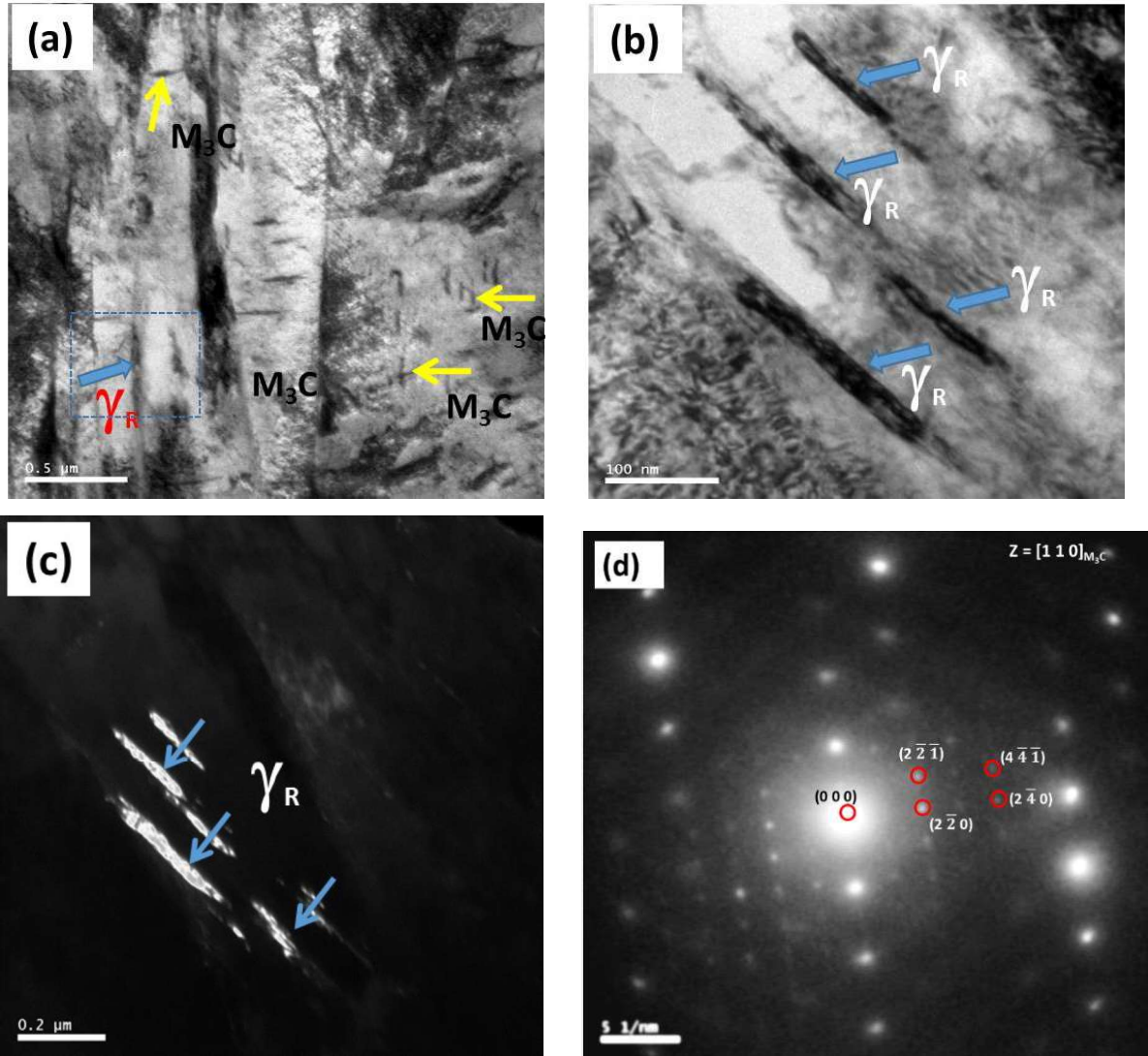


Fig. 3.7 TEM micrographs of 13 wt.% Cr MSS tempered at 300 °C, (a) bright filed image showing lath martensite with retained austenite and M_3C type carbides, (b) magnified image of (a) showing retained austenite at lath interfaces, (c) dark filed image showing carbides and (d) SAD pattern of the carbide showing as M_3C type carbide.

Tempering at 550 °C: TEM micrographs of the specimen tempered at 550 °C are shown in Fig. 3.8. The tempered microstructure consists of lath martensitic structure with 100 to 200 nm in width with undissolved carbides at discrete locations, huge amount of fine nano-sized precipitates at lath interfaces and also within the laths and few sub-microscopic precipitates as indicated by the arrows in Fig. 3.8(a)-(b). The precipitates are also observed at PAG boundaries as shown in Fig. 3.8(b).

The lath interfaces are covered by continuous precipitation of nano-sized carbides as shown in Fig. 3.8(b).

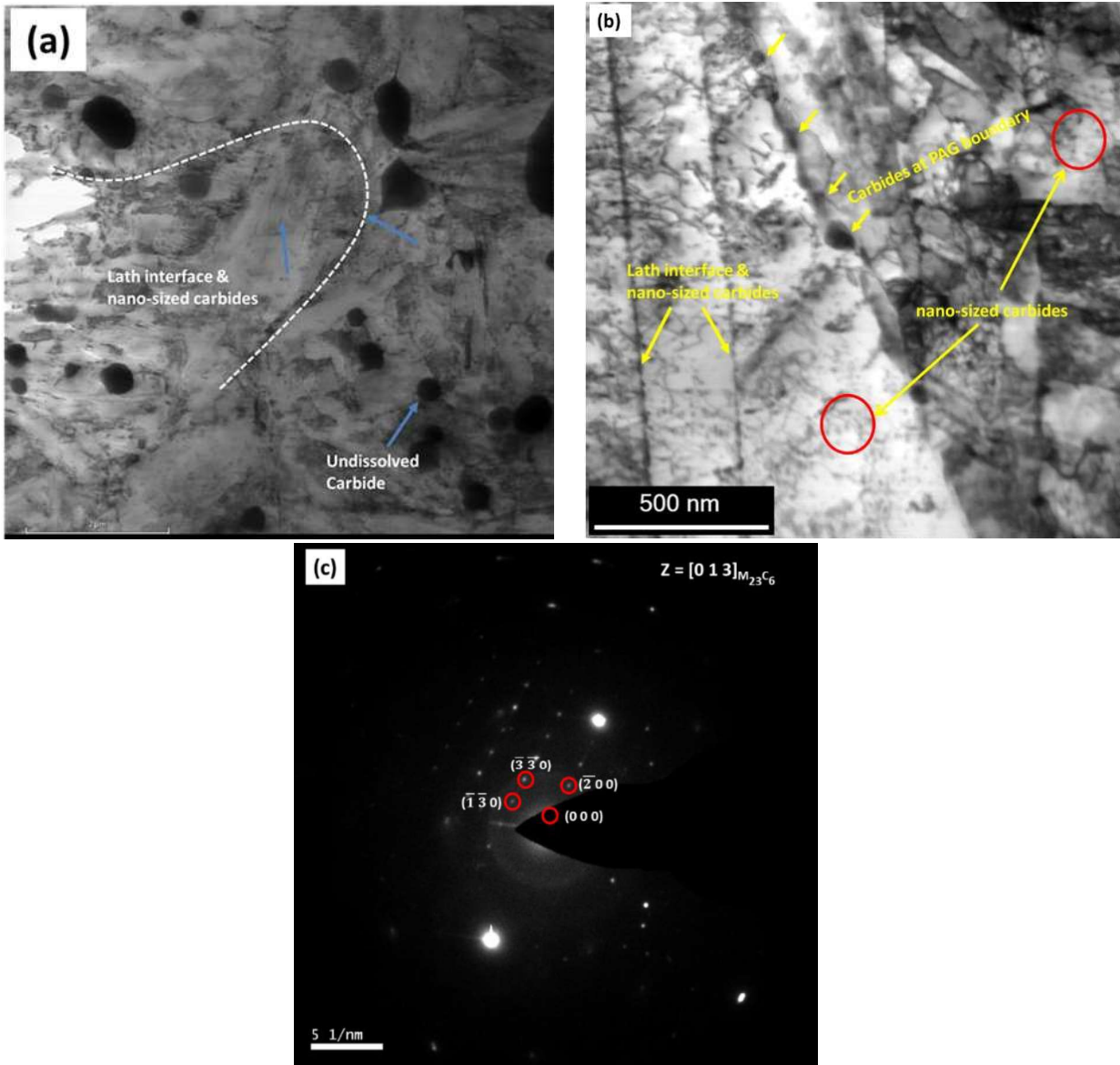


Fig. 3.8 TEM micrographs of the specimen tempered at 550 °C (a) showing lath martensitic structure with in PAG and undissolved carbides (b) showing the lath interface covered by precipitation of fine nano-sized carbides and also presence of nano-sized carbides in laths and carbides at PAG boundary (c) SAD pattern of the carbide present at PAG boundary.

The chemical analysis of the nano-sized precipitates by TEM-EDS analysis with 2.5 nm probe size on different carbides showed different concentrations of Cr from 27 wt.% to 52 wt.%. The SAD

pattern acquired from the globular shaped sub-microscopic sized precipitate present at the PAG boundary is indexed as $M_{23}C_6$ type carbide with face centred cubic (FCC) structure, as shown in Fig. 3.8(c). It is difficult to acquire the SADP of these nano-sized precipitates present within the lath due to their small size. The SADP analysis of the fine nano-sized carbides needs to be carried out by high resolution analysis by TEM.

Tempering at 700 °C: The TEM micrographs of the specimen tempered at 700 °C for 2.5 h are shown in Fig. 3.9.

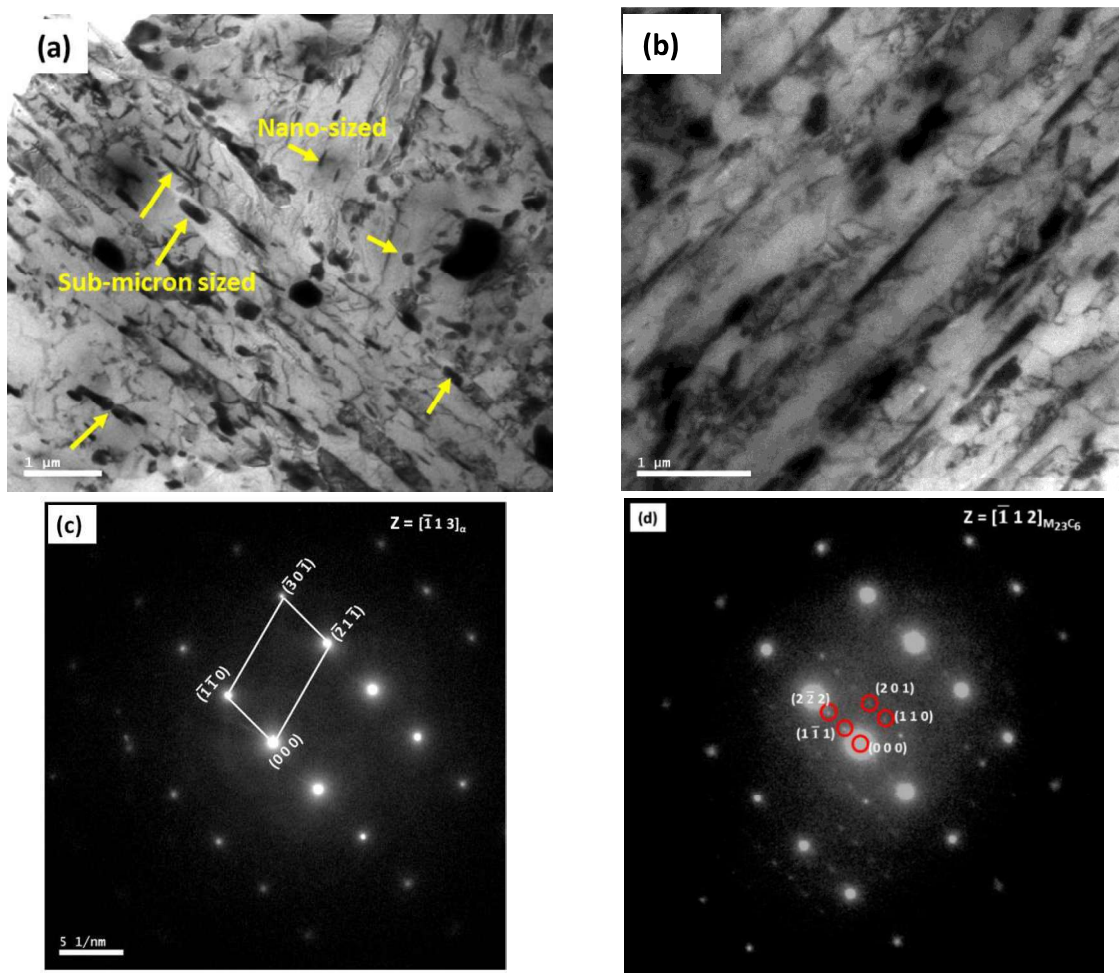


Fig. 3.9 TEM micrographs of the specimen tempered at 700 °C (a) showing carbides at lath interfaces, (b) magnified image of (a) showing sub-micron sized carbides at lath interfaces, (c) SAD pattern of the matrix and (d) SAD pattern of the lath interface round shaped carbide.

Fig. 3.9(a) shows lath martensitic microstructure and the width of the laths is 140 to 600 nm. The presence of needle shaped (length much more than width) carbide precipitates with 100 to 1000 nm size in length and 20 to 40 nm in width at the lath interface and along the direction of martensitic laths is clearly observed in Fig. 3.9(a)-(b). In addition, sub-micron sized round precipitates are also present at the lath interfaces. But as compared to 550 °C tempered specimen, very few nano-sized carbide precipitates are present within the martensitic laths. As shown in Fig. 3.9(a), the round bigger precipitates are undissolved carbides during the austenitization. The SAD pattern acquired from the matrix is shown in Fig. 3.9(c) and is indexed as ferrite (BCC) phase. The SAD pattern of the round shaped carbide is indexed as $M_{23}C_6$ type carbide with FCC structure as in Fig. 3.9(d). The Cr content (wt.%) in the two carbides analyzed (Cr ~42% and ~56%) is much higher than that in the matrix region (Cr ~ 13%). The undissolved carbides and carbides formed during tempering can be easily distinguished as the sizes of the undissolved carbides are much bigger than carbides precipitated during the tempering.

The as-quenched condition with lath martensitic structure contained dense tangled dislocations (indicated by arrows) which is the result of strain produced during martensitic transformation as shown in Fig. 3.10(a). Specimen tempered at 300 °C has a high density of dislocations within the laths, as shown in Fig. 3.10(b). Dislocations within the laths formed a network type array after tempering at 550 °C as shown in Fig. 3.10(c) and most of the dislocations are annihilated after tempering at 700 °C as shown in Fig. 3.10(d). From the images, it could be inferred that the dislocations created during the austenitization, annihilated and relatively dislocation density decreased with increase of tempering temperature as shown in Fig. 3.10(a)-(d).

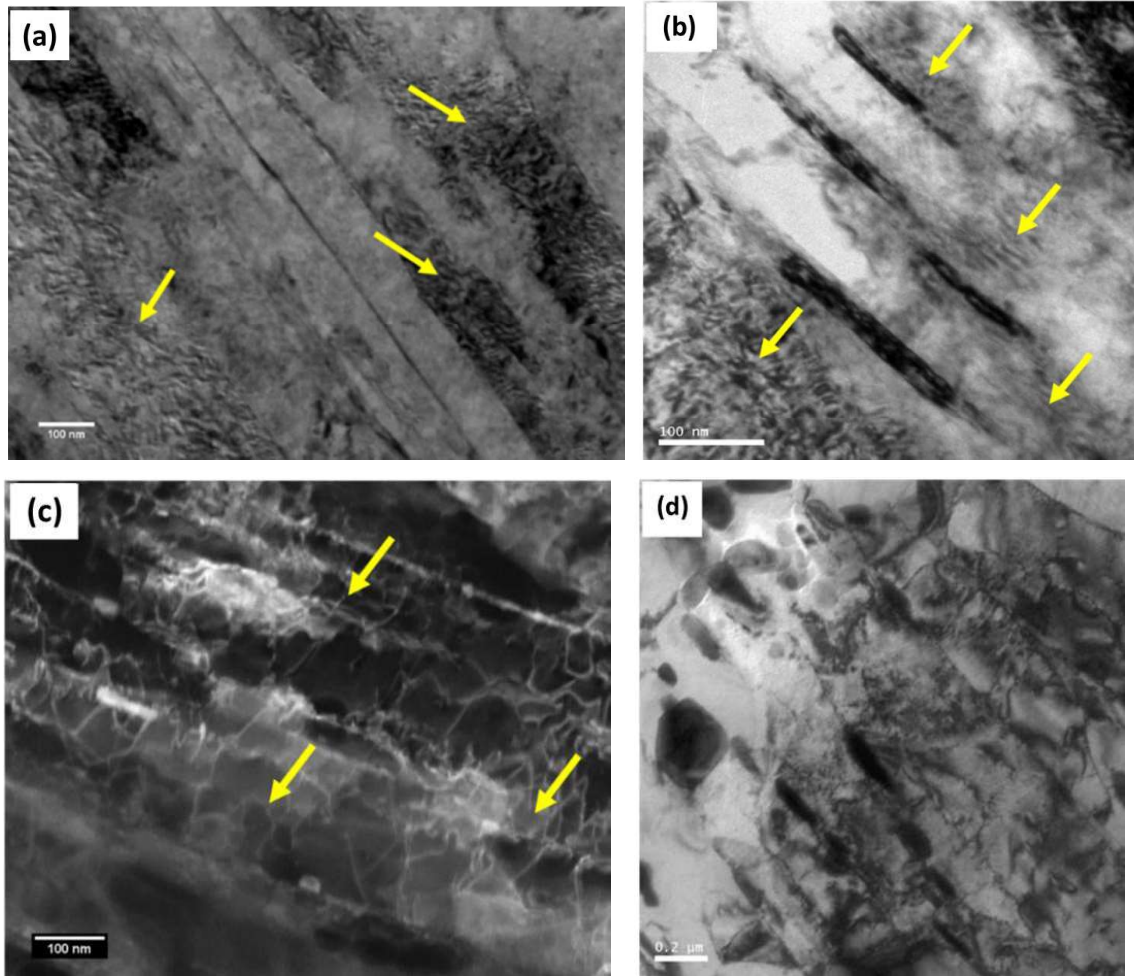


Fig. 3.10 TEM images showing dislocations as indicated by arrow marks within the martensitic laths in (a) austenitized condition, tempered at (b) 300 °C, (c) 550 °C and (d) 700 °C. All tempering treatments are done for 2.5 h.

3.3.2.4. XRD analysis of the precipitates extracted from tempered specimens

Fig. 3.11 shows the XRD patterns of the precipitates electrolytically extracted from martensitic matrix of the specimens tempered at 550 and 700 °C. As shown in Fig. 3.7, only a few carbide precipitates are present in the specimen tempered at 300 °C and the amount of the precipitates extracted is therefore too low for carrying out the XRD analysis. The XRD peaks observed are the same for the specimens tempered at 550 and 700 °C and well matched with the standard XRD pattern of $M_{23}C_6$ type carbides (JCPDS No. 00-035-0783, coll. code: 62670) as shown in Fig. 3.11.

So, the carbides formed are $M_{23}C_6$ with different sizes in both the conditions. Based on XRD and TEM observations, the sequence of precipitation in 13 wt.% Cr MSS was observed to be formation of (a) nano-sized M_3C type carbides at 300 °C, (b) nano-sized Cr-rich $M_{23}C_6$ carbides at 550 °C and (c) sub-micron sized Cr-rich carbides at 700 °C. The stable carbide for MSS at a tempering temperature of 700 °C is $M_{23}C_6$ (equilibrium carbide with ferrite phase at 700 °C is $M_{23}C_6$) (Thomson *et al.*, 1992, Tao *et al.*, 2014). The present results also showed the presence of $M_{23}C_6$ type carbides in the specimen tempered at 700 °C.

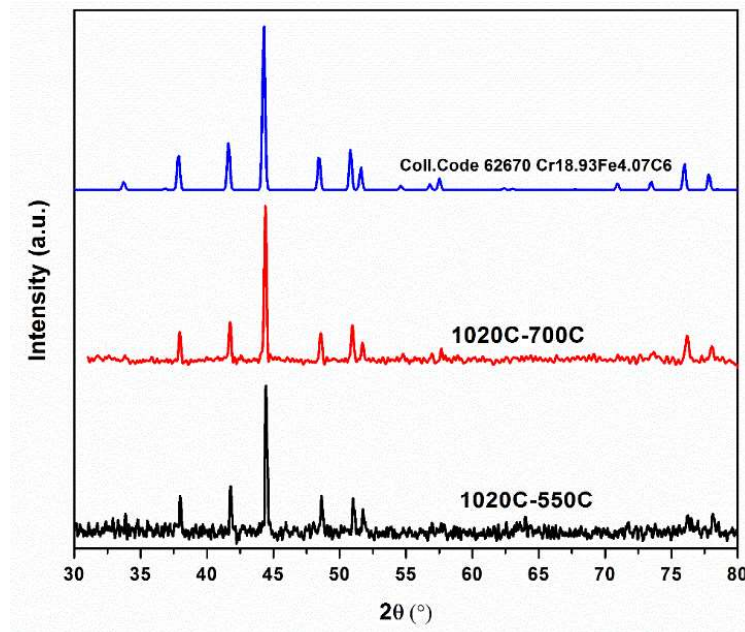


Fig. 3.11 XRD patterns of the precipitates extracted from specimens tempered at 550 and 700 °C along with the standard XRD pattern of $M_{23}C_6$ carbide, showing extracted precipitates are $M_{23}C_6$ type carbides.

Chakroborty *et al.* reported the presence of Fe_2C type carbide along with the $M_{23}C_6$ carbide in the XRD analysis of the extracted residue of Type 410 stainless steel with 11.2 wt.% Cr after tempering at 550 °C for 1 h (Chakroborty *et al.*, 2015). But in the present study, no traces of Fe_2C/Fe_3C carbides are observed in the XRD analysis of extracted precipitates from 13 wt.% MSS tempered at 550 °C for 2.5 h. At lower tempering temperature of 300 °C, the carbides precipitated

are expected to be Fe-rich carbides even though these carbides are not equilibrium carbides. During the tempering process, the super saturated carbon ejected from the martensitic matrix and the Cr atoms having high reactivity with carbon, combine to form the carbides. At lower tempering temperatures, the diffusivity of the Cr is low and the ejected carbon from the matrix reacts with the neighborhood Fe to form Fe-rich carbides. As the tempering temperature increases, the Cr-rich carbide precipitation and its growth by the diffusion process with tempering time increases. The formation of Cr-rich carbide leads to Cr-depletion at carbide-matrix interface regions and is a well-established phenomenon for austenitic stainless alloys (Kain *et al.*, 2002, Sathirachinda *et al.*, 2009, Hall *et al.*, 1984).

3.3.2.5. TEM analysis of the extracted precipitates

Fig. 3.12 shows the TEM images of the carbide precipitates extracted from specimens tempered at 550 and 700 °C for 2.5 h. The precipitates formed in 550 °C tempered condition are nano-sized $M_{23}C_6$ carbides, carbide size is about 20 nm with a globular morphology as shown in Fig. 3.12(a).

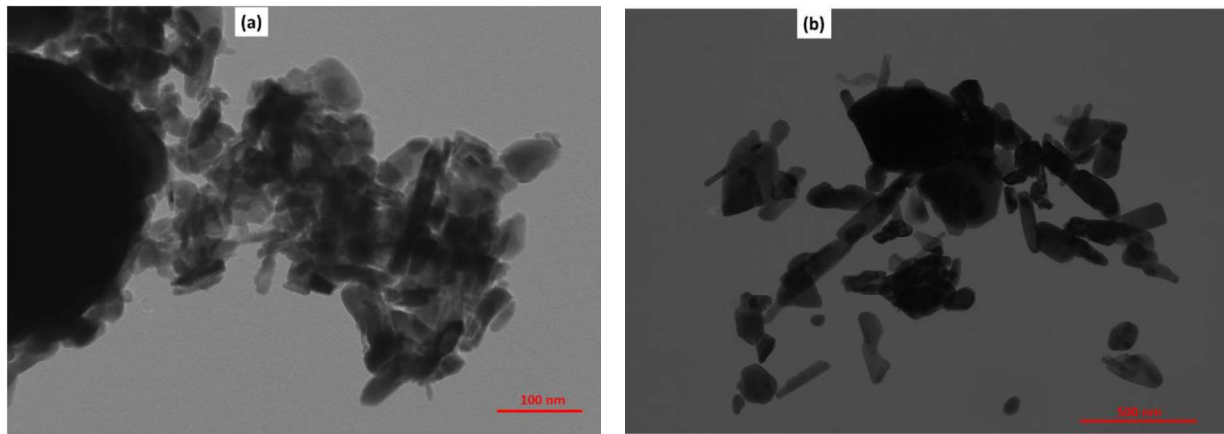


Fig. 3.12 TEM images of the extracted carbide precipitates: (a) tempered at 550 °C showing nano-sized precipitates and (b) tempered at 700 °C showing sub-micron sized carbides.

The precipitates formed in 700 °C tempered condition are in sub-micron sized $M_{23}C_6$ carbides with few carbides in nano-sized (about 50 nm). The carbides size is in the range of 50 to 120 nm with a needle and globular morphology as shown in Fig. 3.12(b). The XRD and TEM analysis confirm the carbides formed are nano and sub-micron sized Cr rich $M_{23}C_6$ after tempering at 550 and 700 °C respectively.

3.3.2.6. TEM-EDS analysis

The TEM-EDS analysis across the carbide-matrix interface region of specimen tempered at 550 °C is done in the present study to evaluate the Cr - depletion zone associated with nano-scaled carbide formation and location of the carbides studied are shown in Fig. 3.13(a). Fig. 3.13(b) shows the concentration profiles of the Cr across two nano-sized (15-20 nm) carbide-matrix interface regions of the specimen tempered at 550 °C for 2.5 h. The TEM-EDS analysis is carried out in the thin region of the specimen with electron beam size of 2.5 nm in order to obtain optimal spatial resolution during chemical analysis. The Cr concentration in the two carbides analyzed (at the center of the carbide) is 47 and 29 wt.% as shown in Fig. 3.13(b). The measured Cr concentration is not uniform in the carbides formed in 13 wt.% MSS during the tempering treatment at 550 °C. The nucleation and growth of Cr-rich carbides is a diffusion controlled process and is influenced by the nature of interface, temperature and duration. The growth of the carbide precipitates occurs by the diffusion of Cr and C. But the growth of the carbide is essentially governed by the diffusion of Cr as the diffusion rate of interstitial C is very fast as compared to Cr in the matrix. The measured Cr concentration, 2.5 nm away from the carbide with 47 wt.% Cr is 9 wt.% whereas the carbide with 29 wt.% Cr has the interfacial (2.5 nm away from the interface) Cr concentration of 11.97 wt.%.

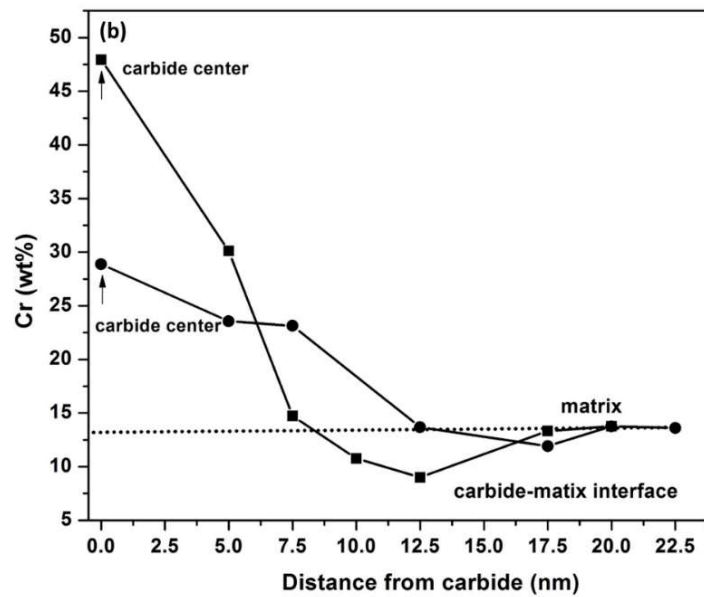
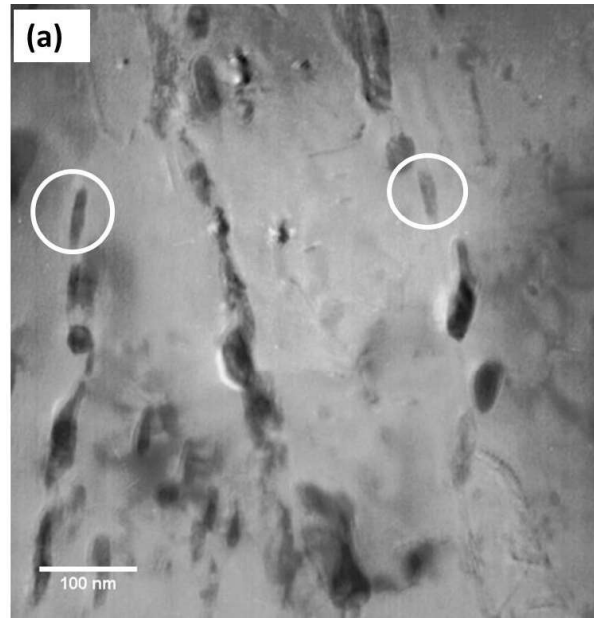


Fig. 3.13 TEM-EDS analysis across the carbide-matrix interface region of specimen tempered at 550 °C (a) showing the region used for TEM-EDS analysis and (b) showing the Cr concentration profiles of carbide-matrix interface regions.

The measured Cr-depleted zone width is 9 nm for the carbide with 47 wt.% Cr and is 7.5 nm for the carbide with 27 wt.% Cr as shown in Fig. 3.13(b). The Cr concentration in the carbide-matrix interface region decreased due to the Cr-enrichment in the carbide precipitate and by the diffusion

of Cr at a given tempering temperature. The average Cr concentration in the matrix region, 10 nm away from the carbide is 13.7 wt.% by considering only Fe and Cr elements in the matrix.

Nakamichi et al. showed the width of the Cr depletion region measured across PAG boundary in between Cr-rich carbides is around 10 to 15 nm in low carbon MSS tempered at 650 °C (Nakamichi *et al.*, 2008) and showed no Cr-depletion at carbide-matrix interface. The present results clearly show the existence of narrow Cr depletion of 7 to 9 nm at the nano-scaled carbide-matrix interface regions after tempering at 550 °C as shown in Fig. 3.13(b). The minimum Cr concentration and width of the Cr depleted zone are dependent on the temperature, time and also the composition of the steel (Brummer *et al.*, 1986). The Cr depletion widths reported for sensitized austenitic stainless alloys is several tens of nm from the grain boundary/carbide interface (Bruemmer, 1994, Chen *et al.*, 1990, Kain *et al.*, 2002). The diffusion coefficient of Cr in ferrite matrix is 10 times faster than in the austenite matrix (Sathirachinda *et al.*, 2009, Ebrahimi *et al.*, 2011). Therefore, the Cr depletion width in MSS with 13 wt.% Cr is expected to be smaller and narrower as compared to that in austenitic stainless steels with 18 wt.% Cr. The narrow Cr-depletion zone of 7-9 nm at the carbide-matrix interface is shown in present study and the average Cr concentration in the interface region falls to 76% of matrix concentration. Nakamachi *et al.*, (2008) showed that the width of Cr-depletion region measured across the PAGB in tempered low carbon MSS was around 10 nm – 15 nm and Cr concentration in the depleted region was shown to be 9-10wt.%

Fig. 3.14 shows the TEM-EDS analysis performed on undissolved carbide and regions around the undissolved carbide.

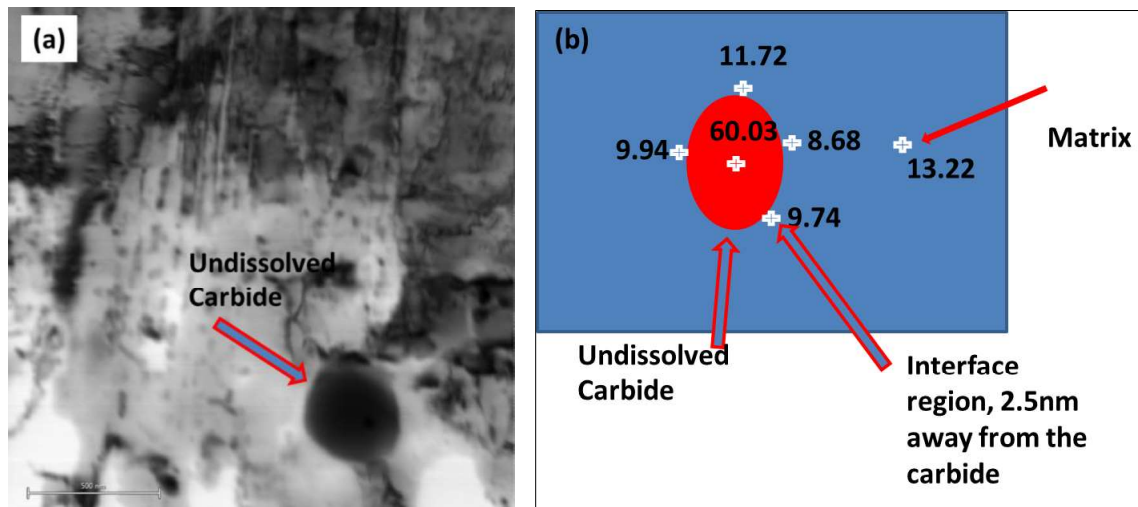
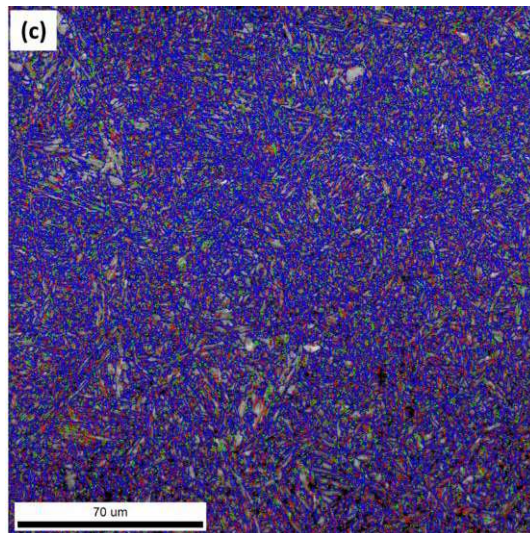
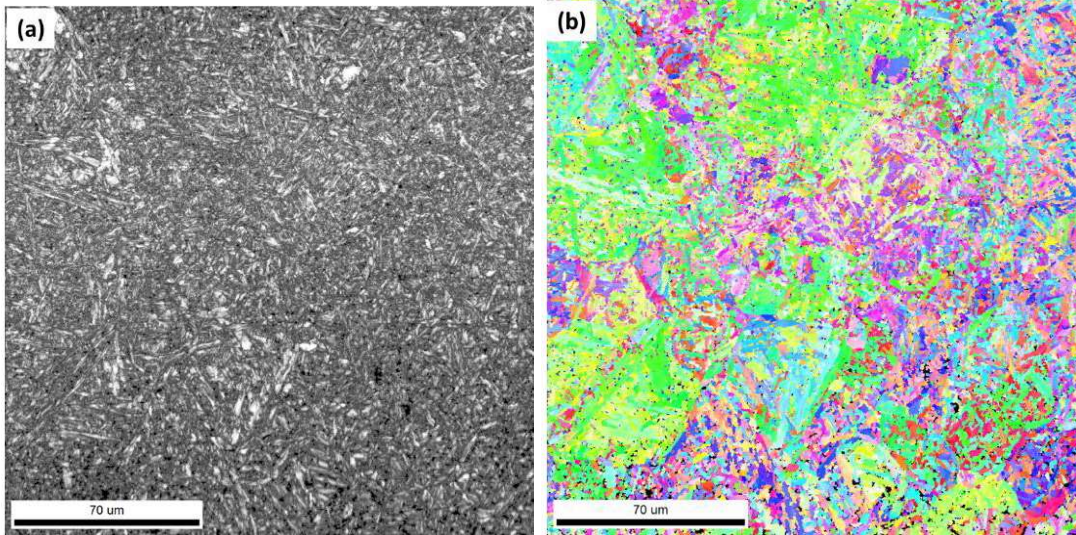


Fig. 3.14 (a) TEM image of the specimen tempered at 550 °C showing the undissolved carbide and (b) schematic of TEM- EDS analysis location and Cr concentrations.

The TEM-EDS analysis also performed on the undissolved Cr-rich $M_{23}C_6$ carbide (Fig. 3.14(a)) and the Cr concentrations measured on the carbide and 2.5 nm away from matrix - undissolved Cr-rich $M_{23}C_6$ interface region are shown in Fig. 3.14(b). The undissolved carbide has Cr concentration of 60.03 wt.%. The Cr concentration is varied from 8.68 to 11.72 wt.% in the interface region whereas matrix Cr concentration is 13.22 wt.%.

3.3.2.7. EBSD studies on austenitized and tempered specimens

The EBSD examination on austenitized and specimen tempered at 700 °C were done to find the high and low angle grain boundary fraction to explain the HE phenomenon (Chapter 6). Fig. 3.15 shows the FE-SEM image, orientation image and low and high angle grain boundaries in austenitized condition. The high angle grain boundaries are 63.6% as shown in Fig. 3.15(c) for austenitized condition. The specimen tempered at 700 °C also showed high angle grain boundaries of 67.1% as shown in Fig. 3.16. After tempering, there is no significant change in the percentage of high and low angle grain boundaries. The high resolution EBSD scan of 700 °C is shown in Fig. 3.16.

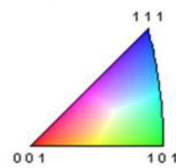


Boundaries: Rotation Angle

	Min	Max	Fraction	Number	Length
—	2°	5°	0.256	270983	3.13 cm
—	5°	15°	0.108	113920	1.32 cm
—	15°	180°	0.636	671842	7.76 cm

*For statistics - any point pair with misorientation exceeding 2° is considered a boundary
total number = 1056745, total length = 12.20 cm)

Iron (Gamma)



Iron (Alpha)

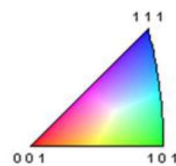
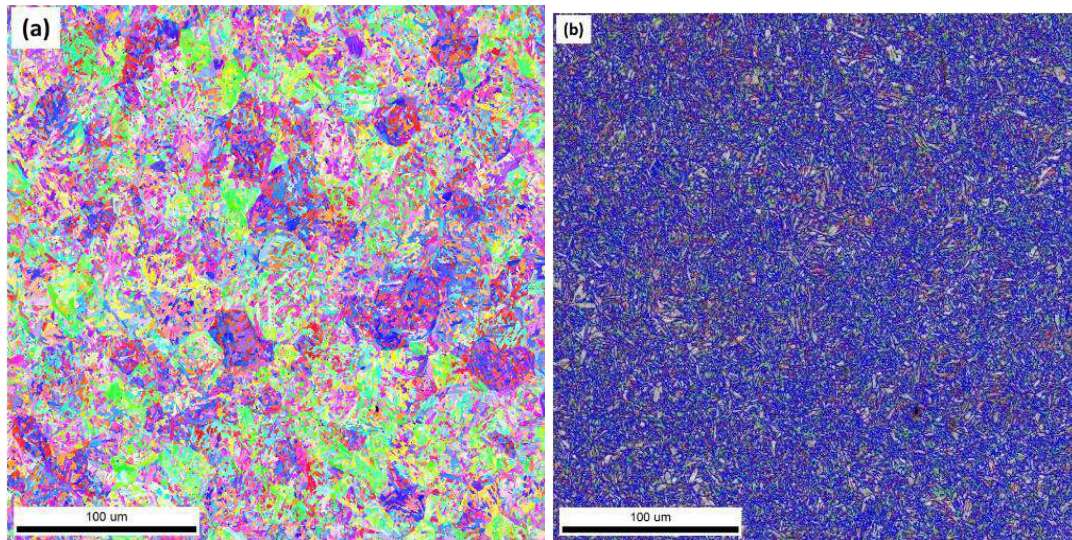


Fig. 3.15 (a) FE-SEM image, (b) orientation map, (c) low and high angle grain boundaries distribution in austenitized condition obtained by EBSD technique.



Boundaries: Rotation Angle					
	Min	Max	Fraction	Number	Length
—	2°	5°	0.207	410005	4.73 cm
—	5°	15°	0.122	242254	2.80 cm
—	15°	180°	0.671	1331679	15.38 cm

*For statistics - any point pair with misorientation exceeding 2° is considered a boundary
total number = 1983938, total length = 22.91 cm)

Fig. 3.16 (a) Orientation map and (b) low and high angle grain boundaries distribution in 13wt.% Cr MSS tempered at 700 °C condition obtained by EBSD technique.

Fig. 3.17(a)-(c) shows the FE-SEM image, orientation image and phase map of the tempered MSS obtained by EBSD technique. The red color in Fig. 3.17(c) corresponds to bcc lattice (martensite and ferrite) and the green color corresponds to fcc lattice ($M_{23}C_6$ type carbides). Figs. 3.4 & Fig. 3.9 clearly show the absence of retained austenite in the tempered condition and the green regions shown in the phase map (Fig. 3.17(c)) correspond to $M_{23}C_6$ type carbides which have fcc lattice structure (Lu *et al.*, 2015). Therefore, the green regions shown in the phase map (Fig. 3.17(c)) are the micron (undissolved carbides) and sub-micron sized $M_{23}C_6$ carbides.

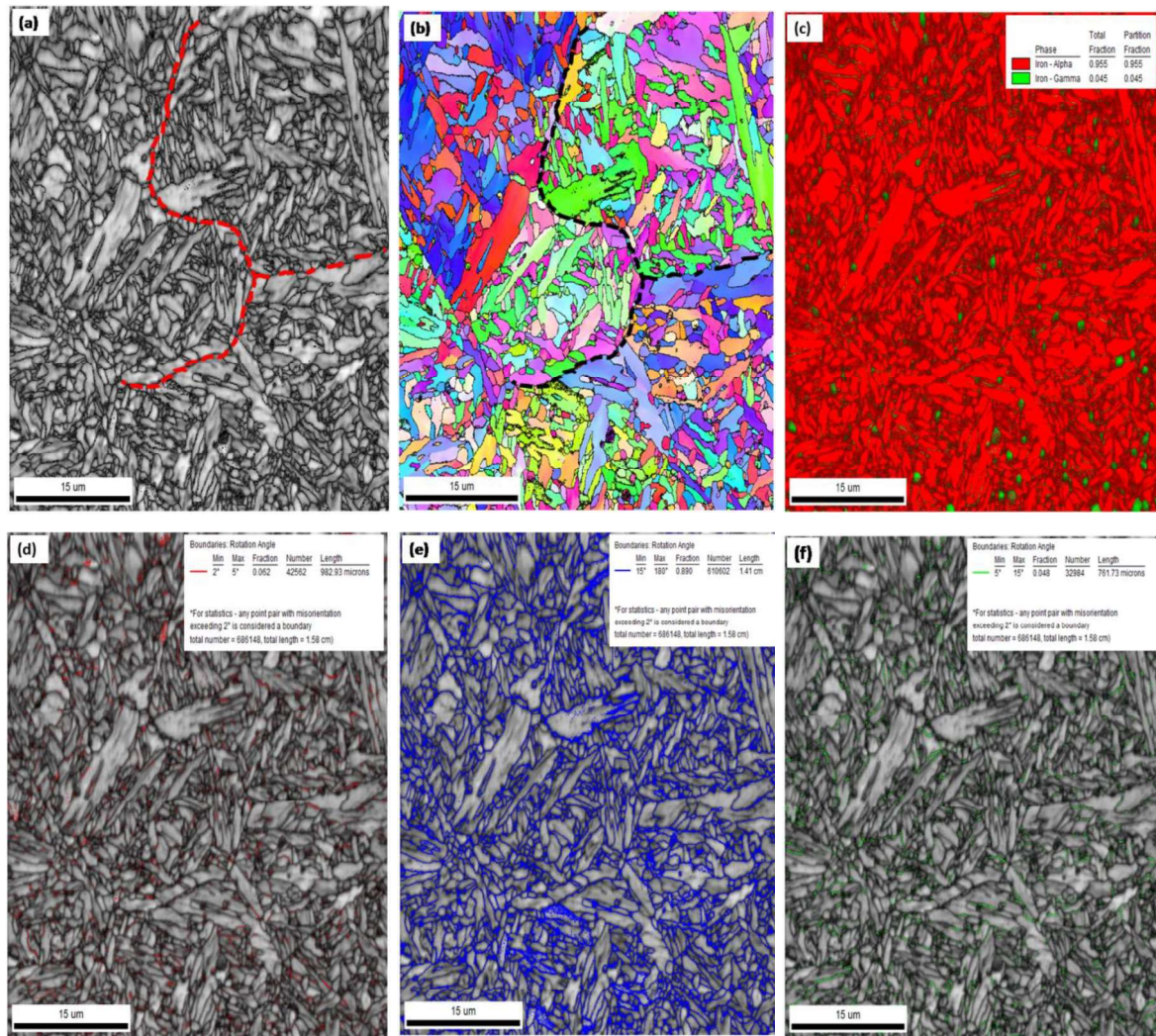


Fig. 3.17 (a) FE-SEM image, (b) orientation map, (c) phase distribution and (d)-(f) shows the low and high angle grain boundaries distribution in the 13wt.% Cr MSS tempered at 700 °C obtained by EBSD technique (dotted lines in image (a) and (b) indicate the PAG boundaries).

The sub-micron sized carbides formed during tempering are at the interfaces of martensitic laths as shown in Fig. 3.17(c) and the same is also shown in Fig. 3.9(a) by TEM examination. The PAG size is $16 \pm 4 \mu\text{m}$ and within the PAG, many martensitic laths with different orientations are present as shown in Fig. 3.17(a)-(b). Fig. 3.17(d)-(f) shows the grain/lath boundaries having the low and high angle misorientation. The boundaries with misorientation angle less than 15° are considered as low angle boundaries (Smith, 1986, Avner, 1997). As shown in Fig. 3.17(d)-(f), the fraction of

high angle grain boundaries is more than 85% whereas the low angle grain boundaries are less than 11% (Fig. 3.17(d) & (f) in studied region).

3.4. Highlights

The microstructural changes and precipitation sequence with tempering temperature of 13 wt.% Cr martensitic stainless steel were investigated using XRD, SEM, EBSD and TEM. The salient results obtained from this study are summarized below.

1. Austenitization at 1040 °C followed by oil quenching showed formation of δ -ferrite stringers and also quench cracks along PAG boundaries. Therefore, austenitizing above 1040 °C followed by oil quenching increases chances of formation of quench cracks. The as-received MSS specimens heat treated at 1200 °C for 1 h followed by air cooling also produced quench cracks along PAG boundaries.
2. The austenitization at 1020 °C for 30 min followed by oil quenching produced fine lath martensitic structure with a retained austenite film at lath interfaces. The austenitization heat treatment at 1020 °C did not dissolve the carbides completely and there were undissolved carbides at discrete locations in the martensitic matrix.
3. Microstructural examination by TEM and XRD revealed formation of nano-sized M_3C type carbides at lower tempering temperature of 300 °C, whereas formation of nano-sized chromium rich $M_{23}C_6$ type carbides at tempering temperature of 550 and sub-micron sized chromium rich $M_{23}C_6$ type carbides at higher tempering temperatures of 700 °C was observed. The retained austenite fraction decreased with tempering temperature and no retained austenite was observed after tempering at 550 and 700 °C.
4. Formation of the Cr-rich carbide precipitates led to Cr-depletion at carbide-matrix interface region. The narrow Cr depletion zone of 7 to 9 nm associated with nano-sized Cr-rich carbide

precipitation is observed in tempered condition at 550 °C and Cr concentration fell to 76% of matrix concentration in Cr depleted interface regions.

5. The fraction of the high angle grain boundaries in the austenitized and tempered MSS were more than 65%.

Effect of tempering treatments on intergranular corrosion

4.1. Background

IGC in stainless steels is due to formation of Cr-rich carbides or nitrides or both, at the grain boundaries resulting in creation of Cr-depleted regions at precipitate-matrix/grain boundary interface regions to a level of 11-12wt.% Cr. Most of the technical papers available in literature, provide information about IGC of austenitic stainless steels. But, there are no standard ASTM tests for MSSs to check the susceptibility to IGC. The microstructure of the tempered MSS consists of tempered martensite and carbides. Therefore, the Cr-rich carbides formed during the tempering treatments degrade the corrosion resistance of tempered MSS. In the present work, the susceptibility to IGC with tempering treatments was evaluated by nitric acid immersion test and the corrosion rates were correlated with the polarization tests and DL-EPR values measured in a modified DL-EPR test. Post immersion and electrochemical tests, the exposed surfaces were characterized using optical, SEM and XRD. The surface films formed on austenitized and tempered condition in nitric acid solution at passive potential was characterized by XPS. The changes in corrosion behavior were correlated with microstructural changes occurred during the tempering treatments and with nature of surface films. The present results brings out the important differences in IGC behavior, type of attack and nature of surface films formed for 13wt.% Cr MSS in austenitized and different tempered conditions and have been reported in section 4.3.

4.2. Experimental

4.2.1. Susceptibility to IGC by immersion tests in 5% HNO₃ solution

The solutions used in A262, ASTM and A763, ASTM standard tests (the boiling solution of 65% nitric acid and the boiling solution of 50% sulfuric acid - 25g ferric sulfate) for evaluating the susceptibility to IGC are too aggressive for 13wt.% Cr MSSs. Therefore, in the present study, the susceptibility to IGC of austenitized and tempered specimens was evaluated by immersion tests in a lower concentration of 5% nitric acid (HNO₃) solution at room temperature. The 5% HNO₃ solution at room temperature has been shown in a previous study to establish the susceptibility to IGC of MSSs (Sedriks, 1996). The heat treatments used in the study were provided in Chapter 3, section 3.2.1. The austenitized and tempered specimens were mechanically ground on successively finer silicon carbide papers, from 80 to 600 grit and were cleaned in water and ultrasonically in acetone for 5 min. These specimens were immersed in 5% nitric acid solution for 24 h at room temperature. After the tests, the exposed specimens were cleaned in distilled water and in acetone with ultrasonic agitation. The initial and final weights of the specimens were measured with an accuracy of 1 µg and corrosion rates were calculated in mm/y. The immersion tests were done twice and average corrosion rates are reported. The microstructural examination was carried out on the exposed surfaces. The cross-section of the tested specimens was metallographically prepared as described for microstructural characterization in Chapter 3, section 3.2.2., to examine the nature of attack.

4.2.2. Susceptibility to IGC by electrochemical measurements

All the electrochemical tests were carried out in a conventional three-electrode cell using a Pt foil as the auxiliary (counter) electrode and a saturated calomel electrode (SCE) as the reference electrode. An ACM Instruments Gill AC electrochemical workstation was used to perform all the

electrochemical tests. The working electrode was constructed using the MSS specimen mounted in an epoxy resin to obtain an exposed area of at least 10 mm x 10 mm. The test specimen was provided an electrical contact from one side of the specimen and was set in a cold setting resin to expose the opposite side of the specimen. The electrical connection wire was insulated to avoid contact with the test solution. For all the electrochemical measurements, the specimens were mechanically ground and polished to mirror finish using 1 μm diamond paste, rinsed in acetone and dried before each experiment, as described for the microstructural characterization (Chapter 3, section 3.2.2.). The contact regions between the test specimen and the resin were covered with a lacquer to avoid any crevice when exposed to the test solution.

4.2.2.1. Potentiodynamic polarization in H_2SO_4 solutions

Potentiodynamic polarization tests were performed in 0.25 and 0.03 M sulfuric acid (H_2SO_4) solutions at room temperature (26 $^\circ\text{C}$). The test solution was deaerated by bubbling Argon gas for 45 minutes before start of the test and also during the test. The tests were initiated after nearly steady-state open circuit potential (OCP) had developed after exposure in the test solution for 5 minutes. A potential sweep with a scan rate of 1.0 mV/s was employed.

4.2.2.2. Potentiostatic polarization

Potentiostatic polarization experiments were carried out at a fixed potential in 0.03 M H_2SO_4 (deaerated by bubbling Argon gas for 45 minutes before start of the test and also during the test).

4.2.2.3. DL-EPR test for DOS determination

The DL-EPR tests were done to determine the DOS of specimen after different tempering treatments. Since, there is no standard solution for evaluating DOS for 13wt.% Cr MSS, the DL-EPR tests on the specimen tempered at 550 $^\circ\text{C}$ for 100 h were carried out in different

concentrations of H₂SO₄ solution (as shown in Table 4.1) at room temperature in deaerated condition to establish the optimum concentration of the test solution for the DL-EPR test. Deaeration was done by bubbling Argon gas for 45 minutes before start of the test and also during the test. With the optimum concentration of H₂SO₄ solution, the DL-EPR tests were then done to determine DOS with different tempering conditions. After obtaining the stable OCP, the potential was scanned from -0.1 V negative to the OCP to + 0.5 V_{SCE} (activation scan) and then scanned back to the OCP (reactivation scan) at a scan rate of 100 mV/min at room temperature. The DL-EPR value was evaluated from the ratio I_r/I_a multiplied by 100, where I_a is the maximum current density in the activation (forward) scan and I_r is the maximum current density in the reactivation (reverse) scan. After the tests, the exposed surface was examined using FE-SEM. The cross-sections of the specimen tempered at 550 °C for 2.5 h, perpendicular to the surfaces tested at different potentials in DL-EPR test, were prepared for studying the nature of attack by optical microscopy and FE-SEM coupled with EDS. The electrochemical polarization and EPR tests were repeated twice.

Table 4.1 DL-EPR electrolyte concentrations (deaerated) used for evaluating the DL-EPR value of the specimen tempered at 550 °C for 100 h.

Serial Number	Solution concentration
1	0.25 M H ₂ SO ₄
2	0.1 M H ₂ SO ₄
3	0.05 M H ₂ SO ₄
4	0.03 M H ₂ SO ₄
5	0.03 M H ₂ SO ₄ + 20 ppm KSCN

4.2.2.4. Potentiodynamic polarization & EIS in 5% HNO₃ solution

The electrochemical measurements were also done in 5% HNO₃ solution at room temperature (25 °C) in deaerated condition. The austenitized and tempered specimens were polished to 1 μm diamond finish as described above in section 4.2.2. The steady-state OCP was obtained within five min and all the tests were started after obtaining the steady state OCP. The EIS were carried out in the frequency range of 0.01 to 10 kHz by super imposing sinusoidal potential of 10mV amplitude at OCP using AUTOLAB potentiostat. The experimental EIS results were fitted with suitable equivalent circuit using GPES-FRA software of AUTOLAB potentiostat. A potential sweep with a scan rate of 1.0 mV/s was employed for anodic polarization tests. The surface films were developed on austenitized and tempered at 550 °C by apply a potential of 0.6 V_{SCE} for 15 minutes.

4.2.3. GI-XRD analysis of surface films after electrochemical tests

After the potentiodynamic polarization of specimen tempered at 550 °C for 2.5 h in 0.25 M H₂SO₄ solution, surface was characterized by grazing incidence X-ray diffraction (GI-XRD) (Rigaku make operating with Cu tube, Cu K_α with a wavelength of 1.506 Å was used) with 2 degree grazing angle for establishing the black surface layer formed on the surface. For comparison, unexposed specimen tempered at 550 °C for 2.5 h was also characterized by XRD.

4.2.4. X-ray photoelectron spectroscopy (XPS) analysis

The passive film formed on austenitized and specimen tempered at 550 °C at passive potential in 5% HNO₃ is analyzed for composition with sputtering time using XPS (SPECS). The XPS analyses were carried out in an electron spectrometer using a monochromatic Al K_α X-rays (hν = 1486.74 eV) as the primary radiation source. The binding energies were calibrated with respect to the Ag 3d_{5/2} peak occurring at 368.26 eV. The energy spectra of the photoelectrons were analyzed by

DLD-Phoibos-HSA 2500 (hemispherical channel analyzer). The takeoff angle of the electrons detected by detector was 45 degrees. A survey scan was taken in the binding energy range from 0-750 eV with pass energy in the range 11-15 eV to identify the major elements present at the surface. The major elements identified were Fe, Cr and O with elemental C. High resolution energy spectra were recorded for Fe 2p, O 1s and Cr 2p peaks. All binding energies were referenced to the adventitious carbon C 1s peak at a binding energy of 284.6 eV to correct the charging shifts while the baseline correction was done by Shirley method using Origin 8.5 software. No flood gun correction was needed indicating the surface films were conducting in nature. The depth profile analysis of the oxide layer was performed with 5 keV Ar⁺ ions for sputtering times 30 - 195s. The ion current was recorded to be ~48μA and the sputtered spot size is 2mm x 2mm.

4.3. Results and Discussion

4.3.1. 5% Nitric acid immersion test - Susceptibility to IGC

The susceptibility to intergranular corrosion of all the tempered conditions was evaluated by immersion tests in 5% HNO₃ solution at room temperature for a period of 24 h. The corrosion rates in 5% HNO₃ with tempering temperature are shown in Fig. 4.1.

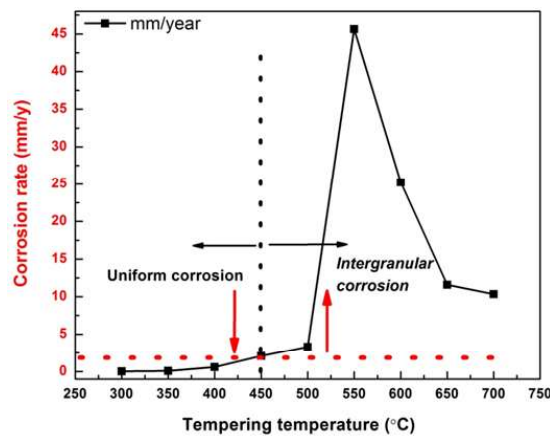


Fig. 4.1 Corrosion rates in 5 % HNO₃ immersion test with tempering temperatures showing regimes of uniform and intergranular corrosion. All the tempering treatments are for 2.5 h.

The immersion corrosion test was repeated for all the specimens and showed a variation of 4% in corrosion rates. The average values of corrosion rates are reported. The highest corrosion rate of 45.64 mm/y was observed in 550 °C tempered condition. The specimen tempered at 300 °C for 2.5 h showed a very low corrosion rate of 0.04 mm/y. The microstructural examination of the cross-section of the exposed surface of austenitized specimen and that of the specimens tempered below 450 °C for 2.5 h showed uniform corrosion (Fig. 4.2(a)-(b)) whereas all the specimens tempered above 450 °C showed grain dropping and martensite lath dropping as shown in Fig. 4.2(c)-(d).

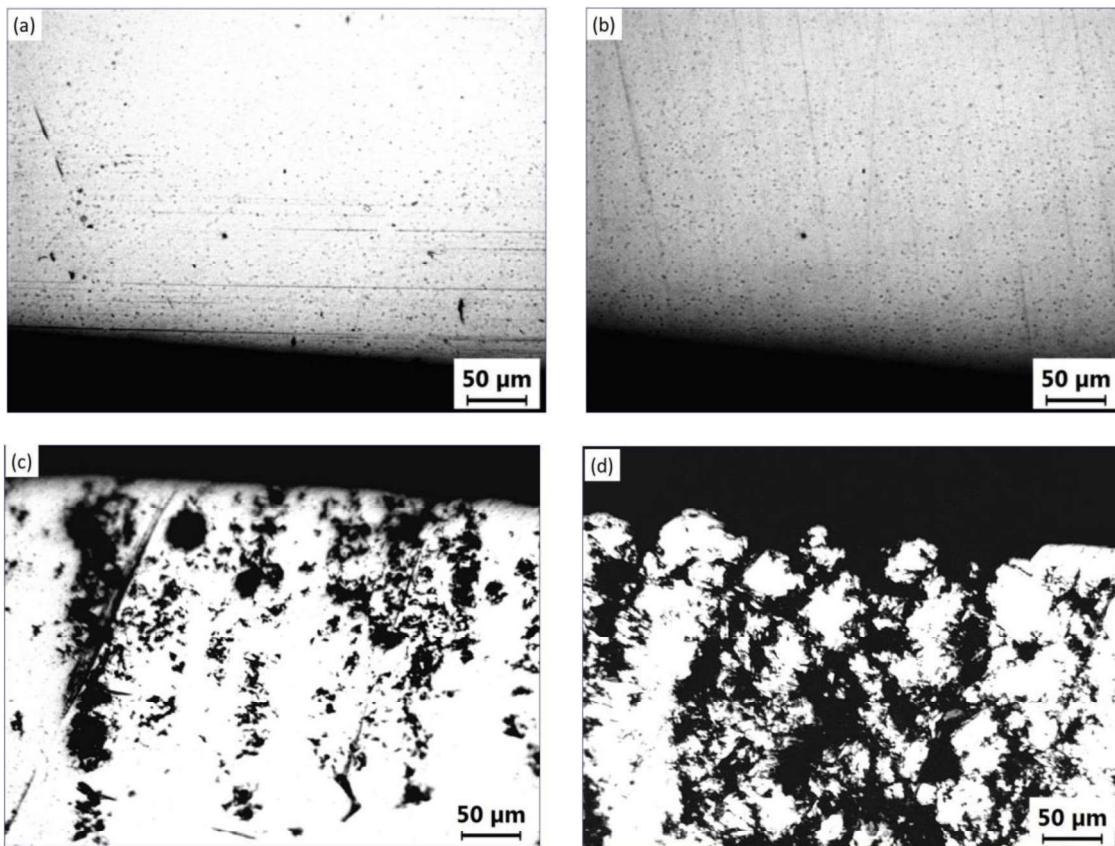


Fig. 4.2 Cross-sectional optical microscopy images of 13wt.% Cr martensitic stainless steel showing absence of intergranular attack in (a) austenitized and (b) tempered at 400 °C for 2.5 h specimens and severe attack in (c) 550 °C for 2.5 h and (d) 650 °C for 2.5 h tempered specimen after IGC test in 5% HNO₃ solution.

Fig. 4.3 shows the SEM images of the longitudinal surface of the specimens tempered at 550 and 700 °C after immersion in 5% HNO₃ solution. Fig. 4.3 clearly shows preferential attack along the martensitic lath interfaces. These results are consistent with the results from TEM examination as shown in Fig. 3.8(b) and Fig. 3.9(a). The carbides are seen to be formed along the interface of martensitic laths (Fig. 3.8(b) and Fig. 3.9(a)) and also inside the laths (Fig. 3.8(b)) and the preferential attack is also observed along the lath-lath interfaces in 5% HNO₃ immersion test as shown in Fig. 4.3(c)-(d). It is reported that the HNO₃ preferentially attacks the Cr depleted regions and also dissolves chromium carbides in sensitized austenitic stainless steels (Adhe *et al.*, 1996, Kain, 1997).

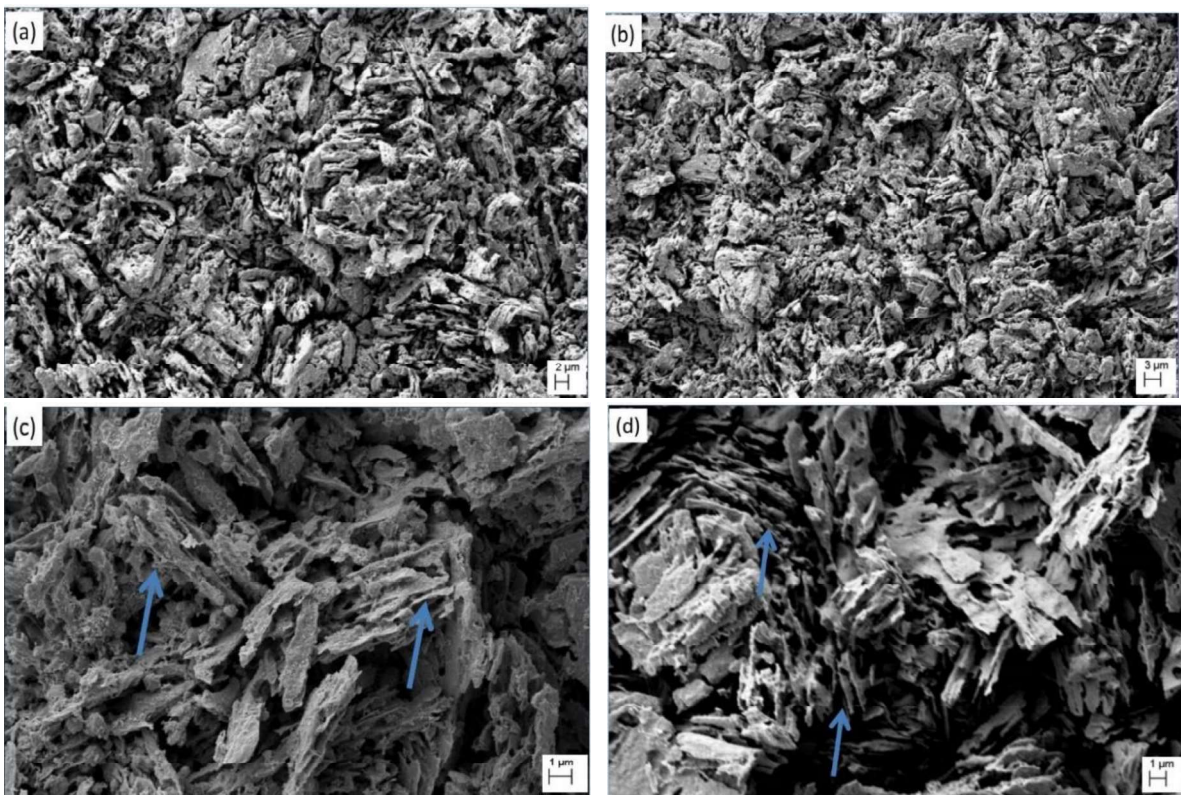


Fig. 4.3 SEM images of IGC tested (a) 550 °C for 2.5 h, (b) 700 °C for 2.5 h tempered specimens and (c) and (d) are magnified images of (a) and (b) showing corrosion attack preferentially along the lath boundaries (arrow indicating the corrosion attack at martensitic laths).

The formation of Cr- rich carbides results in depletion of Cr in the regions adjacent to carbides (matrix-carbide interface region). If the level of Cr is less than 11-12 wt.% in the Cr depletion zone, it would show a higher intergranular corrosion rate than that for the tempered condition having higher levels of Cr wt.% in the depletion zones (Sedriks, 1996, Kain, 1997). There are no studies or data available on the extent of Cr deletion at the carbide-matrix interface in these types of materials after tempering. In the present study, the presence of narrow Cr depletion zone of 7 to 9 nm at the nano-scaled carbide-matrix interface regions with a Cr concentration of 9 wt.% in depleted region after tempering at 550 °C is shown in Fig. 3.13(b). The MSS used in the present study has 13wt.% Cr and precipitation of carbides during tempering renders the Cr concentration to fall below 13wt.% in the matrix-carbide interface region depending upon the tempering temperature and duration. The high corrosion rates observed for the specimens tempered at 550 °C for 2.5 h showed that the material is in highly sensitized condition and nitric acid attacked both the Cr depleted regions and dissolved the chromium carbides leading to high a corrosion rate. When the tempering temperature increased above 550 °C, the corrosion rate decreased. This could be due to Cr diffusion from the lath/grain matrix to the depleted regions. The diffusion rate of Cr in ferritic/martensitic matrix is ~10 times higher than that in the austenitic matrix (Ebrahimi *et al.*, 2011, Kain, 1997). The diffusion of Cr from the matrix to the Cr depleted regions was also confirmed by 5% HNO₃ immersion tests of the specimens tempered at 550 °C for 100 and 500 h. The specimens tempered at 550 °C for 100 and 500 h showed low corrosion rates of 14.3 and 3.5 mm/y respectively. Even after a long duration tempering for 500 h at 550 °C, the corrosion rate did not come down to the corrosion rate for the specimen that developed little carbide precipitation (tempered at 300 °C for 2.5 h). This could be due to the fact that the specimen tempered at 550 °C for 500 h had a very high fraction of carbides though the Cr depletion regions had been erased by

the long term tempering at this temperature. The carbides themselves get attacked in the nitric acid therefore the IGC rate was still 3.5 mm/y. The nitric acid immersion test results together with TEM results clearly indicated that the specimens tempered at 550 and 700 °C for 2.5 h are sensitized and susceptible to IGC even in a low concentration of HNO₃, acidic (oxidizing) solution. The immersion test results are subsequently corroborated with electrochemical measurements.

4.3.2. Potentiodynamic polarization tests

The potentiodynamic polarization curves for specimen austenitized and then tempered at different temperatures in 0.25 M and 0.03 M H₂SO₄ (deaerated) solution are shown in Fig. 4.4(a)-(b). These experiments were repeated and showed a variation of 2%. The austenitized and tempered specimen's polarization curves showed the typical active - passive transition behavior in H₂SO₄ solutions. The critical current density (i_{crit}) is the maximum current density during the anodic dissolution stage of the specimen and is marked as i_{crit} and shown in Fig. 4.4(a). The i_{pass} is the passivation current density corresponding to the potential of 0.4 V_{SCE} and is marked in Fig. 4.4(a) for clarity. The i_{crit} is minimum for the austenitized specimen while the i_{crit} tends to increase with tempering temperature till 550 °C and thereafter it decreases (Fig. 4.4(a)-(b)). The i_{pass} is the minimum for the austenitized specimen and maximum for the specimen tempered at 550 °C. Tempering at a temperature above 550 °C reduced the i_{pass} (Fig. 4.4(a)-(b)). The critical and passive current density values for austenitized and tempered specimens increased for higher concentration of H₂SO₄ solution as shown in Fig. 4.4(a).

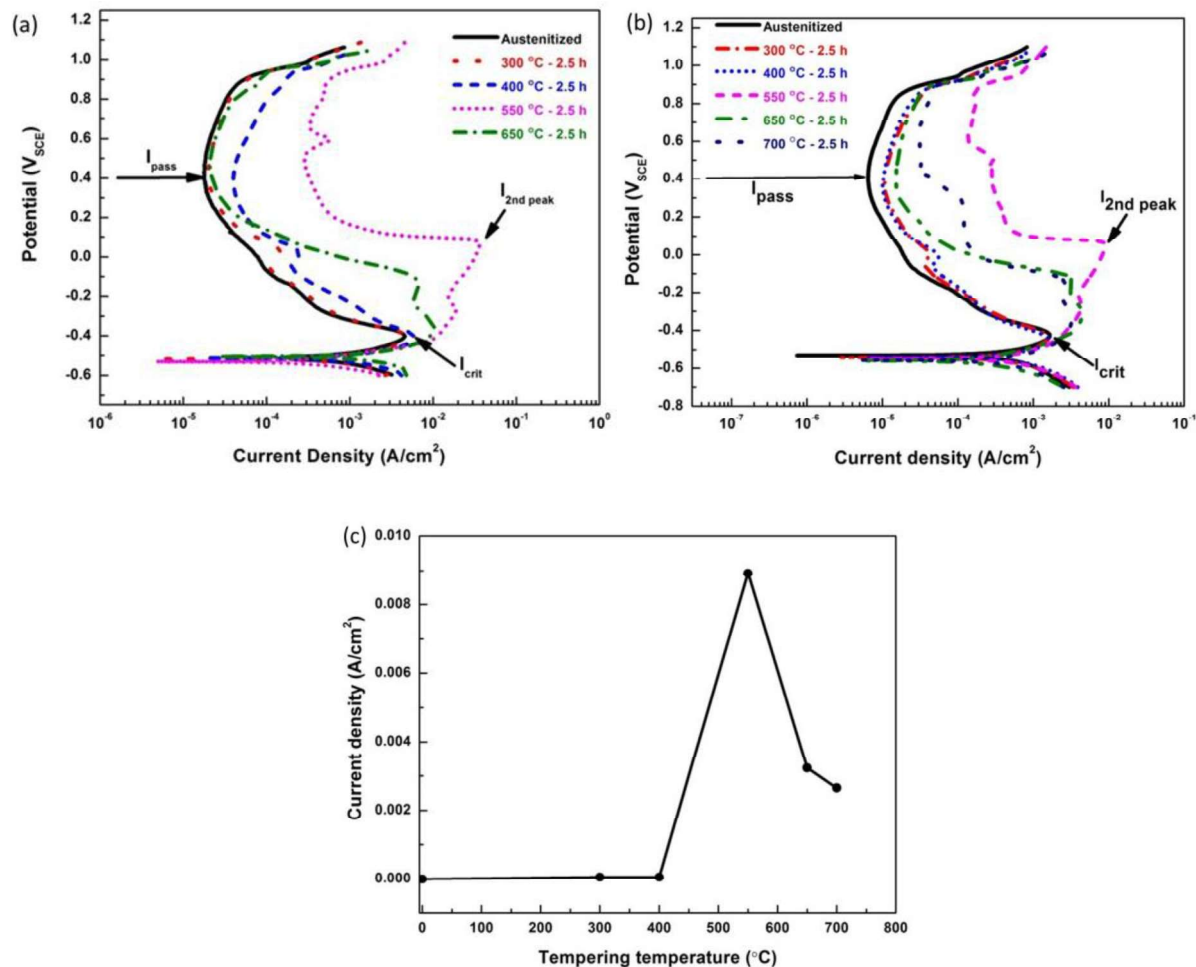


Fig. 4.4 Potentiodynamic polarization curves in (a) 0.25 M and (b) 0.03 M H₂SO₄ solutions and (c) variation of second anodic peak current density with tempering temperature for austenitized and tempered specimens in 0.03 M H₂SO₄ solution. All the tempering treatments are for 2.5 h.

The higher concentration of H₂SO₄ solution is aggressive for the MSS as the i_{crit} and i_{pass} values are higher compared to the values in 0.03 M solution (Fig. 4.4(b)). In comparison to the austenitized condition, there was a change in the shape of the polarization curve for the tempered specimens. The potentiodynamic polarization curve of the austenitized specimen did not have a second anodic peak but the specimen tempered at 300 °C and 400 °C showed small peaks at a given region of potential values (Fig. 4.4(a)-(b)). The second anodic peak current density was the maximum for the specimen tempered at 550 °C and decreased for specimens tempered above 550 °C, as shown in Table 4.2 and Fig. 4.4(a)-(b). After the polarization tests, it was observed that the tempered

specimens surface was covered with a black layer in higher concentration (0.25 M) solution. However, in the 0.03 M H₂SO₄ solution, the specimen tempered at 550 °C and above also developed a black layer.

Table 4.2 Comparison of electrochemical parameters obtained from the polarization curves in 0.25 M H₂SO₄ with different tempering treatments.

Temperature (°C)	i_{crit} (A/cm ²) x 10 ⁻³	I_{pass} (A/cm ²) x 10 ⁻⁵	i_{2max} (A/cm ²) x 10 ⁻³	Q_{2max} (C/cm ²) x 10 ⁻³	i_{2max}/i_{crit}
austenitized	4.61	1.79	Not observed	Not observed	0
300	4.65	1.94	0.14	0.015	0.030
400	6.42	4.08	0.24	0.25	0.037
550	18.57	33.33	35.32	37.81	1.92
650	10.02	2.71	6.53	6.49	0.62

GI-XRD analysis showed that the black surface on the specimen tempered at 550 °C for 2.5 h after the anodic polarization in 0.25 M H₂SO₄ solution composed of martensitic matrix and M₂₃C₆ type carbides as shown in Fig. 4.5. The XRD peaks are corresponding to martensitic matrix and M₂₃C₆ type carbides with a single XRD peak matching with M₇C₃ type carbide (JCPDS number. 85-1281 and 36-1432) as indicated in Fig. 4.5. For comparison, XRD pattern of the unexposed specimen tempered at 550 °C for 2.5 h is also shown in Fig. 4.5. The XRD peaks are corresponding to martensitic matrix only. The presence of the carbides on the surface of the specimen tempered at 550 °C for 2.5 h after anodic polarization test indicates that the H₂SO₄ solution attacked the Cr

depleted regions and dissolved the matrix leaving the carbides unattacked. This result also confirms that EPR tests using H_2SO_4 solutions would not result in attack on carbides.

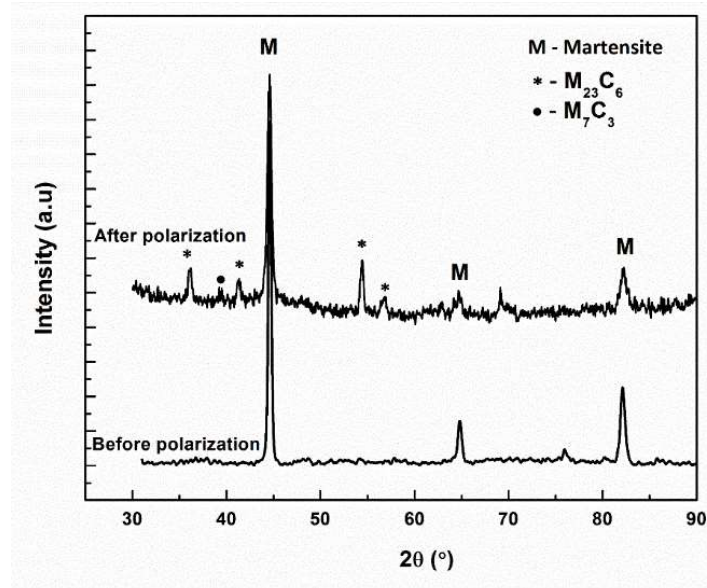


Fig. 4.5 XRD patterns of specimen tempered at 550 °C for 2.5 h before and after potentiodynamic polarization in 0.25 M H_2SO_4 showing presence of carbides in black layer formed after polarization.

This second anodic peak has been reported for martensitic stainless steels and it is reported that in stainless steels tested in 0.5 M H_2SO_4 solution, the known cause of the second anodic peak could be (a) oxidation of atomic hydrogen absorbed by the metal, (b) oxidation of Fe^{+2} ions in the acid solution, (c) Ni enrichment on the surface and (d) presence of Cr impoverished regions and (e) microstructure and compositional effect (Frangini *et al.*, 1992, Felloni *et al.*, 1973, Hermas *et al.*, 1999). The observed second anodic peak in 0.03 M H_2SO_4 solution in our study is in the range of -40 mV_{SCE} to 70 mV_{SCE} for the specimens tempered at 300 and 400 °C (Fig. 4.4). The peak potentials also shifted to more anodic values for the specimens tempered above 400 °C. For the second peak, the probable reason among all the possibilities mentioned above, could be Cr depletion in the vicinity of Cr-rich carbides. This stems from the fact that the secondary peaks for

the specimen tempered at 550 and 650 °C are the highest. These temperatures of 500-650 °C showed the maximum interlath attack in nitric acid immersion test indicating maximum depletion of Cr due to chromium carbide formation in these specimens. To confirm this fact, potentiodynamic polarization curves of specimens tempered at 550 °C for 100 and 500 h in 0.03 M H₂SO₄ solution are shown in Fig. 4.6(a). It is observed that there is a decrease in the peak current density for the second anodic peak for 100 and 500 h tempered specimens compared to that for the specimen tempered at 550 °C for 2.5 h, as shown in Fig. 4.6(b).

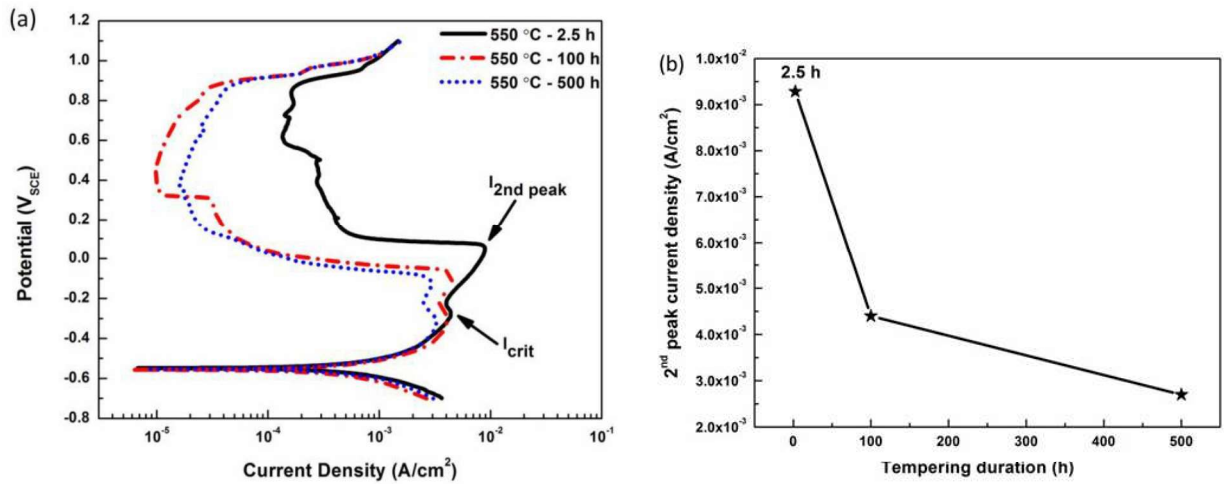


Fig. 4.6 (a) Potentiodynamic polarization curves in 0.03 M H₂SO₄ solution for 550 °C tempered specimens for different durations (b) Variation of second anodic peak current density with tempering duration at 550 °C.

This is due to the fact that the fast diffusion of Cr takes place from the martensitic matrix to the Cr depleted regions with the tempering duration increasing from 2.5 h to 100 h (Kain, 1997). This is also supported by the IGC rates for these specimens (Fig. 4.1). Further replenishment of Cr in the depletion regions is slower due to decreasing difference of Cr in the matrix and that in the depletion regions. Therefore, the IGC rates in nitric acid also drop to a lesser extent upon increasing the tempering duration from 100 to 500 h. This is also reflected in the slower change in drop of second peak potential and current density values (Fig. 4.6).

Since the maximum second anodic peak current density may not be a true reflection of the changes occurring with tempering, so the charge density under the second anodic peak was calculated from the integration of the second anodic current peak and is shown in Fig. 4.7(a). The charge density was the maximum for the specimen tempered at 550 °C for 2.5 h and decreased with increase of tempering temperature. The integrated charge density also decreased with tempering duration at 550 °C due to replenishment of Cr, as shown in Fig. 4.7(b). This confirms that the second anodic peak was due to the preferential attack at the Cr depleted regions present in the tempered MSS.

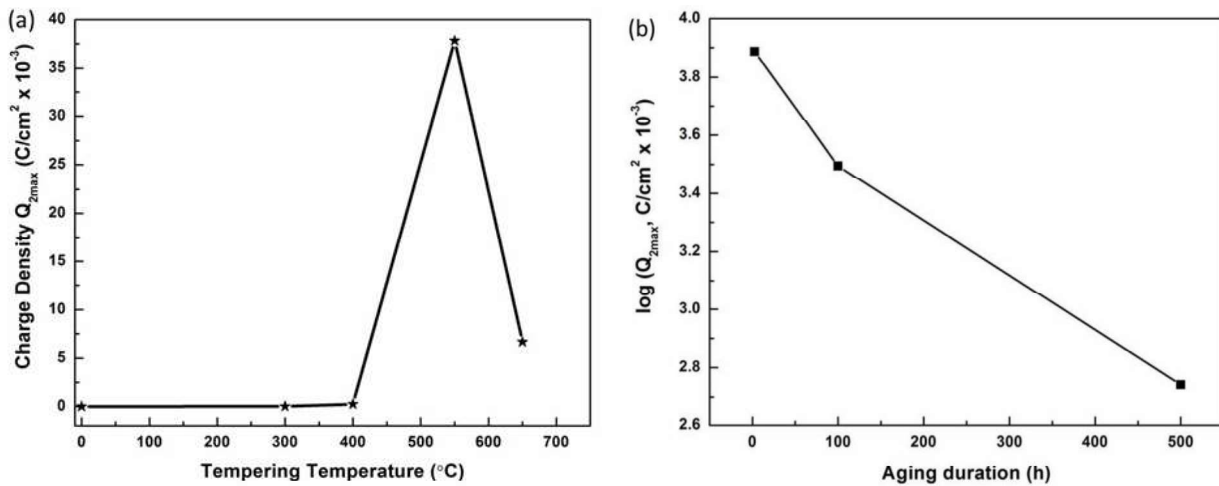


Fig. 4.7 Variation of second anodic peak charge density in 0.25 M H₂SO₄ solution (a) with tempering temperature and (b) with tempering at 550 °C up to 500 h.

The results from potentiodynamic polarization tests are also in line with results from the immersion test in 5% nitric acid. The maximum current density as well as the maximum charge density corresponding to the second peak is observed for the specimen tempered at 550 °C in the polarization test (Figs. 4.6-4.7) and the maximum corrosion rate in the immersion test for the specimen tempered at 550 °C for 2.5 h (Fig. 4.1). The magnitude of second anodic peak current density in potentiodynamic polarization in 0.03 M H₂SO₄ solution (Fig. 4.4(b)) is also in line with the immersion test corrosion rates with tempering temperature. Therefore, the higher anodic peak

potential for the second peak corresponds to the Cr depleted regions (IGC attack) and matrix uniform corrosion at lower anodic peak potential in the polarization curve (Fig. 4.4).

Fig. 4.8 shows the current density variation with time in the potentiostatic tests for the specimen tempered at 400 and 550 °C for 2.5 h at 0 mV_{SCE} in 0.03 M H₂SO₄ (deaerated) solution. This potential of 0 mV_{SCE} potential lies in the second anodic current density peak in the potentiodynamic polarization curve shown in Fig. 4.4. The current density of the specimen tempered at 550 °C was higher and it increased with time whereas the specimen tempered at 400 °C showed a very low and gradually reducing current density with time as shown in Fig. 4.8. The increase in current density with time at 0 mV_{SCE} for the specimen tempered at 550 °C for 2.5 h indicates that the specimen tempered at 550 °C for 2.5 h is heavily sensitized hence is undergoing severe corrosion attack. The specimen tempered at 400 °C, on the other hand is not sensitized and is developing a gradually stronger passive film; therefore, the current density is reducing with time (Fig. 4.8).

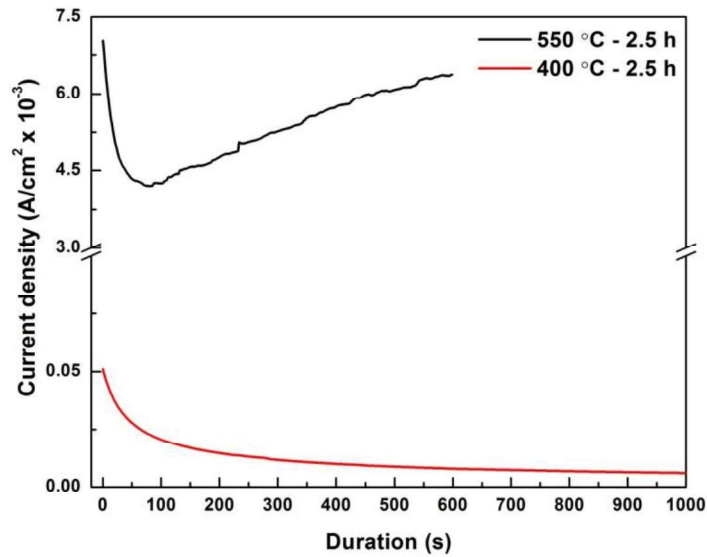


Fig. 4.8 Potentiostatic tests held at 0 mV_{SCE} in 0.03 M H₂SO₄ solution.

The results from polarization (Fig. 4.4) and potentiostatic (Fig. 4.8) tests together with results from GI-XRD (Fig. 4.5) indicate that the 0.03 M H₂SO₄ solution attacked Cr depletion regions in sensitized MSSs and the second anodic peak in anodic polarization is due to attack at the Cr depletion regions present at the carbide-matrix interface.

4.3.3. DL-EPR test for determination of DOS with tempering temperature

The EPR test solution 0.5 M H₂SO₄ + 0.01 M KSCN (deaerated) commonly used for austenitic stainless steels is too aggressive for 13 wt.% Cr MSSs and use of KSCN as a depassivator for MSSs is also not recommended as it leads to pitting and excessive uniform corrosion during the test (Tavares *et al.*, 2010). The H₂SO₄ solution has been used for evaluating the DOS of MSSs (Taji *et al.*, 2015, Alonso *et al.*, 1999). For choosing an appropriate test solution for EPR test, the criterion was that it should (a) not lead to localized attack e.g. pitting, (b) allow as much passivation of the stainless steel (i.e. low current density) before reactivation starts and (c) distinguish between a heavily sensitized material from a non-sensitized material (Kain, 2002, Cihal, 2004). Therefore, the material tested was the one that had the carbides but had shown signs of low DOS (i.e. tempered at 550 °C for 100 h, with long term aging expected to lead to diffusion of Cr into Cr depleted regions). This tendency of diffusion of Cr into Cr depleted regions is also indicated in anodic polarization in H₂SO₄ solution (Fig. 4.6) and also in 5% HNO₃ immersion test corrosion rates.

The DL-EPR tests in different concentrations of H₂SO₄ solution were performed on austenitized and specimen tempered at 550 °C for 100 h and the influence of H₂SO₄ concentration on DL-EPR values are shown in Table 4.3. The reactivation current density (i_r) of specimen tempered at 550 °C for 100 h was more than the activation current density (i_a) in 0.25 and 0.1 M H₂SO₄ solutions whereas lower values were observed for i_r than that of i_a in dilute solutions, i.e. 0.05 and 0.03 M H₂SO₄ as shown in Fig. 4.9. The i_r decreased with decrease in H₂SO₄ solution concentration. The

current in reactivation scan i_r is due to depassivation of weak passive films formed on Cr depleted regions during the activation scan. The passive films formed over Cr depleted regions are weak and depassivated during the reactivation scan. So, i_r is due to preferential attack at the chromium depleted regions. Therefore, i_r cannot be greater than i_a . A higher value of i_r (than that of i_a) would indicate that dissolution during reactivation could be from all the regions of the specimen and not necessarily from the Cr depletion regions. The DL-EPR values for tests done in solutions of 0.05 and 0.03 M H_2SO_4 were the same, as shown in Table 4.3 but 0.03 M H_2SO_4 was chosen for determining the DL-EPR values as it showed a lower i_a and i_r value. Therefore, with 0.03 M H_2SO_4 solution, lesser attack on the martensitic matrix and Cr depleted regions would be expected during DL-EPR test (lower values of i_r than i_a) although carbides would not get attacked even in higher concentration of the H_2SO_4 solution (0.25 M) as shown by GI-XRD results (Fig. 4.5).

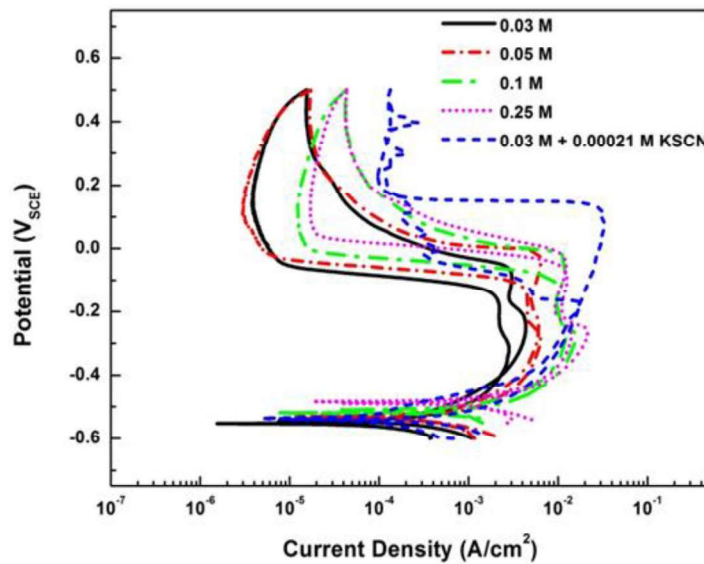


Fig. 4.9 DL-EPR curves of 550 °C for 100 h tempered specimen in different concentrations of H_2SO_4 solution.

As shown in Fig. 4.9, addition of 20 ppm KSCN (0.00021 M) to 0.03 M H_2SO_4 solution increased the i_a and i_r current densities to much higher value than the current density values (i_a and i_r)

observed with 0.03 M H₂SO₄ solution only. The i_a and i_r values are also equal with addition of 20 ppm of KSCN to 0.03 M H₂SO₄ solution as shown in Fig. 4.9. This is an unusual behavior in DL-EPR test, indicating the excessive uniform corrosion or pitting corrosion during reactivation scan. The i_r value should always lower than the i_a value since the i_r value represents a fraction of the area which is not passivated due to the presence of Cr depletion (Tavares *et al.*, 2010, Kain, 1997). The similar behavior of increase in i_a and i_r values with addition of 0.01M KSCN to H₂SO₄ solution is also observed by other researchers for 11wt.% Cr martensitic stainless steel and also in UNS S17400 stainless steel (Tavares *et al.*, 2010, Taji *et al.*, 2015). In the present study also, addition of 20 ppm KSCN (0.00021 M) to 0.03 M H₂SO₄ increased the i_a and i_r values and these values are equal. Therefore, the use of KSCN as a stimulator for depassivation in DL-EPR test is not used in the present work and also not recommended by other researchers for MSSs as it leads to excessive uniform corrosion or pitting corrosion during the test. All the EPR tests were repeated and showed a variation of 2%.

Table 4.3 DL-EPR values of the specimen tempered at 550 °C for 100 h in different concentrations of H₂SO₄ solution.

Solution concentration	DL-EPR value
0.25 M H ₂ SO ₄	100.8
0.1 M H ₂ SO ₄	80.54
0.05 M H ₂ SO ₄	70.77
0.03 M H ₂ SO ₄	69.9

Fig. 4.9 also shows the presence of two anodic peaks in the activation and reactivation process. As it was shown in potentiodynamic polarization results (Fig. 4.4), the second anodic current density peak is due to the Cr depletion (associated with Cr-rich carbides). Therefore, for calculating the

DL-EPR values, the ratio of the second anodic peak current densities during reactivation and activation were taken. The DL-EPR values measured for the specimen tempered from 300 °C to 700 °C for 2.5 h are shown in Fig. 4.10. It is observed that the specimen tempered at 550 °C for 2.5 h showed the maximum DL-EPR value of 88.2. The DL-EPR values for specimens tempered below 550 °C are very low indicating that only slight sensitization had occurred. As shown in Fig. 4.10, the DL-EPR values increased substantially when tempering temperature is raised from 450 °C to 550 °C. However, tempering above 550 °C resulted in decrease in DL-EPR values (from 550 °C till 700 °C).

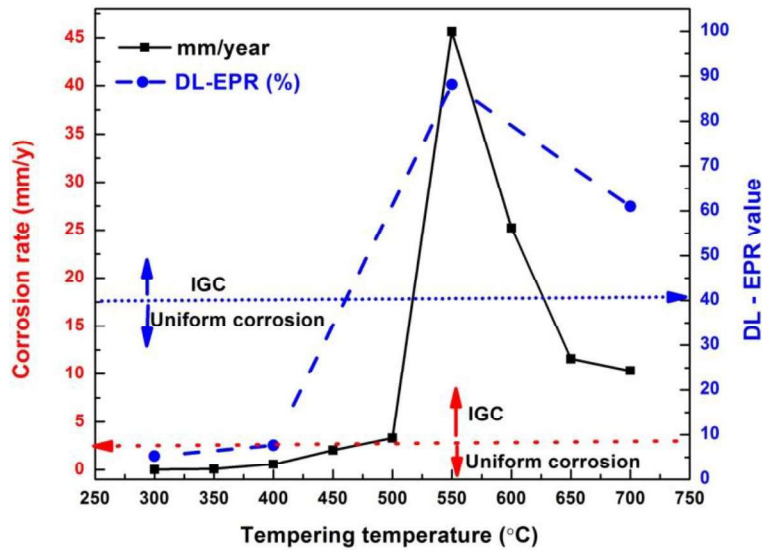


Fig. 4.10 DL-EPR values and corrosion rates in 5 % HNO₃ immersion test with tempering temperatures. All the specimens are tempered for 2.5 h.

As shown in Fig. 3.6 to Fig. 3.11, the size of carbide increased with tempering temperatures from 300 till 700 °C. The growth and formation of new carbides lead to Cr depletion in the adjacent areas of the carbides. However, tempering at temperatures above 550 °C, also leads to a very fast diffusion of Cr into the Cr depleted regions of the martensitic matrix, erasing the Cr depletion regions. Thus at temperatures of tempering above 550 °C, there are more carbides (and coarse carbides, Fig. 3.9(a) and Fig. 3.11(b)) but the Cr depletion regions get reduced/erased due to fast

diffusion of Cr in martensitic SS matrix. Tempering at 550 °C for durations longer than 2.5 h also decreased the DL-EPR values (Table 4.3). DL-EPR values reduced to 58.7 for 500 h tempered condition from 88.2 for the specimen tempered at 550 °C for 2.5 h. This is due to the fact that, the Cr diffuses from the bulk martensitic matrix to Cr depleted areas around the carbides with increase in tempering temperature as well as with increase in duration of exposure at a given temperature (Kain, 1997, Adhe *et al.*, 1996).

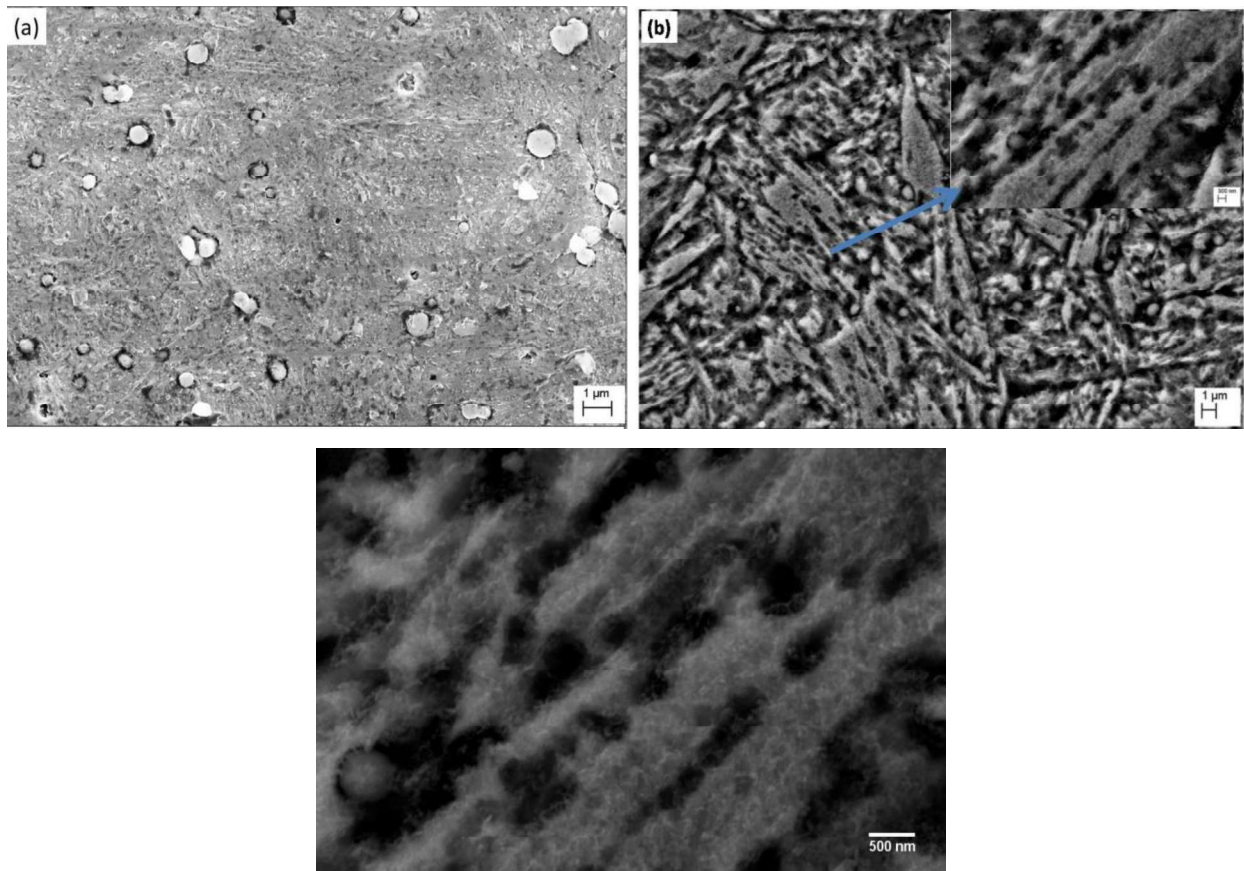


Fig. 4.11 FE-SEM images of the DL-EPR tested surface (a) austenitized, (b) tempered at 550 °C for 2.5 h and (c) magnified image of (b).

This desensitization effect (Cr replenishment with increased aging duration) is also reported for austenitic stainless steels but due to a slower diffusion rate for the austenitic matrix, it takes much longer for desensitization to take place (Kain *et al.*, 2004a, Thompson *et al.*, 1992). It is reported

in our previous studies that the desensitization in Type 304 stainless steel takes 15 days at 750°C and 5 days at 800 °C (Adhe *et al.*, 1998). The SEM observations after the DL-EPR test showed that the austenitized specimen did not show localized corrosion whereas the specimen tempered at 550 °C for 2.5 h showed preferential attack along the lath interfaces as shown in Fig. 4.11(a). The extent of attack at martensite lath interfaces due to carbide precipitation is much more than that at the prior austenite grain boundaries as shown in Fig. 4.11(b). The maximum width of the EPR attacked regions at lath interfaces are around 200 to 600 nm. The width of attacked regions in EPR test is shown to be much more than the width of Cr depletion regions associated with chromium carbide which is around 7-9 nm. Some of the laths are also dislodged from the matrix as shown in Fig. 4.11(c).

Fig. 4.10 also shows the DL-EPR values and the IGC test results in 5% HNO₃ for all the tempered conditions are in good agreement. Therefore, as the DOS increased with tempering temperature till 550 °C, IGC rates in HNO₃ also increased (Fig. 4.10). Subsequently, as the DL-EPR values decreased on tempering above 550 °C, the IGC rates also dropped as shown in Fig. 4.10. As it is well established that continuous and discrete Cr depletion regions in the stainless steel get attacked in the EPR test (and not the chromium carbides), the EPR test results lead to infer that tempering led to formation of carbides and Cr depletion around these Cr-rich carbides (Fig. 4.10). The results of DL-EPR and IGC tests are consistent but there is a difference in the nature of corrosive attack. In DL-EPR test, the solution attacked preferentially the Cr depleted regions (also confirmed by GI-RXD, Fig. 4.5) and corresponding current density is measured whereas the HNO₃ solution attacked the Cr depleted regions and also dissolved the chromium carbides (Kain, 1997). Hence these two tests are relative. From these results (Fig. 4.1 and Fig. 4.10), it is clear that 13wt.% Cr

MSS should be tempered at a temperature below 450 °C to avoid the interlath/intergranular corrosion.

It is also clear from Fig. 4.10 that IGC was clearly observed after the test in 5% HNO₃ solution for the specimen that was tempered above 450 °C and it showed a corrosion rate of 2.5 mm/y. Observations after the IGC test indicated that IGC occurred for all the specimens that showed a corrosion rate of more than 2.5 mm/y and it was uniform corrosion for all the specimen that showed a corrosion rate less than 2.5 mm/y in 5% nitric acid solution. Similarly, it is clear from Fig. 4.10 that the specimen had a high susceptibility to IGC (actually showed IGC, Fig. 4.1) when its DL-EPR value was more than 40. These threshold values for IGC are valid for the 5% HNO₃ test used in this study and for the DL-EPR test parameters established in this study.

As stated above, there are two anodic current density peaks in the activation and reactivation scans of the DL-EPR test as shown in Fig. 4.9. In order to investigate the nature of the corrosion attack at different anodic peaks, the DL-EPR tests were performed on the specimen tempered at 550 °C for 2.5 h and the test was stopped at four different potentials. The cross-section perpendicular to the tested surface was prepared for microscopic examination to study the nature of attack after DL-EPR test. DL-EPR tests were stopped at (a) the 1st anodic peak potential in the forward scan (P₁), (b) the start of the reactivation scan (P₂), (c) the start of the 2nd anodic peak in the reactivation scan (P₃) and (d) after completion of the EPR test (P₄) as indicated in Fig. 4.12. In the present study, the depth of the EPR attacked regions during the test terminated at different potentials was also measured by cross-sectional examination. In the EPR tests for austenitic stainless steels, it had been shown that the width of the attacked regions is much higher than the width of the Cr-depleted regions (Kain *et al.*, 2002, Ahemdabadi *et al.*, 2013). It had been clearly demonstrated in sensitized Alloy 600 that the width of the Cr-depleted regions are in the range of 60 nm to 410 nm whereas

the maximum width of the attacked regions in EPR test are in the range of 8.9 μm to 11 μm (Kain *et al.*, 2002).

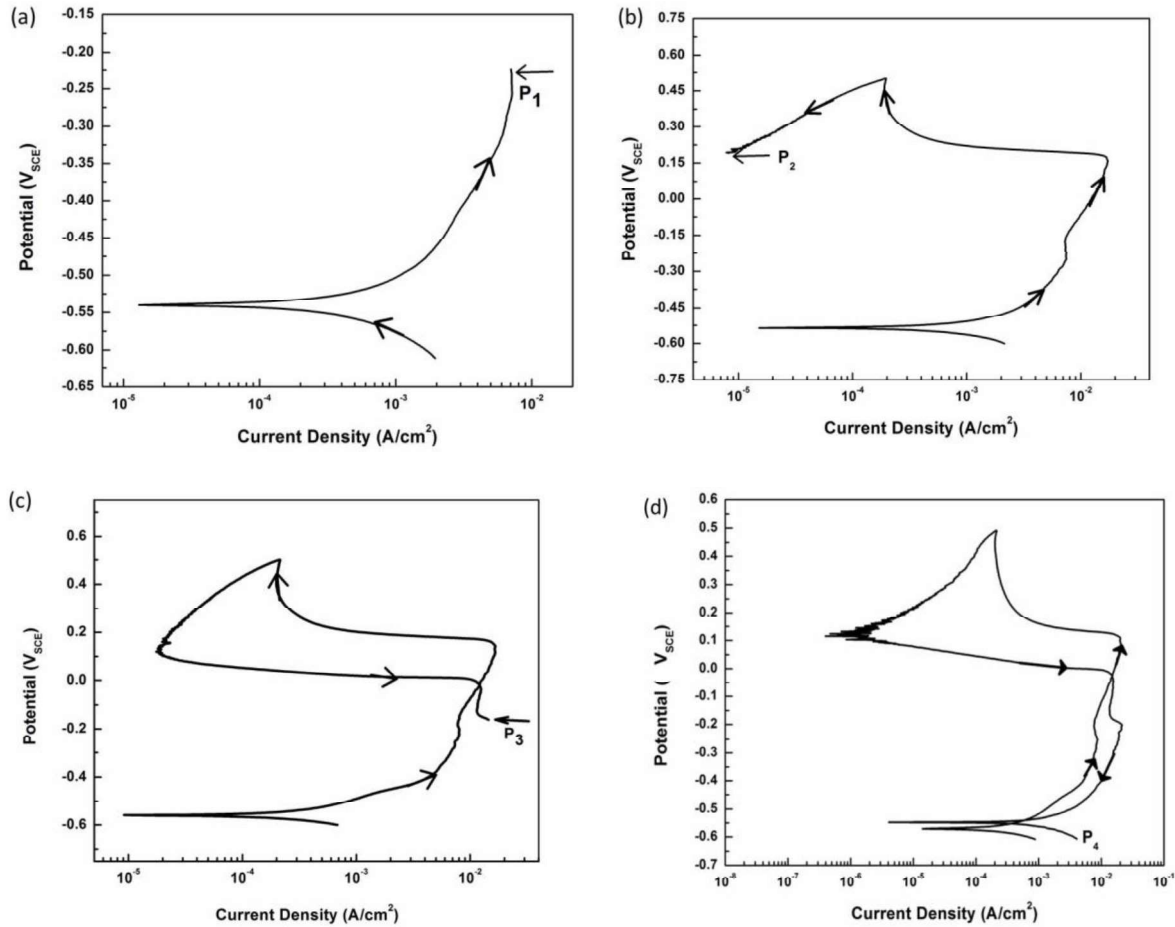


Fig. 4.12 DL-EPR tests stopped at (a) 1st anodic peak potential in the forward scan (P_1), (b) start of the reactivation scan (P_2), (c) start of the 2nd anodic peak in the reactivation scan (P_3) and (d) after complete EPR test (P_4).

Fig. 4.13 shows the attacked regions in the cross sections after the EPR tests at different potentials. No preferential attack was observed when the test was stopped at potential P_1 as shown in Fig. 4.13(a). Therefore, the 1st peak in the activation scan symbolizes uniform dissolution of the martensitic matrix. When the test was stopped at P_2 potential, it showed some attacked regions with a depth in the range of 1 μm to 1.5 μm , and the attacked locations are shown by arrow marks in Fig. 4.13(b). Therefore, the second peak in DL-EPR scan indicates attack at the martensitic laths

boundaries, as indicated by arrow marks. As shown in the TEM images (Fig. 3.8 & 3.9), the size of the martensitic laths is in the range of 140 to 600 nm for 550 and 700 °C tempered specimens. The SEM image for the specimen, when the test was stopped at P₃ potential is shown in Fig. 4.13(c). The depth and number of attacked regions were more during the reactivation scan and the average depth of attack was in the range of 4 to 5 μm with a maximum of 29 μm when the test was stopped at P₃ potential, as shown in Fig. 4.13(c) compared to 1-1.5 μm depth of attack at P₂ potential. Fig. 4.13(d) shows the micrograph after the complete EPR scan and attack at martensitic laths was clearly observed.

The magnified image of Fig. 4.13(c) is shown in Fig. 4.13(f). As shown in Fig. 4.13(f), the corrosion attack observed during reverse scan of DL-EPR test (P₃ potential) is along the interfaces of chromium carbide and martensite laths and the undissolved chromium carbides indicated with arrow marks left at the attacked interfaces are also shown in Fig. 4.13(f). The carbides formed in this tempered condition are in nano-size as shown in Fig. 3.8 and difficult to observe in SEM. The SEM-EDS analysis on the carbides left in the attacked regions (indicated as spot 1 and spot 2 in Fig. 4.13(f)) showed that the carbides are composed of Fe and Cr with 23 wt.% of Cr for spot 1 and 37 wt.% of Cr for spot 2 indicating that the spot 2 carbide is undissolved carbides. The continuous and local Cr depletion regions present in the specimen tempered at 550 °C for 2.5 h got attacked in the DL-EPR test reverse scan.

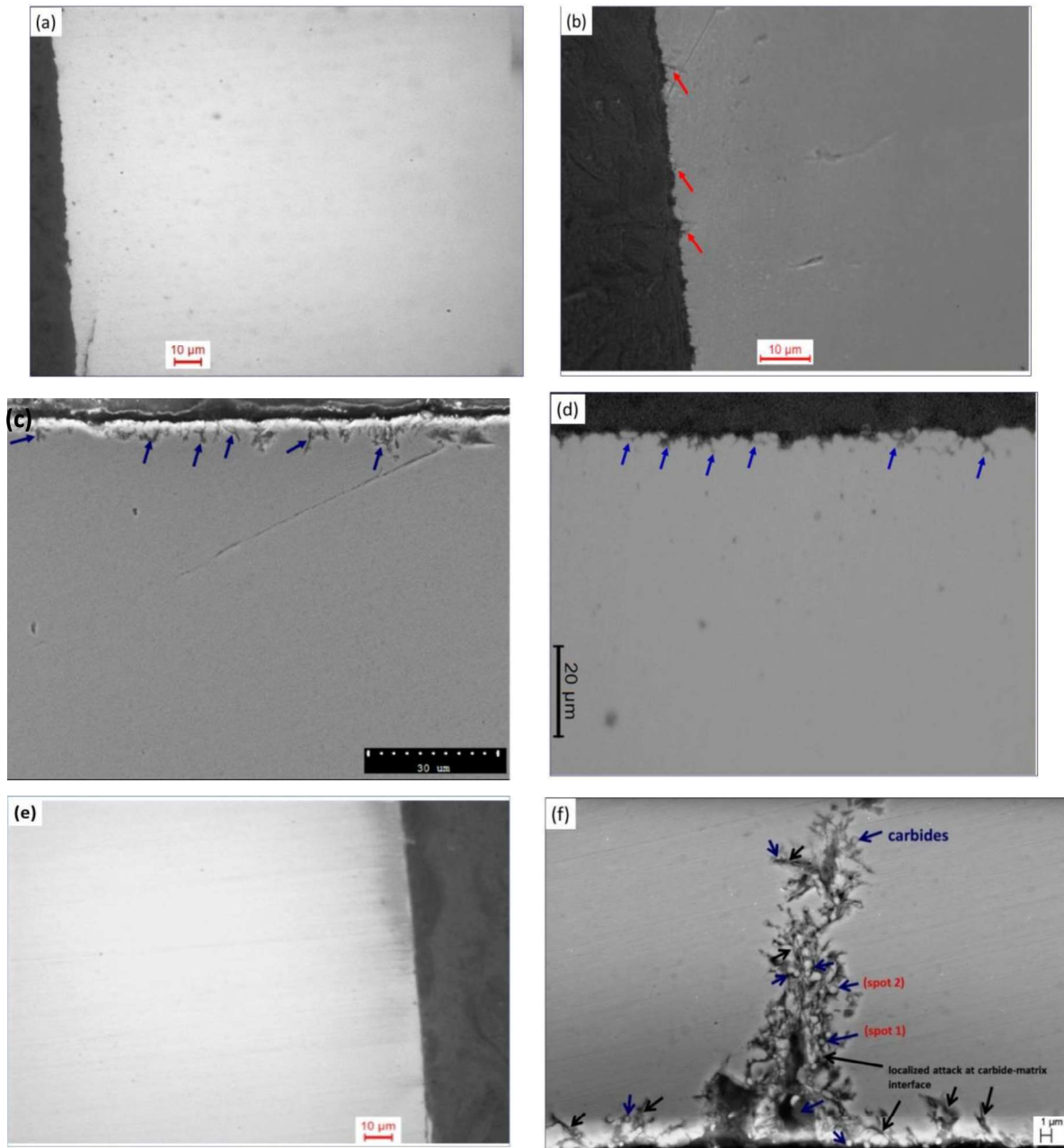


Fig. 4.13 Cross-sectional images of the 550 °C for 2.5 h tempered specimen tested at different potentials, (a) 1st anodic peak potential in the forward scan (P_1), (b) start of the reactivation scan (P_2), (c) start of the 2nd anodic peak in the reactivation scan (P_3) and (d) after complete EPR test (P_4), (e) opposite side of the EPR tested cross-sectional image. Arrow indicate EPR test attacked regions and (f) magnified view of the depth of attacked regions in the cross-sectional surface (shown in Fig. 4.13(c)) after DL-EPR test stopped at potential P_3 .

The cross-sectional examination of 550 °C, 2.5 h specimen (when the DL-EPR test was stopped at P₃ potential) clearly demonstrated that the 1st reactivation current peak is due to preferential attack at lath interfaces due to Cr impoverishment at these interfaces. From the above observations, it is confirmed that the second anodic current density peak in electrochemical tests such as anodic polarization and EPR in 0.03 M H₂SO₄ solution is due to the preferential attack at the Cr depleted regions around carbides hence can be used for quantifying the DOS in 13wt.% Cr MSS in different tempered conditions.

4.3.4. Potentiodynamic polarization studies in 5% HNO₃ solution

The results of potentiodynamic polarization in 5% HNO₃ (deaerated) solution for the specimen austenitized and then tempered at different temperatures are shown in Fig. 4.14. The polarization results are reproducible and different electrochemical parameters deduced from polarization curves are given in Table 4.4. The austenitized and tempered specimen's polarization curves show the typical active - passive transition behavior in 5% HNO₃ solution. The E_{corr} and transpassive potentials did not change with tempering treatments as shown in Fig.4.14 and Table 4.4. However, significant changes observed in polarization curves with tempering treatments are in i_{corr}, i_{crit} and i_{pass}. The i_{crit} is the maximum current density during the anodic dissolution stage of the specimen whereas i_{pass} is the passivation current density corresponding to the potential of 0.4 V_{SCE} and all these parameters are marked in Fig.4.14 for clarity. The i_{corr} and E_{corr} values were determined using Tafel extrapolation method. The scan rate used in the anodic polarization tests was relatively faster (60 mV/min) than the scan rate normally used in anodic polarization for performing the Tafel analysis. The electrochemical parameters extracted from Tafel analysis were used for comparative purpose only. The E_{corr} values are considered as quantitative values representing the thermodynamic driving force for the corrosion or electrochemical process. As value of E_{corr}

increases, the tendency towards corrosion decreases. The i_{corr} values are attributed to the kinetics of corrosion. As shown in Fig.4.14 and Table 4.4., there is no change in i_{corr} values for the austenitized and tempered specimens indicating the electrochemical process are similar for the austenitized and tempered specimens during the corrosion process. The increase in i_{corr} values with tempering indicates that significant active dissolution has occurred on the specimen surfaces with tempering. The i_{corr} and i_{crit} value is minimum for austenitized specimen while i_{corr} and i_{crit} tend to increase with tempering temperature till 550 °C. However, when the tempering temperature is 550 °C, i_{corr} and i_{crit} are at maximum and thereafter it decreases (Fig.4.14.).

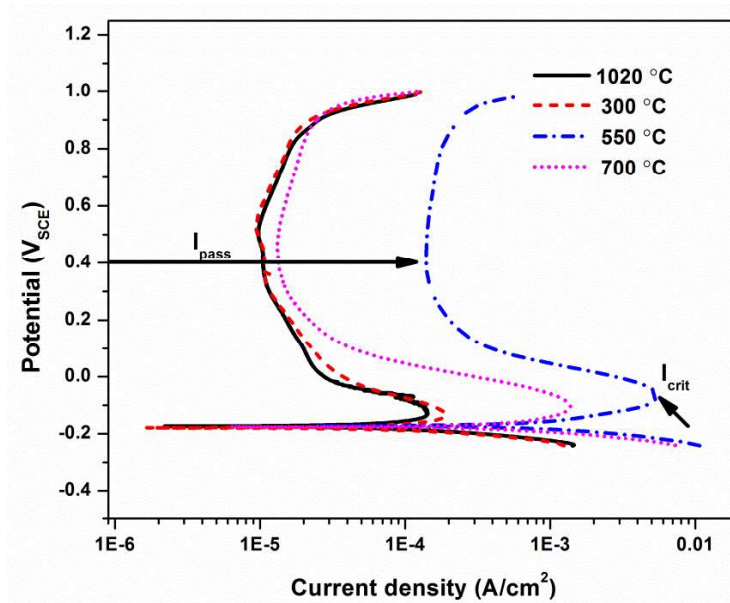


Fig. 4.14 Potentiodynamic polarization curves of austenitized and different tempered specimens in 5% HNO_3 solution.

The i_{corr} , i_{crit} and i_{pass} is the minimum for the austenitized specimen and maximum for the specimen tempered at 550 °C. The determination of the susceptibility of stainless steels to IGC using electrochemical measurements depends on the sensitivity of the polarization curve to the amount of Cr present in solid solution (Stanbury & Bachanan, 2000). The shift in polarization curve of tempered MSS to the larger peak current density values as compared to austenitized condition as

shown in Fig.4.14 indicates that the increase in measured current density is due to the presence of greater amount of Cr depletion at the lath interfaces or prior austenite grain boundaries. It is also reported that the shift in polarization curve of sensitized stainless steel (held at longer durations at sensitization temperature) to the larger current density values is either due to presence of greater amount of Cr depletion in the grain boundaries or consequent grain growth of the chromium-rich intergranular precipitates at these sensitization conditions (Zhao *et al.*, 2016, Lo *et al.*, 2011). But in the present study, the increase in current density is due to presence of narrow Cr-depletion zone of 7-9 nm associated with Cr-rich carbide precipitation in the specimen tempered at 550 °C (Fig. 3.8). The increase in i_{pass} and i_{crit} by an order of one decade for 550 °C tempered specimen as compared to austenitized condition and specimen tempered at 300 °C is related to the presence of greater amount of Cr depletion regions at martensite lath interfaces. Fig. 4.15 shows the SEM images of the austenitized and tempered specimens after polarization test in 5% HNO₃ solution. As shown in Fig. 4.15, the austenitized and specimen tempered at 300 °C did not show any attack along the martensitic lath interfaces but a few PAGBs showed attack along the grain boundaries. There is no Cr- rich carbide precipitation at lath interfaces or at the PAGBs for austenitized and tempered at 300 °C conditions (Figs. 3.6 - 3.7). The SEM images as shown in Fig. 4.15(b)-(c) show that the width of attack at the PAGB is more in the specimen tempered at 300 °C as compared to the austenitized specimen. The number of PAGBs attacked in the test is also more in the tempered specimen as compared to that in the austenitized condition. This might have led to a slight increase in i_{crit} of specimen tempered 300 °C. But none of the PAGB completely got attacked after polarization. The dissolution/attack in austenitized and 300 °C specimens occurred at the carbide-matrix interface as shown in Fig. 4.15(c) which is a magnified image of Fig. 4.15(a) and also at PAGBs. The i_{pass} value is almost the same for the austenitized and 300 °C tempered

specimens. Even though, the tempering at 300 °C lead to formation of nano-sized Fe-rich M₃C type inter and intra lath precipitates (shown in Fig. 3.7) but the effect of these precipitates on IGC or interlath corrosion was not observed in 5% HNO₃ anodic polarization tests as it only showed a slight increase in i_{crit} . The SEM examination of specimen tempered at 300 °C after polarization at higher magnifications showed no interlath attack, as shown in Fig. 4.14(c). This is due to the fact that the tempering treatments at these temperatures form fine precipitates of M₃C type Fe-rich carbides (M= Fe and Cr) but do not lead to an appreciable Cr depletion at the carbide-matrix interface regions. The specimen tempered at 550 °C showed the maximum i_{crit} and i_{pass} in anodic polarization as shown in Fig. 4.14 and Table 4.4.

Table 4.4 Potentiodynamic polarization test results for austenitized and specimens tempered at different temperatures in 5% HNO₃ solution.

Specimen condition	E_{corr} (V _{SCE})	i_{corr} (A/cm ² x 10 ⁻⁵)	i_{crit} (A/cm ² x 10 ⁻⁴)	i_{pass} (A/cm ² x 10 ⁻⁵)
Austenitized	-0.179	1.066	1.408	1.074
300 °C	-0.178	1.466	1.797	1.075
550 °C	-0.174	64.43	52.64	13.95
700 °C	-0.178	19.27	13.26	1.363

The SEM examination after the polarization test showed extensive attack at lath interfaces and also showed complete dissolution of some of the laths. The nature of corrosive attack is essentially interlath corrosion as shown in Fig. 4.15(d) and not IGC where the preferential attack is along the grain boundaries, leading to complete dislodgement of the grains into the solution. The formation of Cr-depleted zones can increase the ion transport and accelerates dissolution in tempered MSS during corrosion process. Fig. 4.15(d) shows the preferential attack along the martensitic lath

interfaces in specimen tempered at 550 °C after anodic polarization. These results are consistent with the results from TEM examination, as shown in Figs. 3.8(a) to 3.9(c). The carbides are formed along the interface of martensitic laths and the preferential attack is also observed along the lath-lath interfaces in 5% HNO₃ solution anodic polarization test, as shown in Fig. 4.15(d). The high i_{crit} and i_{pass} values observed for 550 °C, 2.5 h tempered condition is due to the attack by HNO₃ at both Cr depleted regions and it subsequently dissolving the chromium carbides. When the tempering temperature increased above 550 °C, i.e. to 700 °C, i_{crit} and i_{pass} values are decreased as shown in Fig.4.14 and Table 4.4. This could be due to Cr diffusion from the grain matrix to depleted regions. The higher current density in specimen tempered at 550 °C as compared to austenitized condition is due to the formation of less protective passive film and is shown and explained in subsequent results.

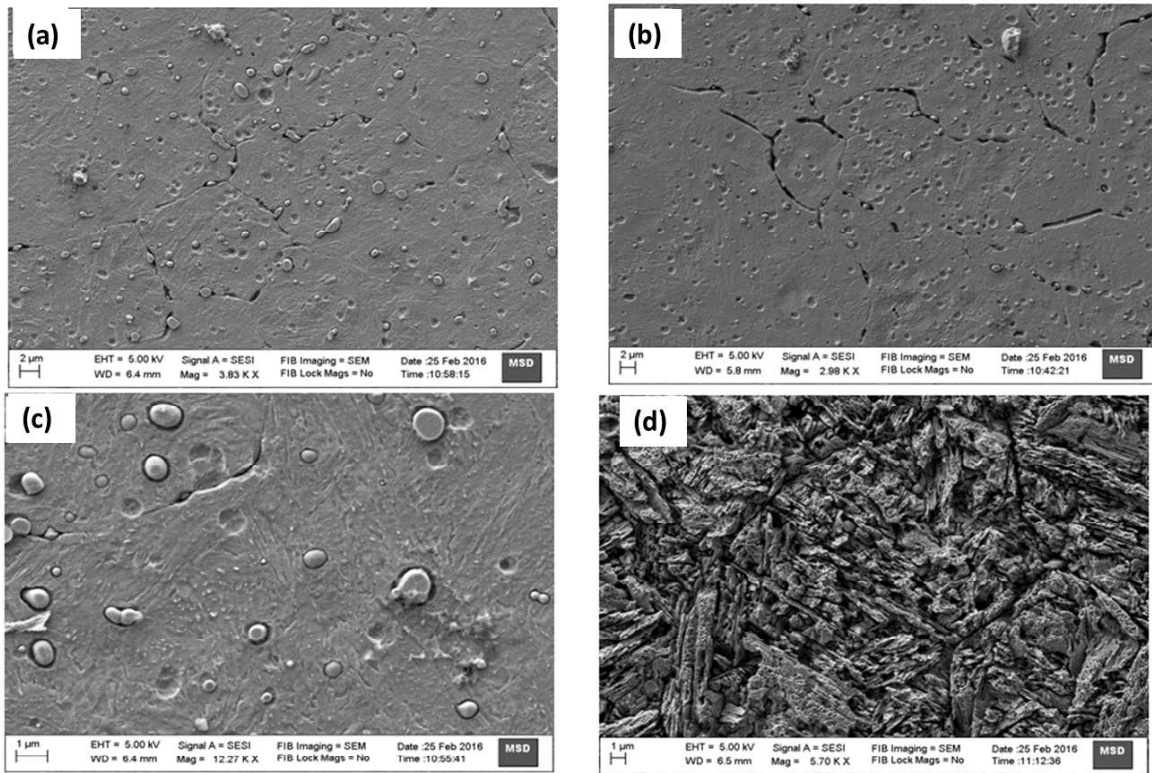


Fig. 4.15 SEM images of (a) austenitized, (b) tempered at 300 °C, (c) magnified view of (b) and (d) tempered at 550 °C for 2.5 h after potentiodynamic polarization in 5% HNO₃ solution.

4.3.5. Electrochemical impedance spectroscopy studies in 5% HNO₃ solution

Fig. 4.16(a)-(b) shows the Nyquist and bode plots of tempered specimens obtained after immersion in 5% HNO₃ solution at OCP. As shown in Fig. 4.16, the tempered specimens showed similar EIS spectra indicating the same mechanism of electrochemical process at OCP in 5% HNO₃ solution.

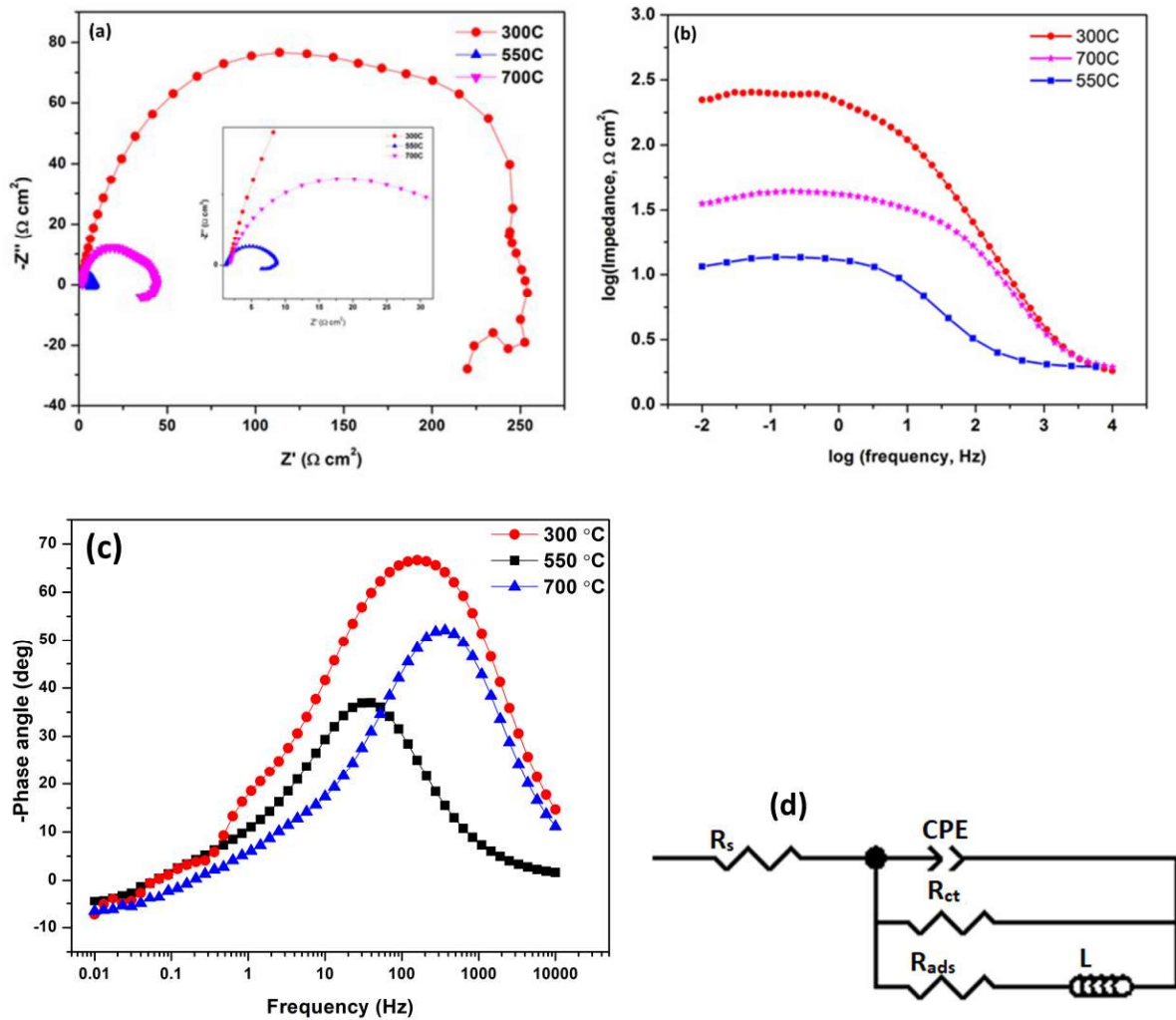


Fig. 4.16 EIS spectra of the 13wt.% Cr martensitic stainless steel in different tempered conditions in 5% HNO₃ solution at 25 °C, (a) Nyquist plot, inset of (a) shows the expanded view of specimen tempered at 550 °C, (b) bode impedance plot, (c) Bode phase angle plot and (d) Equivalent circuit used for fitting the experimental EIS data (Zhao et al., 2016, Behbahani et al., 2016).

The EIS spectra comprised of capacitive loop in the high frequency range and incomplete inductive loop in the low frequency range. The equivalent circuit used for fitting the experimental data was chosen from the reported literature (Zhao *et al.*, 2016, Behbahani *et al.*, 2016). In the equivalent circuit, R_s is the solution resistance, R_{ct} is the charge transfer resistance, CPE is constant phase element, represents the total capacitance of the double layer and the surface film, R_{ads} is the intermediate adsorption resistance and L is the inductance (Zhao *et al.*, 2016) represents transport of dissolution products in the partially protective oxide layer. The EIS fitted equivalent circuit elements are tabulated in Table 4.5. The goodness of the fit was high upto capacitance loop and the Chi square parameter (χ^2) value is less than 0.01 whereas χ^2 value is high for inductive loop fitting and is in the range of 0.1 to 0.05 for the fitted data. As suggested in literature, for the best fit, the Chi square parameter was reported to be less than 0.001. The inductive loop part of impedance data was not fitted well and has errors reaching 15 to 25%. The R_{ads} and inductance (L) values are used for comparative purpose.

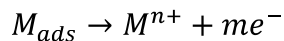
Table 4.5 Fitted results to the experimental EIS data of tempered specimens in 5% HNO_3 solution at corrosion potential at room temperature.

specimen	R_s	$CPE \times 10^{-4}$	n	R_{ct}	R_{ads}	L
	$\Omega \text{ cm}^2$	$F \cdot \text{cm}^{-2} \cdot \text{S}^{n-1}$		$\Omega \text{ cm}^2$	$\Omega \text{ cm}^2$	H cm^2
300 °C	1.76	2.81	0.76	297.6	936.7	16654
550 °C	1.92	0.37	0.78	11.96	35.8	318.9
700 °C	1.63	0.42	0.77	40.3	150.6	1662

Two-time constants are clearly observed for tempered specimens as shown by Nyquist and Bode-phase angle plots, as shown in Fig. 4.16. One time constant (R_{ct} - CPE) in the high frequency region is corresponding to capacitance loop (i.e charge transfer resistance associated with double layer

capacitance) and the other time constant in the low frequency region is corresponding to inductive loop ($R_{ads} - L$). The presence of an inductive loop in Nyquist plot is attributed to contribution from adsorbed species on corroding metal surface formed by corrosion process. The nature of the adsorbed species in stainless steels in acidic solutions are the ions of Fe as the Fe is the major element and also the other elements present in stainless steels (Orazem & Tribollet, 2008, Pardo *et al.*, 2008, Keddam *et al.*, 1986).

The two-time constants and formation of surface film on tempered specimens after impedance measurements in nitric acid solution suggest that the metal atoms (Fe & Cr) undergo anodic process producing n electrons and adsorbed species. The adsorbed species will cover certain amount of the surface and produce m electrons and metallic ions which go into the solution (Pardo *et al.*, 2008, Keddam *et al.*, 1986). The adsorbed species layer is considered as the precursor for protective passive film formation (Pardo *et al.*, 2008, Keddam *et al.*, 1986).



The R_{ct} , R_{ads} and L values are minimum for the specimen tempered at 550 °C compared to the specimens tempered at 300 and 700 °C (Table 4.5) indicating the higher desorption of the adsorbed species for 550 °C tempered condition. The R_{ads} and L values shown in Table 4.5 indicate that the surface film formed in HNO_3 solution is most protective for 300 °C followed by 700 °C, and then 550 °C. The alloying element responsible for passive layer formation in MSSs is Cr. The specimens tempered at 550 °C produced the nano-sized carbides with 7-9 nm of Cr depletion and is responsible for low R_{ct} , R_{ads} and L values. The increased values of R_{ct} and L for the specimen tempered at 700 °C, indicating desensitization behavior at tempering temperature of 700 °C. The EIS results obtained at OCP are also in line with the anodic polarization test results.

A black color film of corrosion products is observed on the specimen tempered at 550 and 700 °C after impedance measurements in 5% HNO₃ solution. A pale black colored film was formed on the specimen tempered at 300 °C. XPS analysis of the surface films was carried out to understand the changes in surface films formed at passive potential of 0.5 V_{SCE}.

4.3.6. Surface film formed in 5% HNO₃ solution at passive potential: XPS study

It is well known that the localized corrosion resistance of stainless steels reduces significantly if the solid solution Cr concentration falls below 11-12 wt.% The IGC of stainless steels is strongly dependent on passive film properties. The Cr concentration at the interface region of nano-sized Cr-rich carbide-matrix is around 9 wt.% in the specimen tempered at 550 °C as shown in Fig. 3.13(b) and hence these regions have a diminished ability to form the passive film and corrode preferentially. So XPS studies were carried out on the surface films developed on the austenitized (less susceptible to IGC) and tempered (at 550 °C, highly susceptible to IGC) conditions held potentiostatically at a potential of 0.5 V_{SCE} in 5% HNO₃ solution. The major elements observed in the XPS survey scan of the surface film formed on the austenitized and tempered at 550 °C specimen were C, O, Cr and Fe as shown in Fig. 4.17.

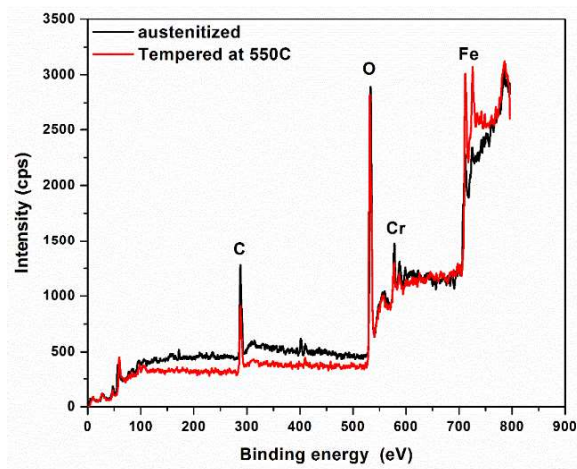


Fig. 4.17 XPS survey scan of the surface film formed on austenitized and specimen tempered at 550 °C at 0.5 V_{SCE} in 5% HNO₃ solution.

Table 4.6 shows the parameters for the deconvolution of the narrow XPS spectra with the possible chemical states and BE values used. The BE values for the chemical states reported in the Table 4.6 are within ± 1 eV of the literature reported BE values. Fig. 4.18(a)-(c) show high resolution XPS spectra of Fe 2p_{3/2}, Cr 2p_{3/2} and O 1s elements present in the surface film formed on austenitized condition. The Fe 2p_{3/2} spectrum composed of six peaks located at binding energies (BEs) of 706.1 eV, 707.2 eV, 709.6 eV, 710.9 eV and 712.8 respectively as shown in Fig. 4.18(a). These BEs are nearer/close to the BEs of metallic Fe, Fe-carbide, FeO, Fe₂O₃ and FeOOH respectively (Ghods *et al.*, 2011, Li *et al.*, 2015. Marcelin *et al.*, 2013). The peak at 715.1 is satellite peak of Fe²⁺. The decomposed Cr 2p_{3/2} spectrum consists of metallic Cr, oxide and hydroxides of Cr as shown Fig. 4.18(b). The BEs of the peaks are 573.9 eV, 576.5 eV and 578.5 eV respectively (Ghods *et al.*, 2011, Li *et al.*, 2015. Marcelin *et al.*, 2013). The decomposed spectra of O 1s showed oxide and hydroxide peaks with bound water as shown in Fig. 4.18(c). The peaks BEs are located at 530.2 eV, 531.9 eV, 533.6 eV respectively (Ghods *et al.*, 2011, Li *et al.*, 2015. Marcelin *et al.*, 2013). The XPS narrow spectrum of Fe, Cr and O shows that top layer surface film consists of oxides and hydroxides of Fe and Cr. The relative concentrations of the elements was estimated based on peak areas and sensitivity factors using the equations reported in (Fu *et al.*, 2009, Liu *et al.*, 2007) by considering the detected metallic elements are present at below the oxide layer and oxidized elements are part of the oxide layer and are given in Table. 4.6.

$$C_M^{OX} = \left(\frac{A_M^X}{S_M} \right) / (\sum A_i / S_i) \dots \dots \dots (4.1)$$

Where C_M is the atomic percentage, A_i is the peak intensity corresponding to the area of the element *i* in surface film (including metal, oxide and hydroxide), S_i is relative sensitivity factor of the corresponding element ‘*i*’. The value of S_M for Fe, Cr and O used in the present study are 10.82, 7.69 and 2.93 respectively (Fu *et al.*, 2009, Liu *et al.*, 2007). The relative Fe/Cr ratio of the surface

film was calculated from the ratio of atomic percentages of Fe to Cr present in oxide and hydroxides. The surface oxide film formed on the austenitized condition without any sputtering showed Fe/Cr ratio of 1.76, indicating the outer layer is enriched in Fe oxide and hydroxides.

Table 4.6 Parameters used for the deconvolution of the narrow XPS spectra with the main chemical species present in surface film formed in 5% HNO₃ solution.

Element	Chemical state	BE (eV)	FWHM ^a
Fe	Fe (0)	706.1	1.2
	Fe (carbide)	707.2	1.40
	Fe ²⁺ 2p _{3/2} (oxide)	709.1	2.8
	Fe ³⁺ 2p _{3/2} (oxide)	710.9	2.4
	Fe ³⁺ 2p _{3/2} (hydroxide)	712.8	2.7
Cr	Cr (0)	573.9	1.4
	Cr ³⁺ 2p _{3/2} (oxide)	576.5	2.4
	Cr ³⁺ 2p _{3/2} (hydroxide)	578.2	1.9
O	O ²⁻ 1s (oxide)	530.2	1.4
	OH ⁻ (hydroxide)	531.9	1.6
	O ²⁻ (water)	533.6	2.1

^aFWHM: full width at half maxima

Fig. 4.19(a)-(c) show high resolution XPS spectra of Fe 2p_{3/2}, Cr 2p_{3/2} and O 1s elements present in the surface film formed on austenitized condition after sputtering for 30 s. The metallic Fe peak intensity increased as shown in Fig. 4.19(a). The Fe/Cr ratio of the oxide film decreased to 1.16 after 30 s of sputtering. The changes in Fe/Cr ratio with sputtering time are given in Table 4.7. The

metallic Fe peak intensity increased after 30 s sputtering as compared to without sputtering as shown in Fig. 4.18(a) and Fig. 4.19(a) respectively.

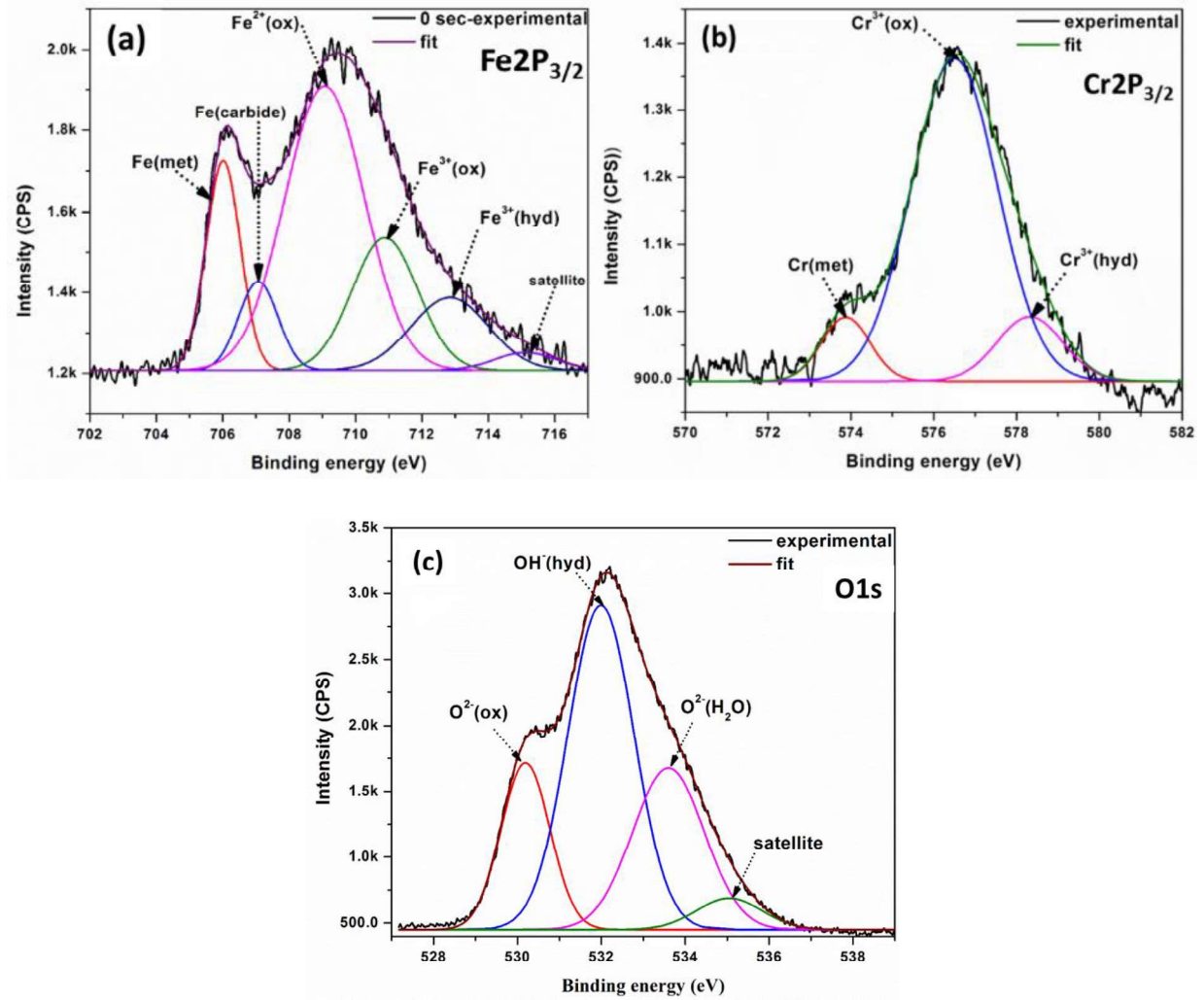


Fig. 4.18 High resolution XPS spectra of (a) Fe 2p_{3/2}, (b) Cr 2p_{3/2} and (c) O 1s element present in the surface film formed on austenitized condition in 5% HNO₃ solution without sputtering.

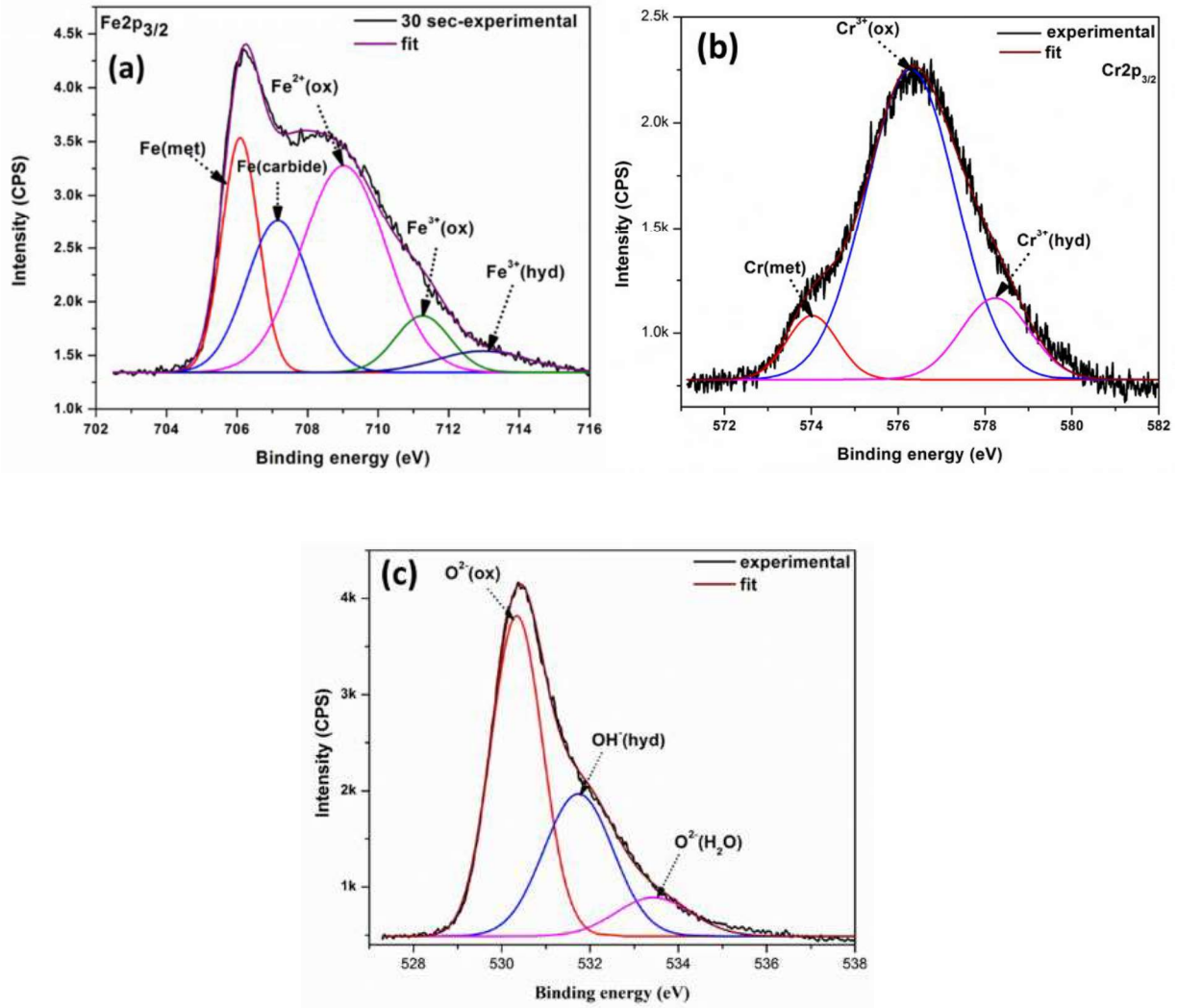


Fig. 4.19 High resolution XPS spectra of (a) Fe 2p_{3/2}, (b) Cr 2p_{3/2} and (c) O 1s element present in the surface film formed on austenitized condition in 5% HNO₃ solution after sputtering for 30 s.

As shown in Fig. 4.20, the surface film developed on 550 °C tempered condition also showed the similar chemical species to that of surface film formed on austenitized condition but with different atomic concentration of elements. The Fe/Cr ratio of the surface film with different sputtering times is calculated for 550 °C tempered condition and given in Table 4.7. For the same sputtering time from the surface film, the Fe/Cr ratio of the oxide film is higher for tempered condition as compared to the austenitized condition as shown in Table 4.7.

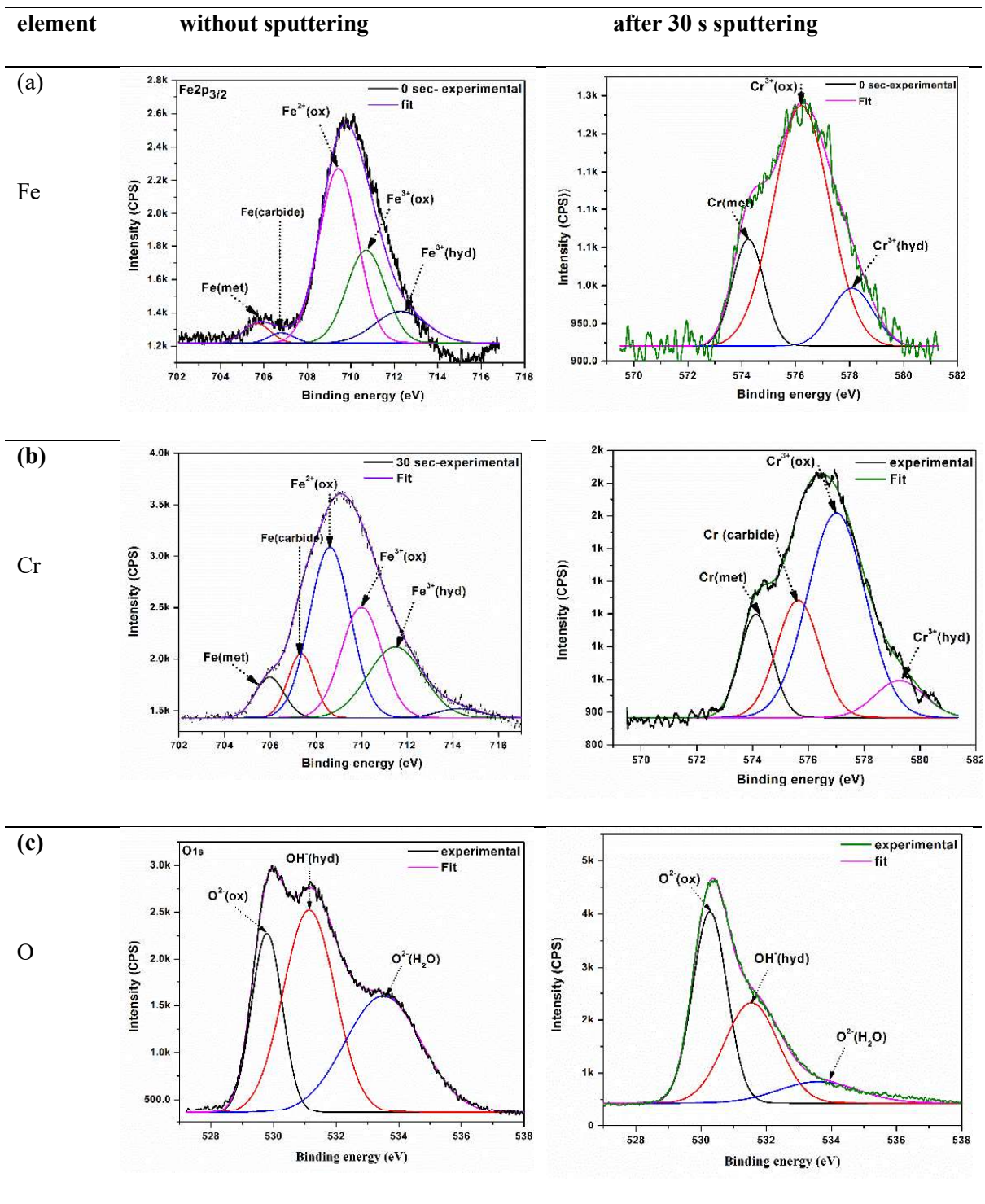


Fig. 4.20 High resolution XPS spectra of (a) Fe $2p_{3/2}$, (b) Cr $2p_{3/2}$ and (c) O $1s$ element present in the surface film formed on specimen tempered at $550\text{ }^{\circ}\text{C}$ condition in 5% HNO_3 solution without and after sputtering for 30 s.

Table 4.7 Fe/Cr ratio of the surface film formed in 5% HNO₃ solution with sputtering time.

Sputtering time (s)	Austenitized	Tempered at 550 °C
0	1.76	3.035
30	1.16	3.18
75	1.09	2.51
135	0.89	2.27

The surface film formed on austenitized condition showed an increase of Cr³⁺ (Cr₂O₃) peak intensity and decrease of Cr³⁺ (Cr(OH)₃) with sputtering time. The Fe³⁺ peak was observed upto a sputtering depth of 75 s and continuous decrease of Fe²⁺ peak intensity was observed with sputtering as shown in Fig. 4.21(a). The variation in atomic concentrations of Cr³⁺, Fe³⁺ and Fe²⁺ with sputtering time for austenitized condition is shown in Fig. 4.21(a). The Cr³⁺, Fe³⁺ and Fe²⁺ peak intensities (atomic concentration) increased up to a sputtering time of 75 s and after decreased with sputtering time for specimen tempered at 550 °C as shown in Fig. 4.21(b). As shown in Fig. 4.21(c), the Cr³⁺ (Cr₂O₃) atomic concentration of the surface film is higher for austenitized condition as compared to tempered condition at the same sputtering duration. The metallic Cr and Fe peak intensity increased with sputtering time for both austenitized and tempered conditions. The XPS spectra O 1s showed presence of oxides, hydroxides and bound water. The oxide peak intensity enhanced and hydroxide and bound water peak intensity weakened with sputtering time for both austenitized and tempered conditions as shown in Figs. 4.18 - 4.20.

The corrosion resistance exhibited by stainless steels is due to the presence of Cr (III) oxide-hydroxide layers in the surface film. The Cr is an important alloying element and forms insoluble Cr₂O₃ and also a continuous network of Cr-O-Cr-O which prevents the dissolution of Fe. The

electrochemical results showed decreased surface film resistance (Fig. 4.16) and increased i_{cirt} and i_{pass} values (Fig. 4.14 & Table 4.4) in 5% HNO_3 solution for the specimen tempered at 550 °C and is mainly due to the formation of less protective Fe-rich surface film. The decrease in Cr atomic concentration (Fig. 4.21(c)) or the high Fe/Cr ratio (Table 4.7) of the surface film formed on specimen tempered at 550 °C is due to massive carbide precipitation and associated Cr depletion in the matrix at this tempering temperature.

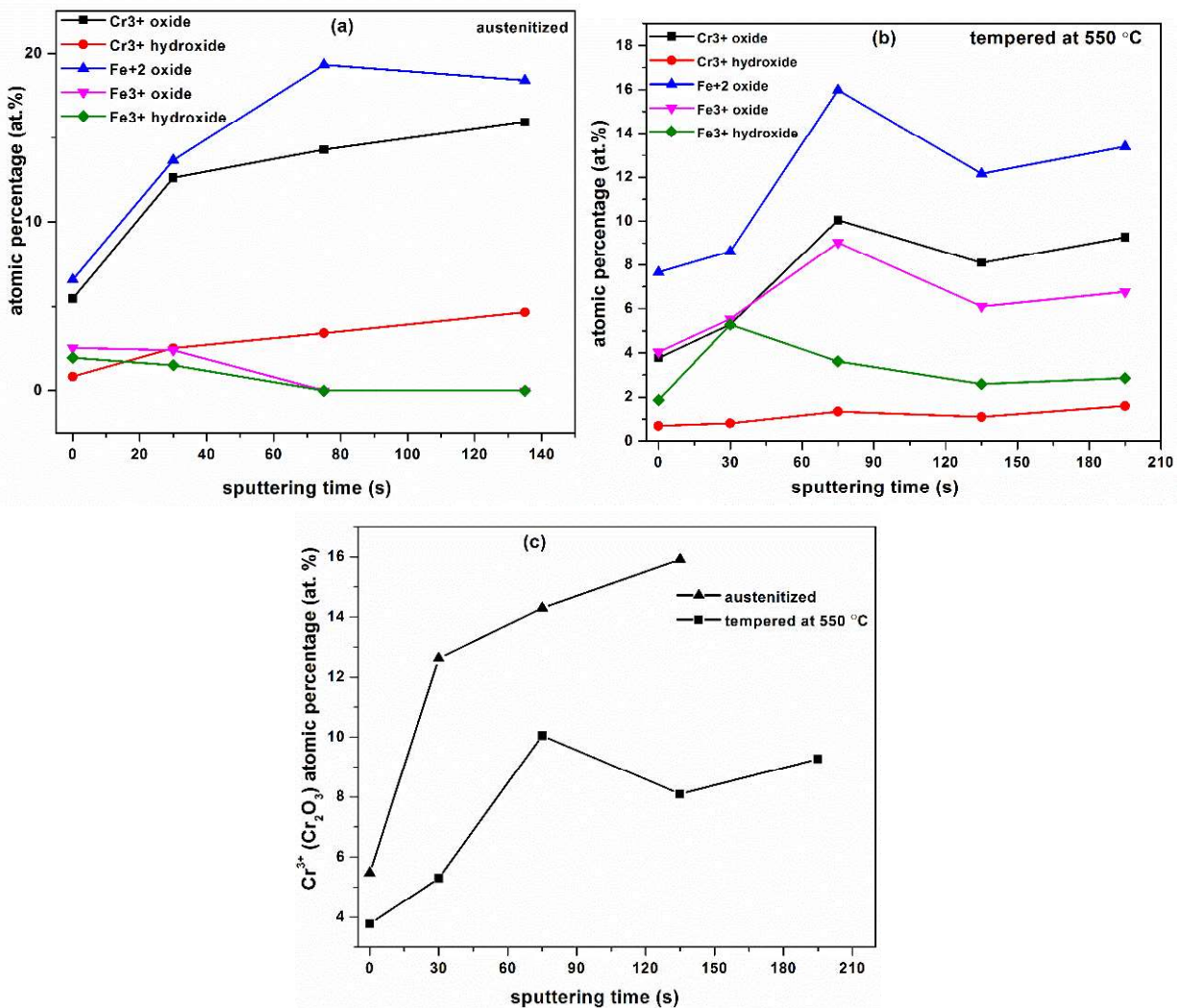


Fig. 4.21 Variation in atomic concentrations of Cr^{3+} , Fe^{3+} and Fe^{2+} chemical species in surface film formed in 5% HNO_3 solution with sputtering time: (a) austenitized and (b) tempered at 550 °C. (c) Cr^{3+} (Cr_2O_3) atomic concentration of the surface film formed on austenitized and tempered at 550 °C with sputtering time.

4.4 Highlights

The salient results obtained on IGC behavior of 13wt.% Cr MSS with different tempering treatments using immersion tests and electrochemical methods followed by characterization of tested/exposed surfaces by SEM, GI-XRD and XPS techniques are summarized below.

1. The nitric acid immersion test results indicated that the specimens tempered above 450°C were susceptible to interlath corrosion and the preferential attack was along the martensitic lath interfaces. IGC tests in nitric acid solution showed that a corrosion rate of more than 2.5 mm/y indicated intergranular attack while a rate lower than 2.5 mm/y indicated uniform corrosion for 13wt.% Cr martensitic stainless steel. The formation of chromium rich carbides at tempering temperatures higher than 450°C resulted in formation of chromium depletion regions adjacent to matrix/carbide interface. The location of the attacked regions was shown to be the interfaces of martensitic laths.
2. The second anodic current density peak in potentiodynamic polarization is shown to be due to the presence of chromium depletion and the current density at the second anodic peak was the maximum for the specimen tempered at 550 °C for 2.5 h indicating maximum degree of sensitization.
3. The 0.03 M sulfuric acid solution is shown to be suitable for measuring the DL-EPR values and DL-EPR results showed maximum DL-EPR value (88.2) for the specimen tempered at 550 °C for 2.5 h.
4. Cross-sectional examination of the specimen tempered at 550 °C for 2.5 h after DL-EPR tests showed that the first anodic potential peak during the forward scan corresponded to martensitic matrix dissolution whereas the second anodic potential peak during forward scan corresponded to preferential attack at the interfaces of laths. The maximum attack at

chromium depletion regions took place at potentials corresponding to the first peak during reactivation. The average depth of the EPR attack was shown to be around 4 - 5 μm and maximum width of the attack was around 400 to 600 nm on the specimen tempered at 550 $^{\circ}\text{C}$ for 2.5 h.

5. The DL-EPR test optimized in this study was able to clearly follow desensitization at tempering temperatures above 550 $^{\circ}\text{C}$ (for 2.5 h) and also at 550 $^{\circ}\text{C}$ for durations of 100 h and 500 h. The optimized parameters of DL-EPR test are: solution 0.03 M H_2SO_4 (deaerated), scan from OCP to +0.5 V_{SCE} and scan back to OCP at 100 mV/min. The desensitization effect was confirmed by 5% HNO_3 immersion tests. The DL-EPR values in 0.03 M sulfuric acid solution correlated well with immersion tests in 5% HNO_3 . DL-EPR values greater than 40 indicated susceptibility to IGC in the nitric acid test while DL-EPR values lower than 40 indicated uniform corrosion.
6. Potentiodynamic polarization studies in 5% HNO_3 solution also indicate the occurrence of sensitization after tempering. The surface films formed on specimen that were austenitized and that were austenitized and tempered at 550 $^{\circ}\text{C}$ consist of oxides and hydroxides of Fe and Cr. But the Fe/Cr ratio of the surface film is higher for the specimen tempered at 550 $^{\circ}\text{C}$ as compared to that for the austenitized condition for the same sputtering time.
7. The decreased intergranular corrosion resistance of the specimen tempered at 550 $^{\circ}\text{C}$ in nitric acid solution is attributed to the less protective, Fe-rich, surface film formation.

Influence of tempering treatments on pitting corrosion

5.1. Background

In general, pit nucleation occurs at the surface active sites/heterogeneities such as inclusions, precipitates and the regions with weak passive films (Sedriks, 1996, Adhe *et al.*, 1996, Vignal *et al.*, 2014, Palit *et al.*, 1993). The surface oxide film formed over Cr depleted regions (sensitized regions) is known to be weak (and not stable) therefore leads to preferential corrosion attack. Sensitization increases the susceptibility to localized corrosion due to the formation of the Cr-rich carbides and associated Cr-depletion at the carbide-matrix interface. Pitting corrosion of sensitized stainless steels has been shown to be dependent on the carbide interfaces and also the carbide interfaces having Cr depletion regions (Park *et al.*, 2005, Chandra *et al.*, 2013a, Kain *et al.*, 1989). The determination of pitting potential (E_{pit}) in chloride environment provides the material susceptibility to pitting corrosion.

Until now, a few studies are available on the pitting corrosion behaviour of MSS with different tempering treatments (Lu *et al.*, 2016, Lu *et al.*, 2015, Taji *et al.*, 2015, Qi *et al.*, 2017, Muller *et al.*, 2015). The microstructure of the 13wt.% Cr MSS after tempering treatment consist of tempered martensite and carbides. Pitting corrosion is a crucial issue for its performance due to the presence of carbides and associated Cr depletion after tempering. The corrosion resistance of the stainless steels is attributed to the thin, adherent passive film composed of Cr_2O_3 . The breakage

or rupture of the passive film exposes the underlying base material leading to localized corrosion. The composition of the passive film formed dependent on microstructure, environment and time of exposure. There are no reported studies on the nature of the passive films formed on tempered 13 wt.% Cr MSS and their influence on localized corrosion. Therefore, still the questions remain on how to relate microstructure (carbide precipitation and extent of Cr depletion at carbide matrix interface) and passive film properties with pit initiation in MSS with different tempering treatments.

Pitting corrosion studies were carried in 0.1M NaCl solution using electrochemical techniques and passive films formed at OCP were characterized by XPS. The relationship between type of the precipitates formed during tempering and pitting corrosion behaviour of 13 wt.% Cr MSS in NaCl solution is discussed. The present study brings out salient results on pitting corrosion of 13wt.% Cr MSS with tempering treatments and differences in surface film formed on austenitized and tempered conditions at OCP in 0.1M NaCl solution.

5.2. Experimental

5.2.1. Electrochemical measurements

All the electrochemical studies were carried out in a conventional three-electrode cell using a Pt foil as the auxiliary (counter) electrode, SCE as the reference electrode and the MSS specimen as the working electrode. The MSS specimen was provided an electrical contact from one side of the specimen and was set in a cold setting resin to expose the opposite side of the specimen. The electrical connection wire was insulated to avoid contact with the test solution. All the specimens were ground metallographically using emery papers with grit size up to 1200 and then mirror polished using 1 μm diamond paste before each electrochemical experiment. The specimens were cleaned with a soap solution, degreased in ethanol and dried in warm air. The contact regions

between the test specimen and the resin were covered with a lacquer to avoid presence of any crevice when exposed to the test solution. The 0.1 M NaCl solution was prepared using distilled water and reagent grade NaCl. The solution was deaerated for 45 min using Ar gas and then the working electrode was introduced into the cell. The Ar gas bubbling was continued during the experiment. All the specimens were cleaned cathodically at $-1 V_{SCE}$ for 2 min to remove the air formed oxide film after specimen's immersion into the solution. The potentiodynamic polarization tests were performed in 0.1 M NaCl solution at room temperature in deaerated condition. A scan rate of 1 mV/s was employed. After polarization tests, the tested specimens were examined using optical and field emission - scanning electron microscopy (FE-SEM; Carl Zeiss make). The potentiodynamic polarization tests were repeated twice for each specimen. The average and standard deviation (σ) was calculated from the set of three data points and reported in Table 5.1.

Potentiostatic polarization tests were also performed in 0.1 M NaCl solution to investigate the metastable pitting corrosion for MSS specimen tempered at different temperatures. The potentiostatic polarization tests were carried out at -100 mV below the E_{pit} expect for the specimen tempered at 550 °C, for which the test was carried out at 20 mV above the E_{corr} . The EIS studies were carried out in the frequency range of 0.01 to 10 kHz by super imposing sinusoidal potential of 10 mV amplitude at OCP using AUTOLAB potentiostat.

5.2.2. Surface film characterization by XPS

Rectangular coupons of the austenitized and specimens tempered at 550 °C were exposed in deaerated 0.1 M NaCl solution for period of 15 h and the formed surface film was characterized by XPS (SPECS) technique. After immersion in the test solution, the specimens were polarized at $-1 V_{SCE}$ for 2 min to remove any air formed oxide film. The XPS analyses were done similar to the procedure mentioned in Chapter 4, section 4.2.4. The major elements identified were Fe, Cr and O

with elemental C. High-resolution energy spectra were recorded for C 1s, Fe 2p, O 1s and Cr 2p peaks. All binding energies were referenced to the C1s peak at a binding energy of 284.6 eV. The baseline correction was done by Shirley method (Jung *et al.*, 2012, Ghods *et al.*, 2011) using Origin 8.5 software. The high resolution/narrow XPS spectra of the individual element is separated into the most probable chemical states using the deconvolution method of the peaks using Origin 8.5 software with an optimum number of the peaks.

5.3. Results and Discussion

5.3.1. Electrochemical results in chloride solution

5.3.1.1. Potentiodynamic polarization

The potentiodynamic polarization curves for various tempering temperatures in 0.1 M NaCl solution are shown in Fig. 5.1. The significant changes in polarization curves are decrease in E_{pit} , E_{corr} and increase in passive current density with tempering temperature. The E_{corr} and i_{corr} are measured from Tafel analysis and E_{pit} was measured from the potential when the current density starts to increase from the value of current density corresponding to the passive region and these values are given in Table. 5.1. As shown in Fig. 5.1, the austenitized condition has a higher (more anodic) E_{corr} as compared to tempered conditions and the E_{corr} decreased (or became more cathodic) with tempering temperature. The low value of E_{corr} for the specimens tempered at 550 and 700 °C, indicates a higher tendency towards oxidation. The i_{corr} values as shown in Table 5.1 also show that the specimen tempered at 550 °C has a higher dissolution rate (corrosion rate, i_{corr}) than that for the austenitized and other tempered conditions indicating that the passive film formed at E_{corr} is less compact and less stable (Zheng *et al.*, 2012, Lv *et al.*, 2016, Kim *et al.*, 2015). The austenitized specimen showed highest E_{pit} and E_{pit} values decreased with tempering temperature. The passive current density also increased with tempering temperature indicating the dissolution

of the passive film is higher for tempered specimens as compared to austenitized condition with application of anodic potential. The specimen tempered at 550 °C showed increased current density with increase of anodic potential as shown in Fig. 5.1 and did not show passivity.

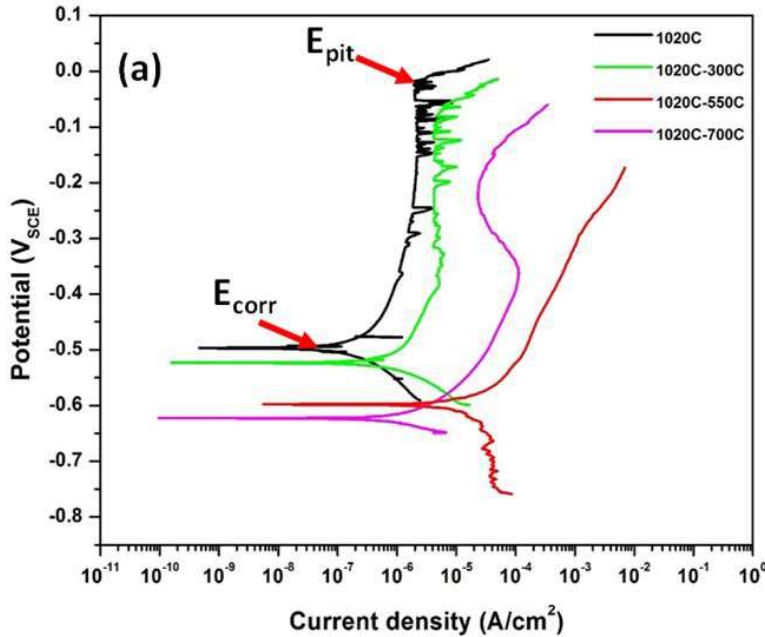


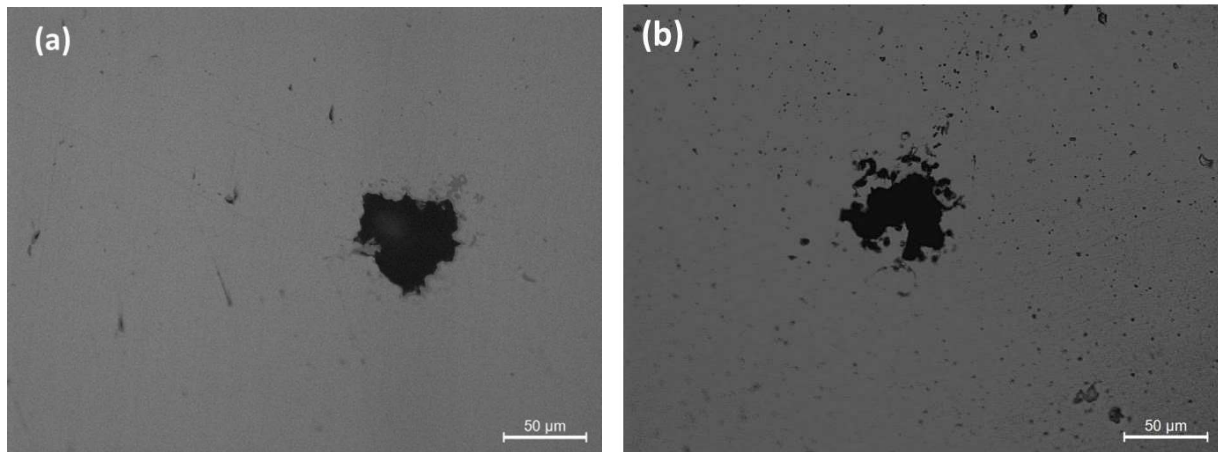
Fig. 5.1 Potentiodynamic polarization curves of austenitized and different tempered specimens in 0.1 M NaCl solution.

The E_{pit} of the specimen tempered at 550 °C is taken to be E_{corr} in this work as pitting occurred quite early and shown in Table 5.1. The E_{pit} value increased for the specimen tempered at 700 °C compared to that for the specimen tempered at 550 °C. The similar behaviour of decrease in current density is also observed for the specimen tempered at 700 °C as shown in Fig. 5.1 and Table 5.1.

Table 5.1 Potentiodynamic polarization test results for austenitized and specimens tempered at different temperatures in 0.1 M NaCl solution.

Specimen condition	E_{corr} (V _{SCE})	i_{corr} (A/cm ² x 10 ⁻⁶)	i_{pass} (at -0.35V) (A/cm ² x 10 ⁻⁶)	E_{pit} (V _{SCE})
1020°C	-0.460 ± 0.033	0.24 ± 0.16	1.54 ± 0.64	-0.051 ± 0.031
1020°C-300°C	-0.557 ± 0.037	0.38 ± 0.13	3.59 ± 1.45	-0.080 ± 0.015
1020°C-550°C	-0.585 ± 0.032	7.22 ± 4.14	No passivation	-0.585 ± 0.032
1020°C-700°C	-0.591 ± 0.026	8.59 ± 1.79	93.76 ± 10.80	-0.152 ± 0.041

The morphology of the largest pits on austenitized and tempered specimens after polarization is shown in Fig. 5.2. The specimen tempered at 550 °C for 2.5 h showed larger diameter pits as compared to the other conditions as shown in Fig. 5.2(c). Fig. 5.3(a) shows the SEM image of the specimen tempered at 550 °C after the polarization test in 0.1M NaCl solution. Pits with sizes up to 100 μm were also seen after the polarization test as shown in Fig. 5.3(a). The lath interfaces and PAG boundaries of the specimen tempered at 550 °C with nano and sub-micron sized carbides got attacked during the test and are the preferential sites for pitting corrosion as shown in Fig. 5.3(a).



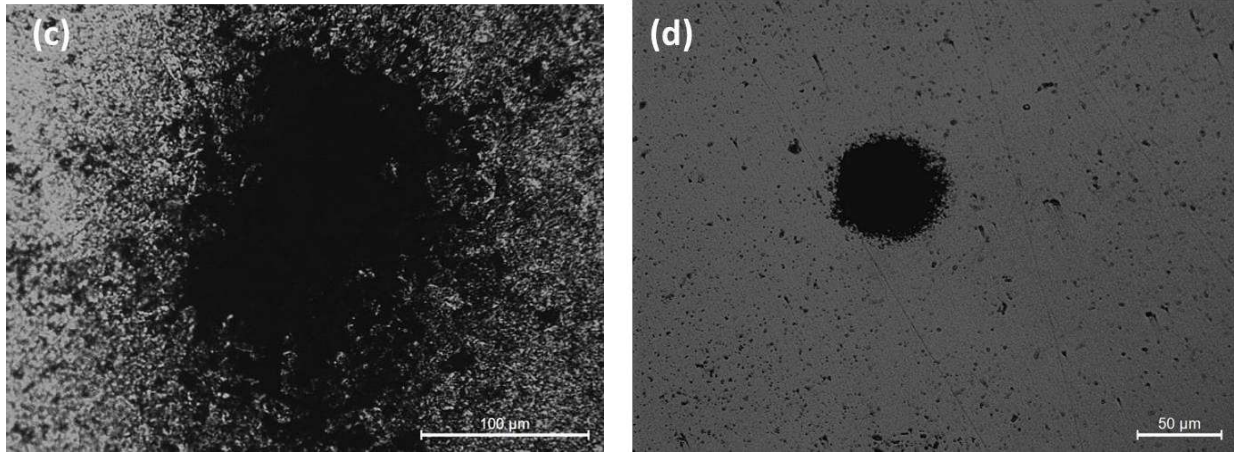


Fig. 5.2 Optical images showing the pit morphology of (a) austenitized condition, (b) tempered at 300 °C, (c) tempered at 550 °C and (d) tempered at 700 °C.

The magnified image of Fig. 5.3(a) clearly shows the pit initiation around the undissolved Cr-rich $M_{23}C_6$ carbide-matrix interface as shown in Fig. 5.3(b). The TEM-EDS analysis at the undissolved Cr-rich $M_{23}C_6$ carbide-matrix interface showed average Cr concentration of 9 wt.% showing the region around the undissolved Cr-rich carbide is also depleted of Cr (Fig. 3.14). It is already shown in the austenitic stainless steels that the Cr depleted regions adjacent to the grain boundary Cr-rich carbides/sigma phase act as a discontinuity and also the chemical changes in the interface region influence the stability of the passive film and so, these locations are preferential sites for the pit initiation (Kain *et al.*, 1989, Chandra *et al.*, 2013a, Sunil Kumar *et al.*, 2013, Aquino *et al.*, 2009). Kain *et al.* reported that the desensitization in 304 stainless steel improved the IGC but showed decreased pitting corrosion resistance compared to solution-annealed condition. But the pitting corrosion resistance improved as compared with the sensitized condition (Kain *et al.*, 1989).

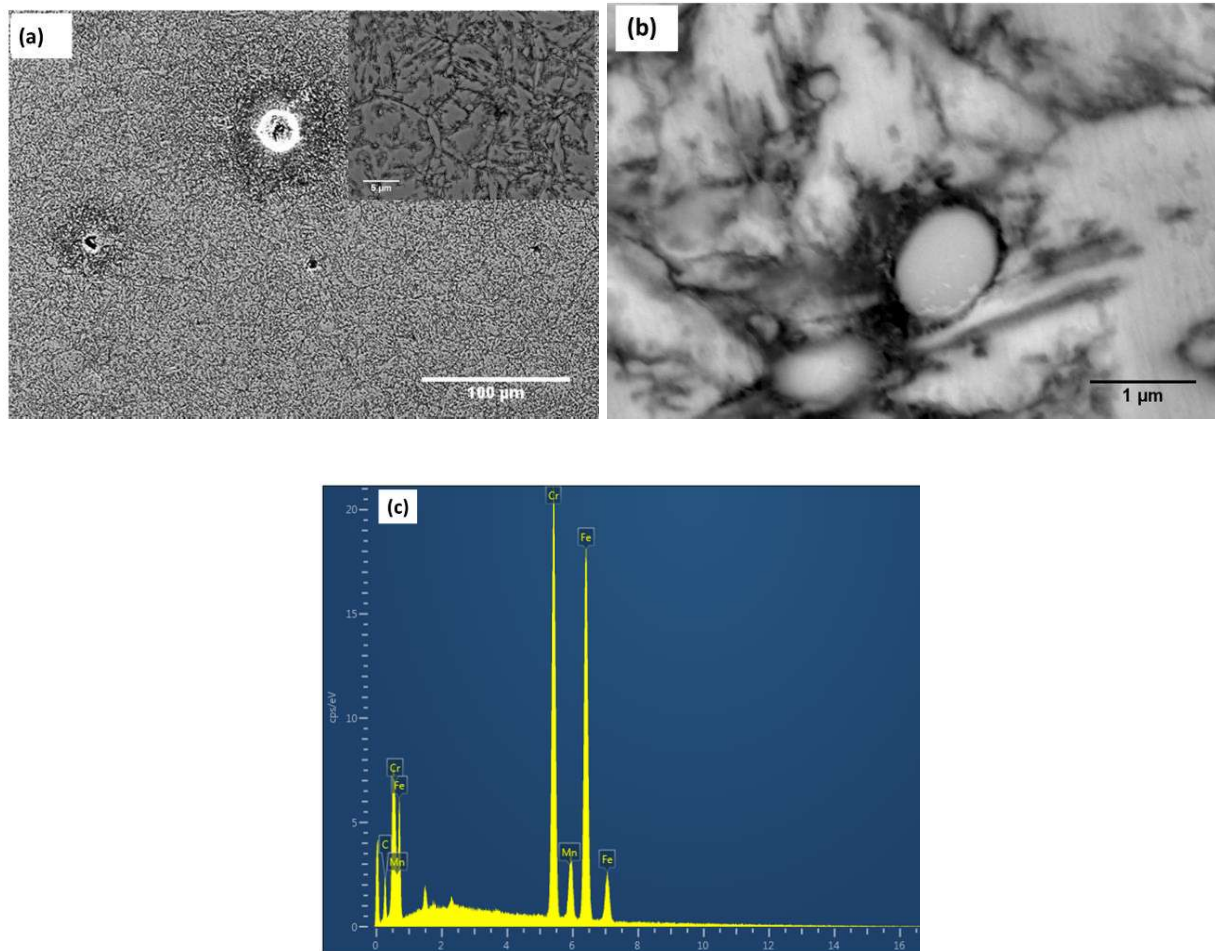


Fig. 5.3 (a) SEM image of the specimen tempered at 550 °C after polarization test (inset showing attack at PAG boundaries and laths), (b) magnified image of (a) showing pitting at undissolved carbide-matrix interface region and (c) SEM-EDS analysis showing the undissolved Cr- rich carbide.

Therefore, the presence of Cr-depletion at carbide-matrix interface region, further decreases the pitting corrosion resistance. The Cr content in these MSSs is around 13 wt.% and any depletion of the Cr content ($< 11\%$) at the interfaces would lead to weak passive film formation that makes easy chloride ion penetration and acts as a preferential site for pit nucleation in a chloride solution. The E_{pit} value is higher for the specimen tempered at 700 °C as compared to that for the specimen tempered at 550 °C, as shown in Fig. 5.1. The specimen tempered at 550 °C has more numbers of pit initiation sites due to massive precipitation of nano-sized carbides with Cr-depletion at lath

interfaces and also inside the laths as compare to specimen tempered at 700 °C with sub-microscopic carbides mostly at lath interfaces (Figs. 3.8 & 3.9). This indicates that the pitting resistance is associated with the number of pit initiation sites (carbides) and also the extent of Cr-depletion around these carbides. The increased value of the E_{pit} for the specimen tempered at 700 °C, as compared to tempering done at 550 °C, is due to the diffusion of the Cr to the depleted regions and thereby healing the Cr depletion zone (desensitization) and also decrease in number of pit initiation sites (carbides) by carbide coarsening at 700 °C. The phenomenon of desensitization at tempering temperatures higher than 550 °C is already shown in Fig. 4.10. The E_{pit} value of the specimen tempered at 700 °C is low as compared to austenitized and tempered condition at 300 °C because of increased fraction of carbide precipitate-interface regions which act as a site for pit initiation. The decrease in the pitting corrosion resistance with tempering treatments is due to the formation of Cr-rich carbides and the associated narrow Cr depletion zone with carbide formation.

5.3.1.2 Potentiostatic polarization

The potentiostatic static polarization studies were carried out to correlate the pit initiation frequency with the pit initiation sites i.e carbide –matrix interfaces in tempered MSS. The current fluctuations in Fig. 5.1, e.g. specimen tempered at 300 °C, are due to initiation and repassivation of metastable pits. Fig. 5.4(a) shows the current transients for metastable pit initiation for austenitized specimen and specimens tempered at 300 and 700 °C. The current transients or spikes due to pit initiation/repassivation are laid-over the background (passive) current density, as shown in Fig. 5.4(a). The sudden increase in current (spikes) is associated with passive film breakdown process happening in the event of metastable pit formation. As shown in Fig. 5.4(a), each current transient shows metastable pit. Many current transients or metastable pit events are observed

before a stable pit formation. The metastable pits may grow into stable pits if pit depth is sufficient enough to maintain the environment that is aggressive enough to prevent repassivation at the metal surface inside the pit (Burstein *et al.*, 2001, Jung *et al.*, 2012). The duration for pit initiation and repassivation is in the range of the 8 to 42 s and showed a statistical variation. The shape of the current transient gives the information about the initiation, growth and repassivation of a metastable pit (Aghuy *et al.*, 2015) and typical metastable pitting event is shown in Fig. 5.4(b). Fig. 5.4(c) shows the metastable pitting events with time.

The austenitized and specimen tempered at 300 °C showed less number of current transients and stable pitting is not observed in the tested duration of 3 h. The specimen tempered at 700 °C, showed metastable pits before a stable pit formation and stable pit (continuous increase in the background current density) with time as shown in Fig. 5.4(a). Stable pit formation is observed after 1.2 h duration of the test. The specimen tempered at 550 °C showed increased current density with time after application of potential (20 mV_{E_{corr}}) and showed stable pitting within 5 min of the test as shown in Fig. 5.4(d). The specimen tempered at 300 °C with Fe-rich carbide precipitates did not show the stable pit in the tested duration but the specimens tempered at 550 and 700 °C with Cr-rich carbides showed the stable pit formation in potentiostatic tests. The potentiostatic polarization results clearly showed that the metastable pitting events/frequency increased with increase of carbide-matrix interface regions with Cr depletion at the interface. The results indicate the fact that the nucleation and initiation of pitting corrosion depends on Cr depletion associated with Cr-rich carbide precipitation at the grain and lath boundaries in the MSS. The possible reason for improved pitting corrosion resistance for the specimen tempered at 700 °C is re-diffusion of Cr from the matrix to depleted regions thereby minimizing the discontinuity at the interfacial regions.

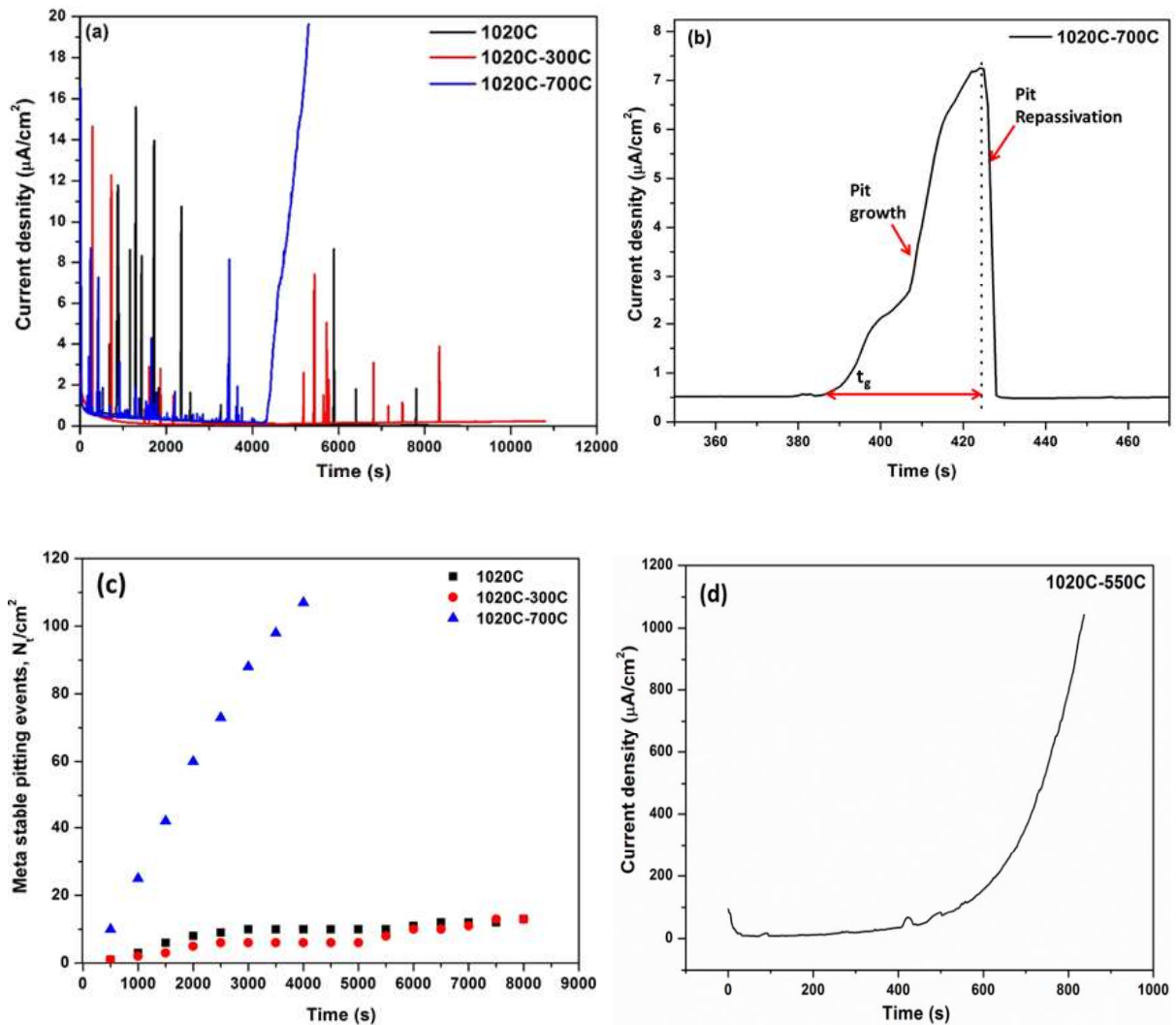


Fig. 5.4 Potentiostatic polarization on austenitized and specimens tempered at 300 and 700 °C in 0.1M NaCl solution (a) showing current transients from meta stable pitting with time, (b) typical current transient showing the pit growth and repassivation, (c) meta stable pitting events with time and (d) potentiostatic polarization of specimen tempered at 550 °C in 0.1M NaCl solution at 20 mV above E_{corr} .

5.3.1.3 Electrochemical impedance spectroscopy

The impedance for austenitized and tempered specimens was recorded at OCP after 30 min immersion in 0.1M NaCl solution to investigate the relative stability of the surface film. Figs. 5.5(a)-(b) shows the Nyquist and Bode plots of the austenitized and tempered specimens respectively.

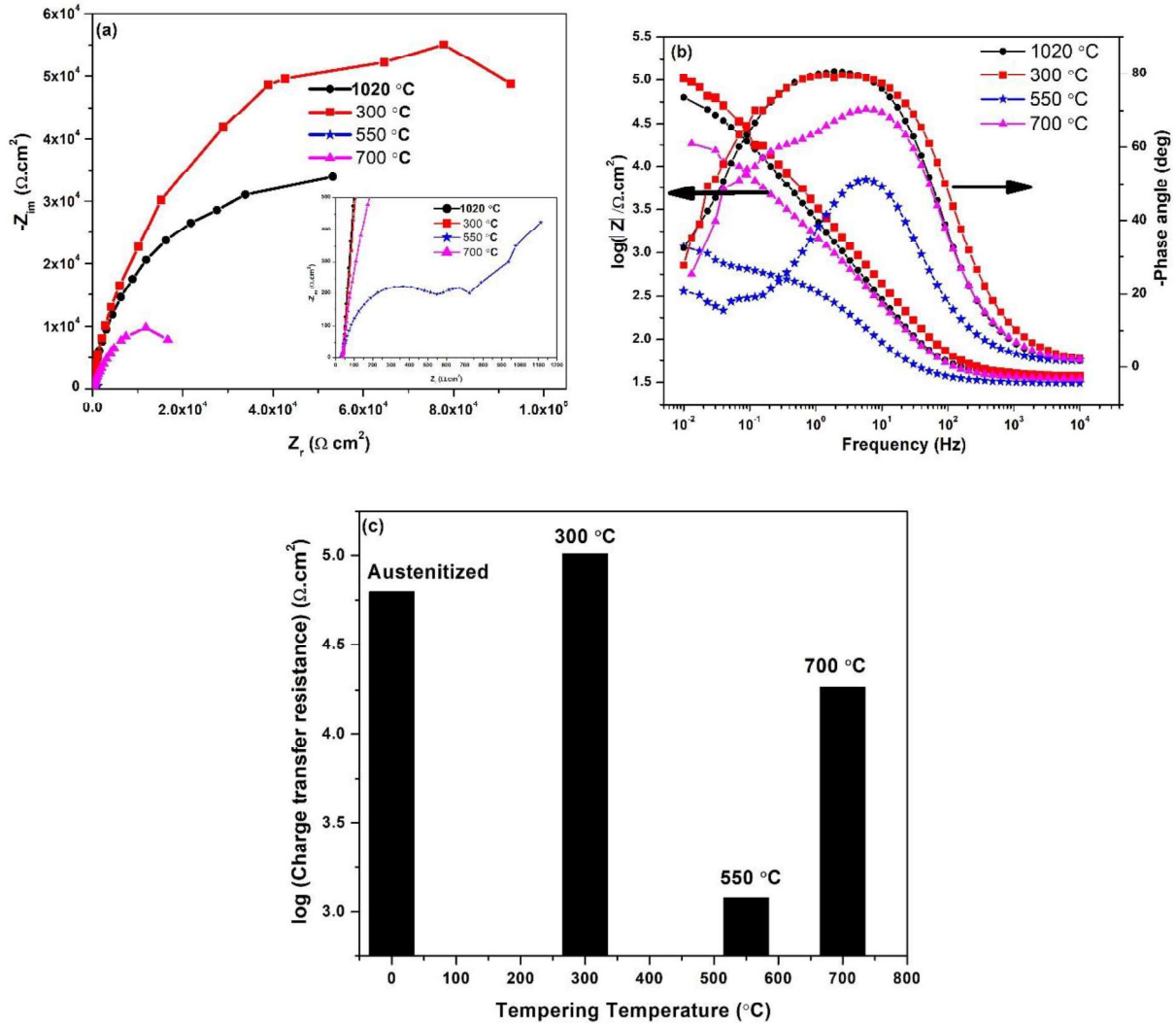


Fig. 5.5 (a) Nyquist, (b) Bode plot and (c) polarization resistance plots for austenitized and tempered specimens recorded at OCP.

The impedance value was drastically decreased for specimen tempered at 550 °C as shown in Fig. 5.5(c) as compared to other tempered conditions and austenitized condition, indicating a surface film formed has low polarization resistance. The impedance value is higher for specimen tempered at 300 °C than the austenitized condition. The impedance value is increased for specimen tempered at 700 °C as compared to 550 °C showing the surface film has increased polarization resistance than 550 °C condition as shown in Fig. 5.5(c). The EIS results also support the anodic polarization

and potentiostatic polarization results showing the specimen tempered at 550 °C is having high susceptibility to pitting corrosion.

5.3.2 Surface film characterization by XPS

The passive film formed on the surface of the stainless alloys plays an important role in initiation of pitting corrosion (Stansbury & Buchanan, 2000, Burstein *et al.*, 2001). The composition of the passive films formed at corrosion potential in 0.1M NaCl solution on austenitized specimen and after tempering at 550 °C were determined by XPS analysis. The XPS survey scan showed that the film consists of elements of Fe, Cr and O. The chloride and nickel are not observed in the film's XPS survey scans in both the conditions. Fig. 5.6(a)-(c) and Fig. 5.7(a)-(c) show high resolution XPS spectra of Fe 2p_{3/2}, Cr 2p_{3/2} and O 1s elements present in the film formed on austenitized and tempered at 550 °C conditions respectively. The XPS spectra of individual elements is deconvoluted into optimum number of peaks based on their binding energies. The Fe 2p_{3/2} spectrum composed of four peaks located at binding energies (BEs) of 706.8 eV, 708.8 eV, 710.6 eV and 712.6 eV respectively as shown in Fig. 5.6(a) & Fig. 5.7(a).

These BEs are nearer/close to the BEs of metallic Fe, FeO, Fe₂O₃ and FeOOH respectively (Ghods *et al.*, 2011, Li *et al.*, 2015. Marcelin *et al.*, 2013). The decomposed Cr 2p_{3/2} spectrum consists of metallic Cr, oxide and hydroxides of Cr as shown Fig. 5.6(b) & Fig. 5.7(b). The BEs of the peaks are 573.9 eV, 576.4 eV and 577.8 eV respectively (Ghods *et al.*, 2011, Li *et al.*, 2015. Marcelin *et al.*, 2013). The decomposed spectra of O 1s showed oxide and hydroxide peaks with bound water as shown in Fig. 5.6(c) & 5.6(c). The peaks BEs are located at 530.1 eV, 531.8 eV, 533.7 eV respectively (Ghods *et al.*, 2011, Li *et al.*, 2015. Marcelin *et al.*, 2013). In both the conditions, the film consists of oxides and hydroxides of Fe and Cr. The presence of the metallic Fe and Cr in the XPS spectra indicates that the films formed on the austenitized specimen and on specimen

tempered at 550 °C conditions are thinner than the XPS analysis depth which is about 10 nm (Gillard *et al.*, 2015).

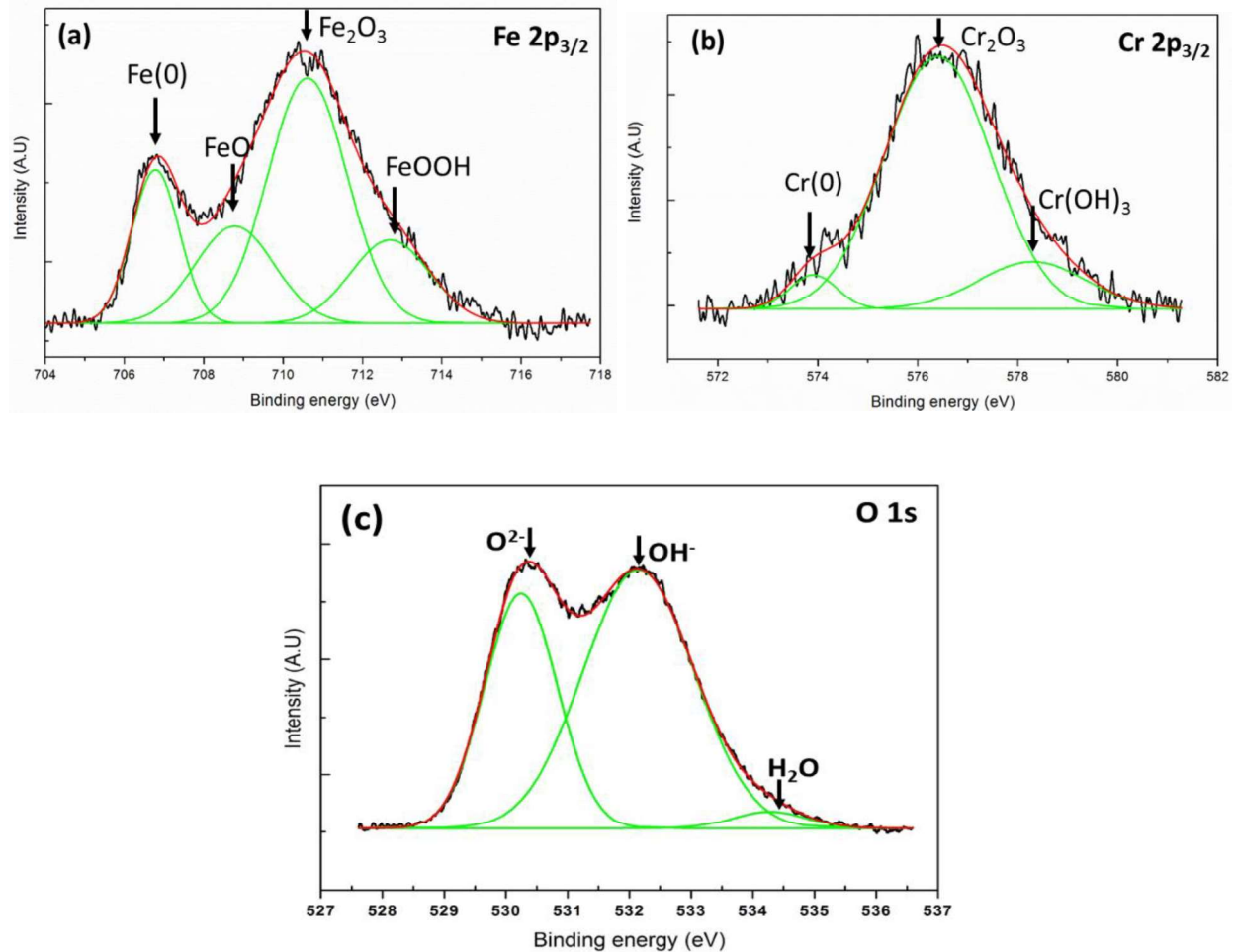


Fig. 5.6 Experimental and fitted narrow XPS spectra of (a) Fe 2p_{3/2}, (b) Cr 2p_{3/2} and (c) O 1s of the surface film formed on austenitized specimen in 0.1 M NaCl solution at OCP.

The atomic concentrations of elements in the passive film are calculated based on peak areas and sensitivity factors using the equations reported in (Fu *et al.*, 2009, Liu *et al.*, 2007). The quantitative XPS analysis showed the differences between the films formed on austenitized and tempered conditions. Fe/Cr ratio for tempered condition is 4.1 whereas the ratio for austenitized specimen is 1.5. This shows that the passive film formed on tempered condition of MSS is enriched in Fe and on austenitized condition is enriched in Cr. The lower Cr content in the passive film of

tempered condition is attributed to massive precipitation of Cr-rich carbides during tempering treatment at 550 °C which led to decrease in Cr content in the matrix which is an important element influencing the passive film properties.

As shown in the potentiostatic polarization test results (Fig. 5.4), passive (background) current density values are very high for specimen tempered at 550 °C as compared to other tempered and austenitized conditions indicating higher dissolution rates for the specimen tempered at 550 °C in 0.1 M NaCl solution. As shown in Fig. 5.6(c) & Fig. 5.7(c), the hydroxide peak intensity is higher than the oxide peak intensity in tempered condition with hydroxide/oxide ratio of 2.8 where the hydroxide to oxide ratio for austenitized condition is 1.7. The film formed in tempered condition is rich in hydroxide i.e. Fe-hydroxide (Fe/Cr: 4.1) as compared to that formed on austenitized condition. The metallic contribution is also quite high in the tempered condition as compared to austenitized condition indicating film formed on tempered condition is thinner than the austenitized condition at E_{corr} . It is reported that the thicker hydroxide films give better pitting resistance in chloride environment than the thin passive hydroxide films (Phadnis *et al.*, 2003). The less protective and thin Fe-rich hydroxide on the tempered condition is the reason for its lower film resistance in compared to that formed on austenitized condition. The higher i_{corr} value at E_{corr} , increased current densities with application of anodic potential in the potentiodynamic and potentiostatic polarization tests (Fig. 5.1 & Fig. 5.4) of tempered condition at 550 °C also show that the surface film is less protective and easy penetration of chloride ions increases the susceptibility to pitting. The local breakage of the passive film by chloride ions exposes the underlying base metal to the environment and leads to accelerated corrosion. The above results support the suggestion that tempering of 13 wt.% Cr MSS should be done at 700 °C as it also provides resistance to pitting corrosion.

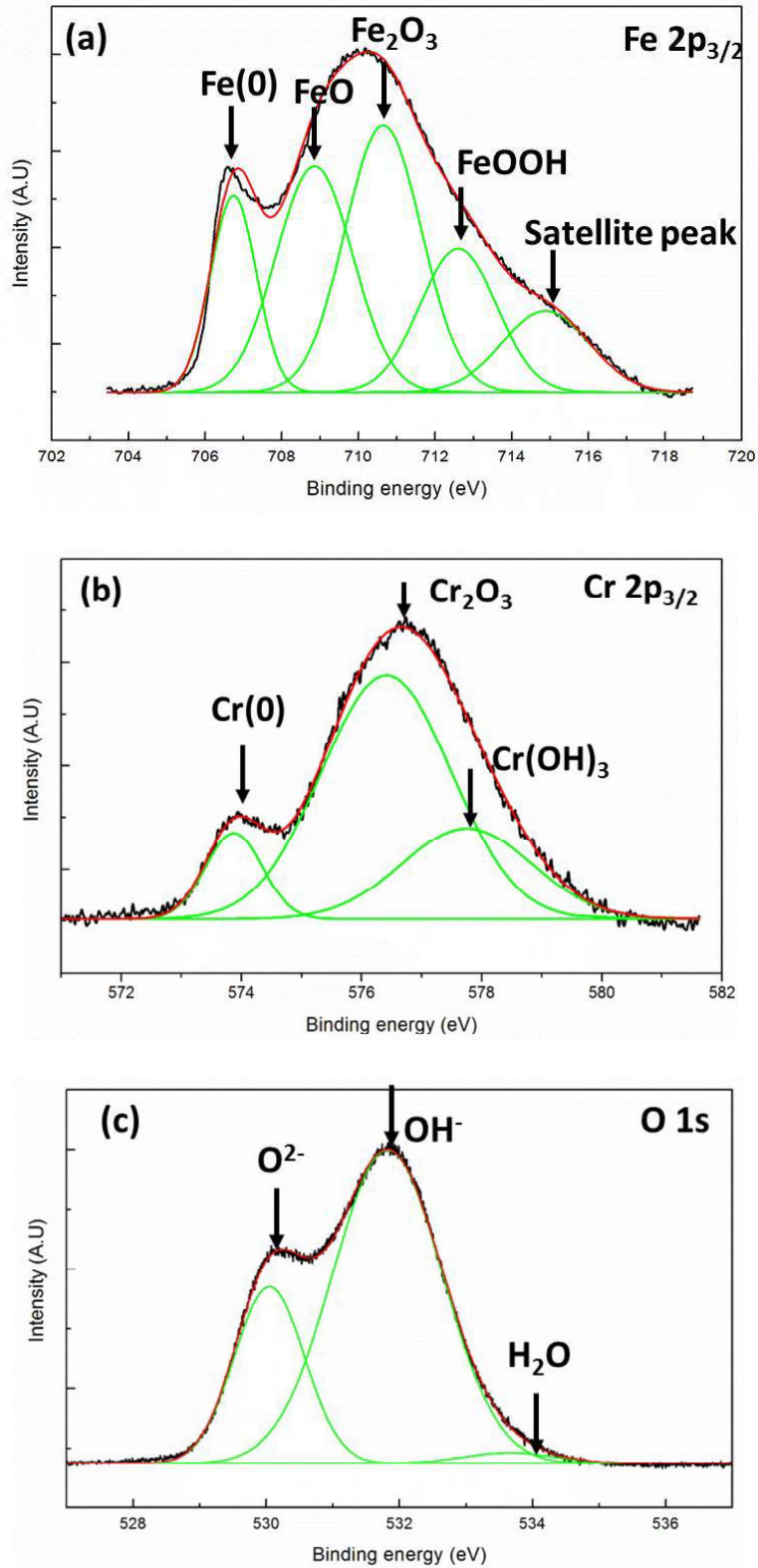


Fig. 5.7 Experimental and fitted narrow XPS spectra of (a) Fe 2p_{3/2}, (b) Cr 2p_{3/2} and (c) O 1s of the surface film formed on specimen tempered at 550 °C in 0.1 M NaCl solution at OCP.

5.4. Highlights

The effect of tempering temperature on pitting corrosion of 13wt.% Cr MSS was investigated using electrochemical techniques followed by surface film characterization by EIS and XPS. The results are correlated with microstructural changes occurred with tempering and some salient results which are highlighted in the present work are summarized as follows:

1. Tempering decreased the pitting potential and increased the metastable pitting. Especially tempering at 550 °C made 13 wt.% Cr MSS highly prone to pitting corrosion in 0.1 M NaCl solution. The pits initiated at the carbide-matrix interface region in the 550 °C tempered condition due to the presence of Cr depletion regions associated with massive Cr-rich carbide precipitation.
2. The E_{pit} value is higher for the specimen tempered at 700 °C as compared to that for the specimen tempered at 550 °C and the possible reason is re-diffusion of Cr from the matrix to depleted regions thereby minimizing the discontinuity at the interfacial regions.
3. The polarization resistance is drastically decreased for specimen tempered at 550 °C as compared to 700 °C and 300 °C tempered conditions showing weak surface film formation in chloride solution.
4. The passive film formed at corrosion potential is enriched with iron species in 550 °C tempered condition whereas chromium enriched passive film is formed in austenitized condition. The less protective passive film formed on MSS tempered at 550 °C at corrosion potential increased the corrosion current density and also showed no passivity in 0.1M NaCl solution above corrosion potential.
5. The above results support the suggestion that tempering of 13 wt.% Cr MSS should be done at 700 °C as it also provides resistance to pitting corrosion.

Temper and hydrogen embrittlement: Effect of tempering

6.1. Background

The effect of tempering treatments on mechanical properties of steels has been a topic of interest over the past few decades as the properties of these steels could be tailored by the heat treatments. The final microstructure obtained after heat treatments plays an important role in controlling the mechanical properties. Significant number of failures of high strength martensitic stainless steel such as Type 410 and similar MSSs used in PWR primary water circuit components such as bolts, springs and valve stems have been reported (Scott, 2000). Some of valve seats and stem rods made from 13wt.% Cr MSS are reported to have cracked due to SCC or HE in PWRs (Scott, 2000). It has been reported in the previous studies that 12wt.%-0.1C wt.% MSS are susceptible to temper embrittlement in the temperature range of 450 to 600 °C (Prabhu Gaunkar *et al.*, 1980, Bhambri, 1986, Tsay *et al.*, 2002). The sensitivity to HE increases with increasing steel strength levels. But there are no such trends observed for steels with strength values between 400 and 1000 MPa indicating that the microstructure of such steels plays a predominant role despite the fast diffusible rates of hydrogen in the high strength steels with ferritic or martensitic structures (Depover *et al.*, 2016, Matsuoka *et al.*, 2006, Eliaz *et al.*, 2002, Michler *et al.*, 2010, Sun *et al.*, 2011). It is also observed that the temper embrittled steel is highly susceptible to HE than the de-embrittled steel (Hippesley *et al.*, 1988, Yoshini *et al.*, 1974, Bandyopadhyay *et al.*, 1983, Xu *et al.*, 2012). But the

literature available on the role of impurity segregation and the precipitates formed during tempering on HE in high Cr alloyed MSS is limited.

In the present chapter, the effect of hydrogen on 13wt.% Cr MSS tempered at different temperatures is studied by SSRT tests with strain a rate of 10^{-6} /s followed by fracture surface examination. The susceptibility to temper embrittlement was evaluated by Charpy V-notch impact tests followed by fracture surface examination. The microstructural changes with tempering temperature and temper embrittlement phenomena were corroborated to HE susceptibility of 13wt.% Cr MSS with tempering. The susceptibility to HEE of tempered MSS also studied by introducing the hydrogen during strain at different cathodic current densities. Detailed fracture surface examination after SSRT tests were carried out to explain the mechanisms of HE in tempered 13wt% Cr MSS.

6.2. Experimental

6.2.1. Hardness measurements

The austenitized and tempered specimens were polished metallographically as mentioned in Chapter 3, section 3.2 and hardness values were measured using Vickers micro hardness tester with a load of 500gf and dwell time of 15 seconds.

6.2.2. Charpy V-notch Impact testing

The specimens of size 60 mm × 12 mm × 12 mm were cut from the AR MSS. These specimens were austenitized and tempered at different temperatures (Chapter 3, section 3.2.1.). The specimens of size specimens of size 55 mm × 10 mm × 10 mm were machined from the heat treated specimens and Charpy V-notch impact tests were carried out at room temperature as per standard ASTM E23. For each condition, three specimens were tested and the average value was

reported. Some of the austenitized specimens which were tempered at 550 °C for 100 h and 500 h followed by air cooling were also impacted tested at room temperature. The fracture surface examination of all the tested specimens was carried out using SEM.

6.2.3. Slow strain rate tensile tests

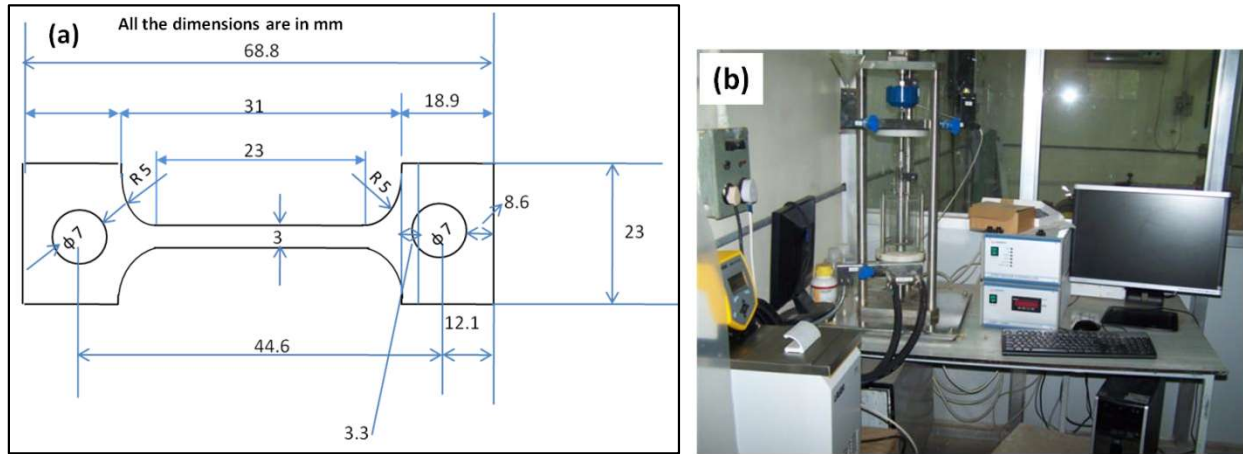


Fig. 6.1 (a) Specimen design used for SSRT tests and (b) SSRT unit used to generate stress-strain plots.

Flat tensile specimens of gauge length 23 mm, gauge width of 3 mm and thickness of 3 mm were machined using EDM from AR MSS. After the heat treatments, the tensile specimens were polished metallographically as mentioned in Chapter 3, section 3.2. SSRT tests were done at a strain rate 1×10^{-6} /s using CORMET tensile testing machine in air and fracture surface examination was carried out using SEM. All the specimens were loaded at preload of 80N.

6.2.4. Electrochemical Hydrogen charging and quantification of hydrogen

Firstly coupons of dimension 1.0 cm × 0.5 cm × 0.1 cm were cut from heat treated samples by using diamond cutting machine. These specimens were polished metallographically as mentioned in Chapter 3, section 3.2 Spot welding with stainless steel wire was done to provide the electrical connection. The electrochemical hydrogen pre-charging was carried out in 0.25 M H₂SO₄ + 0.5 g/L sodium arsenate (Na₂HAsO₄) solution and also in 0.05 M H₂SO₄+ 0.25g/L Na₂HAsO₄ (a hydrogen recombination poison) solution at a current density of -20 mA/cm² in a galvanostatic mode using Pt foil as counter electrode, specimen as working electrode and SCE as the reference electrode. An ACM instrument Gill AC potentiostat was used for H-charging. Before the start of the H-charging, cathodic cleaning was done at -1000 mV_{SCE} for 90 s then the specimens were allowed to stabilize at the OCP for 5 minutes. Solution was deaerated with argon purging. After hydrogen charging, the samples were cleaned with carbon tetrachloride to remove the water present on the surface and the amount hydrogen diffused into the specimen (bulk hydrogen) was quantified using inert gas fusion (IGF) melt extraction technique.

6.2.5. Hydrogen pre-charging and hydrogen charging during staining

Tensile specimens (tempered at 300, 550 and 700 °C) were ground on successively finer grit of emery papers up to 1200 grit followed by diamond polishing with 1 μm diamond paste. The gauge part of the tensile specimen was pre-charged with hydrogen and the other parts of the tensile specimen were covered with a nonconductive lacquer. The electrochemical hydrogen pre-charging was carried out in 0.05M H₂SO₄ + 0.25g/L Na₂HAsO₄ solution at a cathodic current density of 20 mA/cm² in a galvanostatic mode. The tensile specimens were cathodically (galvanostatic) pre-charged for 1, 3, 15 and 17 h at a cathodic current density of 20 mA/cm². The SSRT tests were conducted immediately after the hydrogen pre-charging operation.

In the second part of the study, hydrogen was introduced continuously into to the gauge part of the tensile specimen (tempered at 700 °C) during the SSRT test with three different cathodic current densities of 20, 5 and 0.01 mA/cm² and tests were done till fracture of the specimen. The rest of the conditions such as tensile specimen preparation, electrochemical hydrogen charging solution and the strain rates are the same as that reported above for tests using hydrogen pre-charged specimen.

The broken tensile specimens were stored in liquid nitrogen after the SSRT test till the bulk hydrogen concentration measurements on the fracture surface (cutting the specimen of 2 mm in length containing the fracture surface using IGF. The fracture surface examination of the broken SSRT specimens was done using FE-SEM. The relative susceptibility to hydrogen embrittlement index (HEI) of the tempered MSS after hydrogen pre-charging was determined by the strain to failure of hydrogen free (E_0 , uncharged) and hydrogen charged tensile (E_H) specimens after the tensile test using equation 1.

$$HEI = ((E_0 - E_H)/E_0) \times 100 \quad (6.1)$$

6.3. Results and Discussion

6.3.1. Variation of hardness with tempering temperature

Fig. 6.2 shows the variation in hardness with tempering temperature when the tempering duration is 2.5 h. Hardness value for each specimen reported in Fig. 6.2 is an average of 10 measurements. As shown in Fig. 6.2, hardness is almost constant for tempering temperatures up to 300 °C. Slight increase in hardness from 500 to 526 HV during tempering in the range of 300 - 400 °C can be attributed to the secondary hardening phenomenon. Secondary hardening is generally associated with the formation of fine carbide precipitates within the martensite laths.

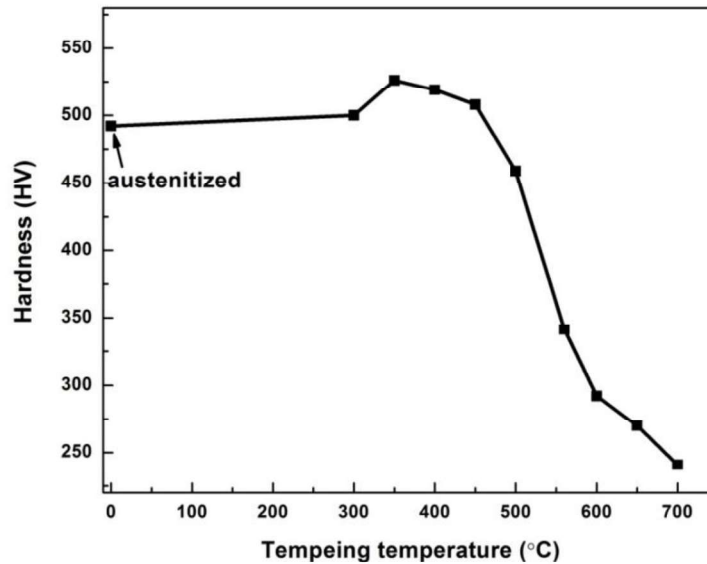


Fig. 6.2 Variation of hardness with tempering temperature for 13wt.% Cr martensitic stainless steel. All the tempering treatments are for 2.5 h.

It can also be seen from Fig. 6.2 that hardness decreased sharply in the tempering temperature range of 450 - 700 °C and a hardness value for 700 °C tempered specimen is 240 HV. This softening occurs when fine Cr-rich carbides start to coarsen and partially transform to other Cr-rich carbides with tempering temperature and are shown in Figs. 3.4 - 3.9. So the decrease in the hardness with tempering is due to increased carbide size and volume fraction with increasing

tempering temperature. The increase in carbide size and volume fraction is evident in Figs. 3.4-3.9. This decrease in hardness with tempering temperature is also reported by other researches for different MSS (Isfahany *et al.*, 2011, Prabhu Gaunkar *et al.*, 1980). The hardness values measured for the specimens tempered at 550 °C for 100 h and 500 h are 298 and 270 HV respectively. The hardness value after tempering for 2.5 h is 341 HV. With tempering duration at 550 °C, hardness value is decreased. The measured hardness distribution along the thickness (12 mm) of the tempered specimens is almost uniform indicating the microstructural uniformity of the tempered specimens throughout its thickness.

6.3.2. Changes in mechanical properties with tempering

The engineering stress-strain plots of 13wt.% Cr MSS in austenitized and specimens tempered at 300, 550 and 700 °C for 2.5 h followed by air cooling are shown in Fig. 6.3(a). The strain to failure increased with increasing tempering temperature whereas yield strength (YS) and ultimate tensile strength (UTS) decreased as shown in Fig. 6.3 and Table 6.1. The specimen tempered at 700 °C showed a maximum strain to failure of 14.4% with (YS) of 602 MPa whereas austenitized specimen showed zero plasticity with YS/UTS of 1200 MPa. In the austenitized condition, the martensite formed is super saturated with C and had a high amount of dislocations (Fig. 3.6) (Tasi *et al.*, 2002, Prabhu Gaunkar *et al.*, 1980, Chakroborty *et al.*, 2015). By tempering treatments, dislocations formed during austenitization are annihilated by recovery and is accelerated at higher tempering temperatures. The super saturated C diffuses out from the martensitic matrix and forms Cr-rich carbides and martensite turns to ferrite (Bhambroo *et al.*, 2013, Chakroborty *et al.*, 2015). The increase in the ductility at the expense of strength with tempering temperature is attributed to the formation of the carbides (Figs. 3.4 - 3.9) which led to the softening of the martensitic matrix.

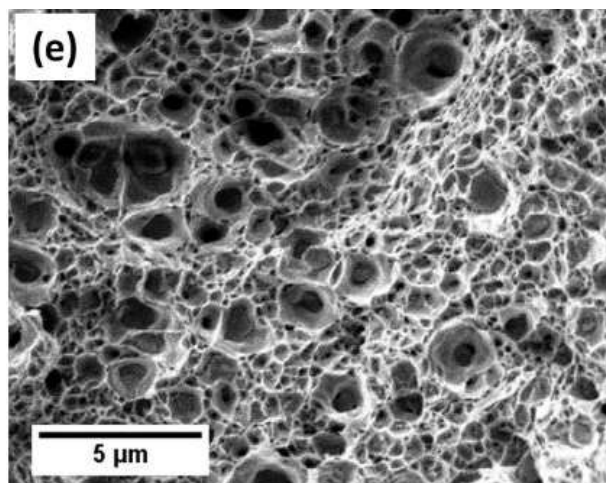
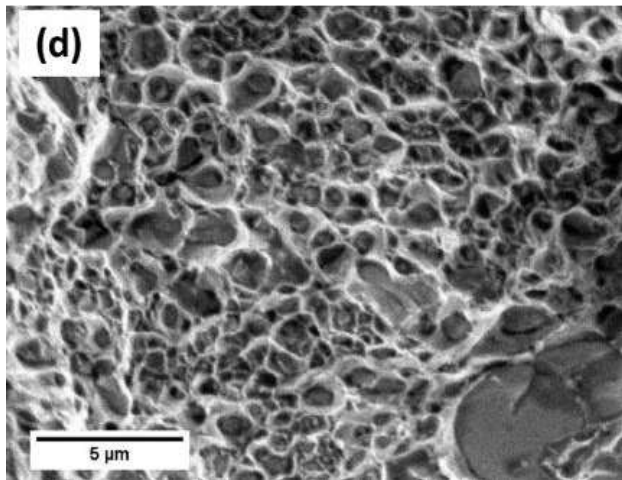
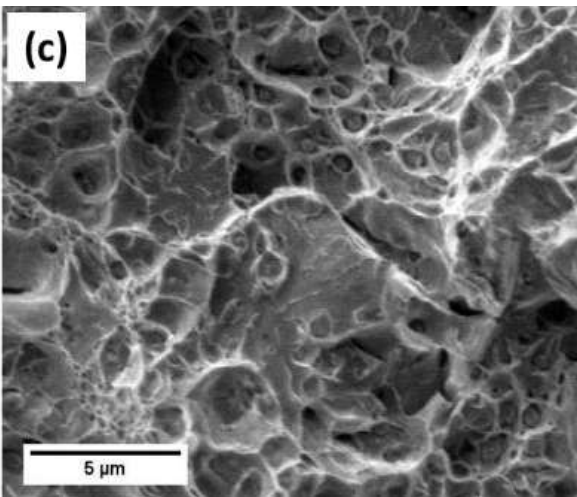
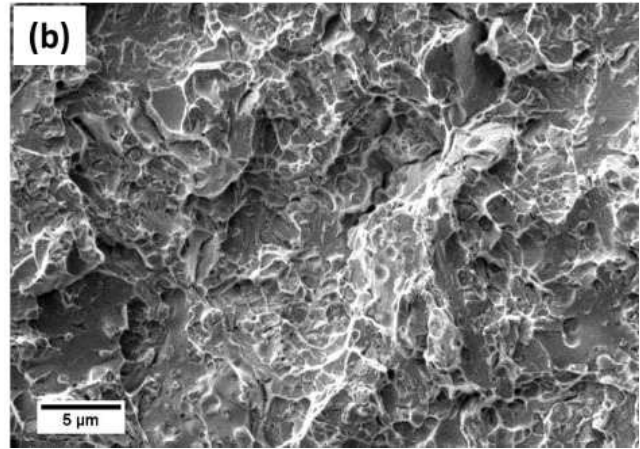
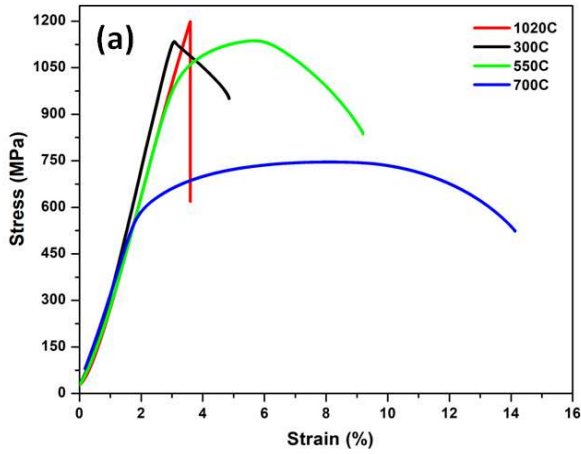


Fig. 6.3 (a) Engineering stress-strain curves and fracture surface at the central region of the 13wt.% Cr MSS after SSRT in air in different conditions, (b) austenitized, (c) tempered at 300 °C, (d) tempered at 550 °C (e) tempered at 700 °C. Tempering duration is 2.5 h.

As shown in Fig. 6.3(a), fracture surface showed brittle quasi cleavage fracture/facets as observed no plastic deformation in austenitized condition. However, there are some regions of plastic deformation and micro-voids in specimens tempered at 300 °C along with cleavage facets as shown in Fig. 6.3(c). It is observed that more of ductile fracture with cleavage regions in specimen tempered at 550 °C and complete ductile fracture in specimen tempered at 700 °C occurred as shown in Fig. 6.3(d)-(e) respectively. In the fracture surface of tempered specimens, the central fibrous region increased with increase of tempering temperature. The fracture appearance in specimen tempered at 700 °C is essentially ductile with different sizes of dimples and fracture occurred by micro void coalescence mechanism. The presence of carbides in the tempered specimens led to micro void coalescence fracture as shown in Fig. 6.3(d)-(e).

6.3.3. Changes in impact toughness and fracture behaviour with tempering temperature

The fracture toughness value for as-quenched condition is 3 J and showed predominantly brittle cleavage/transgranular fracture with ductile dimples at some places at carbide-matrix interfaces as shown in Fig. 6.4(a). The impact toughness value increased to 12 J after tempering at 300 °C and showed quasi cleavage fracture with river patterns and ductile dimples at few locations as shown in Fig. 6.4(b). Tempering at 550 °C showed impact toughness value of 14 J but the fracture is brittle with complete intergranular (IG) cracking with grain boundary cracks as shown in Fig. 6.4(c). Tempering at 700 °C, increased the fracture toughness value to 23 J with riverine facets and ductile dimples as shown in Fig. 6.4(d). The presence of secondary IG cracks are also evident in the fracture surface as shown Fig. 6.4(d). It has been reported that the MSSs are susceptible to temper embrittlement in the temperature range of 450 to 600 °C with a low fracture toughness value and brittle IG cracking along PAG boundaries (Prabhu Gaunkar *et al.*, 1980, Bhambri, 1986, Tsay *et al.*, 2002). The specimen tempered at 550 °C with IG cracking has the temper

embrittlement and is believed to be due to impurity segregation at PAG boundaries. The absence of IG fracture in austenitized condition, specimens tempered at 300 °C and 700 °C conditions as shown in Fig. 6 substantiates that there is no impurity segregation at PAG boundaries.

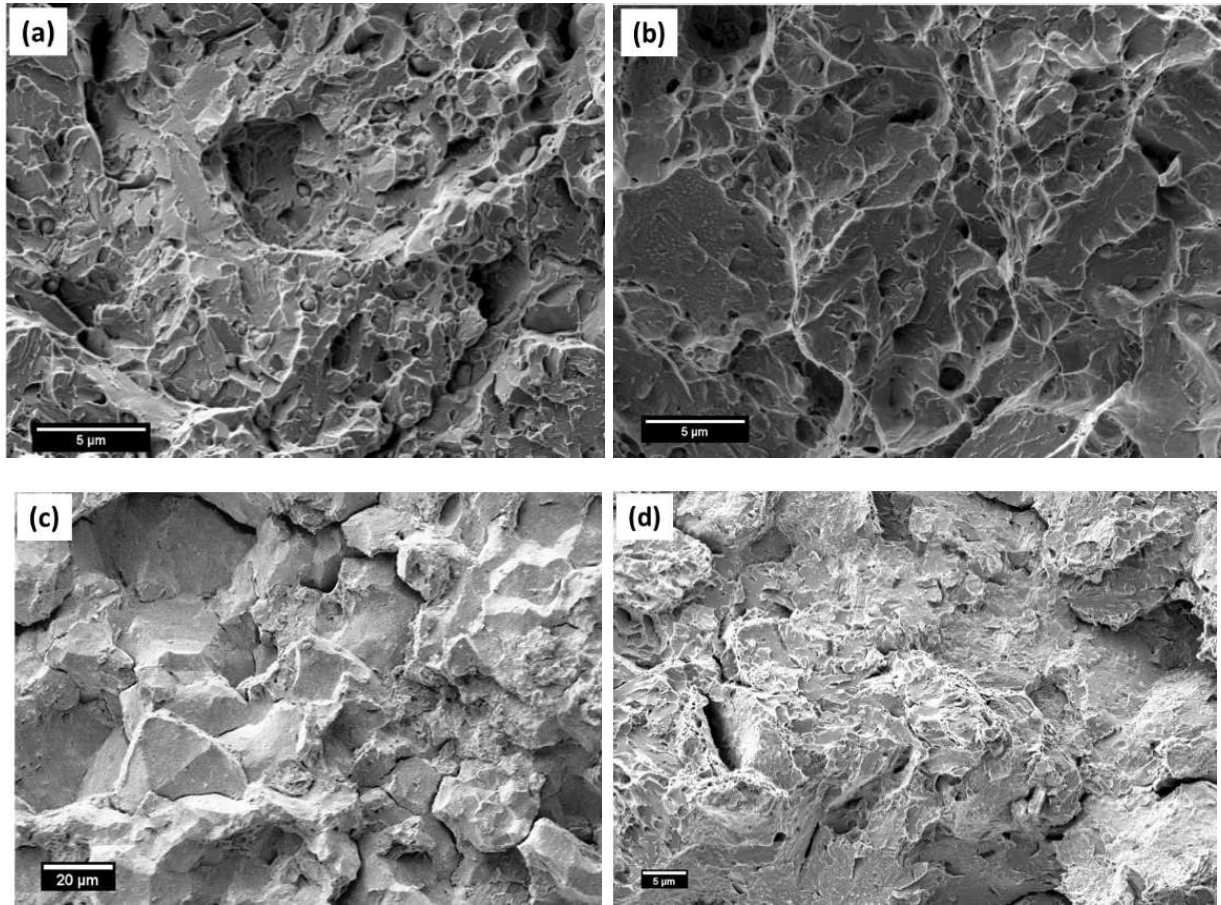


Fig. 6.4 SEM images of the fracture surface of (a) austenitized and tempered at (b) 300 °C, (c) 550 °C and (d) 700 °C after Charpy V-notch impact tests. Tempering duration is 2.5 h.

The etching of PAG boundaries by picric acid (Vilella's reagent) as shown in Fig. 3.5(c) also indicates the presence of impurity segregation at PAG boundaries as picric acid has higher sensitive to attack at P segregated grain boundaries as shown in previous research articles (Viswanathan *et al.*, 1985, Ogura *et al.*, 1984, Zhai *et al.*, 2014). It has been reported by Prabhu *et al.* that the P content measured at the grain boundary is increased after tempering at 550 °C for 100 h as compared to 550 °C for 1 h in 12wt.% Cr-0.1wt.% C MSS (Prabhu Gaunkar *et al.*, 1980). The

specimens tempered at 550 °C for 100 h and 500 h showed impact toughness values of 16 and 14 J respectively and showed IG fracture as shown in Fig. 6.5. This result confirms the role of impurity segregation in temper embrittlement of 13wt.% Cr MSS. The impact test results also showed that changes in toughness value with tempering duration at 550 °C is not significant.

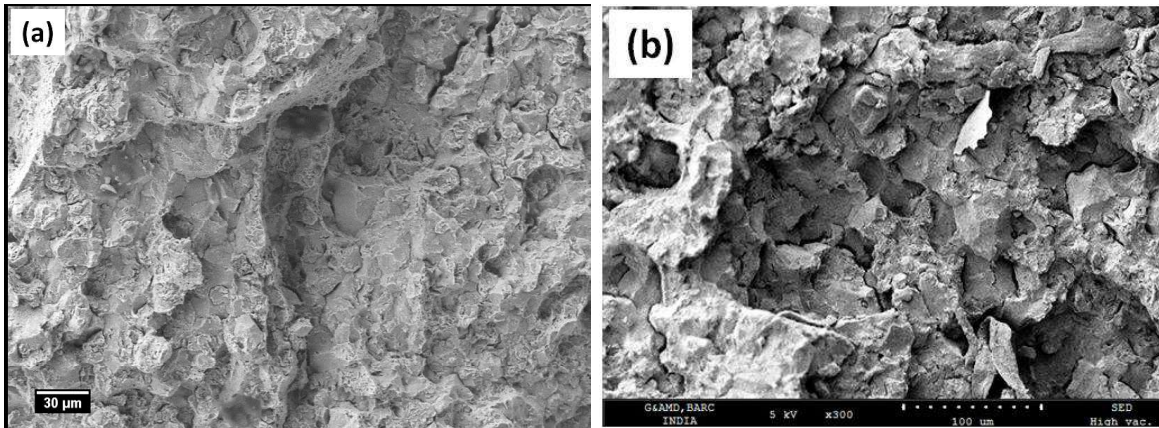


Fig. 6.5 SEM images of the fracture surface of specimens tempered at (a) 550 °C for 100 h and (b) 550 °C for 500 h after Charpy V-notch impact tests.

6.3.4. Susceptibility to HE with tempering temperature

Austenitized condition showed cracking during hydrogen pre-charging and are along PAG boundaries as shown in Fig. 6.6(a) and PAG boundaries are also got etched as shown in Fig. 6.6(b). No cracks were observed on tempered specimens after hydrogen pre-charging as shown in Fig. 6.6(c)-(d). The cracking of austenitized specimen during hydrogen charging is due to its high strength and brittleness as evidenced in tensile tests (Fig. 6.3 (a)-(b)).

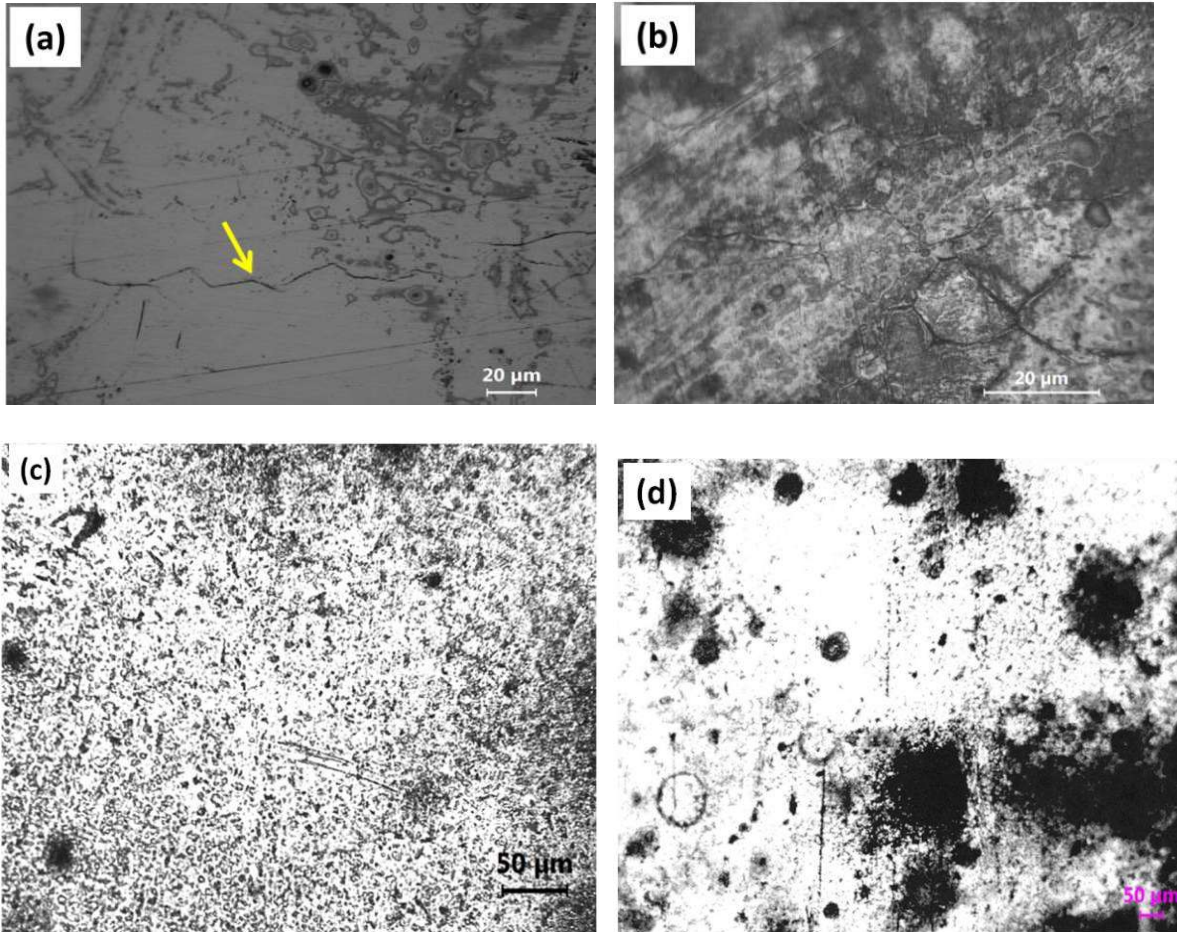


Fig. 6.6 Optical images after hydrogen pre-charging: (a) austenitized condition showing cracks along PAG boundaries after hydrogen pre-charging for 3 h and (b) PAG boundaries etched during hydrogen pre-charging, (c) tempered at 550 °C for 2.5 h and (d) tempered at 700 °C for 2.5 h showing no cracks.

Tempering at 300 °C: Fig. 6.7(a) shows the engineering stress- strain curve of specimen tempered at 300 °C for 2.5 h with and without hydrogen pre-charging. The changes in mechanical properties after hydrogen pre-charging are given Table 6.1. The specimen tempered at 300 °C for 2.5 h fractured below yield stress (elastic regime) of uncharged condition with a drastic decrease in strain to failure after hydrogen pre-charging with HEI of 75.7% as shown in Fig. 6.7(a) and showed predominantly IG cracking along the PAG boundaries and transgranular (TG) cracking as shown in Fig. 6.7(b).

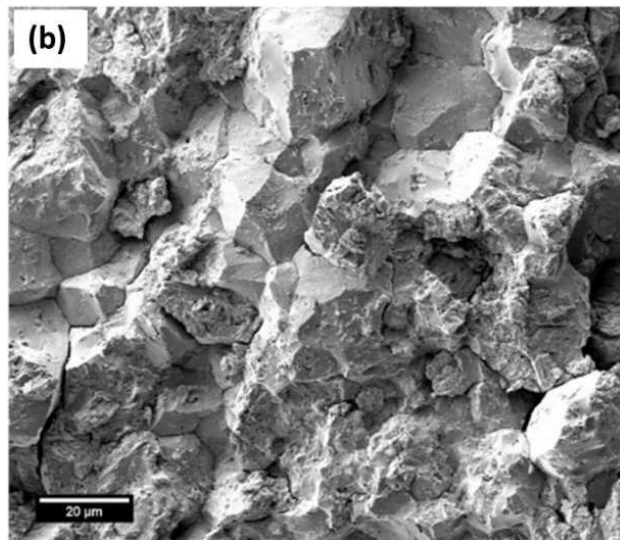
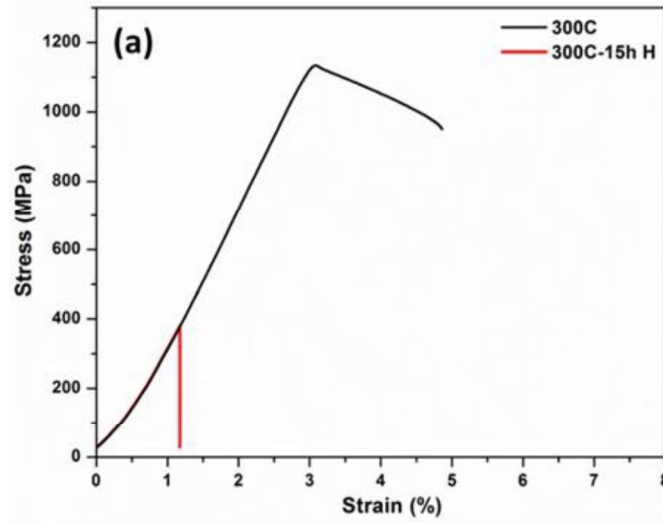


Fig. 6.7 (a) Engineering stress- strain curves of specimen tempered at 300 °C for 2.5 h with and without hydrogen and (b) fracture surface of hydrogen pre-charged specimen showing IG fracture.

Tempering at 550 °C: Fig. 6.8(a) shows the engineering stress- strain curve of specimen tempered at 550 °C for 2.5 h with and without hydrogen pre-charging for 3 and 15 h durations. The changes in mechanical properties after hydrogen pre-charging are given Table 6.1. The specimen tempered at 550 °C for 2.5 h also fractured below yield stress (elastic regime) of uncharged condition with

a drastic decrease in strain to failure after hydrogen pre-charging as shown in Fig. 6.8(a). and showed complete IG cracking along the PAG boundaries as shown in Fig. 6.8(b)-(c).

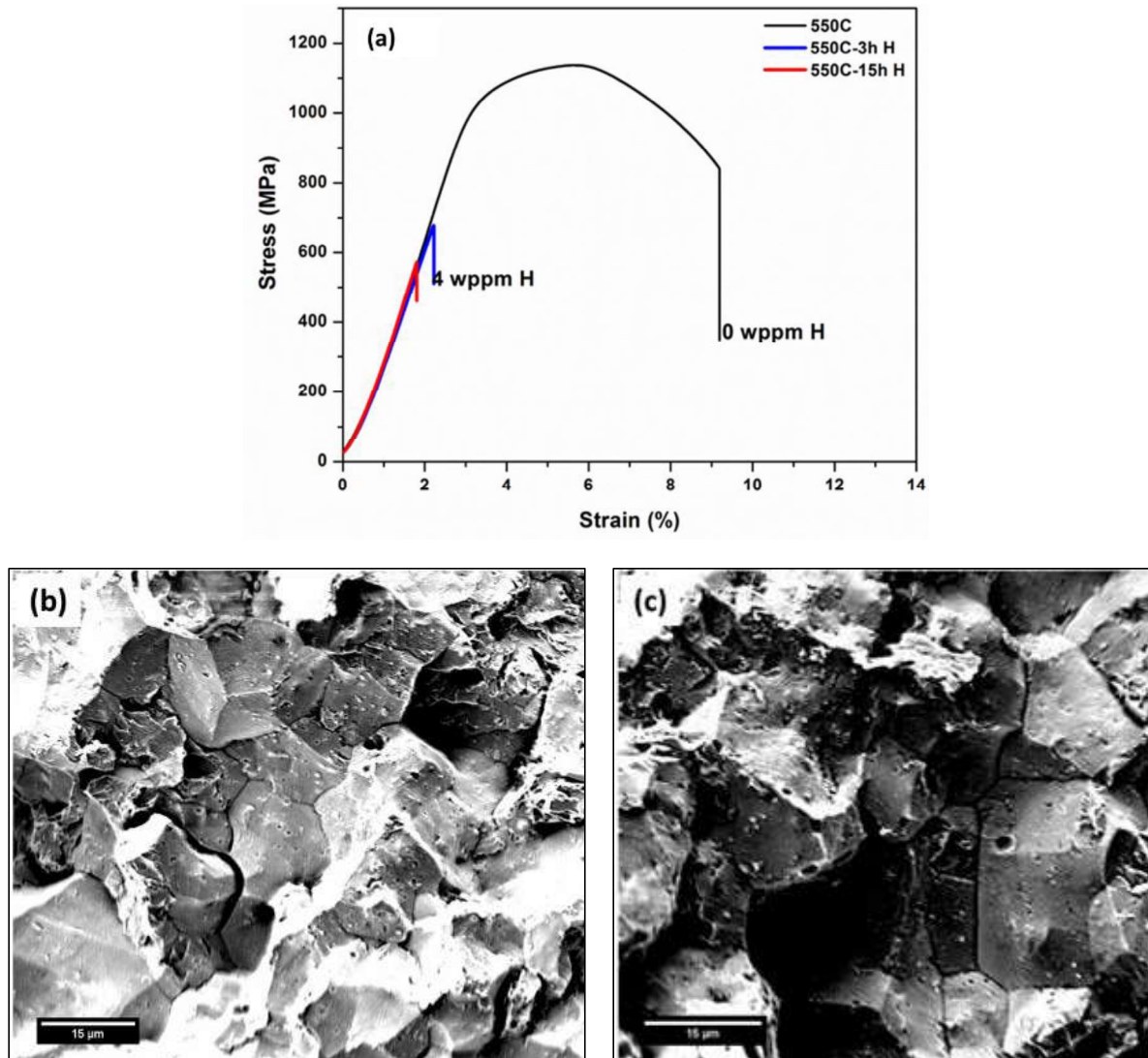


Fig. 6.8 (a) Engineering stress- strain curves of specimens tempered at 550 °C for 2.5 h with and without hydrogen and fracture surface of hydrogen charged specimen showing IG fracture (b) 550 °C - 3 h pre-charging and (c) 550 °C - 15 h pre-charging.

Tempering at 700 °C: Fig. 6.9(a) shows the engineering stress-strain curve (measured in air) of the uncharged and tensile specimens hydrogen pre-charged for different durations and their properties are summarized in Table 6.1. The intrinsic effect of the hydrogen (hydrogen introduced

into the specimen by hydrogen pre-charging method on the mechanical properties of the specimen tempered at 700 °C is the loss in the strain to failure (ductility) which decreased from a value of 14.4% for the uncharged specimen to 12.7, 11.9, 4.2 and 3.7% for 1, 3, 15 and 17 h of hydrogen pre-charging, respectively.

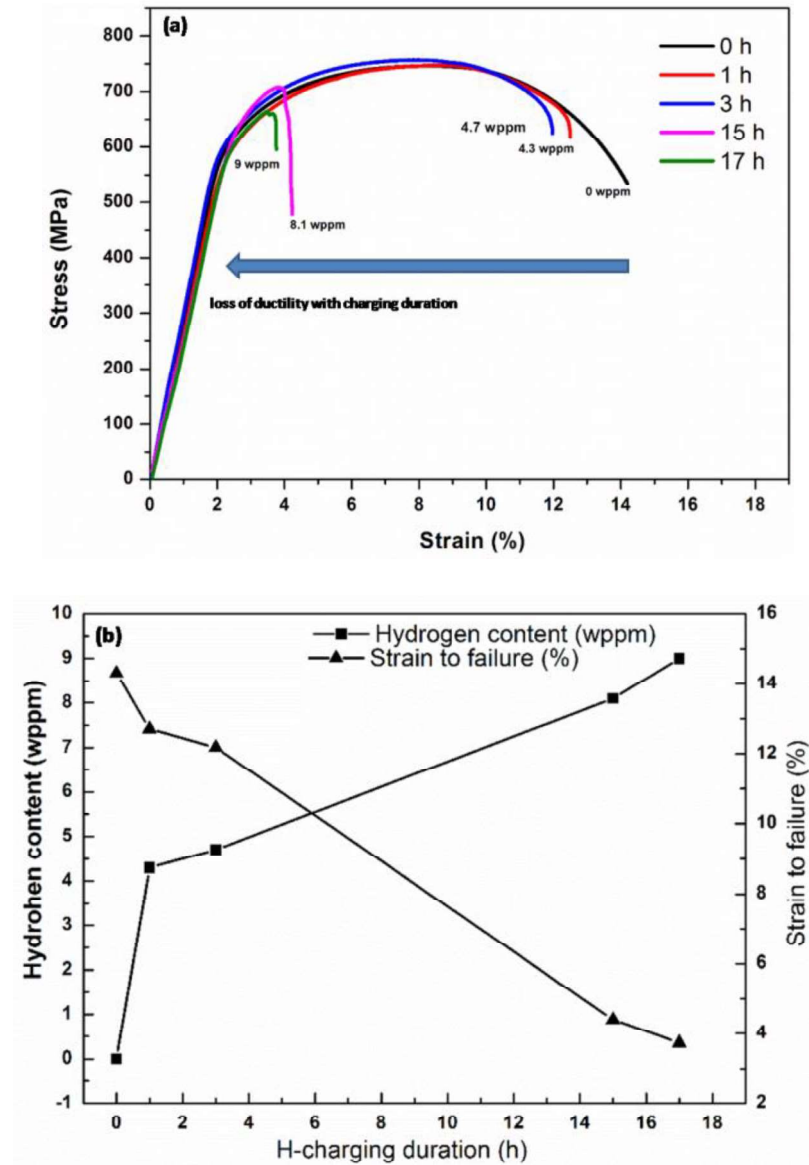


Fig. 6.9 (a) Engineering stress-strain curves of the uncharged and hydrogen pre-charged specimen tempered at 700 °C for different hydrogen pre-charging durations and (b) showing duration of hydrogen pre-charging vs. strain to failure and concentration of bulk hydrogen in the fracture surface.

Table 6.1 Mechanical properties of the 13wt.% Cr MSS tempered at different temperatures with and without hydrogen pre-charging.

Tempered condition (2.5 h)	Pre-charging duration (h)	H content (wppm)	YS (MPa)	UTS (MPa)	Strain to failure (%)	HEI (%)
300 °C	0	0	1133	1137	4.87	0
	15	ND	383	383	1.18	75.7
550 °C	0	0	1022	1140	9.21	0
	3	4	688	688	2.23	75.8
	15	ND	580	580	1.79	80.5
700 °C	0	0	602	743	14.4	0
	1	4.3	594	742	12.7	11.8
	3	4.7	603	756	11.9	17.4
	15	8.1	647	706	4.2	70.8
	17	9.0	616	665	3.7	74.3

ND: not done

Fig. 6.9(b) shows the strain to failure and the hydrogen content in the fracture surface measured using IGF technique with hydrogen pre-charging duration. The hydrogen content in the bulk fracture surface increased with pre-charging duration (Fig. 6.9(b)). As evident in Table 6.1, no predominant changes are observed in YS and ultimate tensile strength (UTS) of the 1 and 3 h hydrogen pre-charged specimens as compared to uncharged specimen. But, slight increase in the

YS and decrease in UTS is observed for higher hydrogen pre-charging durations of 15 and 17 h, as shown in Fig. 6.9(a) and Table 6.1. As shown in Fig. 6.9(a), the deformation ability after necking decreased for initial charging durations of 1 and 3 h as compared to that for the uncharged condition. As the hydrogen pre-charging duration increased to 15 and 17 h, the hydrogen caused, reduced strain after the onset of yielding, leading to premature failure.

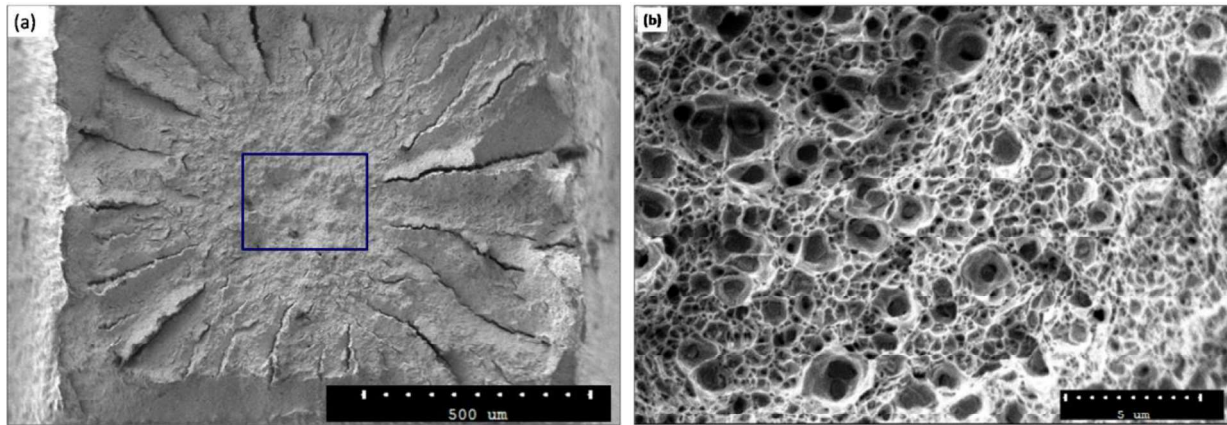


Fig. 6.10 (a) Fracture surfaces of uncharged tempered 13wt% Cr martensitic stainless steel after SSRT in air and (b) magnified view of the central region (blue box) of (a) showing ductile dimples.

A detailed fracture surface examination was carried out using SEM after the SSRT experiments to observe the internal hydrogen effects on the HE mechanism. Fig. 6.10(a)-(b) shows the SEM images of the fracture surface of the uncharged 700 °C tempered MSS. In the uncharged specimen, necking around the fracture is observed and fracture occurred by MVC mechanism with ductile dimples of two distinct size, as shown in Fig. 6.10(b). In the fracture surface of uncharged tempered specimen, cracks were also observed, as shown in Fig. 6.10(a) and these cracks have been reported to form in materials with high strength (Bhambroo *et al.*, 2013). Figs. 6.11 - 6.14 show the fracture surfaces of the hydrogen pre-charged specimens for different durations after SSRT. In contrast to fracture surface of the uncharged specimen, distinguishing features are observed for fracture

surfaces of hydrogen pre-charged specimens, consisting of ductile (dimple) patterns, elongated ductile dimples with flat facets, IG regions and brittle region having riverline features.

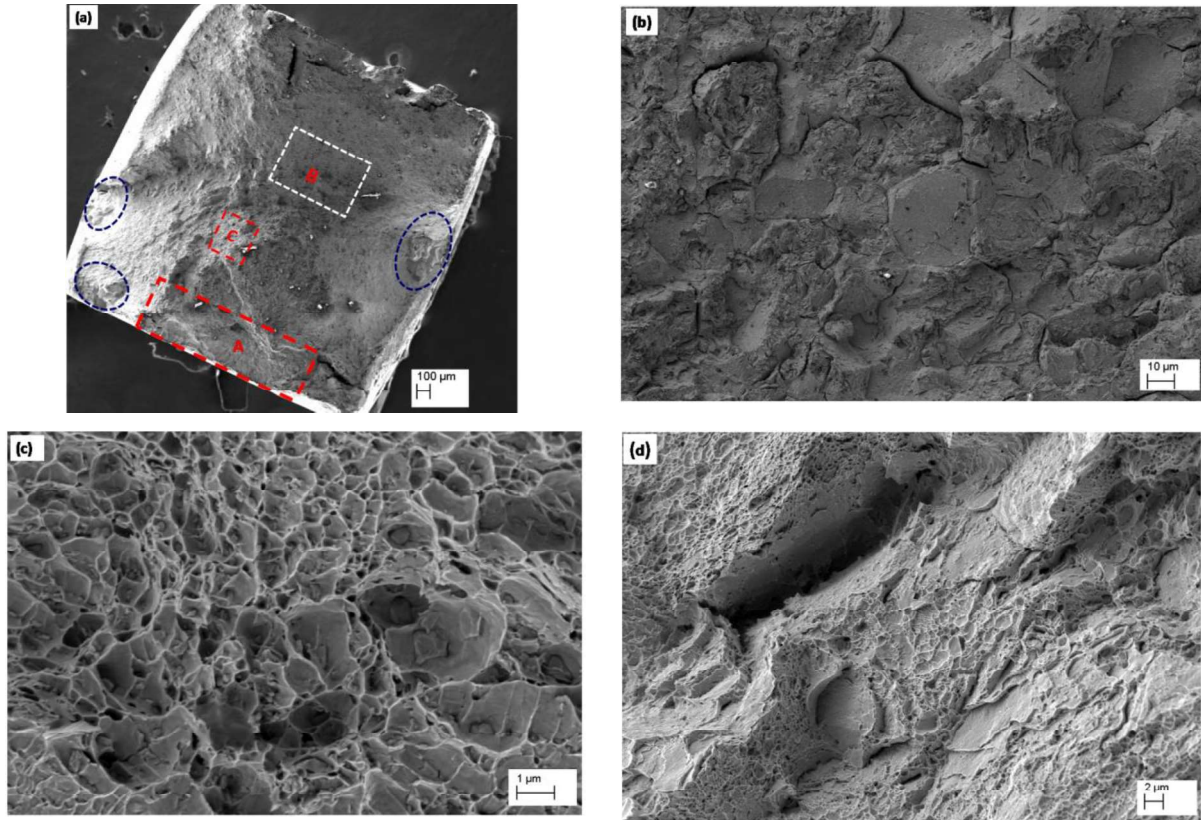


Fig. 6.11 Fracture surface of the 1 h hydrogen pre-charged tempered specimen showing (a) intergranular and ductile fracture, (b), (c) and (d) are the magnified images corresponding to regions marked A, B and C respectively in image (a). Blue color marked regions are showing the brittle intergranular regions in Fig. 6.11(a).

The fracture surface of 1 h hydrogen pre-charged specimen (Fig. 6.11(a)) shows brittle IG and ductile dimples with flat facet regions at the edge section of the fracture surface as shown in Fig. 6.11(b)-(c) and ductile dimple fracture by MVC in the central region as shown in Fig. 6.11(d). The regions of Fig. 6.11(b) to (d) are marked in Fig. 6.11(a) as regions A, B and C respectively. The regions marked in Fig. 6.11(a) with blue color are showing the brittle IG features similar to those in region A as shown in Fig. 6.11(b). Fig. 6.11(c) shows tear ridges with ductile dimples and flat facets, suggesting a local cleavage by presence of hydrogen.

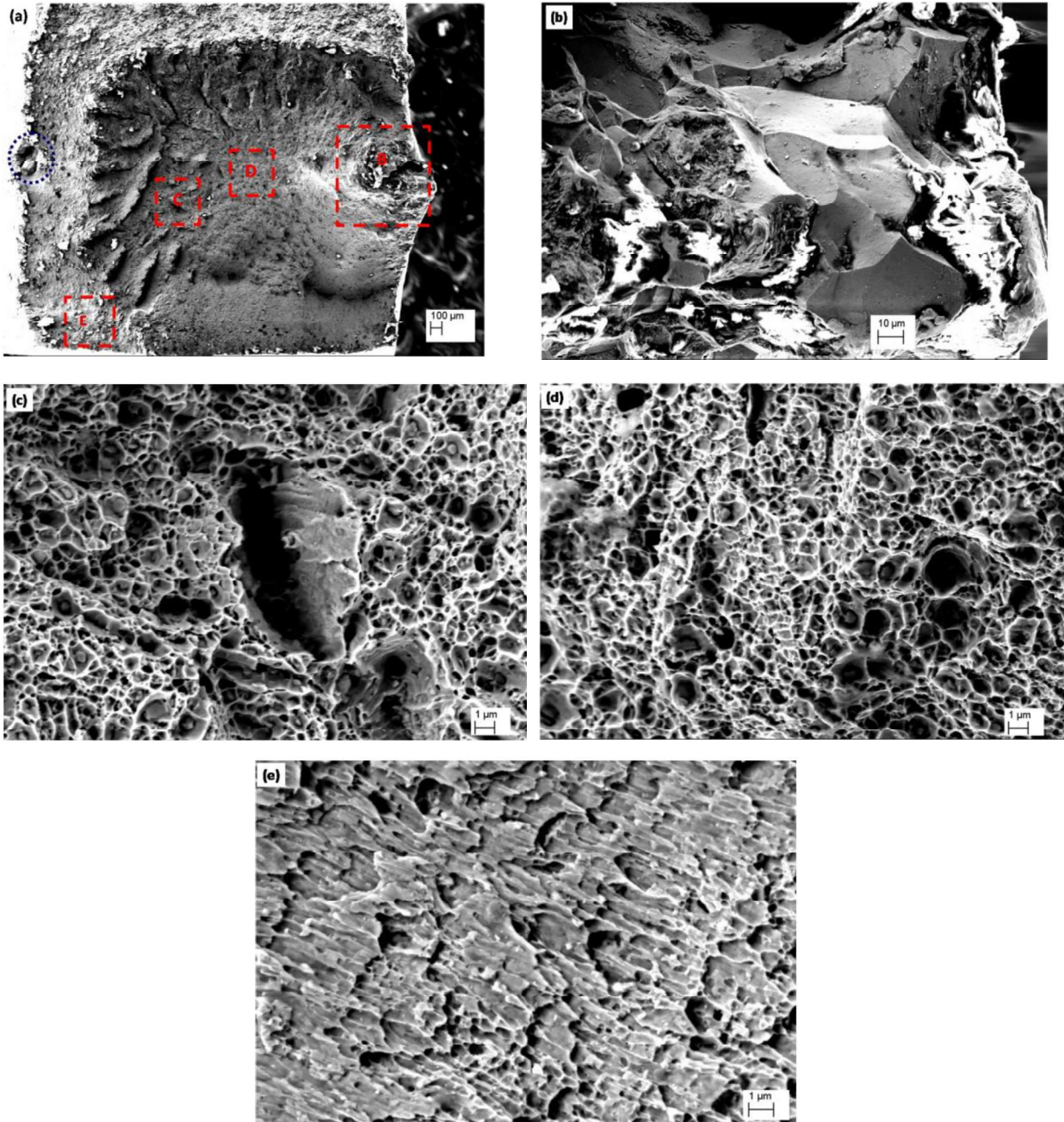


Fig. 6.12 Fracture surface of the 3 h hydrogen pre-charged tempered specimen showing (a) intergranular and ductile fracture, (b), (c), (d), and (e) are the magnified images corresponding to regions marked B, C, D and E respectively in image (a). Blue color marked regions are showing the brittle intergranular regions in Fig. 6.12 (a).

The fracture surface (Fig. 6.12(a)) of 3 h hydrogen pre-charged specimen showed three different regions, i.e., IG region (Fig. 6.12(b)) and brittle region having riverline pattern (Fig. 6.12(c)) at

the edges and elongated dimples with tear ridges and ductile region with dimples (Fig. 6.12(d)-(e)) in the central region. The IG facets in fracture surface are comparable with PAG size. The fracture surface of 3 h hydrogen pre-charged specimen showed the same three regions (Fig. 6.12(a)) as of 1 h pre-charged specimen (Fig. 6.11(a)) but the width of brittle region is increased. As shown in Fig. 6.11 - Fig. 6.12, very clear distinct localized regions of ductile and brittle features are present on fracture surface of MSS tempered at 700 °C with hydrogen pre-charging charging durations of 1 and 3 h.

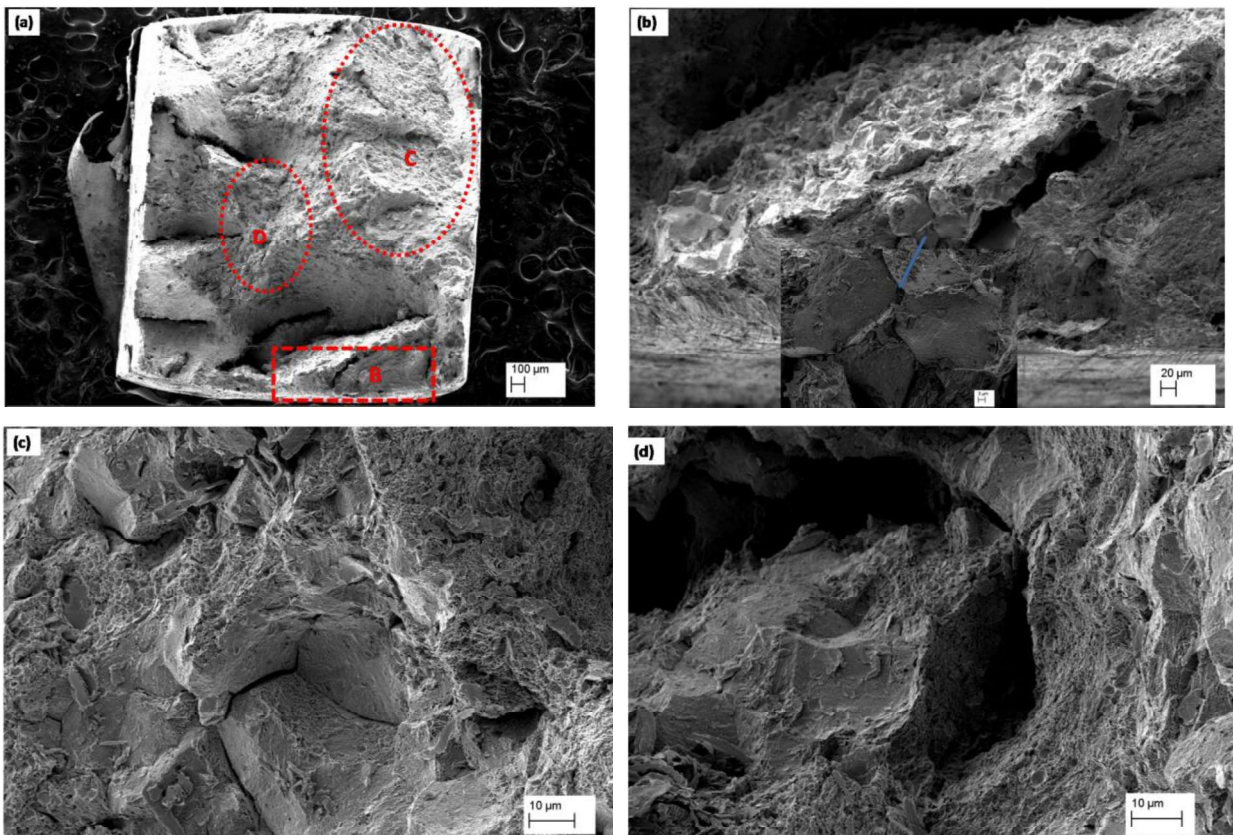


Fig. 6.13 Fracture surface of the 15 h hydrogen pre-charged tempered specimen showing (a) more of intergranular and ductile fracture, (b), (c) and (d) are the magnified images corresponding to regions marked as B, C and D respectively in image (a). The inset in Fig. 6.13(b) shows the intergranular cracking along the prior austenite grain boundaries.

Fig. 6.13(a) shows the fracture surface of the 15 h hydrogen pre-charged specimen and shows a mixture of brittle IG and ductile regions. As shown in Fig. 6.13(b), the edge regions of the fracture surface show the IG features and the inset in Fig. 6.13(b) shows the IG cracking along the PAG boundaries. The ductile dimples are in between the IG facets as shown Fig. 6.13(c)-(d). Fig. 6.14(a) shows the fracture surface of the 17h hydrogen pre-charged specimen. The fracture is mainly by brittle IG cleavage along the PAG boundaries as shown in Fig. 6.14(b)-(d). The edge and central region of the fracture has IG nature as shown in Fig. 6.14(b)-(c). The IG fracture region is increased after 15 h and 17 h of hydrogen pre-charging as compared to 1 h and 3 h hydrogen pre-charged specimens.

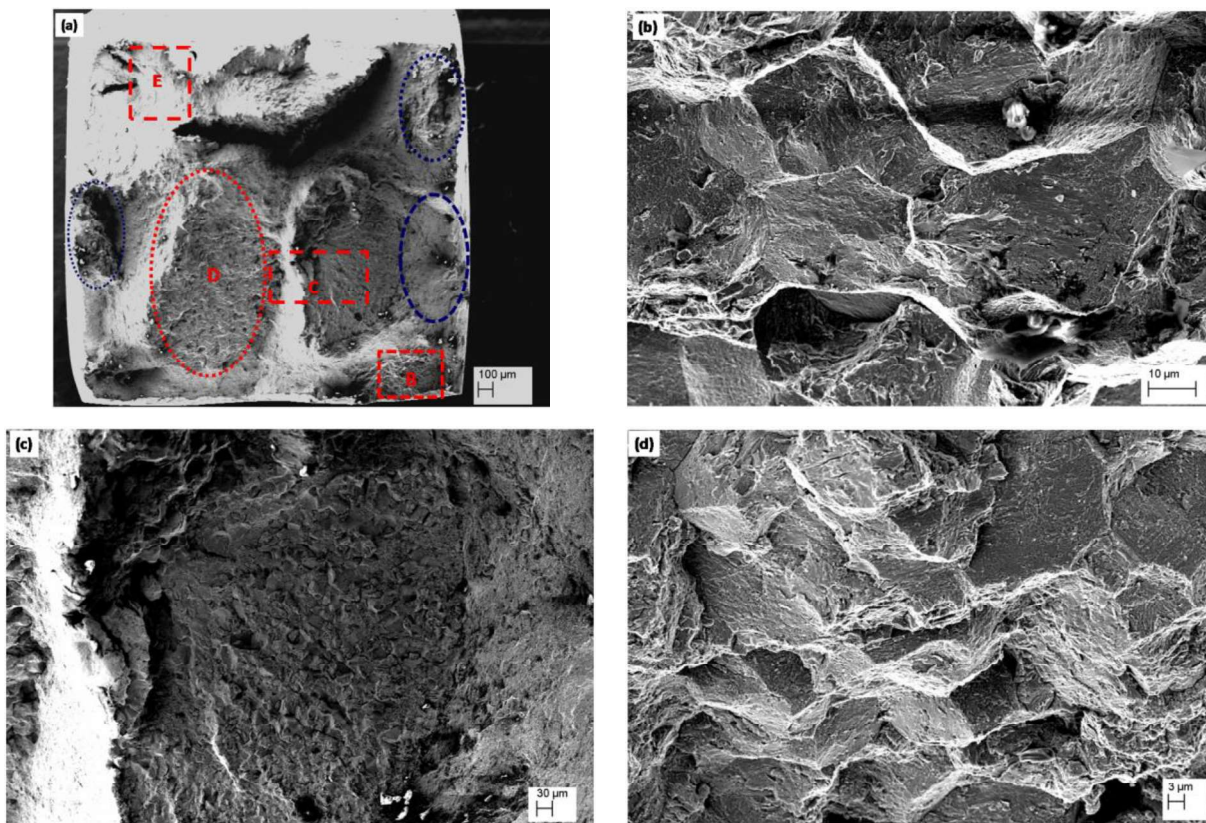


Fig. 6.14 Fracture surface of the 17 h hydrogen pre-charged specimen tempered at 700 °C for 2.5 h showing (a) IG fracture along the prior austenitic grain boundaries, (b), (c) and (d) are the magnified images corresponding to regions marked as B, C and D respectively in image (a).

6.3.5. Mechanism of internal (pre-charged) HE with tempering temperature

6.3.5.1. Tempered at 300 and 550 °C

The microstructural changes observed with tempering temperature are formation of tempered martensite, coarsening of carbides and decrease in dislocation density as shown in Figs. 3.5 to 3.10. The strength of the tempered martensite has decreased with tempering temperature as indicated by hardness values as shown in Fig. 6.3(a). The changes in mechanical properties (Table 6.1) of MSS with tempering temperature after hydrogen pre-charging are due to trapping of hydrogen at various locations in matrix and the interaction of hydrogen with these traps. The present results clearly show that the austenitized condition is highly susceptible to HE and tempering increases the resistance to HE. As shown in Table. 6.1, the specimen tempered at 550 °C showed larger HEI of 80.5% after 15 h hydrogen pre-charging as compared to specimens tempered at 300 and 700 °C with HEI values of 75.7% and 70.8%. Fracture surfaces of the hydrogen pre-charged specimens showed IG cracking along PAG boundaries indicating the diffusion of hydrogen to grain boundaries during slow straining. The reported D_H value in quenched (austenitized) AISI 420 stainless steel (with 13 wt.% Cr) is $3.60 \times 10^{-8} \text{ cm}^2/\text{s}$ (Bernabal *et al.*, 1993) and used for calculation of hydrogen penetration depth. Assuming the penetration depth of hydrogen due to lattice diffusion is 'd' (in cm) for the hydrogen charging duration of t (h), it is expressed as

$$d = \sqrt{2D_H t} \quad (6.2)$$

The estimated hydrogen depth penetration in the gauge section of tempered 13wt.% Cr MSS with width and thickness of 3 mm after hydrogen pre-charging for 15 h duration is 623 μm from one side of the specimen. The hydrogen is therefore confined to the surface while charging is done and central portion of gauge section of the tensile specimen (3 mm thickness) is free from hydrogen after electrochemical hydrogen charging even after 15 h duration.

The subsurface hydrogen which is relatively mobile at room temperature tends to trap at defects present in the MSS specimen to lower the misfit energy of the matrix (Hippesley *et al.*, 1988). The interstitials, grain boundaries, lath interfaces and dislocations are reversible trap sites with low bonding energies (< 60 kJ/mol) whereas the second phases like carbides, nitrides and oxides are typically irreversible trap sites where hydrogen strongly binds (binding energy > 60 kJ/mol) with the trap sites [Pressouyre, 1979, Bhadeshia, 2016, Tiwari *et al.*, 2000, Maroef, 2002]. The hydrogen trapped at low binding energy trap sites fed to higher binding energy trap sites during plastic deformation or application of load.

In the present study, the SSRT experiments were carried with a strain rate of 1×10^{-6} /s and at a lower strain rate, the hydrogen transported by the mobile dislocations during deformation will predominantly concentrate at the grain boundaries/martensitic laths (Santos *et al.*, 2015, Birnbaum, 2003). This process can increase the hydrogen concentration at the interface and decohesion of the interface occurs after reaching a critical hydrogen concentration at the interface. The IG fracture occurs if the critical hydrogen concentration reaches first at PAG boundaries. In the present study, hydrogen induced the complete brittle IG fracture for specimen tempered at 550 °C (Fig. 6.8) and mixture of IG and TG for specimen tempered at 300 °C (Fig. 6.7) even after hydrogen charging for 3 h indicating that the hydrogen absorbed on the subsurface during the electrochemical charging predominantly accumulated at the PAG boundaries during slow straining. The hydrogen segregated to PAG boundaries decreased the cohesive strength leading to a brittle fracture at load well below the YS of the tempered condition without hydrogen. Dislocation strengthening is one of the strength mechanisms for quenched and tempered martensitic steels. In general, the HE susceptibility increases with strength. The specimen tempered at 300 °C with high strength (high dislocation density) should be expected to have high susceptibility to HE. But, the specimen

tempered at 550 °C showed high HEI value of 80.5. The carbides act as trap sites for hydrogen and increases the resistance to HE (Moon *et al.*, 2016, Deveper *et al.*, 2016, Dadfarnia *et al.*, 2011). Tempering at 550 °C produced nano-sized carbide precipitates as shown in Fig. 3.8 whereas sub-microscopic carbides are observed in the specimen tempered at 700 °C as shown in Fig. 3.9. Recently, Deveper *et al.* reported that that the hydrogen trapped at Cr₂₃C₆ precipitates has binding energy of 50-55 kJ/mol which is less than 60 kJ/mol and so acts a reversible trap site (Deveper *et al.*, 2016, Dadfarnia *et al.*, 2011). It is also reported that the MC type carbides of Ti, Nb, V with less than 100 nm size can pin the dislocations, decrease the dislocation mobility and improve the HE resistance by redistribution of the hydrogen (Moon *et al.*, 2016). Therefore, the specimen tempered at 550 °C with M₂₃C₆ type carbides of size less than 100 nm (Fig. 3.12(a)) and decreased dislocation density should have increased resistance to HE than the specimen tempered at 300 °C. But, in the present study, drastic degradation in the mechanical properties is observed for specimen tempered at 550 °C even after 3 h hydrogen pre-charging. This behaviour is because of an additional factor of temper embrittlement (Fig. 6.4(c)) which is believed to be impurity segregation such as P along the grain boundaries at this tempering temperature (Prabhu Gaunkar *et al.*, 1980, Bhambri, 1986, Tsay *et al.*, 2002).

The IG fracture after impact tests for the specimen tempered at 550 °C indicates its susceptibility to temper embrittlement at 550 °C as shown in Fig. 6.4(c). The temper embrittlement and hydrogen interactions are also observed in low alloy steels (Yoshini *et al.*, 1974, Bandyopadhyay *et al.*, 1983, Xu *et al.*, 2012). Therefore, the reason for least resistance to HEI of 550 °C tempered condition is due to the synergistic effect of impurities segregation to the grain boundaries and their interaction with the hydrogen. The presence of impurity segregation at PAG boundaries might inhibit the hydrogen recombination thereby increasing the hydrogen concentration at the boundaries or

hydrogen itself act as a embrittling element and its effect is added to the PAG boundaries which are already segregated with impurity elements (Hippesley *et al.*, 1988). The critical hydrogen required for brittle fracture of MSS specimen decreased in presence of impurity segregation as shown in Table. 6.1. The specimen tempered at 550 °C showed ductile fracture without hydrogen but presence of hydrogen with impurity segregation reduced strength and strain to failure drastically in SSRT. It is to be noted that HEI reflects the relative effect (reduction of ductility due to hydrogen), therefore there is more effect of hydrogen on specimen tempered at 550 °C than that tempered at 300 °C. However, in absolute terms, 550 °C tempered specimen still retains slightly more ductility (Table 6.1). Therefore, HEI is not indicative of the remaining ductility.

6.3.5.1.1. Confirming the role of phosphorous segregation on HE

It has been reported by Prabhu *et al.* that the P content measured at the grain boundary is increased after tempering at 550 °C for 100 h as compared to 550 °C for 1 h in 12wt.% Cr-0.1wt.% C MSS (Prabhu Gaunkar *et al.*, 1980). To further substantiate the synergistic action of impurity segregation and hydrogen, the 13wt.% Cr MSS specimens tempered at 550 °C for 100 h was hydrogen pre-charging for 3 h. The hardness and room temperature impact toughness values for 550 °C for 100 h specimen are 298 HV and 16 J respectively. The fracture surface examination of impact tested specimen showed mainly IG fracture with ductile dimple ridges on few grain interfaces as shown in Fig. 6.5(a), showing its susceptibility to temper embrittlement. The SSRT tests were carried out with same strain rate of 10^{-6} /s in air. Drastic reduction in strain to failure was observed from 11.27% to 3.24% after hydrogen pre-charging for 3 h with HEI of 71% as shown in Fig. 6.15(a). The fracture surface examination after tensile test of 550 °C for 100 h specimen showed ductile fracture (Fig. 6.15(b)) for uncharged condition and IG fracture for hydrogen pre-charged condition as shown in Fig. 6.15(c). The drastic reduction in strain to failure to 3.24% from

11.27% (uncharged) without plastic deformation after hydrogen pre-charging for 3 h confirms the synergistic interaction between impurity segregation and hydrogen.

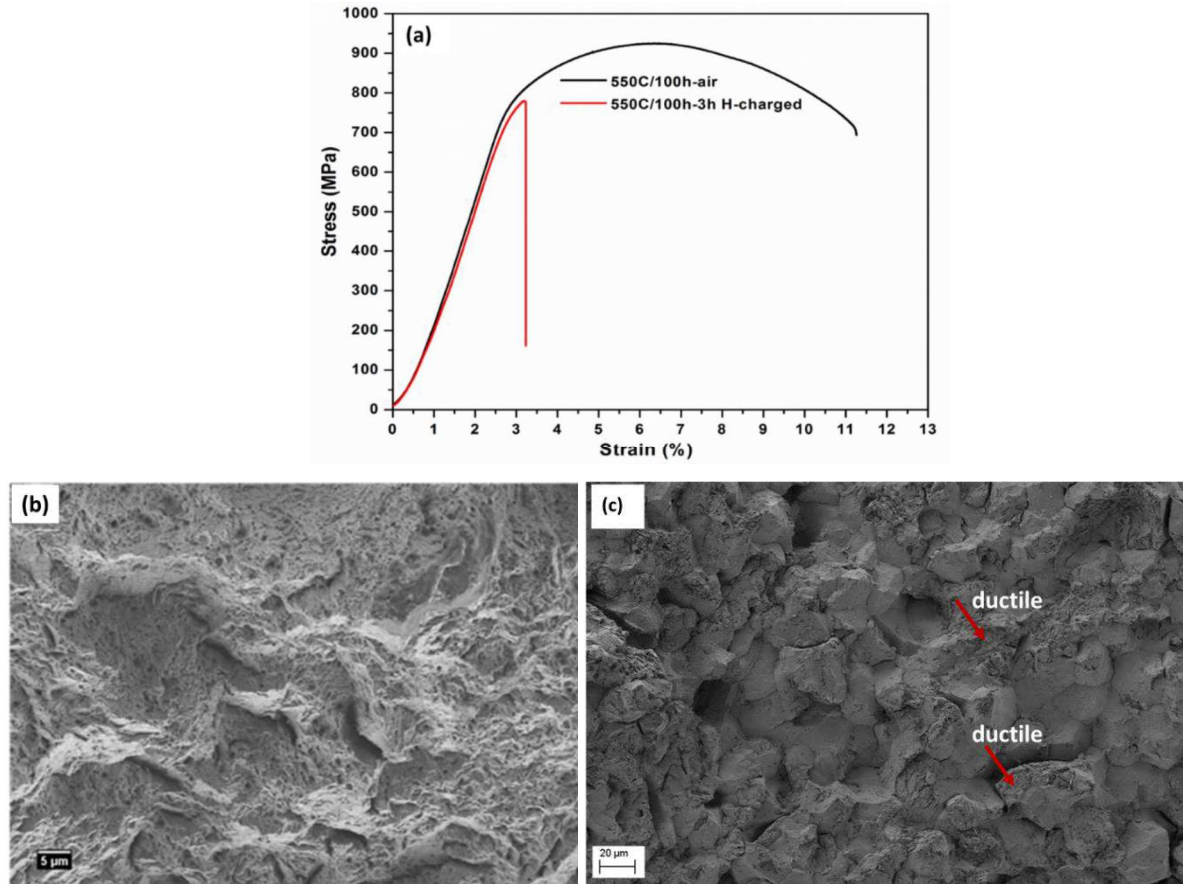


Fig. 6.15 (a) Engineering stress- strain curve of 550°C/100 h specimen in uncharged and hydrogen pre-charged for 3h conditions, fracture surface of (b) uncharged and (c) hydrogen pre-charged 550 °C/100 specimen after SSRT respectively.

Phosphorous is known to act as a hydrogen recombination poison and prevents the formation of hydrogen molecules. The segregation of P at PAG boundaries is likely to enhance the HE effects at PAG boundaries. Table 6.1 clearly shows that higher the hydrogen content in the material, higher is the extent of embrittlement. Therefore, the hydrogen content required for brittle fracture of MSS specimen is expected to decrease in presence of P segregation at PAG boundaries. Prabhu Gaonkar et al. had clearly shown that heat treatment of MSS at 550 C for 100 h had caused segregation of

P at grain boundaries (Prabhu Gaunkar *et al.*, 1980). In our study (Table 6.1.), the specimen tempered at 550 °C showed ductile fracture without hydrogen in SSRT but presence of hydrogen with impurity segregation reduced the strength and strain to failure drastically in SSRT test. The specimens tempered at 550 °C for 2.5 h and 100 h, both showed IG fracture even after 3 h hydrogen pre-charging. This IG (brittle) fracture shows that P is preferentially segregating at the PAG boundaries thereby hydrogen is decreasing the cohesive strength of the PAG boundaries. Therefore, the mechanism of HE in the specimen tempered at 550 °C is suggested to be hydrogen enhanced decohesion (HEDE).

6.3.5.2. Tempered at 700 °C

The specimen tempered at 700 °C showed higher resistance to HE. With the lower strain rates, the hydrogen transported by the mobile dislocations during plastic deformation will predominantly concentrate at the grain boundaries/martensitic laths (Wallaert *et al.*, 2014, Santos *et al.*, 2015). The fracture surface examination showed increased brittle IG region with increase of hydrogen content and as shown in Fig. 6.11.to Fig. 6.14. This showed that the hydrogen absorbed on the subsurface during the electrochemical charging predominantly accumulated at the PAG boundaries during plastic deformation. Nagao *et al.* reported that IG fracture will initiate when the slip systems intersect the PAG boundaries whereas quasi cleavage occurs when slip systems intersect with lath boundaries (Nagao *et al.*, 2014). The initiation of IG or quasi cleavage fracture is dictated by where the local stress accentuation along with the required hydrogen accumulation is attained first (Nagao *et al.*, 2014).

As shown in Fig. 3.16(d), the 700 °C tempered MSS has more than 85% of high angle grain boundaries which include lath and PAG boundaries. It is reported that the PAG boundaries with high misorientation angles in a lath martensitic steel hinder the dislocation movements effectively

and cause greater accumulation of hydrogen near the boundaries with hydrogen transported by mobile dislocations (Bernabal *et al.*, 1993, Luu *et al.*, 1996, Nanninga *et al.*, 2010). A critical concentration of trapped hydrogen at these boundaries reduces the cohesive strength of the grain boundary, decreases the fracture initiation stress and promotes IG cracking and quasi cleavage fracture depending on whether slip systems are interacted first with PAG boundaries or martensitic laths (Santos *et al.*, 2015, Nagao *et al.*, 2014). Hydrogen entered the lattice acts as an interstitial atom and raises the solid solution strength (Ueji *et al.*, 2002). But as shown in the Table 6.1, hydrogen slightly decreased the YS and UTS of 700 °C tempered condition after 17 h hydrogen charging, which may be due to hydrogen enhanced IG cracking/decohesion. The slight decrease in the YS and UTS of 700 °C tempered MSS with 9 wppm hydrogen could be due to the crack initiation in the elastic regime itself. A critical concentration of trapped hydrogen at these boundaries is necessary to initiate a crack or to reduce the cohesive strength of the grain boundaries followed by cracking along the grain boundaries.

The hydrogen concentration in the 700 °C tempered MSS is increased with pre-charging duration and caused reduced strain after onset of yielding by promoting IG cracking along the PAG boundaries. The similar behavior of reduced strain to failure with no significant change in the YS /UTS with the hydrogen is also observed in other alloy systems (Marchetti *et al.*, 2011, Depover *et al.*, 2016). The occurrence of elongated dimples by MVC as shown in Fig. 6.11 & Fig. 6.12 and brittle IG regions in the fracture surface of hydrogen pre-charged specimens suggests occurrence of both hydrogen enhanced localized plasticity (HELP) and hydrogen enhanced decohesion (HEDE) mechanisms for internal HE phenomenon in 700 °C tempered MSS with lath martensitic microstructure. At higher hydrogen concentrations of 8.1 and 9 wppm, HEDE is the dominant mechanism in 700 °C tempered MSS as shown in fracture surfaces of 15 h and 17 h hydrogen pre-

charged specimens (Fig. 6.13 and Fig. 6.14). The extent of the IG brittle zone present at the edge of the specimen increased with increase of hydrogen content indicating that the hydrogen is accumulated preferentially along PAG boundaries. Wang et al. also showed that the hydrogen preferentially accumulates at the martensite lath and PAG boundary (Wang *et al.*, 2013). During the tensile testing with slow strain rate, some amount of the diffusible hydrogen will escape from the tensile specimen. Fig. 6.9(b) shows the bulk hydrogen content present in the specimen at the time of fracture. The strain to failure decreased to 3.7% with total hydrogen content of 9 wppm, trapped at reversible and irreversible traps (depending on the activation energies of the trapping sites) in the 700 °C tempered MSS. But the actual hydrogen concentration present in the tensile specimen before starting of the SSRT experiment is much higher (around 40 wppm in 15 h pre-charged specimen, measured after hydrogen pre-charging on small coupons) than the measured hydrogen in fracture surface. This is due to out-gassing of hydrogen from the fracture surface and also its escape from the tensile specimen during the SSRT test. Even though, with 9 wppm of total internal hydrogen, total strain to failure is 3.7% but the actual mobile hydrogen concentration (trapped at reversible sites) responsible for loss in ductility is less than 9 wppm.

The solubility limit of the hydrogen in the ferrite matrix is ~1 wppm at ambient conditions (Tiwari *et al.*, 2000) and measured value of total bulk hydrogen in all the pre-charged conditions in the present study is more than 1 wppm (Table 6.1.). The large amount of the hydrogen, higher than the equilibrium concentration, can be retained at the room temperature in steels because of the presence of the numerous structural defects such as precipitates, grain boundaries, micro voids, alloying elements, vacancy, interfaces and dislocations etc. which trap hydrogen effectively (Tiwari *et al.*, 2000).

6.3.6. Effect of hydrogen charging during straining on MSS tempered at 700 °C

The MSS specimen tempered at 700 °C for showed higher resistance to internal HE. The effect of hydrogen charging with different cathodic current densities are also studied to understand the tempered MSS susceptibility to external HE where the hydrogen is picked up from the environment.

Table 6.2 shows the mechanical properties of tempered MSS with different cathodic current densities during straining. The results showed that the strain to failure and UTS, both are decreased with increasing cathodic current density as shown in Table 6.2. The tempered MSS with 5 and 20 mA/cm² cathodic current densities during straining fractured in the elastic regime whereas the specimen charged with lower current densities of 0.01 mA/cm² showed ductility before final fracture.

Table 6.2 Mechanical properties of tempered MSS in air and with different cathodic current densities during straining with a strain rate of 1×10^{-6} /s.

Current density (mA/cm ²)	YS (MPa)	UTS (MPa)	Strain to failure (%)	HEI (%)	Time to fracture (h)
0	602	743	14.4	-	40
0.01	579	759	8.74	39.3	24.27
5	-	477	3.27	77.3	9.08
20	-	369	2.43	81.1	6.75

The sharp decrease in the strength and ductility during simultaneous hydrogen charging and straining indicates that the tempered MSS suffers severe hydrogen embrittlement in the presence of strain. A similar kind of behavior is also reported by other researchers for high strength maraging steels (Wang *et al.*, 2013, Santos *et al.*, 2015). The fracture surfaces with higher cathodic

current densities (5 and 20 mA/cm²) are completely brittle (IG) and cracking is along the PAG boundaries as shown in Figs. 6.16 & 6.17.

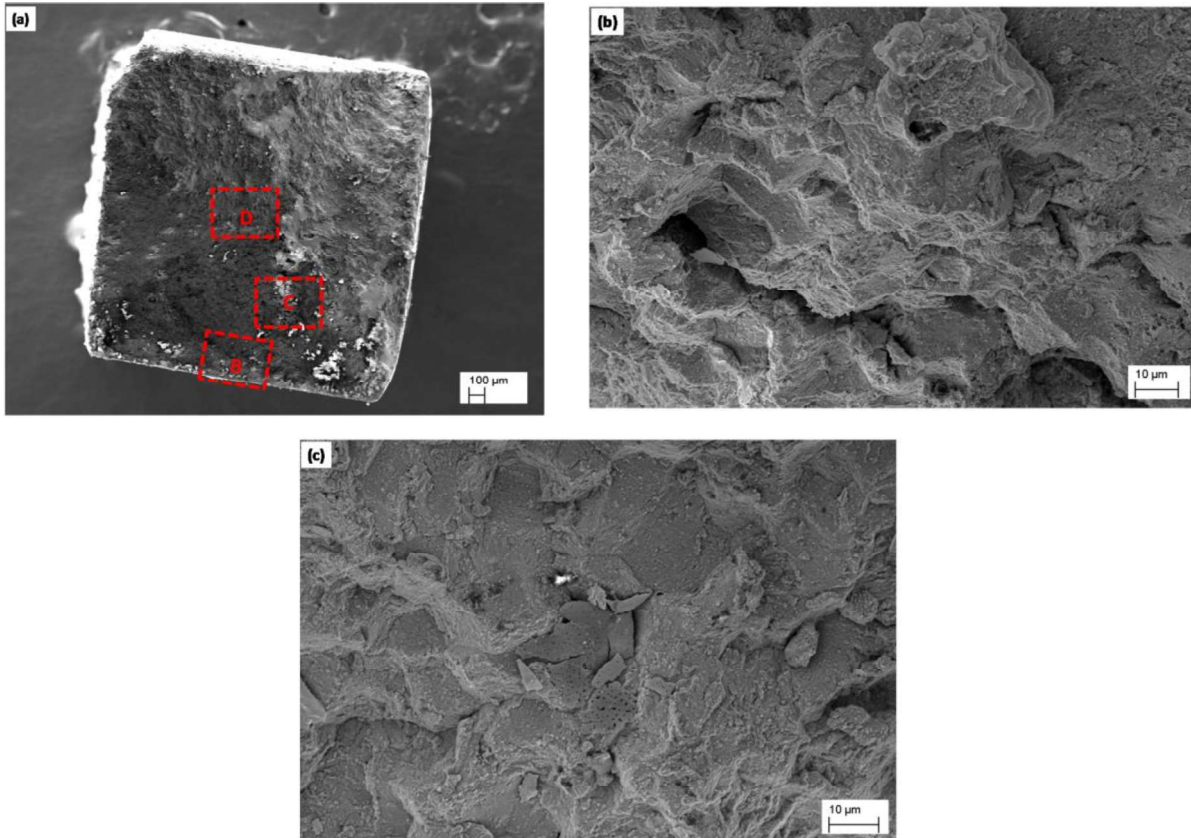


Fig. 6.16 SEM images of the fracture surface of the tempered specimen tested at 20 mA/cm² (a) fracture head showing brittle fracture, (b) and (c) are the magnified images corresponding to regions marked as B and C in image (a) showing IG cracking along prior austenite grain boundaries.

The fracture surface (Fig. 6.18(a)) with 0.01 mA/cm² current density showed a mixture of IG features along the PAG boundaries at the edge regions (Fig. 6.18(b)-(c)) and ductile features with MVC in the middle portion of the fracture surface as shown in Fig. 6.18(d). The fracture surface is exposed to the test solution after the fracture of the tempered specimen and is covered with the corrosion products as shown in the fracture surfaces of Figs. 6.16 to Fig. 6.18.

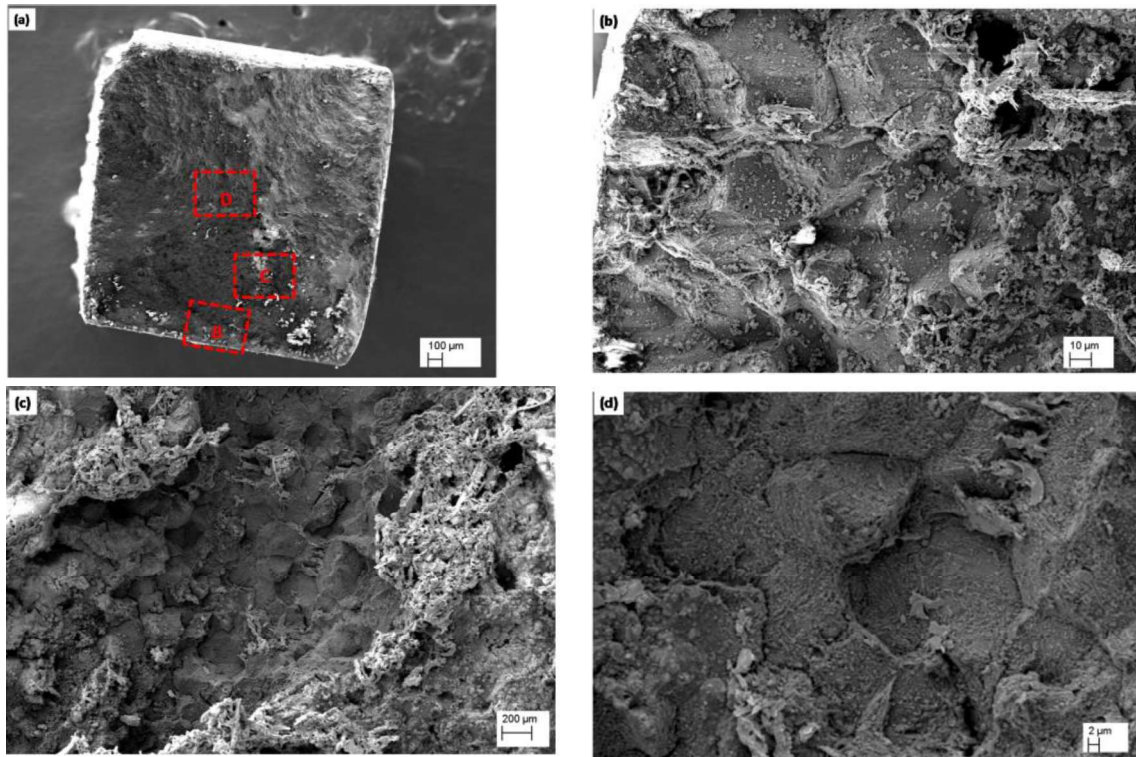


Fig. 6.17 SEM images of the fracture surface of the tempered MSS tested at 5 mA/cm² (a) fracture head showing brittle fracture, (b), (c) and (d) are the magnified images corresponding to regions marked as B, C and D in image (a) showing IG cracking along prior austenite grain boundaries.

As compared to hydrogen pre-charging, the tempered MSS suffered severe HE in the presence strain and hydrogen. The tempered MSS showed IG fracture with 5 and 20 mA/cm² cathodic current densities during straining and fractured in the elastic regime. The time to failure decreased with increase of cathodic current density during straining as shown in Table 6.2. The tempered MSS fractured in 6.75 h with cathodic current density of 20 mA/cm² during straining whereas 15 h hydrogen pre-charged specimen at 20 mA/cm² fractured in 22.2 h. The concentration of the subsurface hydrogen increases with increase in cathodic current density and the presence of stress/strain increase the diffusion of hydrogen into the specimen (Marchetti *et al.*, 2011). Marchetti *et al.* reported that presence of strain during charging process increased the hydrogen trapping rate on pre-existed traps and strain induced traps such as dislocations (Marchetti *et al.*, 2011). In the present study, the tempered MSS cathodically charged with 5 and 20mA/cm² during

straining showed IG fracture in the elastic region. The presence of the strain in the elastic region is not expected to increase the strain induced trap sites but the permeation of hydrogen flux inside the specimen increases due to lattice expansion, as it can accommodate higher amount of hydrogen. The effect of increased permeation rates with strain are also reported in other alloys (Kim *et al.*, 2014, Kim *et al.*, 2014a).

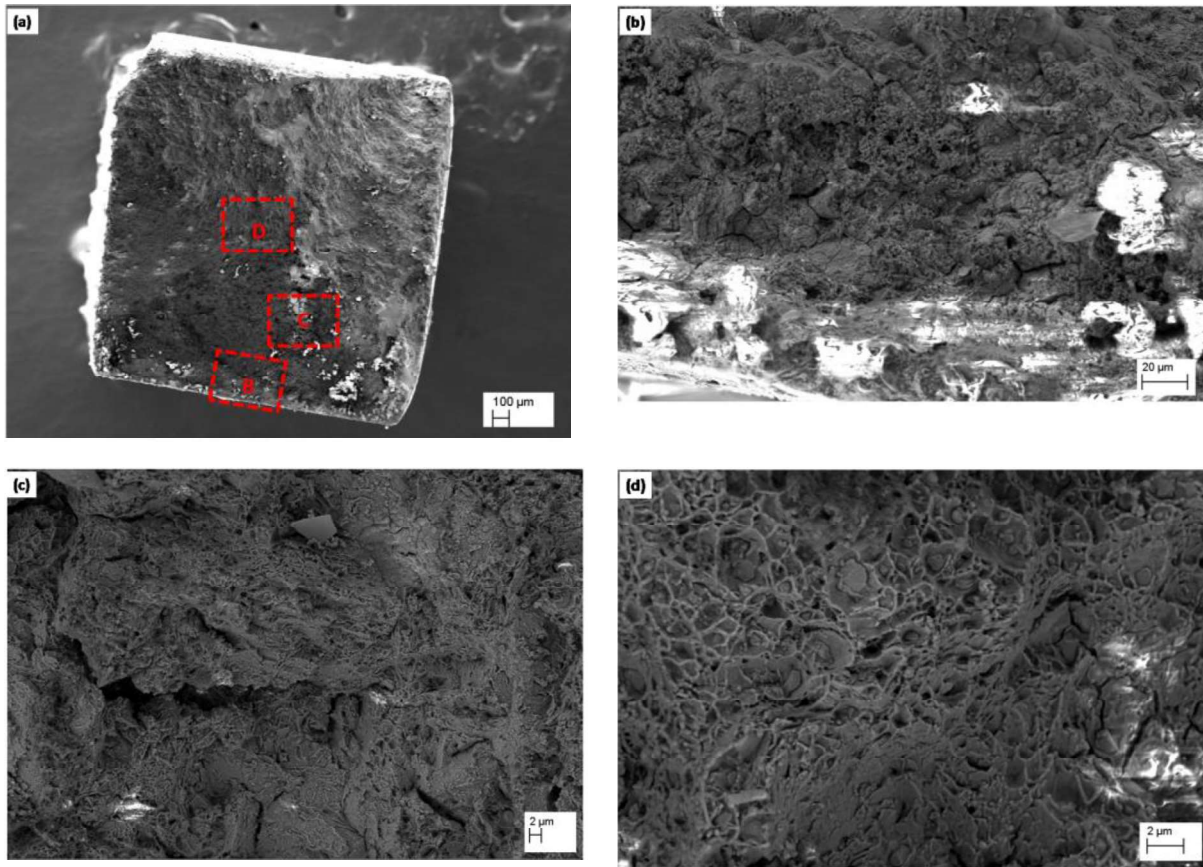


Fig. 6.18 SEM images of the fracture surface of the tempered MSS tested at $0.01\text{mA}/\text{cm}^2$ (a) fracture head showing mixed fracture, (b), (c) and (d) are the magnified images corresponding to regions marked as B, C and D in image (a) showing IG cracking along prior austenite grain boundaries at edges and ductile fracture in the central region.

The diffusible hydrogen concentration generated at the surface of the specimen is less with the lower cathodic current density of $0.01\text{ mA}/\text{cm}^2$. Hence, the hydrogen diffused into the matrix was different at the edges and mid portion of the specimen. The fracture surface examination showed

extent of IG zone is up to 400 μm (Fig. 6.18(a)) from the edge of the fracture surface in 0.01mA/cm². The brittle IG fracture surfaces with higher cathodic current densities showed that the hydrogen concentration is maximum at the PAG boundaries and hydrogen concentration increased with charging current density. The presence of hydrogen at the grain boundaries decreases the cohesive strength. When the hydrogen concentration reaches a critical value at the grain boundary, the cohesive strength at the grain boundary decreases and if it is less than the stress seen by the specimen during SSRT, then the IG crack initiates and will propagate along the grain boundary or lath boundary. The propagation of hydrogen induced crack again depends on the distribution of hydrogen e.g. martensitic lath, resulting in quasi cleavage fracture (Nagao *et al.*, 2014, Santos *et al.*, 2015). The diffusion coefficient of hydrogen also changes within the specimen matrix during straining (Marchetti *et al.*, 2011). This might be due to stress induced hydrogen diffusion in the specimen during straining. Once the hydrogen induced crack is initiated, there is a stress concentration ahead of the crack and the hydrogen diffuses assisted by mobile dislocations. The hydrogen concentration during strain also plays a crucial role in the HE susceptibility of tempered MSS. Based on the observations in the present study, the HEDE is the dominant mechanism for HE of tempered MSS when simultaneous presence of hydrogen and strain and is dependent on hydrogen concentration at the surface. The interesting observation in the fracture surface examination of specimens with different pre-charging durations and with different current densities during tensile testing is appearance of IG region from the edge of the specimen's fracture surface.

6.4. Highlights

The influence of tempering treatments on mechanical properties and hydrogen embrittlement of 13wt.% Cr martensitic stainless steel is investigated by Charpy impact tests and slow strain rate tensile tests under hydrogen charging during straining and also on hydrogen pre-charged specimens. The fracture examination and measurement of hydrogen content was done to identify the nature of fracture and the hydrogen embrittlement mechanism. The following conclusions are drawn:

1. The strain to failure increased with increasing tempering temperature whereas yield strength and ultimate tensile strength decreased in tensile tests. Tempering at 550 °C showed brittle intergranular fracture with grain boundary cracks in the impact test and is inferred to be due to impurity segregation at prior austenite grain boundaries.
2. The austenitized condition is highly susceptible to hydrogen embrittlement and showed cracking during hydrogen pre-charging.
3. The susceptibility to hydrogen embrittlement depends not only on the strength but also on microstructure. Drastic reduction in strength and strain to failure is observed for specimen tempered at 550 °C after hydrogen pre-charging as compared to specimens tempered at 300 and 700 °C This is due to synergistic interaction of hydrogen with impurity segregation at 550 °C. The critical hydrogen required for brittle fracture of MSS specimen decreased in presence of impurity segregation.
4. The hydrogen pre-charging caused embrittlement of 13wt% Cr martensitic stainless steel. The strain to failure was significantly reduced from 14.4% to 3.7% with 9 wppm of bulk hydrogen. The yield strength and ultimate tensile strength did not change significantly. The fracture surface examination showed a transition from ductile microvoid coalescence to brittle intergranular cracking along the prior austenite grain boundaries with increase of hydrogen content in hydrogen pre-charged specimens of MSS tempered at 700 °C.

5. The hydrogen charging during straining severely embrittled the tempered 13wt.% Cr martensitic stainless steel as the strain to failure and strength both decreased with increased hydrogen charging during straining. The severity of hydrogen embrittlement depends on the cathodic current density. The fracture surface examination showed transition from the brittle intergranular facets to mixed morphology of the ductile dimples and intergranular facets with decrease of cathodic current density during straining.
6. Fracture surface examination of tempered martensitic stainless steel with different hydrogen pre-charging durations and with different cathodic current densities during slow strain rate testing showed the appearance of intergranular region from the edge of the specimen's fracture surface where hydrogen had diffused in.
7. Hydrogen enhanced decohesion (HEDE) is the primary mechanism for internal hydrogen embrittlement (hydrogen pre-charged) and external hydrogen embrittlement (hydrogen charged during straining) of 13wt% Cr martensitic stainless steel tempered at 700 °C. The cracking is shown to be along the prior austenite grain boundaries.

Conclusions

The present study is focused on understanding the microstructural changes and its influence on localized corrosion behavior and HE of 13wt.% Cr MSS austenitized and tempered at different temperatures. Detailed characterization of microstructural changes occurred during tempering have been done using TEM, XRD and SEM-EBSD. The susceptibility to IGC with tempering was evaluated by immersion tests and also using electrochemical tests in different electrolytes. Pitting corrosion studies were done in 0.1 M NaCl solution using anodic polarization techniques. Detailed characterization of exposed surfaces was carried out using different techniques such as SEM, XRD and XPS to explain the nature of attack and degradation mechanism. The changes in room temperature mechanical properties with tempering temperature have been evaluated by SSRT tests, hardness measurements and impact tests followed by fracture surface examination. The susceptibility to HE with tempering has been established by SSRTs on hydrogen pre-charged specimens and also by varying the cathodic current density during straining followed by fracture surface examination. The hydrogen content in fracture surface was measured using IGF technique. Based on the studies carried out on 13wt.% Cr MSS, the following overall conclusions are drawn:

- 1) Austenitization at 1020 °C resulted in lath martensite structure with retained austenite at lath interfaces and undissolved $M_{23}C_6$ carbides. Austenitization at 1040 °C and above resulted in quench cracks along prior austenite grain boundaries.

- 2) The retained austenite fraction decreased with tempering temperature and no retained austenite observed after tempering at and above 550 °C.
- 3) Tempering resulted in formation of (a) nano-sized Fe-rich M_3C carbides, mainly within the martensitic laths at 300 °C, (b) nano-sized Cr-rich $M_{23}C_6$ carbides inside and at martensitic lath interfaces at 550 °C and (c) sub-micron sized Cr-rich $M_{23}C_6$ carbides mainly at martensitic lath interfaces at 700 °C.
- 4) The nano-sized Cr-rich carbides were associated with a narrow depletion zone of 7-9 nm at carbide - matrix interface regions and the Cr concentration in the depleted regions fell to around 76% of the Cr concentration in the matrix.
- 5) Tempering above 450 °C resulted in interlath corrosion in 5% HNO_3 immersion tests. Tempering at 550 °C resulted in a higher corrosion rate and higher DL-EPR value and the preferential attack was along the martensite lath interfaces. Immersion tests, anodic polarization and DL-EPR tests confirmed desensitization above tempering temperature of 550 °C.
- 6) Anodic polarization studies in 5% HNO_3 solution also indicated occurrence of sensitization with tempering. The surface films formed at a passive potential in 5% HNO_3 solution were rich in Fe for 550 °C tempered condition as compared to that formed on austenitized condition.
- 7) Pitting resistance for tempered condition was lower than for the austenitized condition with least pitting resistance when tempered at 550 °C. The metastable pitting frequency increased with increase of carbide interfaces associated with Cr-depletion. The Fe/Cr ratio of the surface film was higher for tempered condition than for the austenitized condition.
- 8) The least localized corrosion (intergranular and pitting) resistance after tempering at 550 °C was due to massive nano-sized Cr-rich carbide precipitation associated with Cr-depletion and formation of less protective Fe-rich surface film.

- 9) Tempering treatments improved the ductility but decreased the strength and hardness. Temper embrittlement appeared in 550 °C tempered condition with a low impact toughness value and brittle intergranular fracture.
- 10) Temper embrittled condition was highly susceptible to hydrogen embrittlement, both strength and strain to failure decreased with hydrogen content and showed a brittle intergranular fracture even after hydrogen pre-charging for 1 h.
- 11) Tempering at 700 °C improved the resistance to hydrogen embrittlement, however its susceptibility increased with increased hydrogen content. Compared to internal (pre-charged) hydrogen, presence of hydrogen during straining drastically reduced the ductility and yield strength of 700 °C tempered condition.
- 12) Fracture surface examination of tempered martensitic stainless steel with different hydrogen pre-charging durations and with different cathodic current densities during slow strain rate testing showed the appearance of intergranular region from the edge of the specimen's fracture surface where hydrogen had diffused in.
- 13) Hydrogen enhanced decohesion (HEDE) is indicated to be the main mechanism for internal (hydrogen pre-charged) and external hydrogen embrittlement (hydrogen charged during straining) of tempered MSS.

The results obtained in the present study suggest that 13wt.% Cr MSS when tempered at 700 °C, provides optimum mechanical properties, moderate resistance to localized corrosion and hydrogen embrittlement.

SCOPE FOR FUTURE WORK

The work reported in this thesis relevant to understanding the microstructural changes and its influence on localized corrosion behavior and HE of 13wt.% Cr MSS austenitized and tempered at different temperatures. In this study, microstructural changes occurred at 300, 550 and 700 °C for fixed duration of 2.5 h were characterized in depth and correlated to corrosion behavior and HE of 13wt.% Cr MSS. Some future studies which are required to be done are listed below.

- Microstructural changes after tempering from 450 to 500 °C, 500 to 550 °C and 550 to 600 °C to know the carbide transformation mechanisms.
- Detection of P- segregation at PAGBs in 13wt.% Cr MSS tempered at 550 °C using atom probe field ion microscopy and correlating with electrochemical methods.
- Effect of tempering duration at 700 °C on microstructure, mechanical properties and corrosion behavior to choose optimum tempering duration.
- Susceptibility to SCC of 13wt.% Cr tempered at 700 °C in simulated PWR environment.

REFERENCES

- Abe F, Bainitic and martensitic creep-resistant steels, *Curr. Opin. Solid State Mater. Sci.* 8 (2004) 305-311.
- Adhe K. M, Kain V, Madangopal K, Gadiyar H. S, Influence of sigma-phase formation on the localized corrosion behavior of a duplex stainless steel, *J. Mater. Eng. Perform.* 5 (4) (1996) 500-506.
- Adhe K. M, Shibad P. R, Kain V, Chouthai S. S, Gadiyar H. S, Effect of isothermal heat treatment on sensitization behavior of AISI 304 stainless steel, *J. Electrochem. Soc. India.* 37 (3) (1998) 215-219.
- Aghuy A. A, Zakeri M, Moayed M. H, Mazinani M, Effect of grain size on pitting corrosion of 304L stainless steel, *Corros. Sci.* 94 (2015) 368-376.
- Ahmedabadi P. M, Kain V, Dangi B. K, Samajdar I, Role of grain boundary nature and residual strain in controlling sensitization of type 304 stainless steel, *Corros. Sci.* 66 (2013) 242-255.
- Akashi M, Kawamoto T, Umemura F, Gijutsu B, Evaluation of IGSCC susceptibility of austenitic stainless steels using electrochemical reactivation method; *Corros. Eng.* 29 (1980) 163-169.
- Alonso-Falleiros N, Magri M, Falleiros I.G.S, Intergranular corrosion in a martensitic stainless steel detected by electrochemical tests, *Corrosion* 55 (1999): p. 769.
- Anjos A. D, Scheuer C. J, Brunatto S. F, Cardoso R. P, Low-temperature plasma nitro carburizing of the AISI 420 martensitic stainless steel: Microstructure and process kinetics, *Surf. Coat. Technol.* 275 (2015) 51-57.

- Aquino J. M, Della Rovere C. A, Kuri S. E, Intergranular corrosion susceptibility in super martensitic stainless steel weldments; *Corros. Sci.* 51 (2009) 2316–2323.
- Arutunow A, Darowicki K, DEIS evaluation of the relative effective surface area of AISI 304 stainless steel dissolution process in conditions of intergranular corrosion; *Electrochim. Acta* 54 (2009) 1034–1041.
- Arutunow A, Darowicki K, Zielinski A (2011), Atomic force microscopy based approach to local impedance measurements of grain interiors and grain boundaries of sensitized AISI 304 stainless steel; *Electrochim. Acta* 56, 2372–2377.
- Asami K, Hashimoto K, An X-ray photo-electron spectroscopic study of surface treatments of stainless steels, *Corros. Sci.* 19 (1979) 1007-1017.
- ASTM, A 262 (1989) 1-16, Standard practices for detecting susceptibility to intergranular attack in austenitic stainless steels, Annual book of ASTM standards.
- ASTM, A 763 (2004) 1-10, Standard practices for detecting susceptibility to intergranular attack in ferritic stainless steels, Annual book of ASTM standards.
- ASTM, A276/A276M-16a (2016) 1-8, Standard specifications for stainless steel bars and shapes, Annual book of ASTM standards.
- ASTM, E23-07a (2007) 1-28, Standard test method for notched bar impact testing of metallic materials, Annual book of ASTM standards.
- Avner S. H, Introduction to physical metallurgy, 2nd Ed, Mcgraw Higher Ed., (1997).
- Bain E. C, Aborn R. H, Rutherford J. B, The nature and prevention of intergranular corrosion in austenitic stainless steels, *Trans. Am. Soc. Steel Treat.* 21 (1933) 481-509.

- Bal B, Koyama M, Gerstein G, Maieer H. J, Tsuzaki T, Effect of strain rate on hydrogen embrittlement susceptibility of twinning-induced plasticity steel pre-charged with high-pressure hydrogen gas, *Int. J. Hydrogen Energ.* 41 (34) (2016) 15362-15372.
- Balan K. P, Reddy A. V, Sarma D. S, Austenite precipitation during tempering in 16Cr-2Ni martensitic stainless steel, *Scr. Mater.* 39 (9) (1998) 901-905.
- Bandyopadhyay N, Kameda J, McMohan C.J, Jr, Hydrogen- induced cracking in 4340-Type steel: Effects of composition, yield Strength, and H₂ pressure, *Metall. Trans.* 14A (1983) 881-888.
- Barbadikar D. R, Deshmukh G. S, Maddi L, Laha K, Parameswaran P, Ballal A. R, Peshwe D. R, Paretkar R. K, Nandagopal M, Mathew M.D, Effect of normalizing and tempering temperatures on microstructure and mechanical properties of P92 steel, *Int. J. Press. Vessel Pip.* 32-133 (2015) 97-105.
- Barlow L. D, Toit M. D, Effect of austenitizing heat treatment on the microstructure and hardness of martensitic stainless steel AISI 420, *J. Mater. Eng. Perform.* 21 (2012) 1327-1336.
- Behbahani K. M, Najafisayar P, Pakshi M, Study of the intergranular corrosion of sensitized UNS S31803 stainless steel in transpassive region; *J. Mater. Eng. Perform.* 25 (8) (2016) 3418-3429.
- Bernabal U., Biggiero G, Torella R, Thermal analysis on hydrogen charged annealed and hardened AISI 420 stainless steel, *Metall. Sci. Tech.* 11 (2) (1993) 70-77.
- Bhadeshia H. K. D. H, Prevention of hydrogen embrittlement in steels, *J. Iron Steel Inst. Int.* 56 (2016) 24-36.

- Bhambri S. K, Intergranular fracture in 13 wt.% chromium martensitic stainless steel, J. Mater. Sci. 21 (1986) 1741-1746.
- Bhambroo R, Roychowdhury S, Kain V, Raja V. S, Effect of reverted austenite on mechanical properties of precipitation hardenable 17-4 stainless steel, Mater. Sci. Eng. A 568 (2013) 127- 133.
- Biggiero G, Borruto A, Taraschi I, Effects of hydrogen charging methods on ductility and fracture characteristics of AISI 9840 steel, Int. J. Hydrogen Energ. 20 (1995) 465-470.
- Birnbaum H. K, Hydrogen effects on deformation and fracture, MRS Bull. 28 (7) (2003) 479-485.
- Briant C. L, Banerji S. K, Intergranular failure in steel: the role of grain boundary composition, Inter. Met. Rev. (1978) 164-199.
- Bruemmer S. M, Charlot L. A, Development of grain boundary chromium depletion in type 304 and 316 stainless steel, Scr. Mater. 20 (1986) 1019-1024.
- Bruemmer S. M, Microstructural and microchemical mechanisms controlling intergranular stress corrosion cracking in light-water-reactor systems, J. Nucl. Mater. 216 (1994) 348-363.
- Burstein G. T, Vines S. P, Repetitive nucleation of corrosion pits on stainless steel and the effects of surface roughness, J. Electrochem. Soc. 148 (2001) 504-516.
- Chakraborty G, Das C. R, Albert S. K, Bhaduri A. K, Thomas Paul V, Panneerselvam G, Dasgupta A, Study on tempering behavior of AISI 410 stainless steel, Mater. Charact. 100 (2015) 81–87.

- Chandra K, Kain V, Srinivasan N, Samajdar I, Balasubrahmanian A.K, Temper. embrittlement and corrosion behavior of martensitic stainless steel 420, Adv. Mater. Res. 794 (2013) 757-765.
- Chandra K, Kain V, Tewari R, Microstructural and electrochemical characterization of heat-treated 347 stainless steel with different phases, Corros. Sci. 67 (2013a) 118-129.
- Chen J, Radmilovic V, Devine T. M, A comparison of the chromium concentration on the grain boundaries in sensitized stainless steel measured by analytical electron microscopy and an electrochemical technique, Corros. Sci. 30 (1990) 477-494.
- Cheng X. Y, Zhang H. X, Li H, Shen H. P, Effect of tempering temperature on the microstructure and mechanical properties in mooring chain steel, Mater. Sci. Eng. A 636 (2015) 164-171.
- Christian J. W, Crystallographic Theories, Interface Structures, and Transformation Mechanisms. Metall. Trans. A 25 (1994) 1821-1839.
- Cihal V, A potentiokinetic reactivation method for predicting the I.G.C. and I.G.S.C.C. sensitivity of stainless steels and alloys. Corros. Sci, 20 (1980) (6) 737–744.
- Cihal V, Intergranular corrosion of steels and alloys, Materials science monographs-18, SNTL-Publishers, Prague,1984.
- Cihal V, Shoji T, Kain V, Watanabe Y, Stefec R, Electrochemical polarization reactivation technique - A comprehensive review, FRRI publishers, Sendai, 2004.
- Dadfarnia M, Novak P, Ahn D. C, Liu J. B, Sofronis P, Johnson D. D, I. M. Robertson, Recent advances in the study of structural materials compatibility with hydrogen, Adv. Mater. 22 (10) (2010) 1128-1135.

- Dadfarnia M, Sofronis P, Neeraj T, Hydrogen interaction with multiple traps: can it be used to mitigate embrittlement?, *Int. J. Hydrogen. Energ.* 36 (2011) 10141-10148.
- Davis J. R, *Stainless Steels*, ASM International, Materials Park, Ohio, 1994.
- Devover T, Verbeken K, Hydrogen trapping and hydrogen induced mechanical degradation in lab cast Fe-C-Cr alloys, *Mater. Sci. Eng. A* 669 (2016) 134-149.
- Dieter G. E, *Mechanical metallurgy*, 3rd ed., McGraw-Hill Book Company, Singapore, 1988.
- Ebrahimi N, Momeni M, Moayed M.H, Davoodi A, Correlation between critical pitting temperature and degree of sensitization on alloy 2205 duplex stainless steel, *Corros. Sci.* 53 (2) (2011) 637-644.
- Eliaz N, Shachar A, Tal B, Eliezer D, Characteristics of hydrogen embrittlement, stress corrosion cracking and tempered martensite embrittlement in high-strength steels, *Eng. Fail. Anal.* 9 (2) (2002) 167-184.
- Escobar D. P, Depover T, Duprez L, Verbeken K, Verhaege M, Combined thermal desorption spectroscopy, differential scanning calorimetry, scanning electron microscopy and X-ray diffraction study of hydrogen trapping in cold deformed TRIP steel, *Acta Mater.* 60 (2012) 2593-260.
- Escobar D. P, Verbeken K, Duprez L, Verhaege M, Evaluation of hydrogen trapping in high strength steels by thermal desorption spectroscopy, *Mater. Sci. Eng. A* 551 (2012a) 50-58.
- Felloni L, Traverso S. S, Zucchini G. L, Cammarota G. P, Investigation on the second anodic current maximum on the polarization curves of commercial stainless steels in sulphuric acid, *Corros. Sci.* 13 (1973) 773.

- Fontana M. G, Corrosion Engineering, 3rd Edition, Mc Graw-Hill Book Company, 1987.
- Frangini S, Mignone A, Modified electrochemical potentiokinetic reactivation method for detecting sensitization in 12 wt% Cr ferritic stainless steels, Corrosion 48 (1992) 715-726.
- Freire L, Carmezim M. J, Ferreira M. G. S, Montemor M. F, The passive behavior of AISI 316 in alkaline media and the effect of pH: a combined electrochemical and analytical study, Electrochim. Acta 55 (2010) 6174-6181.
- Fu Y, Wu X, Han E, Ke W, Yang K, Jiang Z, Effects of cold work and sensitization treatment on the corrosion resistance of high nitrogen stainless steel in chloride solutions, Electrochim. Acta. 54 (2009) 1618-1629.
- Garcia de Andres C, Caruana G, Alvarez L. F, Control of $M_{23}C_6$ carbides in 0.45C-13Cr martensitic stainless steel by three representative heat treatments, Mater. Sci. Eng. A 241 (1-2) (1998) 211-2015.
- Ghods P, Isgor O. B, Brown J. R, Bensebaa F, Kingston D, XPS depth profiling study on the passive oxide film of carbon steel in saturated calcium hydroxide solution and the effect of chloride on the film properties, Appl. Surf. Sci. 257 (2011) 4669-4677.
- Gillard E. T, Benoit M, Clavier P, Gwinner B, Miserque F, Vivier V, Kinetics of the oxidation of stainless steel in hot and concentrated nitric acid in the passive and transpassive domains, Corros. Sci. 107 (2015) 182-192.
- Hall L, Briant C. L, Chromium depletion in the vicinity of carbides in sensitized austenitic stainless steels, Metall. Trans. A 15 (1984) 793-811.
- Hermas A. A, Morad M. S, Ogura K, A correlation between phosphorous impurity in stainless steel and a second anodic current maximum in H_2SO_4 , Corros. Sci. 41 (1999) 2251-2266.

- Higgins R. A, Engineering Metallurgy, Part 1- Applied Physical Metallurgy, 5th ed., Hodder & Stoughton, New York, 1983.
- Hipsley C. A, Haworth N. P, Hydrogen and temper embrittlement in 9Cr-1Mo steel, Mater. Sci. Technol. 4 (9) (1988) 791-802.
- Honeycombe R. W. K, Bhadeshia H. K. D. H, Steels microstructure and properties. 2nd ed. London, Edward Arnold, 1995.
- Inthidech S, Sricharoenchai P, Matsubara Y, Effect of alloying elements on heat treatment behavior of hypoeutectic high chromium cast iron, Mater. Trans. 47 (1) (2006) 72-81.
- Irvine K. J, Crowe D. J, Pickering F. B, The physical metallurgy of 12% chromium steels, J. Iron Steel Inst. 195 (1960) 386–405.
- Isfahany A. N, Saghafian H, Borhani G, The effect of heat treatment on mechanical properties and corrosion behavior of AISI 420 martensitic stainless steel, J. Alloys Comp. 509 (2011) 3931-3936.
- Janovec J, Svoboda M, Blach J, Evolution of secondary. phases during quenching and tempering 12% Cr steel, Mater. Sci. Eng. A 249 (1998) 184–189.
- Jung P, Hydrogen inventory and embrittlement in low activation steels, J. Nucl. Mater. 124 (9) (1998) 258-263.
- Jung R. H, Tsuchiya H, Fujimoto S, XPS characterization of passive films formed on Type 304 stainless steel in humid atmosphere, Corros. Sci. 58 (2012) 62-68.
- Kain V, Chandra K, Adhe K. N, De P. K, Detecting classical and martensite-induced sensitization using the electrochemical potentiokinetic reactivation test, Corrosion. 61(6) (2005) 587-593.

- Kain V, Chandra K, Adhe K. N, De P. K, Effect of cold work on low-temperature sensitization behaviour of austenitic stainless steels, *J. Nucl. Mater.* 334 (2004a) 115-132.
- Kain V, Chouthai H. S, Gadiyar H. S, Performance of AISI 304L stainless steel with exposed end grain in intergranular corrosion tests; *Br Corrosion J.* 27 (1992) (1) 59 - 65.
- Kain V, Sensitization and susceptibility of austenitic stainless steels to intergranular corrosion and intergranular stress corrosion cracking, Ph. D thesis, 1997.
- Kain V, Watanabe Y, Development of a single loop EPR test method and its relation to microchemistry for alloy 600, *J. Nucl. Mater.* 302 (2002) 49-59.
- Kain V. Palit G. C, Choutai S. S, Gadiyar H. S, Effect of heat treatment on the critical pitting potential of SS 304 in 0.1M NaCl, *J. Electrochem. Soc. India.* 12 (38) (1989) 50-54.
- Kim H, Jeon S, Kim S, Park Y, Influence of the shielding gas composition on the passive film and erosion corrosion of tube-to-tube sheet welds of hyper duplex stainless steel, *Corros. Sci.* 91 (2015) 140-150.
- Kim S. J, Kim K. Y, A review of corrosion and hydrogen diffusion behaviors of high strength pipe steel in sour environment, *J. Weld. Join.* 32 (5) (2014a) 13-20.
- Kim S. J, Yun D. W, Jung H. G, Kim K. Y, Determination of hydrogen diffusion parameters of ferritic steel from electrochemical permeation measurement under tensile loads, *J. Electro. Soci.* 161 (12) (2014) 173-181.
- Kose C, Kacar R, The effect of preheat & post weld heat treatment on the laser weldability of AISI 420 martensitic stainless steel, *Mater. Desi.* 64 (2014) 221–226.
- Krauss G, *Steels heat treatment and processing principles.* Materials Park (OH), ASM International, 1990.

- Lai C. L, Tsay L. W, Chen C, Effect of microstructure on hydrogen embrittlement of various stainless steels. *Mater. Sci. Eng. A* 584 (1) (2013) 14-20.
- Li D. G, Wang J. D, Chen D. R, Influence of pH value on the structure and electronic property of the passive film on 316L SS in the simulated cathodic environment of proton exchange membrane fuel cell (PEMFC), *Int. J. Hydrogen. Energ.* 39 (2015) 20105-20115.
- Li Q. F, Li L, Liu E, Liu D, Cui X. F, Temper embrittlement dynamics induced by non-equilibrium segregation of phosphorus in steel 12Cr1MoV, *Scr. Mater.* 53 (3) (2005) 309-313.
- Li X, Zhang J, Shen S, Wang Y, Song X, Effect of tempering temperature and inclusions on hydrogen- assisted fracture behavior of low alloy steel, *Mater. Sci. Eng. A* 682 (2017) 359-369.
- Lim L. C, Lai M. O, Ma J, Tempering of AISI 403 stainless steel, *Mater. Sci. Eng. A* 171 (1993) 13-19.
- Lippold C, Kotecki D. J, *Welding metallurgy and weldability of stainless steels*, John Wiley & Sons Inc., 2005.
- Liu C. T, Wu J. K, Influence of pH on the passivation behavior of 254SMO stainless steel in 3.5% NaCl solution, *Corros. Sci* 49 (2007) 2198-2209.
- Liu Q, Andrej A, A critical review of the influence of hydrogen on the mechanical properties of medium-strength steels, *Corros. Rev.* 31(3-6) (2013) 85-103.
- Liu Q, Atrens A. D, Shi Z, Verbeken K, Atrens A, Determination of the hydrogen fugacity during electrolytic charging of steel, *Corros. Sci.* 87 (2014) 239-258.

- Liu X. Y, Kameda J, Anderegg J. W, Takaki S, Abiko K, McMohan Jr C. J, Hydrogen induced cracking in a very- high-purity high-strength steel, *Mater. Sci. Eng. A* 492 (2008) 218-220.
- Lo K. H, Kwok C. T, Chan W. K, Characterization of duplex stainless steel subjected to long-term annealing in the sigma phase formation temperature range by the DL-EPR test, *Corros. Sci.* 53 (2011) 3697-3703.
- Lorang G, Da Cuhna Belo M, Simoes A. M. P, Chemical composition of passive films on AISI 304 stainless steel, *J. Electrochem. Soc.* 141 (1994) 3347-3356.
- Louthan M. R Jr, Hydrogen embrittlement of metals: a primer for the failure analyst, *J. Fail. Anal. Prev.* 8 (2008) 289–307.
- Lu S, Yao K, Chen Y, Wang M, Chen N, Ge X, Effect of quenching and partitioning on the microstructure evolution and electrochemical properties of a martensitic stainless steel, *Corros. Sci.* 103 (2016) 95-104.
- Lu S, Yao K, Chen Y, Wang M, Chen N, Ge X, Influence of heat treatment on the microstructure and corrosion resistance of 13 wt.% Cr-type martensitic stainless steel, *Metall. Meta. Trans. A* 46 (2015a) 6090-6101.
- Lu S, Yao K, Chen Y, Wang M, Chen N, Ge X, Liu X, Ge X, Effect of tempering treatments on microstructure and electrochemical properties of 13 wt.% Cr-type, martensitic stainless steel, *Electrochim. Acta* 165 (2015) 45-55.
- Luu W. C, Wu J. K, The influence of microstructure on hydrogen transport in carbon steels, *Corros. Sci.* 38 (2) (1996) 239-245.
- Lv J, Liang T, Wang C, Guo T, Influence of sensitization on passive films in AISI 2205 duplex stainless steel, *J. Alloys Comp.* 658 (2016) 657-662.

- Lynch S. P, Hydrogen embrittlement phenomenon and mechanisms, *Corr. Rev.* 30 (2012) 105-123.
- Lynch S. P, Hydrogen embrittlement phenomenon and mechanisms; Raja V. S, Shoji T, (Eds.) *Stress corrosion cracking: Theory and Practice*, Woodhead Publishing, Cambridge, 2011.
- Maday M. F, Hydrogen embrittlement susceptibility of conventional and reduced activation 9Cr –1Mo steels, *Fusion Sci. technol.* 47 (2005) 861-865.
- Majidi A. P, Streicher M. A, The double loop reactivation method for detecting sensitization in AISI 304 stainless steels, *Corrosion* 40 (1984) 584–593.
- Marcelina S, Peberea N, Regnier S, Electrochemical characterization of a martensitic stainless steel in a neutral chloride solution, *Electrochim. Acta* 87 (2013) 32-40.
- Marchetti L, Herms E, Laghoutaris P, Chene J, Hydrogen embrittlement susceptibility of tempered 9%Cr-1%Mo steel, *Int. J. Hydrogen Energ.* 36 (2011) 15880-15887.
- Maroef I, Hydrogen trapping in ferritic steel weld metal, *Int. Mat. Rev.* 47 (2002) 191-223.
- Maruyama K, Sawada K, Koike J, Strengthening mechanisms of creep resistant tempered martensitic steel, *J. Iron Steel Inst.* 41 (6) (2001) 641-653.
- Matsuoka S, Homma N, Tanaka H, Fukushima Y, Murakami Y, Effect of hydrogen on the tensile properties of 900 MPa-class JIS-SCM435 low alloy steel for use in storage cylinder of hydrogen station, *J. Jpn. Inst. Met.* 70 (12) (2006) 1002-1011.
- Mesquita T. J, Chauveau E, Mantel M, Bouvier N, Koschel D, Corrosion and metallurgical investigation of two super martensitic stainless steels for oil and gas environments, *Corros. Sci.* 81 (2014) 152-161.

- Michler T, Naumann J, Hydrogen embrittlement of Cr–Mn–N–austenitic stainless steels, *Int. J. Hydrogen Energ.* 35 (2) (2010) 821-832.
- Moon J, Choi J, Han S, Huh S, Kim S, Lee C, Lee Z, Influence of precipitation behavior on mechanical properties and hydrogen induced cracking during tempering of hot-rolled API steel for tubing, *Mater. Sci. Eng. A* 652 (2016)120–126.
- Muller T, Heyn A, Babutzka M, Rosemann P, Examination of the influence of heat treatment on the corrosion resistance of martensitic stainless steels, *Mater. Corros.* 66 (7) (2015) 656-662.
- Nagao A, Smith C. D, Dadfarnia M, Sofronis P, Robertson I. M, Interpretation of hydrogen- induced fracture surface morphologies for lath martensitic steel, *Procedia. Mater. Sci.* 3 (2014) 1700 -1705.
- Nakamichi H, Sato K, Miyata Y, Kimura M, Masamura K, Quantitative analysis of Cr-depleted zone morphology in low carbon martensitic stainless steel using FE-(S)TEM, *Corros. Sci.* 50 (2008) 309-315.
- Nanninga N, Grochowski J, Heldt L, Rundman K, Role of microstructure, composition and hardness in resisting hydrogen embrittlement of fastener grade steels, *Corros. Sci.* 52 (2010) 1237-1246.
- Ning L, Zhongnag D, Menggen H, Effect of heat treatment on microstructure and mechanical properties of martensitic- ferritic steel containing 17%Cr and 2%Ni, *Mater. Sci. Technol.* 7 (1991) 1057-1062.
- Ogura T, Makino A, Masumoto T, A grain boundary etching method for the analysis of intergranular P-segregation in iron-based alloys, *Metall. Mater. Trans. A* 15 (8) (1984) 1563-1570.

- Olden V, Thaulow C, Johnsen R, Modelling of hydrogen diffusion and hydrogen induced cracking in supermartensitic and duplex stainless steels, *Mater. Desi.* 29 (2008) 1934-1948
- Orazem M. E, Tribollet B, *Electrochemical impedance spectroscopy*, Wiley & Hoboken New sons Jersey, 2008.
- Palit G. C, Kain V, Gadiyar H. S, *Electrochemical Investigations of Pitting Corrosion in Nitrogen-Bearing Type 316LN Stainless Steel*; *Corrosion* 49 (12) (1993) 977- 991.
- Pardo A, Merino M. C, Coy A. E, Veijo F, Arrabal R, Matykina E, Effect of Mo and Mn additions on the corrosion behavior of AISI 304 and 316 stainless steel in H₂SO₄, *Corros. Sci.* 50 (2008) 780-794.
- Park C. J, Shankar Rao V, Kwon H. S, Effects of sigma phase on the initiation and propagation of pitting corrosion of duplex stainless steel, *Corrosion.* 61 (1) (2005) 76-83.
- Pettersson R, Pan J, Depletion effects at phase boundaries in 2205 duplex stainless steel characterized by SKPFM and TEM/EDS, *Corros. Sci.* 51 (2009)1850-1860.
- Phadnis S. V, Satpati A. K, Muthe K. P, Vyas J. C, Sundaresan R. I, Comparison of rolled and heat treated SS 304 in chloride solution using electrochemical and XPS techniques, *Corros. Sci.* 45 (2003) 2467-2483.
- Porter D. A, Easterling K. E, *Phase Transformations in Metals and Alloys*, 3rd ed., CRC Press, Boca Raton, FL, 2009.
- Prabhu Gaunkar G. V, Huntz A. M, Lacombe P, Role of carbon in embrittlement phenomena of tempered martensitic 12Cr-0.15%C steel, *Metal. Sci.* (1980) 241-252.
- Pressouyre G. M, The classification of hydrogen traps in steel, *Metall. Trans. A* 10 (1979) 157-1573.

- Qi X, Mao H, Yang Y, Corrosion behavior of nitrogen alloyed martensitic stainless steel in chloride containing solutions, *Corros. Sci.* 120 (2017) 90-98.
- Rajasekhar A, Madhusudhan Reddy G, Mohandas T, Murti V, Influence of austenitizing temperature on microstructure and mechanical properties of AISI 431 martensitic stainless steel electron beam welds, *Mater. Desi.* 30 (5) (2009) 1612-1624.
- Sahlaoui H, Sidhom H, Philibert J, Prediction of chromium depleted-zone evolution during aging of Ni-Cr-Fe alloys; *Acta Mater.* 50 (2002) 1383-1392.
- Santos L. P. M, Beres M, Bastos I. N, Tavares S.S.M, Abreu H.F.G, Gomes da Silva, Hydrogen embrittlement of ultra high strength 300 grade maraging steel, *Corros. Sci.* 101 (2015) 12-18.
- Sathirachinda N, Pettersson, Pan J, Depletion effects at phase boundaries in 2205 duplex stainless steel characterized by SKPFM and TEM/EDS, *Corros. Sci.* 51 (2009)1850-1860.
- Scott P.M, Stress corrosion cracking in pressurized water reactors - interpretation, modeling, and remedies, *Corrosion* 56 (2000) 771-782.
- Sedriks A. J, *Corrosion of Stainless Steel*, 2nd ed. John Wiley & Sons Inc., 1996.
- Shi Z. M, Gong W, Tomota Y, Harjo S, Li J, Chi B, Pu J, Study of tempering behavior of lath martensite using in situ neutron diffraction, *Mater. Charact.* 107 (2015) 29-32.
- Siddiqui R. A, Abdullah H. A, Hydrogen embrittlement in 0.31% carbon steel used for petrochemical applications, *J. Mater. Process. Technol.* 170 (2005) 430-435.
- Smith W. F, *Principles of materials science and engineering*, McGraw-Hill, 1986.
- Song Y. Y, Li X. Y, Rong L. J, Ping D. H, Yin F. X, Li Y. Y, Formation of the reversed austenite during intercritical tempering in a Fe–13%Cr–4%Ni–Mo martensitic stainless steel, *Mater. Lett.* 64 (13) (2010) 1411-1414.

- Stansbury E. E, Buchanan R. A, Fundamentals of electrochemical corrosion; Publisher ASM International (2000).
- Strawstrom C, Hillert M, An improved depleted-zone theory of intergranular corrosion of 18–8 stainless steel, *J. Iron Steel Inst.* 207 (1969) 77–85.
- Sun Z, Benoit G, Moriconi C, Hamon F, Halm D, Hamon F, Henaff G, Fatigue crack propagation under gaseous hydrogen in a precipitation-hardened martensitic stainless steel *Int. J. Hydrogen Energ.* 36 (14) (2011) 8641–8644.
- Sunil Kumar B, Kain V, Macro and micro electrochemical techniques to study influence of sigma phase formation in a duplex stainless steel, *Adv. Mater. Res.* 794 (2013) 583-594.
- Taji I, Moayed M. H, Mirjalili M, Correlation between sensitization and pitting corrosion of AISI 403 Martensitic stainless steel; *Corros. Sci.* 92 (2015) 301-308.
- Tao X, Gu J, Han L, Characterization of precipitates in X12CrMoWVNbN10-1-1 steel during heat treatment, *J. Nucl. Mater.* 452 (2014) 557–564.
- Tasi M. C, Chiou C.S, Du J. S, Yang J. R, Phase transformations in AISI 410 stainless steel, *Mater. Sci. Eng. A* 332 (2002) 1-10.
- Tavares S.S.M, Silva F.J. da, Scandian C, Silva G. F. da, Abreu H.F.G. de, Microstructure and intergranular corrosion resistance of UNS S17400 (17- 4PH) stainless steel, *Corros. Sci.* 52 (2010) 3835–3839.
- Thomson R. C, Bhadesia H.K.D.H, Carbide precipitation in 12CrMoV power plant steel, *Metall. Trans. A* 23 (1992) 1171-1179.
- Tiwari G. P, Bose A, Chakravartty J. K, Wadekar S. L, Totlani M. K, Arya R. N, Fotedar R. K, A study of internal hydrogen embrittlement of steels, *Mater. Sci. Eng. A* 286 (2000) 269-281.

- Tsay L. W, Chang Y. M, Torng S, Wu H. C, Improved impact toughness of 13Cr Martensitic stainless steel hardened by laser, *J. Mater. Eng. Perform.* 11(4) (2002) 422-427.
- Ueji R, Tsuji N, Minamino Y, Koizumi Y, Ultra-grain refinement of plain low carbon steel by cold-rolling and annealing of martensite, *Acta Mater.* 50 (2002) 4177-4189.
- Venezuela J, Liu Q, Zhang M, Zhou Q, Atrens A, The influence of hydrogen on the mechanical and fracture properties of some martensitic advanced high strength steels studied using the linearly increasing stress test, *Corros. Sci.* 99 (2015) 98-117.
- Vignal V, Ringeval S, Thiebaut S, Tabalaiev K, Dessolin C, Heintz O, Herbst F, Chassagnon R, Influence of the microstructure on the corrosion behavior of low-carbon martensitic stainless steel after tempering treatment, *Corros. Sci.* 85 (2014) 42-51.
- Viswanathan R, Bruemmer S. M, In-Service degradation of toughness of steam turbine rotors, *J. Eng. Mater. Technol. Trans. ASME* 107 (1985) 316-324.
- Wallaert E, Depover T, Arafin M, Verbeken K, Thermal desorption spectroscopy evaluation of the hydrogen trapping capacity of NbC and NbN precipitates, *Metall. Mater. Trans. A* 45 (2014) 2412-2420.
- Wang G, Yan Y, Li J, Huang J, Qiao L, Volinsky A, Microstructure effect on hydrogen-induced cracking in TM210 maraging steel, *Mater. Sci. Eng. A* 586 (2013) 142-148.
- Wang S. S, Peng D. L, Chang L, Hui X. D, Enhanced mechanical properties induced by refined heat treatment for 9Cr–0.5Mo–1.8W martensitic heat resistant steel, *Mater. Desi.* 50 (2013) 174-180.
- Xu H, Xia X, Hua L, Dai Y, Evaluation of hydrogen embrittlement susceptibility of temper embrittled 2.25Cr-1Mo steel by SSRT method, *Eng. Fail. Ana.* 19 (2012) 43-50.

- Yokota T, Shiraga T, Evaluation of hydrogen content trapped by vanadium precipitates in a steel, *J. Iron Steel Inst. Int.* 2003, 43 (4): 534-538.
- Yoshini K, McMohaon Jr C. J, The cooperative relation between temper embrittlement and hydrogen embrittlement in a high strength steel, *Metall. Trans. A* 5 (2) (1974) 363-370.
- Zhai Z, Abe H, Miyahara Y, Watanabe Y, Effects of phosphorus segregation on stress corrosion cracking in the heat-affected zone of a dissimilar weld joint between a Ni-base alloy and a low alloy steel, *Corros. Sci.* 92 (2015) 32–42.
- Zhai Z, Miyahara Y, Abe H, Watanabe Y, Segregation behavior in the heat effected zone of an A533B/A182 dissimilar weld joint before and after simulated thermal aging, *J. Nucl. Mater.* 452 (2014) 133-140.
- Zhao H, Zhang Z, Zhang H, Hu J, Li J, Effect of aging time on intergranular corrosion behavior of a newly developed LDX 2404 lean duplex stainless steel; *J. Alloys & Comp.* 672 (2016) 147-154.
- Zheng Z. J, Gao Y, Gui Y, Zhu M, Corrosion behavior of nano crystalline 304 stainless steel prepared by equal channel angular pressing, *Corros. Sci.* 54 (2012) 60-67.